PROCEEDINGS

of the

Ninth International Conference on the Ultrasonic Measurement and Imaging of Tissue Elasticity©

Snowbird, Utah, USA
October 16 – 19, 2010

PROCEEDINGS

of the
Ninth International Conference
on the Ultrasonic Measurement and Imaging
of Tissue Elasticity©

Snowbird, Utah, USA
October 16–19, 2010

Table of Contents

QUESTIONS OR COMMENTS ARE WELCOME AT ANY TIME AT <secretariat@elasticityconference.org>

2010 SPONSORS

The Conference Organizers wish to express appreciation
to the following companies
for providing support of this year's Conference:

Ultrasonix Medical Corporation
for sponsoring
the Awards for Best Student Oral Presentation

Medison Corporation, Korea
for sponsoring
Printing of the Conference Proceedings Books

FOREWORD

Dear Conference Delegate:

Welcome to the 9th annual International Conference on the Ultrasonic Measurement and Imaging of Tissue Elasticity©.

The international participation in the Conference includes virtually all global entities engaged in research, development, commercialization and practice in the field. This year, we have returned to the 2006 ITEC venue at Snowbird Ski and Summer Resort in the Wasatch Mountains of Utah.

Last year's Conference feedback was again unanimous in the desire for continuation of the tutorial series. We are pleased that Drs. Tim Salcudean (CA) and Guy Cloutier (CA) have agreed to present this year's exciting tutorials on **prostate elastography** and its applications, and the challenges of potentially high impact clinical imaging methods in non-invasive **vascular elastography**. We are also continuing last year's popular format of the formal Poster Session, where each presenter has the opportunity to give a brief oral summary of his/her poster, and we thank Drs. Michael Richards (US) and Richard Lopata (NL) for their enthusiastic leadership in conducting this event.

This year we continue to attract a rapidly growing number of clinical papers. Following on last year, we continue to have three clinical sessions and one cardiovascular session.

Last year's Student Best Paper Presentations and Awards session was a resounding success. Due to the generous sponsorship from Ultrasonix Medical Corporation of Vancouver, Canada, the Conference will again deliver Student Best Paper certificates and cash awards to the authors of papers that have been judged as most meritorious through independent review cycles. On Saturday afternoon, we will have a special session in which the eight finalists will present their abstracts. The final awardees will be announced during the Conference dinner on Sunday evening.

We welcome and thank Medison Co. Ltd (Seoul, Korea) as a new sponsor of the Conference; this year's printing of the Conference Proceedings book is generously sponsored by Medison.

This year we welcome two new exhibitors to the Conference: Supersonic Imagine, Inc. (US) and E&I, Limited (US).

We would like to thank all the new and returning delegates, reviewers and session chairs for their continuing support of the Conference. Special thanks are in order to our enthusiastic support staff that has worked above and beyond. Ms. Christina Andrews of the Conference Secretariat's office has coordinated the logistics, correspondence and financial aspects of the Conference.; Ms. Karen Ophir volunteered to design the Conference's artwork, publications and the new web site, negotiate the hotel contract, organize the scientific program and edit all abstracts and compile the Conference Proceedings; Ms. Charlene Waldron has volunteered to assist Christina and Karen in various organizational tasks; Dr. Reza Zahiri Azar is acting as our official Conference photographer again this year; and Dr. Helen Feltovich for assisting with local arrangements.

The Conference is conducted under the joint auspices of the University of Rochester Center for Biomedical Ultrasound and the Ultrasonics Laboratory in the Department of Diagnostic and Interventional Imaging at the University of Texas Health Science Center at Houston. These organizations have contributed in personnel and equipment. Most direct funding for the Conference is derived from registration fees, and, with your continued support in abstract submissions and attendance, we are committed to improve and expand the Conference in the years to come. We appreciate your written and oral feedback that always helps us in planning for future Conferences.

We hope that you will enjoy this year's scientific and social programs as well as the Snowbird Resort and the fresh mountain air. We hope to see you again at our special 10th anniversary Conference next year!

J. Ophir and K.J. Parker, Conference Organizers
Snowbird, Utah, October 16th 2010

CONFERENCE–AT–A–GLANCE

Ninth International Conference on the Ultrasonic Measurement and Imaging of Tissue Elasticity©
Snowbird Ski and Summer Resort – Snowbird, Utah, USA October 16–19, 2010

Saturday, October 16		**9:00A – 8:00P**	
9:00A – 12:00P	**Set Up:**	Oral Presenters load presentations (CD or jump drive)	Ballroom I
		Poster Presenters set up presentations	Ballroom III
		Exhibitors set up exhibits	Ballroom III
9:00A – 8:00P		Registration Desk Open	Ballroom Foyer
11:00A – 8:00P	**Session EEX:**	Equipment Exhibit *(during breaks & Reception)*	Ballroom III
12:00P – 2:00P	**Session TUT:**	**Tutorials:**	Ballroom I
2:00P – 2:30P		*Coffee Break*	Conference Foyer
2:30P – 4:30P	**Session SAS:**	**Oral Presentations of Finalists for Student Awards Session**	
		Sponsored by Ultrasonix Medical Corporation	Ballroom I
4:30P – 5:00P		*Recess*	
5:00P – 6:00P	**Session POS:**	**Poster Session – Live Oral Summaries**	Ballroom III
6:00P – 8:00P		*Opening Dinner Reception*	Ballrooms II & III
Sunday, October 17		**7:00A – 10:30P**	
7:00A – 8:00A		*Group Breakfast*	Golden Cliff/Eagles Nest
7:00A – 5:30P		Registration Desk Open	Ballroom Foyer
8:00A – 5:30P	**Session POS:**	Posters	Ballrooms III
8:00A – 5:30P	**Session EEX:**	Equipment Exhibit	Ballrooms III
7:45A – 8:00A		Opening Remarks	Ballroom I
8:00A – 10:00A	**Session MIP–1:**	**Methods for Imaging Elastic Tissue Properties – I**	Ballroom I
10:00A – 10:30A		*Coffee Break*	Ballroom III
10:30A – 12:00P	**Session CAA-1:**	**Clinical and Animal Applications – I**	Ballroom I
12:00P – 1:30P		*Group Lunch*	Golden Cliff/Eagles Nest
1:30P – 3:15P	**Session MPT–1:**	**Mechanical Properties of Tissues – I**	Ballroom I
3:15P – 3:45P		*Coffee Break*	Ballroom III
3:45P – 5:30P	**Session SIP–1:**	**Signal and Image Processing – I**	Ballroom I
5:30P – 6:30P		*Group Photo*	TBA
7:30P – 10:30P		*Conference Dinner & Musical Event*	Ballroom I
		featuring Rich Wyman, pianist, singer, songwriter	
Monday, October 18		**7:00A – 6:30P**	
7:00A – 8:00A		*Group Breakfast*	Golden Cliff/Eagles Nest
7:00A – 5:30P		Registration Desk Open	Ballroom Foyer
8:00A – 5:30P	**Session POS:**	Posters	Ballroom III
8:00A – 5:30P	**Session EEX:**	Equipment Exhibit	Ballroom III
8:00A – 10:00A	**Session CVE:**	**Cardiovascular Elasticity**	Ballroom I
10:00A – 10:30A		*Coffee Break*	Ballroom III
10:30A – 12:00P	**Session MIP–2:**	**Methods for Imaging Elastic Tissue Properties – II**	Ballroom I
12:00P – 1:30P		*Group Lunch*	Golden Cliff/Eagles Nest
1:30P – 2:45P	**Session BTM:**	**Biomechanical Tissue Modeling**	Ballroom I
2:45P – 3:30P	**Session FIP:**	**Forward and Inverse Problems**	Ballroom I
3:30P – 4:00P		*Coffee Break*	Ballroom III
4:00P – 5:30P	**Session CAA–2:**	**Clinical and Animal Applications – II**	Ballroom I
6:15P		*Buses depart from the Cliff Lodge for night out. See Registration Desk for details.*	
Tuesday, October 19		**7:00A – 10:00P**	
7:00A – 8:00A		*Group Breakfast*	Golden Cliff/Eagles Nest
7:00A – 4:00P		Registration Desk Open	Ballroom Foyer
8:00A – 4:00P	**Session POS:**	Posters	Ballroom III
8:00A – 4:00P	**Session EEX:**	Equipment Exhibit	Ballroom III
8:00A – 9:00A	**Session CAA–3:**	**Clinical and Animal Applications – III**	Ballroom I
9:00A – 10:15A	**Session MIP–3:**	**Methods for Imaging Elastic Tissue Properties – III**	Ballroom I
10:15A – 10:45A		*Coffee Break*	Ballroom III
10:45A – 12:00P	**Session MPT–2:**	**Mechanical Properties of Tissues – II**	Ballroom I
12:00P – 1:30P		*Group Lunch*	Golden Cliff/Eagles Nest
1:30P – 3:30P	**Session MIP–4:**	**Methods for Imaging Elastic Tissue Properties – IV**	Ballroom I
3:30P – 4:00P		*Coffee Break*	Ballroom III
4:00P – 5:30P	**Session SIP–2:**	**Signal and Image Processing – II**	Ballroom I
7:00P – 10:00P		*Closing Pizza Party (Proceedings Book Signing)*	Atrium Lounge

PROGRAM

Ninth International Conference
on the Ultrasonic Measurement and Imaging
of Tissue Elasticity©

Snowbird, Utah, USA
October 16 – 19, 2010

Saturday, October 16 9:00A – 8:00P

9:00A – 12:00P Presentation & Exhibit Set Up

All Oral Presenters load presentations onto Conference computers — Ballroom I
Poster Presenters set up presentations — Ballroom III
Exhibitors set up exhibits — Ballroom III

9:00A – 8:00P

Registration Desk Open — Ballroom Foyer

11:00A – 12:00P 2:00P – 2:30P 4:30P – 5:00P 6:00P – 8:00P

Session EEX: Equipment Exhibit — Ballroom III

Saturday 12:00P – 2:00P
Session TUT: Tutorials

Chair: JC Bamber, UK *Co-Chair: R Souchon, France* — Ballroom I

Page No.

12:00P – 12:45P

109 PROSTATE ELASTOGRAPHY AND ITS APPLICATIONS. 24
SE Salcudean[1].*
[1]Univerity of British Columbia, Vancouver, BC, CANADA.

12:45P – 1:00P Discussion

1:00P – 1:45P

110 NON–INVASIVE VASCULAR ULTRASOUND ELASTOGRAPHY: A REVIEW OF CHALLENGES OF POTENTIALLY HIGH IMPACT CLINICAL IMAGING METHODS. 25
G Cloutier[1].*
[1]University of Montréal Hospital Research Center (CRCHUM), Montréal, Québec, CANADA.

1:45P – 2:00P Discussion

2:00P – 2:30P

COFFEE BREAK — Ballroom III

Saturday 2:30P – 4:30P
Session SAS: Oral Presentations of Finalists for Student Awards

Sponsored by Ultrasonix Medical Corporation, Vancouver, BC, Canada

Chair: WE Svensson, UK *Co-Chair: V Egorov, USA* — Ballroom I

Page No.

2:30P – 2:45P

016 REDUCTION OF REVERBERATION ARTIFACTS IN CAROTID STRAIN IMAGES USING BAYESIAN REGULARIZATION. 26
MM McCormick[1], T Varghese[1].*
[1]University of Wisconsin–Madison, Madison, WI, USA.

(Session SAS continues on next page)

** indicates Presenter*

(Session SAS continued from previous page) Page No.

2:45P – 3:00P

031 *IN VIVO* STUDY OF CEREBRAL ISCHEMIA USING SHEAR WAVE IMAGING. 27
E Macé[1], A Martín[2], G Montaldo[1], M Fink[1], B Tavitian[2], M Tanter[1].*
[1]Institut Langevin, ESPCI, Paris, FRANCE; [2]Experimental Molecular Medicine Laboratory, CEA–SHFJ, Orsay, FRANCE.

3:00P – 3:15P

046 SHEAR WAVE INDUCED RESONANCE ELASTOGRAPHY APPLIED TO THE VISCOELASTIC CHARACTERIZATION OF MIMICKING VENOUS THROMBOSIS. 28
C Schmitt[1], A Hadj Henni[1], G Cloutier[1].*
[1]University of Montréal Hospital Research Center (CRCHUM), Montréal, Québec, CANADA.

3:15P – 3:30P

048 CHARACTERIZATION OF TUMOR VASCULARIZATION IN MICE USING MRE AT 7T. 29
L Jugé[1], BT Doan[2], J Seguin[2], D Scherman[2], R Sinkus[3].*
[1]ENSCP, Paris, FRANCE; [2]UPCG, UMR 8151, Paris, FRANCE; [3]Laboratoire Ondes et Acoustique, ESPCI, Paris, FRANCE.

3:30P – 3:45P

052 EARLY DETECTION OF CORONARY STENOSIS WITH MYOCARDIAL ELASTOGRAPHY: A CLINICAL FEASIBILITY STUDY. 30
SJ Okrasinski[1], EY Wan, WN Lee[1], Y Oe, EE Konofagou[1].*
[1]Columbia University, New York, NY, USA.

3:45P – 4:00P

053 MAPPING THE ELECTRICAL ACTIVATION SEQUENCE OF THE HEART USING ELECTROMECHANICAL WAVE IMAGING: A VALIDATION STUDY IN CANINES. 31
J Provost[1], WN Lee[1], K Fujikura[1], EE Konofagou[1].*
[1]Columbia University, New York, NY, USA.

4:00P – 4:15P

071 THYROID ELASTOGRAPHY: EXPERIENCE OF 200 CASES. 32
E Fleury[1].*
[1]CTC Genese Medicina Diagnóstica, São Paulo, BRAZIL.

4:15P – 4:30P

076 TRANS–PERINEAL PROSTATE MRE AT 3T. 33
RS Sahebjavaher[1], R Sinkus[2], SE Salcudean[1].*
[1]Univerity of British Columbia, Vancouver, BC, CANADA; [2]Laboratoire Ondes et Acoustique, ESPCI, Paris, FRANCE.

4:30P – 5:00P

Recess

Saturday 5:00P – 6:00P

(Posters will be available for viewing and Coffee Break Discussion through Tuesday, October 19, 4:00P)

Session POS: Poster Session – Live Oral Summaries

Chair: MS Richards, USA *Co-Chair: R Lopata, The Netherlands* Ballroom III

Page No.

5:00P – 5:02P

013 ANALYSIS OF SHEAR VELOCITY ESTIMATION BIAS FOR PEAK TRACKING ALGORITHMS. 34
CR Hazard[1], S Park[1].*
[1]GE Global Research, Niskayuna, NY, USA.

5:02P – 5:04P

002 CARDIAC DEFORMATION MODEL FOR 3D CARDIAC STRAIN IMAGING. 35
C Ma[1], H Chen[2], T Varghese[1].*
[1]University of Wisconsin–Madison, Madison, WI, USA; [2]Emory University, Atlanta, GA, USA.

** indicates Presenter*

5:04P – 5:06P

5:06P – 5:08P

5:08P – 5:10P

5:10P – 5:12P

5:12P – 5:14P

5:14P – 5:16P

5:16P – 5:18P

5:18P – 5:20P

5:20P – 5:22P

(Session POS continues on next page)

(Session POS continued from previous page) Page No.

5:22P – 5:24P

103 TISSUE MICRO–MOTION IN HUMAN ERECTOR SPINAE AND QUADRICEPS MUSCLES OBSERVED *IN VIVO* USING ULTRASOUND ELASTOGRAPHY TECHNIQUES. 45

JR Fox[1], HM Langevin[1], C Koptuich[1].*
[1]University of Vermont, Burlington, VT, USA.

5:24P – 5:26P

107 REAL–TIME GRAPHICS PROCESSING UNIT BASED ULTRASOUND ELASTOGRAPHY. 46

NP Deshmukh[1], H Rivaz[1], PJ Stolka[1], H Kang[1], GD Hager[1], ME Alaf[2], EM Boctor[1,3].*
[1]Johns Hopkins University, Baltimore, MD, USA; [2]Johns Hopkins Medical Institutions, Baltimore, MD, USA; [3]Johns Hopkins Medicine, Baltimore, MD, USA.

5:26P – 6:00P **Discussion**

Saturday 6:00P – 8:00P

Opening Dinner Reception *Proceedings Book Signing* Ballroom II & III

Sunday, October 17 7:00A – 10:30P

7:00A – 8:00A
GROUP BREAKFAST Golden Cliff/Eagles Nest

7:00A – 5:30P
Registration Desk Open Ballroom Foyer

8:00A – 5:30P **Session POS: Posters** Ballroom III
Session EEX: Equipment Exhibit Ballroom III

Sunday 7:45A – 8:00A

OPENING REMARKS

KJ Parker, J Ophir Ballroom I

Sunday 8:00A – 10:00A

Session MIP–1: Methods for Imaging Elastic Tissue Properties – I

Chair: JL Gennisson, France *Co-Chair: H Eskandari, Canada* Ballroom I

Page No.

8:00A – 8:15A

035 SHEAR WAVE ELASTOGRAPHY OF THE KIDNEY: PRE–CLINICAL STUDY ON A KIDNEY FIBROSIS MODEL AND CLINICAL FEASABILITY STUDY ON 70 HUMAN RENAL TRANSPLANTS. 47

JL Gennisson[1], N Grenier[3], R Hubrecht[3], L Couzy[3], Y Delmas[3], M Derieppe[1], S Lepreux[3], A Criton[2], J Bercoff[2], M Tanter[1].*
[1]Institut Langevin–Ondes et Images, ESPCI ParisTech, Paris, FRANCE; [2]Supersonic Imagine, Aix en Provence, FRANCE; [3]Service de Néphrologie, Hôpital Pellegrin, Bordeaux, FRANCE.

8:15A – 8:30A

004 IMAGING TISSUE MECHANICAL PROPERTIES BY TRACKING HIGH AMPLITUDE SHEAR WAVES GENERATED VIA TRANSIENT NEEDLE PERTURBATION. 48

RJ DeWall[1], T Varghese[1], EL Madsen[1].*
[1]University of Wisconsin–Madison, Madison, WI, USA.

8:30A – 8:45A

007 A NEW METHOD FOR THE ACQUISITION OF STRAIN IMAGE VOLUMES. 49

RJ Housden[1], C Uff[2], L Chen[1], AH Gee[1], GM Treece[1], RW Prager[1], JC Bamber[2].*
[1]University of Cambridge, Cambridge, England, UK; [2]Institute of Cancer Research, Sutton, Surrey, England, UK.

** indicates Presenter*

8:45A – 9:00A

008 ELASTICITY IMAGING USING HARMONIC EXCITATION, ULTRAFAST IMAGING AND PLANAR INVERSION OF THE WAVE EQUATION. 50

R Zahiri Azar[1,2], K Dickie[1], C Chung[1], A Baghani[2], SE Sacludean[2], L Pelissier[1].*
[1]Ultrasonix Medical Corporation, Richmond, BC, CANADA; [2]University of British Columbia, Vancouver, BC, CANADA.

9:00A – 9:15A

029 *IN–VIVO* EVALUATION OF UTERINE ABNORMALITIES BASED ON ULTRASOUND SALINE INFUSED SONOHYSTEROGRAPHY STRAIN IMAGING. 51

EA Omari[1], T Varghese[1], MA Kliewer[1].*
[1]University of Wisconsin–Madison, Madison, WI, USA.

9:15A – 9:30A

032 ON THE PROPAGATION OF GUIDED ELASTIC WAVES IN THIN PLATES FOR QUANTITATIVE SHEAR WAVE ELASTOGRAPHY OF THE CORNEA AND THE SKIN. 52

TM Nguyen[1], JL Gennisson[1], D Touboul[3], P Humbert[4], J Bercoff[2], M Fink[1], M Tanter[1].*
[1]Institut Langevin Ondes et Images, ESPCI ParisTech, Paris, FRANCE; [2]SuperSonic Imagine, Aix en Provence, FRANCE; [3]Centre Hospitalo–Universitaire de Bordeaux, Bordeaux, FRANCE; [4]Centre Hospitalo–Universitaire de Besançon, Besançon, FRANCE.

9:30A – 9:45A

039 A CORRELATION TOMOGRAPHY OF COMPLEX SHEAR WAVE FIELD IN SOFT SOLIDS. 53

S Catheline[1], T Gallot[1], P Roux[1], J Brum[1], C Negreira[2].*
[1]Grenoble University & CNRS, LGIT, Grenoble, FRANCE; [2]Science University, LAU, Montevideo, URUGUAY.

9:45A – 10:00A

036 *IN–VIVO* TIME REVERSAL ELASTOGRAPHY: A PASSIVE CORRELATION TOMOGRAPHY. 54

T Gallot[1], S Catheline[1], P Roux[1], J Brum[1], C Negreira[2].*
[1]Grenoble University & CNRS, LGIT, Grenoble, FRANCE; [2]Science University, LAU, Montevideo, URUGUAY.

10:00A – 10:30A

COFFEE BREAK — Ballroom III

Sunday 10:30A – 12:00P

Session CAA–1: Clinical and Animal Applications – I

Chair: D Cosgrove, UK *Co-Chair: H Langevin, USA* Ballroom I

10:30A – 10:45A

062 PRELIMINARY ASSESSMENT OF SHEARWAVE™ ELASTOGRAPHY FEATURES IN PREDICTING BREAST LESION MALIGNANCY. 55

D Cosgrove[1], C Doré[2], R Hooley[3], E Mendelson[4], L Barke[5], A Cossi[6], B Cavanaugh[7], L Larsen[8].*
[1]Imperial College, Hammersmith Hospital, London, England, UK; [2]London, England, UK; [3]Yale Medical Center, Yale, CT, USA; [4]Northwestern Medical Center, Chicago, IL, USA; [5]Sally Jobe Breast Center, Denver, CO, USA,; [6]Boston Medical Center, Boston, MA, USA; [7]Thomas Jefferson University, Philadelphia, PA; USA, [8]University of Southern California, Los Angeles, CA, USA.

10:45A – 11:00A

009 AXIAL SHEAR STRAIN FEATURE FOR DIFFERENTIATING BREAST LESIONS. 56

H Xu[1], M Rao[1], T Varghese[1], S Baker[1], AM Sommer[1], TJ Hall[1], GA Sisney[1], ES Burnside[1].*
[1]University of Wisconsin–Madison, Madison, WI, USA.

(Session CAA–1 continues on next page)

(Session CAA–1 continued from previous page) Page No.

11:00A – 11:15A

018 ARFI IMAGING OF HUMAN PROSTATE *IN VIVO*: INITIAL FINDINGS FROM 20 PATIENTS. 57
L Zhai[1], S Rosenzweig[1], T Polascik[2], W Foo[2], V Mouraviev[2], J Madden[2], ML Palmeri[1], KR Nightingale[1].*
[1]Duke University; Durham, NC, USA; [2]Duke University Medical Center, Durham, NC, USA.

11:15A – 11:30A

074 ELECTRODE DISPLACEMENT BASED STRAIN IMAGING FOR MONITORING *IN–VIVO* OPEN–SURGERY THERMAL ABLATION THERAPIES. 58
N Rubert[1], S Bharat[1], R J Dewall[1], A Andreano[1], C Brace[1], J Jiang[1], L Sampson[1], T Varghese[1].*
[1]University of Wisconsin–Madison, Madison, WI, USA.

11:30A – 11:45A

028 STRAIN RATIO IN REAL TIME SONOELASTOGRAPHY OF THE PROSTATE AS A SEMI–QUANTITATIVE MEASUREMENT TOOL: IMPACT ON PROSTATE CANCER DETECTION. 59
D Junker[1], F Aigner[1], T De Zordo[1], F Pedross[1], G Schaefer[1], G Mikuz[1], W Horninger[1], W Jaschke[1], F Frauscher[1]. Presented by A Lebovici[1].*
[1]Medical University Innsbruck, Innsbruck, AUSTRIA.

11:45A – 12:00P

104 THORACOLUMBAR FASCIA SHEAR PLANE MOTION IN CHRONIC LOW BACK PAIN. 60
HM Langevin[1], JR Fox[1], C Koptiuch[1], NA Bouffard[1].*
[1]University of Vermont, Burlington, VT, USA.

12:00P – 1:30P

GROUP LUNCH Golden Cliff/Eagles Nest

Sunday 1:30P – 3:15P

Session MPT–1: Mechanical Properties of Tissues – I

Chair: GE Trahey, USA *Co-Chair: CR Hazard, USA* Ballroom I

Page No.

1:30P – 1:45P

024 A FEASIBILITY STUDY OF CALIBRATING OPTICAL STRAIN ELASTOGRAMS WITH BIOMECHANICAL TESTING. 61
H Marie[1], S Vadde[1], H Kukatla[1], S Gadapa[1], Yong Zhang[1], JR Sullins[1].*
[1]Youngstown State University, Youngstown, OH, USA.

1:45P – 2:00P

005 QUANTIFYING STORAGE MODULUS OF HUMAN HEPATIC CANCERS WITH *EX VIVO* DYNAMIC COMPRESSION TESTING. 62
RJ DeWall[1], S Bharat[1], T Varghese[1], ME Hanson[1], MA Kliewer[1].*
[1]University of Wisconsin–Madison, Madison, WI, USA.

2:00P – 2:15P

030 QUANTIFICATION OF THE VISCOELASTIC CHARACTERISTICS OF THE UTERUS AND ASSOCIATED PATHOLOGIES. 63
EA Omari[1], MZ Kiss[1], T Varghese[1], MA Kliewer[1], JM Harter[1], EM Hartenbach[1].*
[1]University of Wisconsin–Madison, Madison, WI, USA.

2:15P – 2:30P

034 NONLINEAR SHEAR MODULUS QUANTIFICATION BY COMBINING STATIC AND DYNAMIC ELASTOGRAPHY. 64
H Latorre–Ossa[1], JL Gennisson[1], E De Brosses[1], M Tanter[1].*
[1]Institut Langevin–Ondes et Images, ESPCI Paris Tech, Paris, FRANCE.

2:30P – 2:45P

075 ULTRASOUND ELASTICITY IMAGING OF HUMAN POSTERIOR TIBIAL TENDON. 65
L Gao[1], C Geffre[1], J Szivek[1], MS Taljanovic[1], LD Latt[1], RS Witte[1].*
[1]University of Arizona, Tucson, AZ, USA.

 ** indicates Presenter*

Page No.

2:45P – 3:00P

096 FREQUENCY DEPENDENCE IN PHASE WAVE SPEEDS RECOVERED FROM INTERFERENCE PATTERNS MADE WITH ARC DATA. 66
A Thomas[1], K Lin[1], JR McLaughlin[1], CR Hazard[2], K Thomenius[2], Z Hah[3], KJ Parker[3], DJ Rubens[4].*
[1]Rensselaer Polytechnic Institute, Troy, NY, USA; [2]GE Global Research, Niskayuna, NY, USA; [3]University of Rochester, Rochester, NY, USA; [4]University of Rochester Medical Center, Rochester, NY, USA.

3:00P – 3:15P

097 NEW COMBINATION OF ARC DATA: IMAGING SHEAR MODULI AND MATCHING PHANTOM RECOVERY FREQUENCY DEPENDENCE TO VISCOELASTIC MODELS. 67
K Lin[1], A Thomas[1], JR McLaughlin[1], CR Hazard[2], K Thomenius[2], Z Hah[3], KJ Parker[3], DJ Rubens[4].*
[1]Rensselaer Polytechnic Institute, Troy, NY, USA; [2]GE Global Research, Niskayuna, NY, USA; [3]University of Rochester, Rochester, NY, USA; [4]University of Rochester Medical Center, Rochester, NY, USA.

3:15P – 3:45P

COFFEE BREAK Ballroom III

Sunday 3:45P – 5:30P

Session SIP–1: Signal and Image Processing – I

Chair: S Catheline, France *Co-Chair: R Zahiri Azar, Canada* Ballroom I

Page No.

3:45P – 4:00P

006 A NORMALIZATION ALGORITHM FOR AXIAL–SHEAR STRAIN ELASTOGRAPHY. 68
L Chen[1], RJ Housden[1], GM Treece[1], AH Gee[1], RW Prager[1].*
[1]University of Cambridge, Cambridge, England, UK.

4:00P – 4:15P

089 LOCAL INVERSION OF THE WAVE EQUATION FOR ELASTICITY IMAGING USING FIR FILTERS. 69
A Baghani[1], R Zahiri Azar[1], SE Salcudean[1], R Rohling[1].*
[1]University of British Columbia, Vancouver, BC, CANADA.

4:15P – 4:30P

033 INVERSE PROBLEMS IN DYNAMIC ELASTOGRAPHY: THEORETICAL, EXPERIMENTAL AND NUMERICAL ANALYSIS. 70
T Deffieux[1], JL Gennisson[1], B Larrat[1], M Fink[1], M Tanter[1].*
[1]Institut Langevin–Ondes et Images, ESPCI Paris Tech, Paris, FRANCE.

4:30P – 4:45P

042 INCREASE IN SPATIAL RESOLUTION OF LATERAL MODULATION IMAGING. 71
C Sumi[1], K Shimizu[1], Y Takanashi[1].*
[1]Sophia University, Chiyodaku, Tokyo, JAPAN.

4:45P – 5:00P

091 BANDPASS SAMPLING OF HIGH FREQUENCY TISSUE MOTION. 72
H Eskandari[1], O Goksel[1], SE Salcudean[1], R Rohling[1].*
[1]University of British Columbia, Vancouver, BC, CANADA.

5:00P – 5:15P

049 A FAST GPU BASED 3D ULTRASOUND DEFORMATION SIMULATION FOR BENCHMARKING MOTION TRACKING ALGORITHMS. 73
TG Fisher[1], TJ Hall[1].*
[1]University of Wisconsin–Madison, Madison, WI, USA.

5:15P – 5:30P

061 A COUPLED SPECKLE TRACKING ALGORITHM FOR ELASTICITY IMAGING: INITIAL *IN VIVO* EXPERIENCE. 74
J Jiang[1], TJ Hall[1].*
[1]University of Wisconsin–Madison, Madison, WI, USA.

Sunday 5:30P – 6:30P

Group Photo TBA
6:30P – 7:30P *No Conference Activities*

Sunday 7:30P – 10:30P
Conference Dinner & Musical Event Ballroom I
Proceedings Book Signing *Announcement of Student Best Paper Award Recipients*
Musical Event: *Selections performed by Rich Wyman, Pianist, Singer, Songwriter*

Monday, October 18 7:00A – 5:30P

7:00A – 8:00A
GROUP BREAKFAST Golden Cliff/Eagles Nest
7:00A – 5:30P
Registration Desk Open Ballroom Foyer
8:00A – 5:30P **Session POS: Posters** Ballroom III
Session EEX: Equipment Exhibit Ballroom III

Monday 8:00A – 10:00A
Session CVE: Cardiovascular Elasticity
Chair: CL de Korte, The Netherlands *Co-Chair: EE Konofagou, USA* Ballroom I

Page No.

8:00A – 8:15A
019 A MODEL–BASED APPROACH TO INTRAVASCULAR ULTRASOUND ELASTOGRAPHY. 75
MS Richards[1], MM Doyley[1].*
[1]University of Rochester, Rochester, NY, USA.

8:15A – 8:30A
020 RF–BASED 2D STRAIN IMAGING IN THE NORMAL AND DISEASED ABDOMINAL AORTA. 76
RGP Lopata[1,2], HHG Hansen[3], GW Schurink[4], CL de Korte[3], EMH Bosboom[1,2], FN van de Vosse[1,2].*
[1]Eindhoven University of Technology, Eindhoven, The NETHERLANDS; [2]Maastricht University Medical Center, Maastricht, The NETHERLANDS; [3]Radboud University Nijmegen Medical Center, Nijmegen, The NETHERLANDS; [4]Maastricht University Medical Center, Maastricht, The NETHERLANDS.

8:30A – 8:45A
021 4D CARDIAC STRAIN IMAGING USING RF–DATA IN YOUNG CHILDREN. 77
RGP Lopata[1,2], MM Nillesen[3], JM Thijssen[3], L Kapusta[3], CL de Korte[3].*
[1]Eindhoven University of Technology, Eindhoven, The NETHERLANDS; [2]Maastricht University Medical Center, Maastricht, The NETHERLANDS; [3]Radboud University Nijmegen Medical Center, Nijmegen, The NETHERLANDS.

8:45A – 9:00A
003 SEGMENTAL DISPLACEMENT AND STRAIN ANALYSIS OF LEFT VENTRICULAR DEFORMATIONS. 78
C Ma[1], H Chen[2], T Varghese[1], PS Rahko[1], AF Kelly[1].*
[1]University of Wisconsin–Madison, Madison, WI, USA; [2]Emory University, Atlanta, GA, USA.

Page No.

9:00A – 9:15A

022 METHOD FOR MINIMIZING THE EFFECT OF CATHETER ECCENTRICITY IN INTRAVASCULAR ULTRASOUND ELASTOGRAPHY. 79
S Jing[1], MS Richards, MM Doyley[1].*
[1]University of Rochester, Rochester, NY, USA.

9:15A – 9:30A

023 PLAQUE VISUALIZATION WITH A COMBINED B–MODE/ARFI/DOPPLER REAL–TIME IMAGING SYSTEM: TEMPORAL AND SPATIAL STABILITY. 80
JR Doherty[1], DM Dumont[1], JJ Dahl[1], JD Allen[1], GE Trahey[1].*
[1]Duke University, Durham, NC, USA.

9:30A – 9:45A

037 NON–INVASIVE MULTI–ANGLE STRAIN IMAGING IN PULSATING VESSELS. 81
HHG Hansen[1], M Keijts[1,2], RGP Lopata[2,3], T Idzenga[1], CL de Korte[1].*
[1]Radboud University Nijmegen Medical Center, Nijmegen, The NETHERLANDS; [2]Eindhoven University of Technology, Eindhoven, THE NETHERLANDS; [3]Maastricht University, Maastricht, The NETHERLANDS.

9:45A – 10:00A

045 INTRAVASCULAR ULTRASOUND ELASTOGRAPHY OF CORONARY ARTERIES: A PRE– AND POST–ATHERECTOMY STUDY. 82
Y Majdouline[1], Y Saijo[2], F Destrempes[1], J Ohayon[3], G Cloutier[1].*
[1]University of Montréal Hospital Research Center (CRCHUM), Montréal, Québec, CANADA; [2]Tohoku University, Aobaku, Sendai, JAPAN; [3]UJF, CNRS UMR 5525, In[3]S, Grenoble, FRANCE.

10:00A – 10:30A

COFFEE BREAK Ballroom III

Monday 10:30A – 12:00P

Session MIP–2: Methods for Imaging Elastic Tissue Properties – II

Chair: B Guzina, USA *Co-Chair: K Kim, USA* Ballroom I

Page No.

10:30A – 10:45A

043 QUANTIFYING THE IMPACT OF SHEAR WAVELENGTH ON SHEAR WAVE SPEED ESTIMATION. 83
ML Palmeri[1], NC Rouze[1], MH Wang[1], X Ding[1], KR Nightingale[1].*
[1]Duke University, Durham, NC, USA.

10:45A – 11:00A

040 INTERNAL INDENTATION FOR DIRECT MODULUS ESTIMATION. 84
J Vappou[1], EE Konofagou[1].*
[1]Columbia University, New York, NY, USA.

11:00A – 11:15A

050 SHEAR STRAIN ELASTOGRAPHY USING OPTICAL COHERENCE TOMOGRAPHY AS A MEANS OF GENERATING CONTRAST. 85
A Grimwood[1], L Garcia[2], JC Bamber[2], J Holmes[3], P Woolliams[4], P Tomlins[4], Q Pankhurst[1].*
[1]Royal Institution of Great Britain, London, England, UK; [2]Institute of Cancer Research, Sutton, Surrey, England, UK; [3]Michelson Diagnostics Ltd., Orpington, Kent, England, UK; [4]National Physical Laboratory, Teddington, Middx, England, UK.

11:15A – 11:30A

055 NUMERICAL EVALUATION OF CORRELATION BASED 3D SPECKLE TRACKING FOR CARDIAC ULTRASOUND ELASTICITY IMAGING. 86
S Tripathy[1], MA Simon[1], K Kim[1].*
[1]University of Pittsburgh, Pittsburgh, PA, USA.

(Session MIP–2 continues on next page)

(Session MIP–2 continued from previous page) Page No.

11:30A – 11:45A

015 TRANSTHORACIC ACOUSTIC RADIATION FORCE IMPULSE IMAGING OF CARDIAC FUNCTION. 87
DP Bradway[1], SJ Hsu[2], PD Wolf[1], GE Trahey[1].*
[1]Duke University, Durham, NC, USA; [2]Siemens Healthcare, Issaquah, WA, USA.

11:45A – 12:00P

064 *EX VIVO* FEASIBILITY OF HARMONIC MOTION IMAGING OF HUMAN BREAST TUMORS. 88
EE Konofagou[1], C Maleke[1].*
[1]Columbia University, New York, NY, USA.

12:00P – 1:30P

GROUP LUNCH Golden Cliff/Eagles Nest

Monday 1:30P – 2:45P
Session BTM: Biomechanical Tissue Modeling

Chair: G Cloutier, Canada *Co-Chair: R Righetti, USA* Ballroom I

Page No.

1:30P – 1:45P

001 PARAMETRIC ANALYSIS OF AXIAL SHEAR STRAIN IMAGING ON ELLIPSOIDAL MASSES. 89
H Xu[1], T Varghese[1].*
[1]University of Wisconsin–Madison, Madison, WI, USA.

1:45P – 2:00P

011 THE FINITE DIFFERENCE MODEL OF SHEAR WAVE PROPAGATION IN VISCOELASTIC TISSUE. 90
G Cheng[1], X Han[1], W Tan[1], CR Hazard[2].*
[1]GE Global Research, Shanghai, Pudong District, CHINA; [2]GE Global Research, Niskayuna, NY, USA.

2:00P – 2:15P

012 FINITE ELEMENT SIMULATION OF SHEAR WAVE PROPAGATION INDUCED BY A VCTE PROBE. 91
S Audière[1,2], M Charbit[1], E Angelini[1], V Miette[2], J Oudry[2], L Sandrin[2].*
[1]Institut Telecom, Telecom ParisTech, CNRS LTCI, Paris, FRANCE; [2]Echosens, Paris, FRANCE.

2:15P – 2:30P

080 EFFECT OF BOUNDARY CONDITIONS ON THE PERFORMANCE OF POROELASTOGRAPHY TECHNIQUES IN COMPLEX SIMULATED MEDIA. 92
A Chaudhry[1], G Unnikrishnan[1], JN Reddy[1], R Righetti[1].*
[1]Texas A&M University, College Station, TX, USA.

2:30P – 2:45P

093 FEM SIMULATION OF HARMONIC TISSUE EXCITATION FOR PROSTATE ELASTOGRAPHY. 93
O Goksel[1], SE Salcudean[1].*
[1]University of British Columbia, Vancouver, BC, CANADA.

Monday 2:45P – 3:30P
Session FIP: Forward and Inverse Problems

Chair: JR McLaughlin, USA *Co-Chair: C Sumi, Japan* Ballroom I

Page No.

2:45P – 3:00P

084 ALGORITHMS FOR QUANTIATIVE NONLINEAR ELASTICITY IMAGING IN THREE DIMENSIONS. 94
S Goenezen[1], JF Dord[1], PE Barbone[2], AA Oberai[1].*
[1]Rensselaer Polytechnic Institute, Troy, NY, USA; [2]Boston University, Boston, MA, USA.

* *indicates Presenter*

3:00P – 3:15P

085 A DIRECT ALGORITHM FOR TIME–HARMONIC ELASTICITY IMAGING WITH MULTIPLE SOURCES. 95
Yixiao Zhang[1], AA Oberai[1], PE Barbone[2], I Harari[3].*
[1]Rensselaer Polytechnic Institute, Troy, NY, USA; [2]Boston University, Boston, MA, USA; [3]Tel Aviv University, Ramat Aviv, ISRAEL.

3:15P – 3:30P

094 MESH ADAPTATION FOR IMPROVING INVERSE–PROBLEM RECONSTRUCTION. 96
O Goksel[1], H Eskandari[1], SE Salcudean[1].*
[1]University of British Columbia, Vancouver, BC, CANADA.

3:30P – 4:00P

COFFEE BREAK Ballroom III

Monday 4:00P – 5:30P

Session CAA–2: Clinical and Animal Applications – II

Chair: W Weitzel, USA *Co-Chair: H Feltovich, USA* Ballroom I

4:00P – 4:15P

038 ULTRASOUND ELASTICITY IMAGING IN THE DETECTION OF INTESTINAL FIBROSIS AND EDEMA/INFLAMMATION IN RATS AND HUMANS WITH CROHN'S DISEASE. 97
JM Rubin[1], RW Stidham[1], PDR Higgins[1], J Xu[2], LA Johnson[1], M Zhang[1], D Moons[1], B McKenna[1], K Kim[2].*
[1]University of Michigan, Ann Arbor, MI, USA; [2]University of Pittsburgh, Pittsburgh, PA, USA.

4:15P – 4:30P

068 CONTRAST DIFFERENCES IN ULTRASOUND B–MODE AND STRAIN IMAGES OF BRAIN TUMORS – PRELIMINARY RESULTS. 98
T Selbekk[1,2], R Brekken[1,2], O Solheim[2,3], G Unsgaard[2,3].*
[1]SINTEF, Trondheim, NORWAY; [2]The Norwegian University of Science and Technology, Trondheim, NORWAY; [3]St. Olav Hospital, Trondheim University Hospital, Trondheim, NORWAY.

4:30P – 4:45P

072 DOUBLE PUSH ARF ASSESSMENT OF MUSCULAR MECHANICAL PROPERTIES IN A DOG MODEL OF DMD WITH MYOSTATIN VARIATION. 99
MR Scola[1], JN Kornegay[1], CM Gallippi[1].*
[1]The University of North Carolina at Chapel Hill, Chapel Hill, NC, USA.

4:45P – 5:00P

069 BREAST ELASTOGRAPHY: EXPERIENCE OF 800 CASES. 100
E Fleury[1].*
[1]CTC Genese Medicina Diagnóstica, São Paulo, BRAZIL.

5:00P – 5:15P

026 DOES THE ELASTOGRAPHY/B–MODE LENGTH RATIO PREDICT BREAST CANCER TUMOR GRADE? 101
RG Barr[1], JR Grajo[2], C Peterson[1].*
[1]Southwoods Radiology Consultants, Youngstown, OH, USA; [2]University of South Florida, Tampa, FL, USA.

5:15P – 5:30P

101 AXIAL–SHEAR STRAIN ELASTOGRAPHY FOR BREAST LESION CLASSIFICATION: INITIAL RESULTS FROM RETROSPECTIVE *IN VIVO* DATA. 102
AK Thittai[1], JM Yamal[2], LM Mobbs[3], CM Kraemer–Chant[3], S Chekuri[1], BS Garra[3], J Ophir[1].*
[1]The University of Texas Medical School, Houston, TX, USA; [2]The University of Texas School of Public Health, Houston, TX, USA;[3]Fletcher Allen Health Care, Burlington, VT, USA.

After 5:30P *No Conference Activities*

Monday 6:15P Bus Departure from Snowbird

A bus will be available for going to dinner for the evening. Ask at the Registration Desk for details.

Tuesday, October 19 7:00A – 10:00P

7:00A – 8:00A
GROUP BREAKFAST — Golden Cliff/Eagles Nest

7:00A – 4:00P
Registration Desk Open — Ballroom Foyer

8:00A – 4:00P **Session POS: Posters** — Ballroom III
Session EEX: Equipment Exhibit — Ballroom III

Tuesday 8:00A – 9:00A
Session CAA–3: Clinical and Animal Applications – III

Chair: JM Rubin, USA *Co-Chair: ML Palmeri, USA* Ballroom I

Page No.

8:00A – 8:15A

063 BREAST FAT: SHEAR–WAVE ELASTICITY MEASUREMENTS. 103
D Cosgrove[1], R Hooley[2], E Mendelson[3], L Barke[4], A Cossi[5], B Cavanaugh[6,7], L Larsen[8].*
[1]Imperial College, Hammersmith Hospital, London, England, UK; [2] Yale Medical Center, Yale, CT, USA; [3]Northwestern Medical Center, Chicago, IL, USA; [4]Sally Jobe Breast Center, Denver, CO, USA; [5]Boston Medical Center, Boston, MA, USA; [6]Thomas Jefferson University, Philadelphia, PA, USA; [7]University of Southern California, Los Angeles, CA, USA.

8:15A – 8:30A

106 MONITORING ABLATIVE THERAPY USING ULTRASOUND ELASTOGRAPHY: CLINICAL RESULTS. 104
H Rivaz[1], U Hamper[2], M Choti[2], GD Hager[1], EM Boctor[1].*
[1]Johns Hopkins University, Baltimore, MD, USA; [2]Johns Hopkins Medical Institutes, Baltimore, MD, USA.

8:30A – 8:45A

070 PROSTATE ELASTOGRAPHY: INITIAL EXPERIENCE AND CLINICAL PERSPECTIVE. 105
E Fleury[1].*
[1]CTC Genese Medicina Diagnóstica, São Paulo, BRAZIL.

8:45A – 9:00A

087 PROSTATE MECHANICAL IMAGING: CLINICAL RESULTS. 106
V Egorov[1], N Sarvazyan[1], RE Weiss[2], M Ankem[2], JW Slaton[3], LA Mynderse[4], PR Sieber[5], MD Efros[6], M Patel[1], AP Sarvazyan[1].*
[1]Artann Laboratories, Trenton, NJ, USA; [2]Robert Wood Johnson Medical School, University of Medicine and Dentistry of New Jersey, New Brunswick, NJ, USA; [3]Minneapolis VA Medical Center, Minneapolis, MN, USA; [4]Mayo Clinic, Rochester, MN, USA; [5]Urological Associates of Lancaster, Lancaster, PA, USA; [6]Accumed Research Associates, Garden City, NY, USA.

Tuesday 9:00A – 10:15A
Session MIP–3: Methods for Imaging Elastic Tissue Properties – III

Chair: TJ Hall, USA *Co-Chair: RJ Housden, UK* Ballroom I

Page No.

9:00A – 9:15A

056 DETECTION OF LAYERS OF ALIGNED COLLAGEN IN HUMAN CERVICAL TISSUE USING ULTRASOUND. 107
LM Reusch[1], J Anderson[1], L Carlson[1], C Pehlke[1], MA Kliewer[1], JM Harter[1], JJ Dahl[2], ML Palmeri[2], K Eliceiri[1], H Feltovich[1,3], TJ Hall[1].*
[1]University of Wisconsin–Madison, Madison, WI, USA; [2]Duke University, Durham, NC, USA; [3]Maternal Fetal Medicine, Intermountain Healthcare, Park City, UT, USA.

9:15A – 9:30A

060 ELASTICITY RECONSTRUCTION WITH DUAL TRANSDUCER MOTION TRACKING. 108
JM Abeysekera[1], A Baghani[1], H Eskandari[1], R Rohling[1].*
[1]University of British Columbia, Vancouver, BC, CANADA.

* *indicates Presenter*

9:30A – 9:45A

066 FREQUENCY DOMAIN EXTRACTION OF VISCOELASTIC PROPERTIES USING ACOUSTIC RADIATION FORCE. 109
SM Frew[1], A Baghani[1], H Eskandari[1], R Zahiri Azar[1], SE Salcudean[1].*
[1]University of British Columbia, Vancouver, BC, CANADA.

9:45A – 10:00A

073 CORTICAL ELASTICITY MEASUREMENT DURING ULTRASOUND-GUIDED KIDNEY BIOPSY: AN *EX–VIVO* STUDY. 110
GH Kruger[1], JM Rubin[1], DW Park[1], A Hinger[1], J Hamilton[2], P Gottschalk[2], WF Weitzel[1].*
[1]University of Michigan, Ann Arbor, MI, USA; [2]Epsilon Imaging, Inc., Ann Arbor, MI, USA.

10:00A – 10:15A

078 HIGH FRAME RATE 2D WAVE IMAGING ON CONVENTIONAL ULTRASOUND USING SECTOR SUBDIVISION, DELAY COMPENSATION, AND ANGULAR COMPOUNDING. 111
R Zahiri Azar[1,2], A Baghani[2], SE Sacludean[2], R Rohling[2].*
[1]Ultrasonix Medical Corporation, Richmond, BC, CANADA; [2]University of British Columbia, Vancouver, BC, CANADA.

10:15A – 10:45A

COFFEE BREAK Ballroom III

Tuesday 10:45A – 12:00P
Session MPT–2: Mechanical Properties of Tissues – II

Chair: KJ Parker, USA *Co-Chair: E Brusseau, France* Ballroom I

10:45A – 11:00A

098 *IN VIVO* FREQUENCY DEPENDENT SHEAR VISCOELASTIC PROPERTIES OF THE BRAIN IN NORMAL PRESSURE HYDROCEPHALUS. 112
K Lin[1], JR McLaughlin[1], KJ Streitberger[2], E Weiner[2], J Hoffmann[2,3], FB Freimann[4], D Klatt[2], J Braun[2], C Sprung[4], R Klingebiel[2,5], I Sack[2].*
[1]Rensselaer Polytechnic Institute, Troy, NY, USA; [2]University Medicine Berlin, Berlin, GERMANY; [3]University of California San Francisco, San Francisco, CA, USA; [4]University Berlin, Berlin, GERMANY; [5]Klinik im Park, Zürich, SWITZERLAND.

11:00A – 11:15A

047 A NOVEL INSTRUMENT FOR THE VISCOELASTIC SPECTROSCOPY OF BIOMATERIALS AND TISSUE MIMICKING MATERIALS FROM 10 TO 1000 HZ. 113
C Schmitt[1], A Hadj Henni[1], MÉ Tremblay[2], M Hamdine[2], MC Heuzey[2], PJ Carreau[2], G Cloutier[1].*
[1]University of Montréal Hospital Research Center (CRCHUM), Montréal, Québec, CANADA; [2]École Polytechnique, Montréal, Québec, CANADA.

11:15A – 11:30A

067 FURTHER CHARACTERISATION OF CHANGES IN AXIAL STRAIN ELASTOGRAMS DUE TO THE PRESENCE OF SLIPPERY TUMOR BOUNDARIES. PART I: SIMULATION STUDY. 114
L Garcia[1], J Fromageau[1], JC Bamber[1], C Uff[1].*
[1]Institute of Cancer Research, Sutton, Surrey, England, UK.

11:30A – 11:45A

081 FURTHER CHARACTERISATION OF CHANGES IN AXIAL STRAIN ELASTOGRAMS DUE TO THE PRESENCE OF SLIPPERY TUMOR BOUNDARIES. PART II: EXPERIMENTAL VERIFICATION. 115
C Uff[1], L Garcia[1], J Fromageau[1], JC Bamber[1].*
[1]Institute of Cancer Research, Sutton, Surrey, England, UK.

11:45A – 12:00P

082 MEASURING THE YOUNG'S MODULUS OF HUMAN BRAIN *IN VIVO* WITH SHEAR WAVE ELASTOGRAPHY. 116
C Uff[1], JC Bamber[1], NL Dorward[2].*
[1]Institute of Cancer Research, Sutton, Surrey, England, UK; [2]Royal Free Hospital, London, England, UK.

12:00P – 1:30P
GROUP LUNCH Golden Cliff/Eagles Nest

Tuesday 1:30P – 3:30P
Session MIP–4: Methods for Imaging Elastic Tissue Properties – IV
Chair: KJ Parker, USA *Co-Chair: J Vappou, USA* Ballroom I

3:30P – 4:00P
COFFEE BREAK — Ballroom III

Tuesday 4:00P – 5:30P
Session SIP–2: Signal and Image Processing – II
Chair: SE Salcudean, Canada *Co-Chair: AK Thittai, USA* — Ballroom I

Page No.

4:00P – 4:15P

086 GPU UTILIZATION FOR FAST 3D MOTION TRACKING ALGORITHMS. 125
TG Fisher[1], TJ Hall[1].*
[1]University of Wisconsin–Madison, Madison, WI, USA.

4:15P – 4:30P

017 SUBSAMPLE DISPLACEMENT INTERPOLATION USING WINDOWED–SINC RECONSTRUCTION WITH NUMERICAL OPTIMIZATION. 126
MM McCormick[1], T Varghese[1].*
[1]University of Wisconsin–Madison, Madison, WI, USA.

4:30P – 4:45P

090 ULTRASOUND ELASTICITY IMAGING USING THE CURL OF THE DISPLACEMENT. 127
A Baghani[1], R Zahiri Azar[1], SE Salcudean[1], R Rohling[1].*
[1]University of British Columbia, Vancouver, BC, CANADA.

4:45P – 5:00P

041 DISPLACEMENT ESTIMATION OF THE CAROTID ARTERY USING SYNTHETIC APERTURE IMAGING. 128
S Korukonda[1], MM Doyley[1].*
[1]University of Rochester, Rochester, NY, USA.

5:00P – 5:15P

105 ROBUST REAL TIME REGULARIZED ULTRASOUND ELASTOGRAPHY. 129
H Rivaz[1], EM Boctor[1], GD Hager[1].*
[1]Johns Hopkins University, Baltimore, MD, USA.

5:15P – 5:30P

010 A METHOD FOR AUTOMATIC PROSTATE SEGMENTATION USING COMBINED ULTRASOUND B–MODE AND ELASTOGRAPHY IMAGES. 130
SS Mahdavi[1], M Moradi[1], WJ Morris[2], SE Salcudean[1].*
[1]University of British Columbia, Vancouver, BC, CANADA; [2]Vancouver Cancer Center of the British Columbia Cancer Agency, Vancouver, BC, CANADA

5:30P – 7:00P *No Conference Activities*

Tuesday 7:00P – 10:00P
Closing Pizza Party
Proceedings Book Signing — Atrium Lounge

Session EEX: Equipment Exhibit

Ballroom III

SuperSonic Imagine, Inc.
Bothell, WA, USA.

E & I, Ltd.
Rochester, NY, USA.

Rich Wyman
International singer, songwriter, pianist.

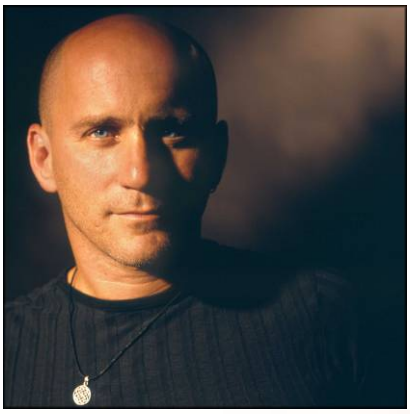

A native of Allentown, Pennsylvania, Rich Wyman discovered the piano at the age of seven, after he taught himself to read music and had taken classical violin at age five. By age eight, he was composing, at 14, performing and at 15, recording. Classically trained for 15 years, Rich graduated from the High School for the Performing Arts in Fort Lauderdale, Florida. He received his college education at New York University and the acclaimed Manhattan School of Music studying composition and piano. Currently, he tours extensively throughout Europe and the U.S. and lives in Park City, Utah with his wife, Lisa, and their two sons.

Rich is also an acclaimed music producer and film composer. The recipient of nine ASCAP Awards, he has worked with top names in the music industry including Eddie Van Halen and Andy Johns and opened concerts for Alanis Morissette and The Goo Goo Dolls.

Rich is a powerful and passionate performer, dedicated to creating original, rock piano with soul. Rich Wyman's accomplishments include award-winning songwriter, pianist, music producer and film composer. Rich is a representative for civil and social improvements, an international ambassador for 1We and, in his spare time, an avid mountain biker and snowboarder.

Tonight's performance will delight you with Rich's original compositions and his unique piano jazz rock style. Get ready to dance, rock or just listen and enjoy!

A detailed program will be available at the Conference Dinner.
Sunday, October 17th, 2010
Performance will start at 9:00 pm

AUTHOR INDEX

AUTHOR INDEX

ABSTRACTS

Ninth International Conference
on the Ultrasonic Measurement and Imaging
of Tissue Elasticity©

Snowbird, Utah, USA
October 16–19, 2010

Session TUT: Tutorials

Saturday, October 16 12:00P – 2:00P

109 **PROSTATE ELASTOGRAPHY AND ITS APPLICATIONS.**

S. E. Salcudean[1].*
[1]Electrical and Computer Engineering Department, University of British Columbia, Vancouver, BC, CANADA.

Elasticity imaging of the prostate has several potential applications, including:
The objective replacement of the digital rectal examination for screening purposes
prostate contouring for radiation treatment, image guidance for biopsy and focal treatment
and deformation modeling for the simulation of prostate interventions such as biopsies and brachytherapy.

This tutorial will describe approaches to prostate elasticity imaging, including magnetic resonance elastography, with an emphasis on ultrasound elastography. We will provide a brief survey of prostate cancer imaging results using elastography. We will then show that ultrasound elastography provides better delineation of the prostate gland than conventional B–mode imaging, and we will outline approaches to prostate intervention simulation using deformable tissue models.

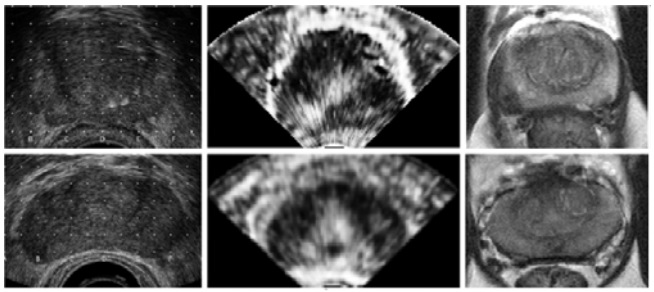

(a) (b) (c)

Figure 1: (a) Transverse Ultrasound B–Mode, (b) Ultrasound Elastography and (c) MRI images of the Prostate for two patients.

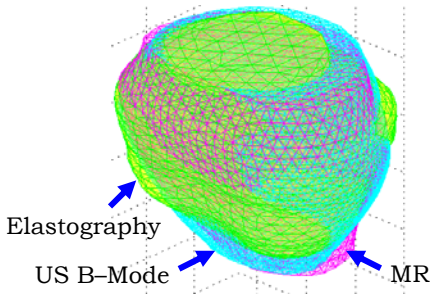

Figure 2: Prostate surface shapes in the three modalities

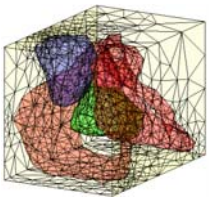

Figure 3: (a) Brachytherapy stepper with endorectal transducer; (b) mesh for patient–specific anatomical finite element model; (c) screen view of brachytherapy simulator with graphical and haptic feedback showing synthesized transversal ultrasound view and the corresponding patient anatomy.

* *indicates Presenter*

110 **NON–INVASIVE VASCULAR ULTRASOUND ELASTOGRAPHY: REVIEW OF CHALLENGES OF POTENTIALLY HIGH IMPACT CLINICAL IMAGING METHODS.**

Guy Cloutier[1]*.

[1]Laboratory of Biorheology and Medical Ultrasonics, University of Montréal Hospital; Radiology, Radio–Oncology and Nuclear Medicine Department, and Institute of Biomedical Engineering, University of Montréal, Montréal, Québec, CANADA.

Background: Only a minority of patients with carotid arterial disease encounter warning symptoms as the majority of strokes are caused by previously–asymptomatic lesions. Since morbidity and mortality after acute stroke are unacceptably high, patients should be diagnosed and treated before they develop any symptoms. Vulnerable carotid plaque usually consists of a thin fibrous cap, a large lipid core and dense macrophage inflammation on or beneath its surface. These tissue transformations are accompanied by changes in vessel wall elasticity. In this context, mechanical properties of arteries are believed to be of predictive values for prevention of plaque rupture and acute thrombosis formation. Within the last few years, non–invasive vascular ultrasound elasticity imaging methods were developed to address this issue, and to provide an objective evaluation of changes in rigidity of the vascular wall before the occurrence of significant atherosclerosis. Methods were conceptualized and tested in phantoms, *in vivo* in animal models, and some technologies were applied on a few human cases *in vivo*. Few studies so far were conducted with large populations, but on–going protocols are currently tested.

Objective: This presentation will be focussing on promising technologies such as pulse–wave velocity imaging with ultrafast scanning, vibroacoustography and supersonic shear–wave elasticity imaging. A comparative review of those methods aimed at quantifying the increase in rigidity of the artery wall due typically to hypertension and early atherosclerosis will be presented. For more advance lesions with atherosclerotic plaque and vessel narrowing, dynamic ultrasound elastography proved to be feasible. A comparative assessment of the acoustic radiation force and supersonic shear–wave imaging methods will be presented. A competing approach also aiming at quantifying the mechanical properties of atherosclerotic plaques is the non–invasive vascular elastography (NIVE) technology that maps tissue deformations produced by the natural pulsation of the artery. Recent achievements of leading groups developing ultrasound NIVE will be summarized.

Critical Opinion: At the end of this tutorial, the audience should have captured major challenges attributed to each of these methods. A summary of on–going activities at the Laboratory of Biorheology and Medical Ultrasonics of the University of Montréal Hospital Research Center will also be described.

016 **REDUCTION OF REVERBERATION ARTIFACTS IN CAROTID STRAIN IMAGES WITH BAYESIAN REGULARIZATION.**

Matthew M. McCormick[1], Tomy Varghese[1].*
[1]University of Wisconsin–Madison, 1111 Highland Ave, Madison, WI, USA.

Background: Motion tracking for ultrasound strain imaging is challenging due to noise sources such as deformation induced decorrelation, decorrelation due to out–of–plane motion and reverberations. Decorrelation can result in erroneous identification of true similarity metric peaks in block matching methods. Reverberations result in a motion of the reverberation echo that is discontinuous with the motion of signals from local tissue.

Aims: A method for Bayesian regularization introduced by Hayton [1] involves treating the similarity metric image (cross–correlation, sum of squared difference, etc.) as a probability image. Each metric image is shifted by the theoretical lower bound and scaled so the members sum to unity. A probability image is iteratively modified by neighboring probability images according to Bayes' Theorem:

$$Pr(u_x|u_{\mathcal{N}_x}) = \frac{Pr(u_{\mathcal{N}_x}|u_x)Pr(u_x)}{Pr(u_{\mathcal{N}_x})}$$

The likelihood term is chosen as the product of the maximum value of neighboring probabilities modulated by a Gaussian like term that falls off in magnitude with distance from the current displacement:

$$Pr(u_{\mathcal{N}_x}|u_x) = \prod_{\mathcal{N}_x} \max_v \left[Pr(v) \exp\left(-\frac{(v \quad u))^2}{2\sigma_u^2}\right)\right]$$

Methods: The effectiveness of the method is demonstrated using a human common carotid artery strain image in longitudinal orientation. Figure 1 shows the B–mode ultrasound and region of interest containing the intimal layer (a) and a large reverberation (b).

Results: Figure 2 shows neighboring probability images located at the reverberation, axial displacement image and axial strain image at iteration 0 (no regularization), and successive iterations. The true peak eventually emerges, and the artifact is removed without loss of resolution in the strain image.

Conclusions: The demonstrated method reduces decorrelation and reverberation noise artifacts by fusing information from neighboring blocks prior to displacement and strain being estimated. It is robust to the decorrelation and reverberation noise present and results in minimal loss of spatial resolution, computational time and additional memory requirements.

Acknowledgements: This work is supported by NIH grant 5R21EB010098–01.

References:

[1] Hayton P. et al.: A Non–Rigid Registration Algorithm for Dynamic Breast MR Images. Artificial Intelligence, V144, pp. 125–156, 1999.

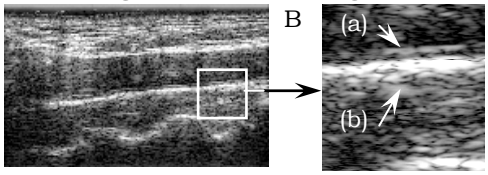

Figure 1: Carotid B–Mode and region of interest. (a) Vessel intima (b) Reverberation.

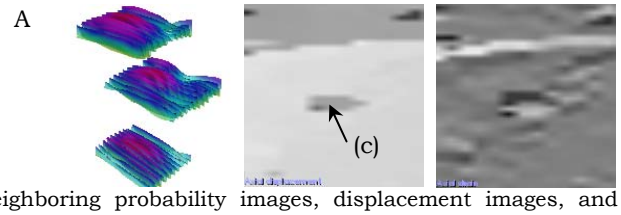

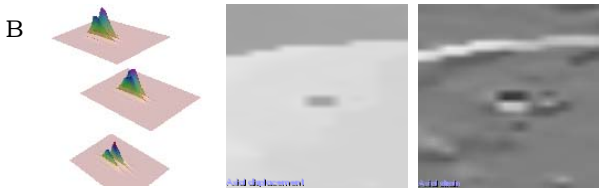

Figure 2: Neighboring probability images, displacement images, and strain images, respectively.
A) Iteration 0: No regularization. (c) Displacement in opposite direction of surrounding tissue due to reverberation.
B) Iteration 2: Regularization isolates bi–modal distribution from the reverb and local tissue.
C) Iteration 3: Further influence from surrounding tissue yields the correct displacement and strain.

* *indicates Presenter*

031 ***IN VIVO* STUDY OF CEREBRAL ISCHEMIA USING SHEAR WAVE IMAGING.**

E Macé[1], A Martín[2], G Montaldo[1], M Fink[1], B Tavitian[2], M Tanter[1].*
[1]Institut Langevin, ESPCI ParisTech, Paris, FRANCE; [2]Experimental Molecular Medicine Laboratory, CEA–SHFJ, Orsay, FRANCE.

Background: Stroke is the third leading cause of death in industrialized countries and the most frequent cause of permanent disability in adults worldwide. So far, neuroimaging methods have been indispensable in understanding the different pathological processes underlying ischemic stroke in both the laboratory and clinic.

Aims: We investigated the potential of Shear Wave Imaging to provide new information on ischemic lesions and in particular to see if, like in many organs [1], stiffness is modified in damaged tissues.

Methods: Focal cerebral ischemia was produced in rats by transient 2 hour occlusion of the middle cerebral artery in the right brain hemisphere [2]. To follow the evolution of the ischemic lesion, rats were trepanned, and Shear Wave Imaging scans were performed *in vivo* in control animals and at 1, 2, 4 and 7 days after the stroke. Shear Wave Imaging consists of generating a shear wave and tracking its propagation using ultrafast ultrasound imaging to obtain a quantitative map of local brain stiffness [3]. We used an ultrafast ultrasound scanner from Supersonic Imagine (France) programmed with custom sequences and an 8MHz linear probe.

Results: The ischemic lesion was found to be very soft compared to healthy brain tissue. The mean value in the ischemic hemisphere was <7kPa compared to 12kPa in the normal brain (ranging from 2 to 25kPa in different regions). An evolution with time was also observed. From 1 to 7 days after occlusion, the soft part of the lesion increased in size, and the mean stiffness value decreased.

Conclusions: Shear Wave Imaging has the potential to provide a new insight into cerebral ischemia for research on small animal models. Stiffness is shown to be a potentially useful parameter for monitoring ischemic lesions because ischemic tissues exhibit a significant contrast in stiffness that evolves over time.

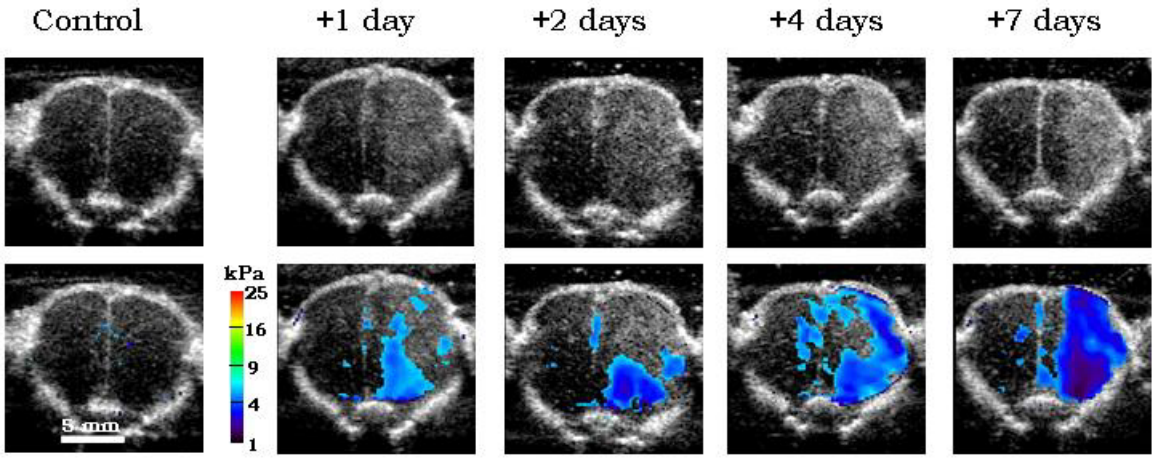

Figure 1: Elasticity maps superimposed on the B–mode images at different times after the occlusion. Only values <5.25kPa are shown to illustrate the difference between healthy and damaged tissues (ischemic hemisphere on the right).

References:

[1] M. Tanter, J. Bercoff, A. Athanasiou, T. Deffieux, J.–L. Gennisson, G. Montaldo, M. Muller, A. Tardivon, and M. Fink: Quantitative Assessment of Breast Lesion Viscoelasticity: Initial Clinical Results using Supersonic Shear Imaging. Ultrasound Med Biol, Vol. 34, No. 9, pp. 1373–1386, Sep 2008.

[2] A. Martin, R. Boisgard, B. Theze, N. Van Camp, B. Kuhnast, A. Damont, M. Kassiou, F. Dolle, B. Tavitian: Evaluation of the PRB/TSPO Radioligand [F–18]DPA–714 in a Rat Model of Focal Cerebral Ischemia. J Cereb Blood Flow Metab, Vol. 30, No. 1, pp. 230–241, Jan 2010.

[3] J. Bercoff, M. Tanter, and M. Fink: Supersonic Shear Imaging: A New Technique for Soft Tissue Elasticity Mapping. IEEE Trans Ultrason Ferroelectr Freq Control, Vol. 51, No. 4, pp. 396–409, Apr 2004.

046 **SHEAR WAVE INDUCED RESONANCE ELASTOGRAPHY APPLIED TO THE VISCOELASTIC CHARACTERIZATION OF MIMICKING VENOUS THROMBOSIS.**

Cédric Schmitt[1], Anis Hadj Henni[1], Guy Cloutier[1].*
[1]Laboratory of Biorheology and Medical Ultrasonics, University of Montréal Hospital Research Center (CRCHUM), Montréal, Québec, CANADA.

Background: Mechanical parameters based on compression elastography were proven adapted to age deep vein thrombosis (DVT) and hence could be of interest for staging recurrent thrombotic events. However, such a technique is subjective and operator dependent. Recently, we proposed SWIR (shear wave induced resonance) elastography [1], as a new imaging technique capable of improving conventional compression and dynamic elastography methods. This technique takes advantage of properly polarized shear waves to induce resonance of a confined mechanical heterogeneity (i.e., cylinder inclusion embedded in a second medium). Such resonance signature is suitable to estimate quantitatively the viscoelasticity of the heterogeneity, and thus of a DVT in the vascular context.

Aim: Our goal is to adapt SWIR elastography for *in vivo* DVT characterization, and to exploit the resonance information to assess viscoelastic parameters of DVT during aging and following therapy.

Methods: Realistic agar–gelatin phantoms composed of a fluid–filled artery and a mimicking incipient total (Figure 1a and 1c) or partial venous clot were built and tested in *in vitro* experiments. Corresponding modeling using the finite element method (FEM) was developed to simulate experimental conditions. Transient shear waves at different frequencies were generated by the vibration of a rigid plate at the medium surface (Figure 1a), or by a needle introduced in proximity of the region of interest and simulating a radiation pressure on a line segment. Induced propagation of shear waves was imaged with an ultrafast Ultrasonix SonixRP scanner (Ultrasonix Medical Corp., Richmond, Canada) with a dedicated post–processing reconstruction strategy to reach a high frame rate (3851 frames/sec). After validation of FEM models, an inverse problem (IP) strategy was formulated to recover, from vibration spectra, mechanical parameters of blood clots. DVT phantoms were then used to characterize mimicking clots with different viscoelasticities using the IP approach.

Results: Vibration spectra were composed of frequencies with high motion amplitude or resonance frequencies which were related to clot mechanical parameters. The frequency of the first resonance was used as input to the IP formulation to estimate mimicking clot elasticity and viscosity that typically ranged between 0.4–3.1kPa and 0.09–0.29Pa's, respectively. Experimental and simulation validation of the displacement map at resonance induced by a plate vibration are depicted in Figure 1d and 1b, respectively. Total and partial clot viscoelasticities calculated using either the plate or needle vibration, were in good agreement with reference measurements.

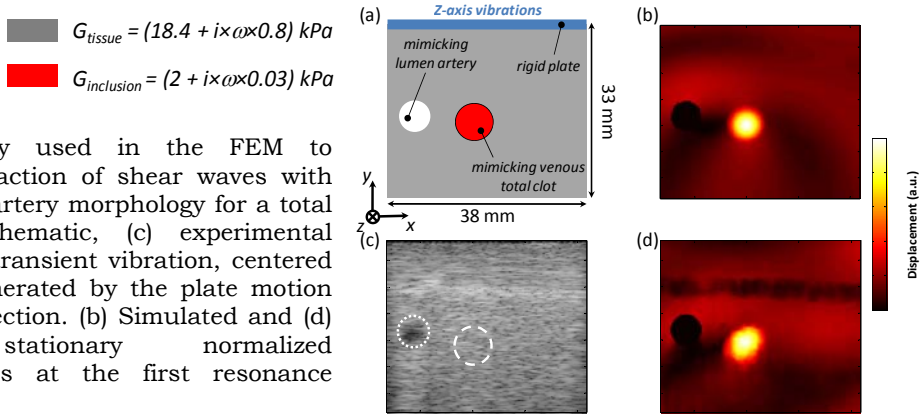

Figure 1: Phantom geometry used in the FEM to simulate the interaction of shear waves with realistic DVT and artery morphology for a total occlusion; (a) schematic, (c) experimental B–mode image. A transient vibration, centered at 125Hz, was generated by the plate motion following the z–direction. (b) Simulated and (d) experimental stationary normalized displacement fields at the first resonance frequency (123Hz).

Conclusions: The feasibility of SWIR to mechanically characterize mimicking DVT was investigated. Such a novel modality has the advantage to estimate clot viscoelastic parameters from the vibration resonance frequencies of the mechanical heterogeneity with a single line of measurement (within the clot). It also provides information which is less dependent on the accuracy of shear wave motion displacements.

Acknowledgment: Funding was obtained from the Canadian Institutes of Health Research (#MOP–84358).

Reference:

[1] Hadj Henni, A., Schmitt, C. and Cloutier, G.: Shear Wave Induced Resonance Elastography of Soft Heterogeneous Media. J. Biomech., 43 (8), pp. 1488–1493, 2010.

* *indicates Presenter*

048 **CHARACTERIZATION OF TUMOR VASCULARIZATION IN MICE USING MRE AT 7T.**

L Jugé[1], BT Doan[2], J Seguin[2], D Scherman[2], R Sinkus[3].*
[1]Service RMN, ENSCP, Paris, FRANCE; [2]UPCG, UMR 8151, Unité de Pharmacologie, Chimique et Génétique, et d'Imagerie, Paris, FRANCE; [3]Laboratoire Ondes et Acoustique, ESPCI, Paris, FRANCE.

Background: Assessment and follow up of neo–angiogenesis are major challenges in studying cancer for the development of new therapeutic strategies. The micro–vascularization of tumors is usually characterized via perfusion MRI. In order to develop new MRI methods for characterizing tumors in mice, we applied Magnetic Resonance Elastography (MRE), a recent technique for assessing the viscoelastic properties of tissues [1, 2]. MRE supplies new physical parameters for improving the specificity in breast cancer diagnosis and liver fibrosis staging [3]. Our working hypothesis is that alterations of tissue vascularization lead to significant changes in the viscoelastic properties which are also accompanied by changes in tissue diffusivity as measured via Diffusion Weighted MRI.

Aims: Characterization of neo–vascularization by MRE during tumor growth in 2 mouse models at 7T.

Methods: CT26 tumors were implanted on the flank (ectotopic model) and in the colon (orthotopic model) of mice Balb–C JRJ (n=6). Five (primitive stage), eleven (angiogenic stage) and eighteen (angiogenic + necrosis stage) days after implantation, tumors were imaged *in vivo* on a horizontal spectrometer 7T (Bruker Pharmascan). Each mouse underwent the following imaging protocol: quantitative T1 T2 relaxation maps, quantitative ADC map (9 b values: 0 to 2000s/mm²), high resolution T2–weighted images for an accurate depiction of the anatomy (RARE sequence, 123µm x123µm in plane resolution) and finally 3D steady–state MRE with a frequency of mechanical excitation of 1000Hz. Reconstructed maps of Gd (elasticity) and Gl (viscosity) had in isotropic voxel resolution of (300µm)³. After MRI study, tumors were taken off and histopathology was performed to assess the details of their microvascular architecture by optical microscopy and morphologic (volume and weigh) parameters.

Results: For the ectotopic model Gd and Gl of CT26 increased significantly (P<0.001) between Days 5 to 11, then reached a plateau on Day 18. The values on Day 18 are in the same range as Day 11. The orthotopic model had a consistent upward trend. Parameters were significantly different between Day 5 and Day 18 (Figure 1). A decrease of the viscoelastic properties was observed for the necrotic areas. We did not measure a difference of viscoelasticity values between the internal and external tumor region. Relaxation times and apparent diffusion coefficient could be correlated with MRE images. Histopathologic data were also coherent. Internal and peripheral regions showed similar homogeneous tissue density for both tumors. The vascular density increased, and the cellular remained stable.

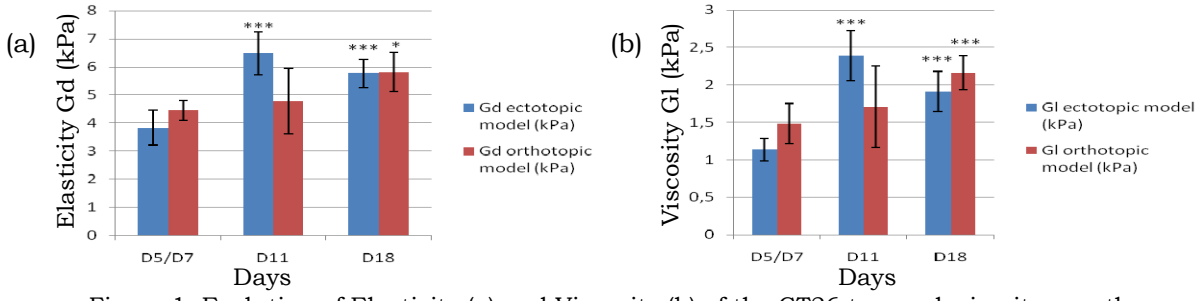

Figure 1: Evolution of Elasticity (a) and Viscosity (b) of the CT26 tumor during its growth.

Conclusions: MRE experiments of *in vivo* mice tumors were performed with high spatial resolution, and the results are very promising. Tumor evolution stages can be characterized by viscoelastic parameters. There is a close correlation between alterations in the viscoelastic parameters and the tumor change in time, and the neo–vascularization. Furthermore, we are currently studying the changes in viscoelastic parameters: (1) of the tumor during anti–angiogenic treatment using the combretastatin A–4 phosphate (CA4P) to validate the use of MRE for the monitoring of new anti–vascular therapies; (2) of the liver where metastasis were developed in the orthotopic model at eighteen days.

References:

[1] Sinkus R et al.: Phys. Med. Biol., 45, pp. 1649–64, 2000.
[2] Pernot M et al.: Ultrasound Med. Biol., 33(7), pp. 1075–85, 2007.
[3] Huwart L et al.: Gastroenterology, 135(1), pp. 299–302, 2008.

052 **EARLY DETECTION OF CORONARY STENOSIS WITH MYOCARDIAL ELASTOGRAPHY: A CLINICAL FEASIBILITY STUDY.**

Stanley J. Okrasinski[1], Elaine Y. Wan[2], Wei–Ning Lee[1], Yukiko Oe[2] and Elisa E. Konofagou[1,3].*
[1]Biomedical Engineering Department, Columbia University, 351 Engineering Terrace, 1210 Amsterdam Avenue, New York, NY, 10032, USA; [2]Cardiology Division, Columbia University, 622 West 168th Street, New York, NY, 10032, USA; [3]Radiology Department, Columbia University, 630 West 168th Street, New York, NY, 10032, USA.

Background: Cardiovascular disease is the leading cause of death worldwide. 2D echocardiography is commonly used in cardiology to assess wall motion abnormalities as a result of coronary artery stenosis (CAS). However, the abnormalities may not be manifested until significant levels of CAS are present. CT angiography is a technique which is regarded as the current gold standard in diagnosing CAS, though it exposes patients to a high level of x–ray radiation. Myocardial Elastography (ME) [1,2] is a non–invasive, radio frequency (RF) based, angle independent [3] technique which has been previously validated against sonomicrometry to provide accurate identification of ischemia at various levels of stenosis in canines [4].

Aims: This study investigates the capability of ME to detect and localize CAS in human subjects.

Methods: Five human subjects, three with CAS, two without CAS, were included in this study. Fluoroscopy and CT angiography following catheterization were performed in all subjects. Short–axis RF frames were acquired using a clinical ultrasound scanner (Ultrasonix SonixRP, Ultrasonix Medical Corporation, BC, Canada) with a 3.3MHz phased array (SA4–2) of up to 300 frames/second using an automated motion–gated technique. Inter–frame axial and lateral displacements were estimated using normalized cross–correlation (window size: 9.2mm, 80% overlap) and were then accumulated throughout the entire systolic phase. Axial and lateral Lagrangian strains were estimated using a least squares estimator (window size: 14mm). The centroid of the segmented endocardium was selected and used to convert axial and lateral strains to radial and circumferential strains. The associated B–mode cine loops were evaluated by a cardiologist for motion abnormalities, and an index of 1 to 7 was assigned to each wall segment according to its contractility, where 1 represented normal contractility.

Results: Table 1 shows the average radial and circumferential strains in the myocardial segment perfused by the stenosed artery. In two of the cases where CAS was present, the left anterior descending (LAD) and left circumflex (LCX) arteries both exhibited stenosis higher than 80% at the ostial level. In the third CAS case, the right coronary artery (RCA) exhibited a mid–level stenosis lower than 40%. However, despite the CAS presence in all pathological cases studied, wall motion scores indicated an absence of abnormalities (index=1).

Angiography results	Myocardial Segment	Radial strain	Circumferential Strain
No stenoses	Anterioseptal	34±5%	-36±8%
>80% LAD stenosis	Anterioseptal	-38±6%	22±20%
>80% LCX stenosis	Posteriolateral	-32±1%	8±5%
<40% RCA stenosis	Inferioseptal	5±5%	6±1%

Table 1: Average strain values found in myocardial segments perfused by arteries with stenosis.

Conclusions: The ME strain findings were consistent with CAS findings from angiography, showing that ME was capable of accurately indicating myocardial strain abnormalities resulting from CAS through a reversal or reduction of radial and circumferential strains relative to the normal cases. ME was found to be more sensitive to stenosis than the wall motion score evaluations, showing that ME may be capable of detecting stenosis at an earlier stage. This preliminary study may indicate an important role for ME to serve as a non–invasive, detection and localization tool of early onset coronary disease in the clinic.

Acknowledgements: This study was supported in part by NIH R01 EB006042.

References:

[1] Konofagou EE et. al.: Myocardial Elastography – A Feasibility Study *In Vivo*. Ultrasound in Med. and Biol., Vol. 28(4), pp. 475–482, 2002.
[2] Lee W–N et al.: Angle–Independent and Multi–Dimensional Myocardial Elastography – From Theory to Clinical Validation. Ultrasonics, Vol. 48, pp. 563–567, 2008.
[3] Zervantonakis I.K. et. al.: A Novel, View–Independent Method for Strain Mapping in Myocardial Elastography: Eliminating Angle– and Centroid–Dependence. Phys Med Biol, Vol. 52(14), pp. 4063–4080, 2007.
[4] Lee W.N. et. al.: Frame Rate Dependence of Myocardial Elastography Estimates Using a Physiologic 3D Biventricular Finite–Element Model of the Heart with Preliminary *In Vivo* Validation. 2008 IEEE IUS, pp. 962–965, 2009.

* *indicates Presenter*

053 **MAPPING THE ELECTRICAL ACTIVATION SEQUENCE OF THE HEART USING ELECTROMECHANICAL WAVE IMAGING: A VALIDATION STUDY IN CANINES.**

Jean Provost[1], Wei–Ning Lee[1], Kana Fujikura[1] and Elisa E. Konofagou[1].*
[1]Columbia University, New York, NY, USA.

Background: Cardiac conduction abnormalities constitute a major cause of death and disability worldwide. However, as of today, no technique routinely used in the clinic can non–invasively provide maps of the electrical activation sequence of the heart for accurate diagnosis and treatment planning and monitoring. Electromechanical Wave Imaging (EWI) is a novel imaging modality that maps the electromechanical activation sequence of the heart non–invasively by estimating regional transient deformations at very high frame rates.

Aims: In this presentation, we demonstrate that the electrical and electromechanical activation sequences are highly correlated during sinus rhythm and pacing in canines.

Methods: Four mongrel canines, ranging from 23 to 32kg in weight, were anesthetized before undergoing lateral thoracotomy. After removal of the pericardium, up to 12 electrodes were implanted epicardially to pace the heart and map the electrical activity. Radio frequency (RF) frames were acquired using an Ultrasonix RP with a 3.3MHz phased array at up to 500 frames/second, using a motion–gated, automated composite technique. Axial incremental displacements and strains were estimated using RF cross–correlation (window size: 4.6mm, 80% overlap) and a least squares estimator (window size: 6.75mm), respectively. In canines, the Electromechanical Wave (EMW), i.e., the propagating deformations resulting from the regional electrical activation of the myocardium, was mapped onto two standard 2D echocardiographic views and displayed in a 3D bi–plane view, during six conduction configurations, i.e., sinus rhythm and five different pacing schemes. Isochrones of the EMW were generated using a novel automatic cross–correlation method. Electrical and electromechanical activation times were then averaged in each echocardiographic segment and compared.

Results: Complex electrical activation patterns were mapped *in vivo* during six conduction schemes in both ventricles. During pacing, the EMW isochrones demonstrated the capability of EWI to localize a unique pacing site in all five pacing cases. 3D isochronal maps of the EMW were obtained when pacing (1) from the basal region of the lateral wall, (2) from the apical region of the lateral wall, (3) from the left–ventricular apex, (4) from the right–ventricular apex and (5) from the mid–level of the posterior wall displayed. In each case, the location of the earliest activation was in excellent agreement with the position of the pacing lead and propagation occurred from the epicardium to the endocardium. During sinus rhythm, the activation patterns obtained were in excellent agreement with transmural propagation patterns available in the literature, i.e., activation was initiated at multiple locations in ventricles, from the endocardium to the epicardium. A monotonic relationship between the electrical and electromechanical activation times was found, hereby confirming that EWI can accurately map the activation sequence.

Conclusions: This initial validation underlines the potential of EWI to serve as a unique non–invasive imaging tool for diagnosis and treatment planning, and monitoring of arrhythmias through ultrasound–based mapping of the transmural electromechanical activation sequence in real–time, reliably and non–invasively.

Acknowledgements: This study was supported in part by the National Institutes of Health (R01EB006042, R21HL096094). J. Provost was supported in part by the Natural Sciences and Engineering Research Council of Canada (NSERC) and Le Fonds Québécois de la Recherche sur la Nature et les Technologies (FQRNT).

071 **THYROID ELASTOGRAPHY: EXPERIENCE OF 200 CASES.**

E Fleury[1].*
[1]CTC Genese Medicina Diagnóstica, São Paulo/SP, BRAZIL.

Background: Thyroid masses are very common in our environment. It is believed that about 50% of the population subjected to ultrasound of the thyroid present with an abnormal result. These abnormalities usually have little clinical significance, nor chance of malignancy and are considered as incidental lesions. Many of these patients undergo fine needle aspiration biopsies for cytological diagnosis of the lesions. However, the rate of malignancy described in the literature of FNA is less than 5%. Sonography is the primary method of screening for thyroid lesions, and, currently, it appears that there is not an auxiliary tool to help on the differentiation of benign and malignant lesions. Studies are being carried out using ultrasound color Doppler scan, but in our practice we do not have good results with it [1]. In this context, studies are being carried out using the elastography as an auxiliary tool for the diagnosis of thyroid lesions, bearing in mind that benign lesions (colloid and goiter) tend to appear as soft, while malignant lesions (papillary and follicular carcinoma) as hard. In our results, we concluded that elastography of thyroid lesions can contribute to reducing the number of biopsies with negative results, without affecting the sensitivity of the method.

Aims: To demonstrate the results of 200 elastographic studies of thyroid lesions.

Methods: The author compares the findings by elastography with the results of 200 fine needle aspirations of thyroid lesions from 01/07/2009 to 01/01/2010. The elastographic studies were performed by two radiologists with 6 and 17 years of experience in thyroid imaging. Examinations were performed using a Sonix SP (Ultrasonix Medical Corporation, Vancouver, Canada) US system and a 5–14MHz multi–frequency linear probe. For the elastography study, special software was used for the Ultrasonix system, version 3.0.2 (Beta1), upgraded to the commercial version 2.6. Was used for elastographic classification a two point score, where score 1 corresponds to soft lesions and 2 to rigid lesions [2,3]. The lesions were divided according to their histology as benign or malignant.

Results: Results showed that all malignant lesions had a rigid appearance on the elastographic study. There were no false negative results. The results shows sensibility for cancer of 100%, specificity of 77.1%, predictive positive value of 38.4%, predictive negative value of 100% and diagnostic accuracy of 80%.

Conclusions: The author demonstrates that elastography can help in the diagnosis of thyroid lesions by sonography.

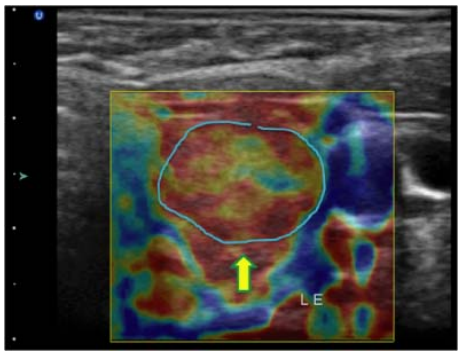

Figure 1: Heterogeneous mass on the left lobe of thyroid, soft on elastography, confirmed as colloid mass by cytology.

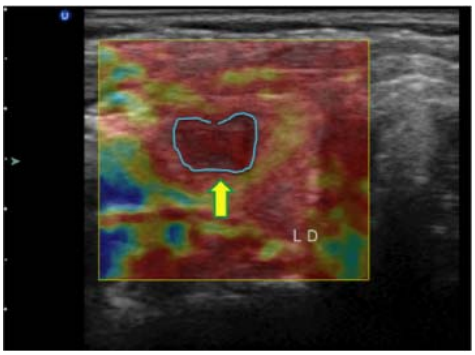

Figure 2: A mass on the right lobe of the thyroid, hard on elastography, confirmed as papillary carcinoma by cytology.

References:

[1] C Asteria, A Giovanardi, A Pizzocaro, L Cozzaglio, A Morabito, F Somalvico, A Zoppo: US–Elastography in the Differential Diagnosis of Benign and Malignant Thyroid Nodules. Thyroid, 18(5), pp. 523–31, May 2008.
[2] EFC Fleury, JC Fleury, S Piato, D Roveda Jr.: New Elastographic Classification of Breast Lesions During and after Compression. Diagn Interv Radiol, 15(2), pp. 96–103, Jun 2009.
[3] EFC Fleury, JC Fleury, VM Oliveira, JF Rinaldi, D Roveda Jr.: Proposal for the Systematization of the Elastographic Study of Mammary Lesions through Ultrasound Scan. Rev Assoc Med Bras, 55(2), pp. 192–6, Mar 2009.

* *indicates Presenter*

076 **TRANS–PERINEAL PROSTATE MRE AT 3T.**

RS Sahebjavaher[1], R Sinkus[2], SE Salcudean[1].*
[1]University of British Columbia, Vancouver, BC, CANADA; [2]Institut Langevin, CNRS UMR 7587, Univ. Paris 7, ESPCI Paristech, Laboratoire Ondes et Acoustique, Paris, FRANCE.

Background: Magnetic resonance elastography (MRE) is a noninvasive technique to image viscoelastic properties *in–vivo* using externally applied vibrations. There has been a great interest to apply MRE techniques for *in–vivo* imaging of prostate cancer. However, current methods [1–3] have limitations with acquiring high-SNR motion encoded MR-signals at 1.5T, and inducing shear waves of sufficient amplitude into the prostate reliably in a patient-friendly manner.

Aims: To assess the feasibility of MR elastography of the prostate with transperineal excitation at 3T.

Methods: To acquire high quality MRE, a second harmonic pulse sequence was implemented on a 3T scanner. The sensitivity loss of the second harmonic approach is offset by the shorter TE thus enabling acquisition of high SNR data especially at higher magnetic fields [4]. The mechanical excitation (~45Hz) is generated by a commercial electromagnetic exciter (4808 Bruehl & Kjaer) that is placed in the console room. The vibrations are transferred to the patient in the scanner (supine position) using a novel hydraulic transmission system that is MR safe. To reliably induce vibrations of sufficient amplitude in the prostate, the distal end of the exciter is applied to the perineal region of the subject as shown in Figure 1a. This allows for efficient transfer of compressional waves to the prostate that are mode–converted to shear waves at tissue interfaces. MRE was performed on five healthy subjects. After a high–resolution anatomical scan, MRE was acquired for a 64x64 matrix and 7 slices centered where the gland appears largest on the transverse plane. The voxel size was 1.5mm^3 isotropic, and the signal was averaged twice with an EPI factor of 5 where the total imaging time was ~20min. A cardiac coil was used. Images were processed offline, similar to the approach described in [4]. A region of interest (Figure 1b) surrounding the prostate was manually segmented, and the values for dynamic shear modulus and amplitude were extracted.

Results: Preliminary results for one of the subjects are shown in Figure 1b–d. Mechanical waves are transmitted effectively into the prostate and produce sufficient shear waves for successful reconstruction. The peak amplitude of the mechanical wave was 7μm (mean 3.3μm) as seen in Figure 1c. A map of the dynamic shear modulus G_d is shown in Figure 1d where we observe a close correspondence between the elasticity and T2 weighted images. For example, regions such as the urethra and the stiffer zones surrounding it can be visually identified Figure 1d. Also, we observed that mechanical excitations applied to the perineum did not cause discomfort for the subjects compared to cases were the excitation was applied to the pelvis (used in previous studies).

Figure 1: (a) Setup of transperineal excitation; images of (b) anatomy, (c) wave amplitude and (d) shear modulus of *in–vivo* prostate.

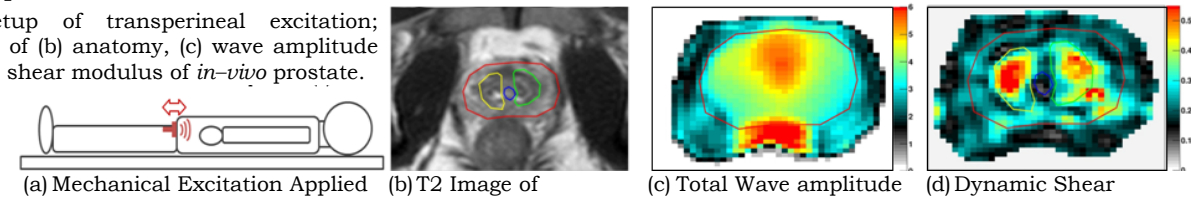

(a) Mechanical Excitation Applied at the Perineum | (b) T2 Image of Segmented Prostate | (c) Total Wave amplitude (μm) | (d) Dynamic Shear Modulus G_d (kPa)

Conclusions: MRE of the prostate at 3T with the second harmonic approach using a hydraulic exciter applied to the perineum is feasible. Applying the mechanical excitation to the perineum is comfortable for the patients even for extended imaging examinations. This method also allows for the use of endorectal coils (not used in this study) to boost SNR. Elasticity values obtained in this study are consistent among subjects, however, these values differ significantly from those reported in the literature (1–71kPa). Further work will characterize the hydraulic actuation system in more detail and will validate the elasticity measurements and their repeatability.

Acknowledgements: This work was supported by NSERC and CIHR.

References:

[1] Sinkus, R., et al.: Proceedings of the 11th Annual Meeting of ISMRM, Toronto, Canada, p. 586, 2003.
[2] Kemper, J., et al.: Fortschr Röntgenstr 176, pp. 1–6, 2004.
[3] Dresner, M.A., et al.: Proceedings of the 10th Annual Meeting of ISMRM, Philadelphia, USA, p. 526, 1999.
[4] Herzka, D.A., et al.: MRM, Vol. 62(2), pp. 284–291, 2009.

* *indicates Presenter*

013 **ANALYSIS OF SHEAR VELOCITY ESTIMATION BIAS FOR PEAK TRACKING ALGORITHMS.**

Christopher R. Hazard[1], Suhyun Park[1].*
[1]GE Global Research, One Research Circle, Niskayuna, NY, 12309, USA.

Background: Quantifying the velocity of shear waves in tissue may have clinical utility in the diagnosis of breast cancer, the staging of liver fibrosis and other applications. Shear velocity provides a quantitative measurement of the stiffness of the tissue. Viscosity is another important parameter that affects the shape of the propagating shear waves [1]. High viscosity values lead to rapid attenuation of the travelling shear waves. Several groups have suggested using radiation force to induce shear waves in the tissue. These acoustically generated shear waves are then tracked with ultrasound to provide displacement profiles at multiple locations in the tissue [2–5]. There are multiple algorithms in the literature for estimating the shear velocity from such displacement profiles. Chen et al., use the dispersion of the shear phase velocity to estimate the viscosity and shear modulus assuming a Voigt model of the tissue [7]. Palmeri et al. developed an algorithm, called Lateral Time To Peak (LTTP), which estimates the shear speed by tracking the peak displacement and assuming that peak travels at the shear velocity [6]. They note that the peak travels at the shear velocity for elastic media.

Aims: The goal of this theoretical study was to better understand the effect of viscosity on the LTTP algorithm.

Methods: Using the Green's function formalism of Bercoff et al. [1] an analytical expression for the velocity estimated by the LTTP algorithm is derived for an impulsive shear wave excitation. This expression gives some insight into the effect of viscosity. Simulations of the shear wave propagation using the Green's function are used to further evaluate the effect of viscosity for more realistic spatially extended excitations.

Results: The derived expression for the estimated velocity using the LTTP algorithm for an impulse is

$$v_{LTTP} = \sqrt{\frac{\upsilon^2}{4r^2} + c_s^2}$$

where v_{LTTP} is the estimated velocity, ν is the viscosity, c_s is the actual shear speed, and r is distance from the impulsive push. The expression shows a bias which occurs at high viscosity and when the observation is made close to the push. Simulations further illustrate this bias and show that qualitatively this holds even for more complicated shear wave excitation functions. Using multiple observation distances allows for a correction when the excitation is impulsive, but this strategy is less successful with more complex excitations such as those created by a push pulse from a standard imaging transducer.

Conclusions: The shear velocity estimated by the LTTP algorithm exhibits a bias when the viscosity is large and the observation is made close to the pushing location. This suggests that the observation location should be as far from the push as possible given the signal–to–noise limitations. This analysis is based on the Green's function derived assuming the Voigt model and is thus limited to situations in which the Voigt model is a good representation of the real tissue response.

References:

[1] Bercoff, J., Tanter, M., Muller, M., Fink, M.: The Role of Viscosity in the Impulse Diffraction Field of Elastic Waves Induced by the Acoustic Radiation Force. IEEE Trans. UFFC, 51(11), pp. 1523–1536, November, 2004.
[2] Sugimoto, T, Ueha, S, Itoh, K: Tissue Hardness Measurement using the Radiation Force of Focused Ultrasound. UFFC Symposium 1990, pp 1377–1380, 1990.
[3] Sarvazyan, AP., Rudenko, OV., Swanson, SD., Fowlkes, JB., Emelianov, SY.: Shear Wave Elasticity Imaging: A New Ultrasonic Technology of Medical Diagnostics. Ultrasound in Med. and Biol., 24(9), pp. 1419–1435, 1998.
[4] Bercoff J, Tanter M, Fink M: Supersonic Shear Imaging: A New Technique for Soft Tissue Elasticity Mapping. IEEE Trans. UFFC, 51(4), pp. 396–409, 2004.
[5] Nightingale K, McAleavey S, Trahey G: Shear Wave Generation using Acoustic Radiation Force: *In Vivo* and *Ex Vivo* Results. Ultrasound Med Biol., 29(12), pp. 1715–1723, 2003.
[6] Palmeri, ML., Wang, MH., Dahl, JJ., Frinkley, KD., Nightingale, KR.: Quantifying Hepatic Shear Modulus *In Vivo* using Acoustic Radiation Force. Ultrasound Med. Biol., 34(4), pp. 546–558, April, 2008.
[7] Chen S, Fatemi M, Greenleaf JF.: Quantifying Elasticity and Viscosity from Measurement of Shear Wave Speed Dispersion. J Acoust Soc Am, 115(6), pp. 2781–5, June, 2004.

002 **CARDIAC DEFORMATION MODEL FOR 3D STRAIN IMAGING.**

Chi Ma[1], Hao Chen[2], Tomy Varghese[1].*
[1]University of Wisconsin–Madison, Madison, WI, USA; [2]Emory University, Atlanta, GA, USA.

Background: Cardiac strain imaging [1-4] is a promising modality for evaluating myocardial functionality by imaging local and global strain distributions. Newer two–dimensional (2D) cardiac ultrasound transducers will enable three–dimensional (3D) cardiac strain imaging. However, most of current echocardiography systems provide data only over small sections and typically only provide 3D B–mode data. A 3D cardiac deformation model is therefore essential for the development of strain estimation algorithms for future 3D cardiac strain imaging or strain imaging applications.

Aims: We propose to develop and incorporate 3D cardiac deformation models with simulated 2D ultrasound transducers enabling evaluation and testing of 3D strain estimation algorithms.

Methods: Finite element analysis (FEA) based canine heart model developed by the Cardiac Mechanics Research Group at UCSD was used to construct a 3D numerical canine heart deformation model. This data set contains the deformation of 1296 points located within the cardiac wall at a sampling rate of 250Hz. The original motion vectors were resampled into 3D continuous smooth surfaces using non–linear 3D interpolation. These finer displacement patterns were used to position scatterers and to track their deformation over the cardiac cycle, which was then incorporated into an ultrasound simulation program [5]. Approximately 1.1 million scatterers were positioned within the cardiac wall, for a number density of around 10 scatterers/cm^3 to ensure Rayleigh scattering statistics. A frequency domain based simulation program [1] for linear/phased array transducers is used to generate simulated ultrasound radiofrequency (RF) data. We obtained a total of 125 RF frames over a cardiac cycle under the 250Hz temporal frame rate. A 2D multi–level strain estimation algorithm was used to estimate frame–to–frame local displacements, with B–Mode data used for the first cross-correlation step to estimate coarse displacements, with the final step using RF data with a 4 wavelength × 5 A–line windows with a 50% overlap to obtain the fine displacement estimates [6]. RF data along both parasternal short axis and long axis of the left ventricle were generated and utilized for strain imaging. Statistically significant simulation results using independent data sets will be presented.

Results: We quantitatively compare the deformation of the cardiac wall obtained from ultrasound RF data to actual scatterer movement or deformation (obtained from FEA). Eleven ROI numbered from one to eleven were used in the comparison as shown on the B–mode image (Figure 1). Estimated mean axial displacements and strains closely match the actual scatterer deformations for the eleven different ROI. Curve shapes comparing the mean estimated and actual displacement and strain for 4 of the ROI in Figures 2 and 3, respectively are almost identical, indicating displacement and strain tracking accuracy.

Conclusions: A 3D cardiac deformation model is proposed for evaluating 3D displacement tracking and strain estimation algorithms for cardiac strain imaging. Validation using ultrasound simulations and 2D strain estimation methods show encouraging results.

Acknowledgements: This work was supported by NIH grants 5R21EB010098 and R01CA112192.

References:

[1] E. Konofagou, J. D'Hooge, J. Ophir: Ultrasound Med Biol, Vol. 27, No. 4, pp. 475–82, 2002.
[2] T. Varghese, JA Zagzebski, PS. Rahko, CS Breburda: Ultrason Imaging, 25(1), pp. 1–16, 2003.
[3] S. Langeland, J. D'hooge, T. Claessens, et al.: IEEE Trans Ultrason Ferroel Freq Cont, 51(11), pp. 1537–46, 2004.
[4] RG. Lopata, MM. Nillesen, CN. Verrijp, et al.: Phys Med Biol, Vol. 55, No. 4, pp. 963-79, 2010.
[5] Y. Li and J. A. Zagzebski: IEEE Trans Ultrason Ferroelectr Freq Control, Vol. 46, No. 3, pp. 690–699, 1999.
[6] H. Chen and T. Varghese: Medical Physics, Vol. 36, No. 6, pp. 2098–2106, 2009.

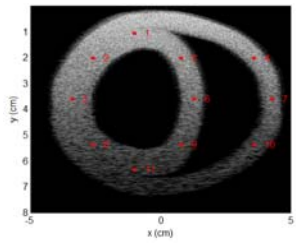

Figure 1: Short axis B–mode image from ultrasound simulation

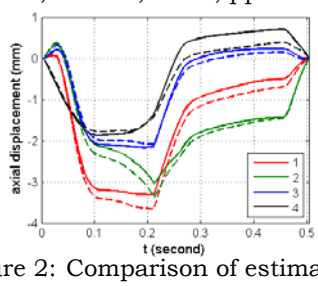

Figure 2: Comparison of estimated and ideal displacement at 4 of the ROI's shown in

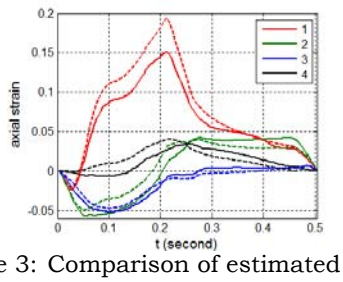

Figure 3: Comparison of estimated and ideal axial strain at 4 of the ROI's shown in Figure 1.

014 **ULTRASOUND ELASTOGRAPHY AS AN ADJUVANT TO CONVENTIONAL ULTRASOUND IN THE PRE–OPERATIVE DIAGNOSIS OF MALIGNANT AXILLARY LYMPH NODES IN PATIENTS WITH SUSPECTED BREAST CANCER: A PILOT STUDY.**

K Taylor[1], S O'Keeffe[1], MG Wallis[1], RJ Housden[2], GM Treece[2].*

[1]Cambridge Breast Unit, Box 97, Addenbrookes Hospital, Hills Rd, Cambridge CB2 2QQ, England, UK; [2]Engineering Department, University of Cambridge, Trumpington St, Cambridge CB2 1PZ, England, UK.

Background: Axillary node status is the most important prognostic indicator for survival from breast cancer. Conventional ultrasound (US) is currently accepted as the imaging modality of choice in the pre–operative assessment of axillary lymph nodes (ALN). However, US has recognized limitations [1], including a false negative rate which means that up to one third of ALNs with apparently normal node morphology are in fact metastatic [2]. Hence, there is a need for an imaging adjunct to US to increase sensitivity. Ultrasound elastography (UE) has been investigated in a wide range of clinical applications, including assessment of breast lesions, with limited research into identification and differentiation of lymph nodes generally. However, there are no published papers to date involving UE of axillary lymph nodes.

Aims: To compare the use of UE with US in the diagnosis of malignant ALNs in patients with suspected breast cancer.

Methods: 50 women with suspected breast cancer on US underwent routine imaging of ipsilateral ALNs, performed on a Toshiba Aplio ultrasound machine (Toshiba Medical Systems, Tochigi, Japan) followed by quasi–static UE performed using Stradwin software [3] interfaced to an Ultrasonix Sonix RP (Ultrasonix Medical Corp., Richmond, Canada) ultrasound machine with an 8–16 MHz transducer. Elastograms were created and displayed in grayscale (white as soft, black as stiff), with conventional US images displayed simultaneously side by side. UE images were visually scored 1–4 (normal–malignant) in terms of apparent stiffness and then compared with visual findings from US and the gold standard of surgical histology. A numerical indication of stiffness was determined from UE by comparison of normalised strain in the lesion and background.

Results: Of the 50 evaluated ALNs, 25 were normal on histology, indistinguishable from background tissue on UE and had normal morphology on US. 25 ALNs were metastatic on histology. Those completely metastatically replaced on US appeared uniformly stiff (black) on UE (Figure 1) and stiffness measurements concurred with this. Evaluation of results is ongoing at present, but preliminary findings suggest that ALNs appearing indeterminate on US nevertheless show a significant degree of stiffness on UE (Figure 2).

Conclusions: For the first time it has been demonstrated that normal and abnormal axillary lymph nodes can be differentiated using UE both visually and with strain values. Practice is needed to perform UE successfully in all cases and further research is necessary to consolidate these promising results.

Acknowledgements: This work was supported by Translation Award 081511/Z/06/Z from the Wellcome Trust and the National Institute for Health Research (NIHR) Cambridge Biomedical Research Centre (BMRC).

References:

[1] Alvarez S. et al.: Role of Sonography in the Diagnosis of Axillary Lymph Node Metastases in Breast Cancer: A Systemic Review. American Journal of Roentgenology, 186, pp. 1342–1348, 2006.

[2] Britton P. et al.: Use of Ultrasound Guided Axillary Node Core Biopsy in Staging of Early Breast Cancer. European Journal of Radiology, 19, pp. 561–569, 2009.

[3] Chen L et al.: Initial Clinical Experience of an Ultrasonic Strain Imaging System with Novel Noise–Masking Capability. British Journal of Radiology, in press 2010.

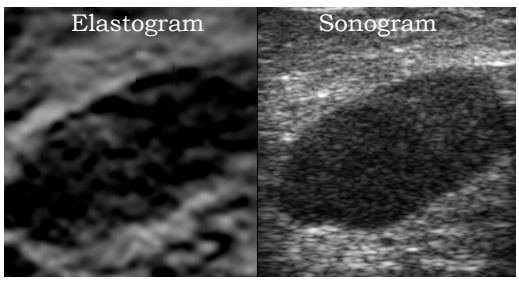

Figure 1: ALN is clear on both UE and US.

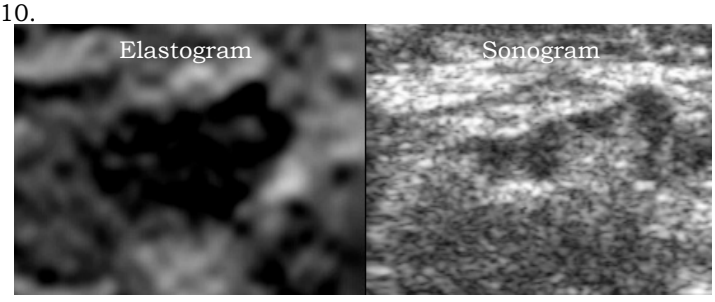

Figure 2: ALN is indeterminate on US but apparent on UE.

* *indicates Presenter*

025 **CHARACTERIZATION OF STRAIN ELASTOGRAMS DURING LARGE TISSUE DEFORMATIONS.**

Hazel Marie[1], Susheel Vadde[1], Shalini Gadapa[1], Harish Kukatla[1], Yong Zhang[1], John R. Sullins[1].*
[1]Youngstown State University, Meshell Hall, One University Plaza, Youngstown, OH, 44555, USA.

Background: The majority of elastography studies deal with tissues under relatively small deformations. An investigation of biomechanical behavior of soft tissue undergone a very large deformation using a noninvasive elasticity imaging method is rare. However, in certain medical applications, it is highly desirable to understand whether and how material property variations associated with large deformations can be observed and evaluated in an elastogram [1, 2].

Aims: To characterize the patterns and variations of optical strain elastograms of soft tissue exhibited during three deformation stages: linear, plastic and rupture. This type of information is potentially useful for assessing tissue damages and early detection of muscle micro–tears or micro–fractures.

Methods: Thirty–one tissue samples harvested from the abdominal areas of hybrid rats were collected. The samples were cut into a roughly dumbbell shape with a width of 1.8–2.5cm at both ends and 0.7–1.3cm in the middle. The sample length is about 8–11cm. With a standard Instron Tensiometer (Model 5500R), a sample was vertically stretched until it reached a breaking point. The entire deformation process was recorded with a SONY HD camcorder. The inter–frame displacement was computed using an optical flow algorithm, and a strain elastogram was obtained by taking the first order derivative of the displacement data.

Results: As can be seen in the figures below, strain elastograms showed distinctive patterns in three deformation stages. In the linear stage, strain pattern was relatively uniform or randomly distributed, suggesting that the original structure of muscle fiber was well maintained which is essential to have a linear response to external forces. In the plastic stage, tissue structure started to differentiate, showing higher strain values at the bottom of sample, indicating that permanent damage has been done to the tissue that was under a continuous tensile stress. Finally, in the rupture stage, a zone of large strain values was observed that corresponds to the location where the sample was completely broken.

Conclusions: Biomechanical tensile tests using thirty–one rat tissue samples demonstrated that an optical strain elastogram has the potential of providing a quantitative spatial description of tissue property changes during three deformation stages.

Acknowledgements: This work was partially supported by Ohio Board of Regents Research Incentive Grant #34241, Youngstown State University URC Grant 08–#8, and St. Elizabeth Health Center.

References:

[1] W.E. Garrett Jr.: Muscle Strain Injuries: Clinical and Basic Aspects. Medicine & Science in Sports & Exercise, 22(4). pp. 436–443, 1990.
[2] R.D. Boutin, R.C. Fritz, and L.S. Steinbach: Imaging of Sports–Related Muscle Injuries. Magnetic Resonance Imaging Clinics of North America, 11(2), pp. 341–371, 2003.

Figure 1:
A tissue sample and its strain elastogram in liner deformation.

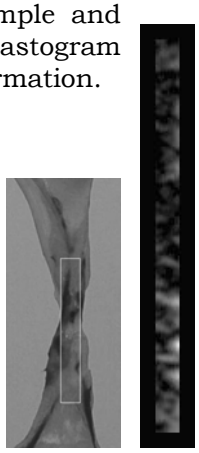

Figure 2:
A tissue sample and its strain elastogram in plastic deformation.

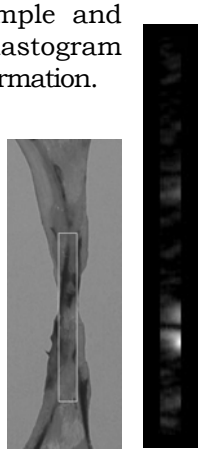

Figure 3:
A tissue sample and its strain elastogram during rupture stage.

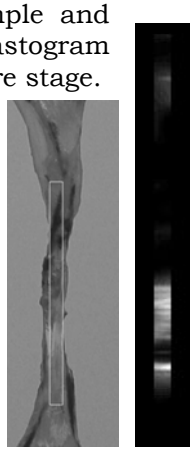

027 **STRAIN MAPPING BY IMAGE CORRELATION FOR X–RAY ELASTOGRAPHY.**

Byung H. Han[1], Min H. Cho[1], Soo Y. Lee[1].*
[1]Kyung Hee University, 1 Seochun, Kiheung, Yongin, Kyungki, SOUTH KOREA.

Background: Ultrasound images and magnetic resonance (MR) images have lower resolution than X–ray images for elastography [1,2]. The high noise level in ultrasound imaging causes the poor quality of an elasticity image due to the uncertainty of signal in the reconstruction process of inverse problem. The MR elastography also needs the additive devices which produce oscillating pulses. The X–ray elastography using the image correlation technique with the image sets of pre– and post–compression has advantages of high resolution owing to short wavelength of X–rays [3] and low–cost realization with a simple compressing device in tomosynthesis or tomography [4].

Aims: To calculate the strain map with a breast–mimicking phantom as a feasibility study of X–ray elastography.

Methods: A breast–mimicking phantom is made of epoxy which consists of a soft background and a hard inclusion around the center (Figure 1). The stiffness level of the soft and hard parts is controlled by the amount of polyamine hardener. In order to mimic glandular ducts of the breast, the phantom contains the tree–shaped red algae soaked into the contrast agent (Omnipaque 300, GE Healthcare, USA) in the soft part as well as the hard part. The Young's moduli of the soft background and the hard inclusion are 60kPa and 2800kPa, respectively. We acquired images of the phantom pre– and post–compression with the depth of 2.66mm in the homemade micro–computed tomography (micro–CT) using a micro–focus X–ray source (L8121–01, Hamamatsu, Japan) and a flat–panel detector (C7943CP–02, Hamamatsu, Japan). In order to calculate the strain map, first, we measured the displacement vectors from the 3D micro–CT images with and without compression using segmentation and digital image correlation techniques. We made the FEM simulation with ANSYS (ANSYS Inc., USA) for the comparison of the strain map with the experimental data.

Results: Experimental results and simulation data are shown in Figure 2.

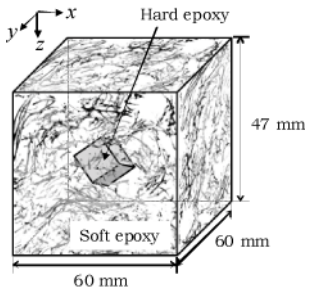

Figure 1: A breast-mimicking phantom.

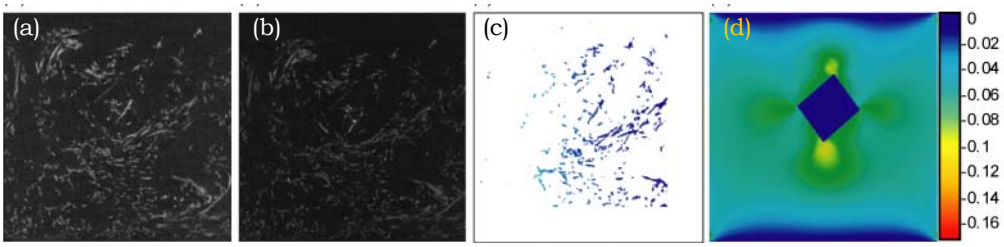

Figure 2: (a) Image before compression, (b) image after compression, (c) *z*–directional strain map in segmented regions, (d) *z*–directional strain map in FEM simulation.

Conclusions: There are common–low strains in the vicinity of the hard part in the simulated strain map and the experimental strains of the segmented regions mimicking glandular ducts and cancerous tissues with high intensity in X–ray images. The proposed method of strain calculation is expected to give the valuable information to find stiff abnormal areas over the other imaging modality.

Acknowledgements: This work was supported by grants from the National Research Foundation of Korea (No: 2009–0078310).

References:

[1] K. Nightingale, S. McAleavey, G. Trahey: Shear–Wave Generation using Acoustic Radiation Force: *In Vivo* and *Ex Vivo* Results. Ultrasound in Medicine and Biology, Vol. 29, pp. 1715–1723, 2003.
[2] A. Manduca, T.E. Oliphant, M.A. Dresner, J.L. Mahowald, S.A. Kruse, E. Amromin, J.P. Felmlee, J.F. Greenleaf, R.L. Ehman: Magnetic Resonance Elastography: Non–Invasive Mapping of Tissue Elasticity. Medical Image Analysis, Vol. 5, pp. 237–254, 2001.
[3] S.C. Lee, H.K. Kim, I.K. Chun, M.H. Cho, S.Y. Lee, M.H. Cho: A Flat-Panel Detector Based Micro-CT System: Performance Evaluation for Small-Animal Imaging. Physics in Medicine and Biology, Vol. 48, pp. 4173–4185, 2003.
[4] J.M. Park, E.A. Franken, M. Garg, L.L. Fajardo, L.T. Niklason: Breast Tomosynthesis: Present Considerations and Future Applications. RadioGraphics, Vol. 27, pp. S231–S240, 2007.

* *indicates Presenter*

051 **NANO–SCALE SHEAR WAVE MEASUREMENTS USING SWEPT-SOURCE OPTICAL COHERENCE TOMOGRAPHY (OCT).**

A Grimwood[1], JC Bamber[2], J Holmes[3], P Tomlins[4], Q Pankhurst[1].*
[1]Royal Institution of Great Britain, London, England, UK; [2]Institute of Cancer Research, Sutton, Surrey, England, UK; [3]Michelson Diagnostics Ltd., Orpington, Kent, England, UK; [4]National Physical Laboratory, Teddington, Middx, England, UK.

Introduction: Shear waves generated with a surface indenter were measured using optical coherence tomography. Analyzing phase information from the image data allowed detection of displacements with amplitudes estimated to be as small as ~20nm. Displacement frequencies were also measured via Fourier Transform to produce spectra containing peaks at the indenter frequency.

Background: Swept–source optical coherence tomography (OCT) is an optical imaging modality with a resolution on the micron–scale. Displacements significantly smaller than the system's pixel size (<4μm) can be measured by analyzing the OCT image signal's phase. Frequency and amplitude measurements of an applied mechanical signal are demonstrated here for vibrations at 400Hz, 600Hz and 800Hz with amplitudes as low as 23nm. Potential applications for such measurements include rheology [1] and contrast enhancement [2].

Aims: This presentation demonstrates OCT's sensitivity to sub–pixel amplitude shear waves generated with a surface indenter. Data from oscillation amplitudes as small as 23nm are recorded for a range of frequencies.

Methods: A surface indenter driven by a 30W loud speaker was used to generate shear waves across agarose samples and pork skin. The frequency and amplitude of the indenter was varied by changing the audio signal passed to the loud speaker. Images of the sample were taken using the OCT system in both B–mode and M–mode configuration. Phase variations for a specific location were measured with respect to time in the M–mode sequences, and combined lateral position/time in the B–mode sequences.

Results: Inspecting the spectrum obtained by Fourier Transforming the phase data with respect to time indicated a peak at the frequency of the indenter (Figure 1). A non–linear relationship between maximum signal voltage and peak intensity was also established for agarose samples and pork skin (Figure 2); however, it is not known if this arises from the loud speaker's signal response or the samples' physical properties.

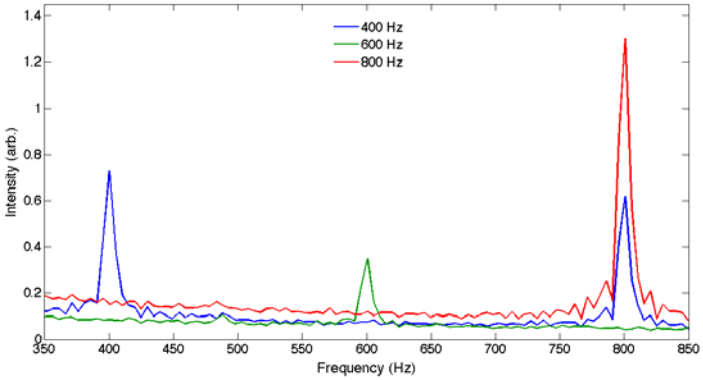

Figure 1: Spectra from phase data at three different indenter frequencies (400Hz spectrum contains harmonic peak at 800Hz).

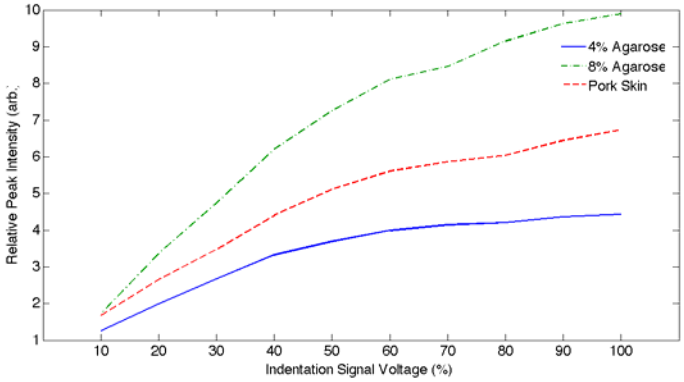

Figure 2: Relative phase amplitude measured from peak in spectrum for a 400 Hz indentation over a range of indenter signal amplitudes.

Conclusions: From the results, the OCT system appears capable of detecting shear waves generated with an indenter at amplitudes on the nano–scale. This is a marked increase on the system's standard resolution of ~10μm. This level of sensitivity has potential applications in rheometry, as contrast agents, and also, in the future, shear wave elastography.

Acknowledgements: This research was funded by an EPSRC CASE Award in conjunction with Michelson Diagnostics Ltd. Both the Biophotonics Dept. at NPL and Elastography Team at ICR are gratefully acknowledged for the support.

References:

[1] Crecea V, et al.: Magnetomotive Nanoparticle Transducers for Optical Rheology of Viscoelastic Materials. Optics Express, 17(25), pp. 23114–23122, 2009.
[2] John R, et al.: *In Vivo* Magnetomotive Optical Molecular Imaging using Targeted Magnetic Nanoprobes. PNAS, 107(18), pp. 8085–8090, 2010.

054 ***IN VIVO* EVALUATION OF FREEHAND STRAIN IMAGING ON BENIGN AND MALIGNANT BREAST LESIONS.**

Elisabeth Brusseau[1], Valérie Detti[1], Agnès Coulon[2], Emmanuele Maissiat[2], Nawèle Boublay[3], Yves Berthezène[2], Jérémie Fromageau[4], Nigel Bush[4], Jeffrey C. Bamber[4].*

[1]CREATIS–LRMN; CNRS UMR5220; Inserm U630; INSA–Lyon; Université Lyon 1, Bât. Blaise Pascal, 7 av. Jean Capelle, 69621 Villeurbanne, FRANCE; [2]Service de Radiologie, Hôpital Croix–Rousse, 69004 Lyon, FRANCE; [3]Pôle Imagerie/IMER, Les Tilleuls, 52 Bd Pinel, 69677 Bron Cedex 03, FRANCE; [4]Institute of Cancer Research, 15 Cotswold Rd, Sutton, Surrey SM2 5NG, UK.

Background: Breast cancer is the most common cancer in women worldwide. In the USA, for the year 2009, 192,370 new cases of invasive breast cancers and 40,170 female deaths were estimated [1]. In this study, the objective is to evaluate the performance of our 2D locally regularized strain estimation technique [2] with clinical data, by examining breast lesions during clinical routine. Our method already provided easily interpretable strain images with data acquired in a freehand configuration on elastography–dedicated phantoms and *ex vivo* dog tissue lesions [3].

Aims: Assessing the quality of strain images with 5 clinical cases of benign and malignant breast lesions.

Methods: Our 2D locally regularized strain estimation method computes the deformation related parameters (translations and scaling factors) as those that produce the best match between an initial ultrasound radio frequency (RF) region and its deformed version. In practical terms, the parameter estimation is performed through the constrained maximization of the normalized correlation coefficient (or NCC) between regions. When a parameter estimate is detected as insufficiently reliable (NCC<0.75), its value is recomputed by ensuring continuity with nearby reliable estimates. This procedure is particularly useful when processing *in vivo* acquisitions. Data were acquired in two centers, at the Hôpital de la Croix–Rousse, Lyon, France, with a Sonix RP ultrasound machine (Ultrasonix Medical Corp., Richmond, BC, Canada) equipped with a L14–5W/60 linear probe and at the Royal Marsden Hospital, London, UK, with an Acuson 128XP ultrasound system (Acuson Corp. now Siemens, Mountain View, CA, USA) working with a L7EF linear probe. Data were sampled at 40MHz and processed off–line. The five clinical cases examined are classified as follows: three fibroadenomas, one ductal carcinoma grade I, and one suspected carcinoma.

Results: For all lesions, movies of tissue strain during compression were obtained, with strains that can reach 15%. The NCC averaged over each movie was computed, leading for the five cases, to a mean value of 0.91, a minimum value of 0.87 and a maximum value of 0.98. These high NCC values confirm the reliability of the strain estimation. Lesions are clearly identified (Figure 1) and, for the five cases investigated, differences were observed in terms of lesion contour sharpness as well as in terms of extent of the lesion in the strain images compared to that in the ultrasound image.

Conclusions: Results demonstrated the ability of our technique to provide good quality strain images with clinical data. Future work will consist of ongoing investigating clinical cases and, in particular, tissue response under compression according to the benign or malignant characteristic of the lesion.

References:

[1] A. Jemal, R. Siegel, E. Ward et al.: Cancer Statistics, 2009. CA Cancer J. Clin, 59(4), pp. 225–249, 2009.

[2] E. Brusseau, J. Kybic, J.F. Deprez et al.: 2D Locally Regularized Tissue Strain Estimation from Radio–Frequency Ultrasound Images: Theoretical Developments and Results on Experimental Data. IEEE TMI, 27(2), pp. 145–160, 2008.

[3] E. Brusseau, J.F. Deprez, F. Duboeuf et al.: Examination of Noninduced Tissue Lesions with Freehand Elastography – An Animal Application. 7th ITEC, Austin, TEXAS, USA, October, 2008.

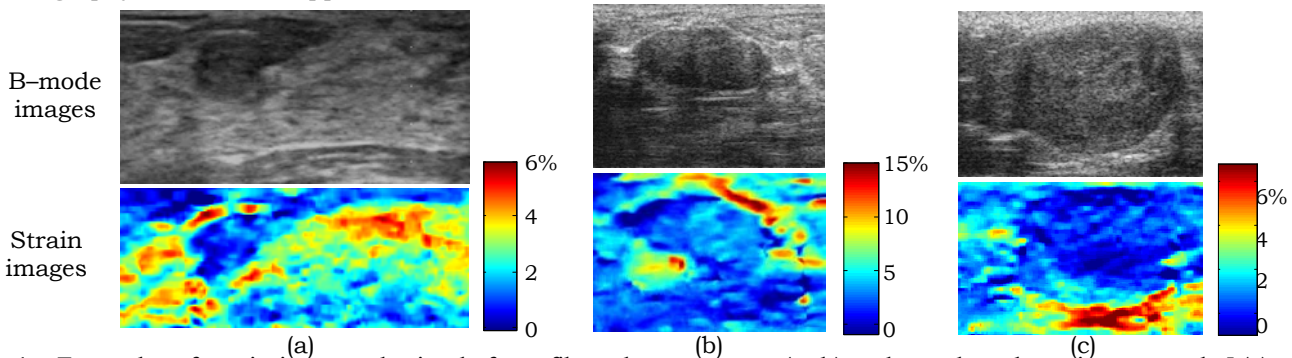

Figure 1: Examples of strain images obtained of two fibroadenoma cases (a, b) and one ductal carcinoma grade I (c).

* *indicates Presenter*

057 **IMAGING OF CARDIOVASCULAR WALL–FLOW COUPLING *IN VIVO*.**

Jianwen Luo[1], Elisa E. Konofagou[1,2].*
[1]Ultrasound and Elasticity Imaging Laboratory, Biomedical Engineering Department, [2]Radiology Department, Columbia University, New York, NY, USA.

Background: Speckle tracking–based methods have been developed to estimate cardiovascular wall motion in normal and pathological cases *in vivo* [1–3], while blood flow velocity is routinely measured in the clinic. The mechanical property and geometry changes as a result of disease may affect both wall motion and blood flow, while the latter two are also coupled and influence one another [4,5]. Simultaneous and registered imaging of both cardiovascular wall motion and blood flow velocity may contribute to more complete computational models of cardiovascular mechanical and fluid dynamics and increase understanding of their interaction, as well as provide additional diagnostic information.

Aims: To determine the feasibility of imaging the coupling of cardiovascular wall motion with blood flow *in vivo*.

Methods: A high frame rate data acquisition system previously described [1] was used here. A normal and an infarcted murine left ventricle (with left anterior descending coronary artery ligation) [2], and a normal and an aneurysmal (with Angiotensin II infusion) abdominal aorta [3] were scanned in longitudinal view with a 30MHz ultrasound probe (VisualSonics Inc., Toronto, Canada). With a retrospective ECG gating technique, 2D radio frequency (RF) frame sequences in a complete cardiac cycle were reconstructed at the very high frame rate of 8kHz [1–3]. The axial wall velocity and blood flow velocity were simultaneously estimated from the same RF data using a time–efficient 1D normalized cross–correlation technique previously described [6].

Results: Simultaneous, correlated, spatially and temporally registered imaging of both cardiovascular wall motion and blood flow in murine left ventricle and aorta was shown to be feasible over the entire cardiac cycle. In the normal aorta, the wall motion (0.4cm/s) and flow velocity (10cm/s) were uniform and synchronized along the entire vessel imaged. The aortic wall expanded as the blood flow velocity increased during systole. The wall motion and flow velocity were thus well coupled and correlated. In the aneurysmal aorta, reduced and spatially varied wall motion (<0.2cm/s) and vortex flow patterns (-2 and 12cm/s) in the aneurysmal sac were found, due to the stiffness, heterogeneity and geometry change. The coupling between wall motion and flow velocity was thus weaker. Reduced wall motion (>10 folds) was detected in the infarcted left ventricle, while vortex flow patterns were imaged in diastolic phases of both normal and infarcted left ventricles. More synchronized coupling between myocardial wall motion and blood flow was depicted in the normal heart, where the blood moves towards the interventricular septum (>8cm/s) after the mitral valve opens (i.e., rapid filling phase), and the septal wall simultaneously undergoes outward motion (>2cm/s). In the infarcted heart, however, the basal septum moves in the rapid filling phase, about 20ms before the mitral valve opens and the blood moves.

Conclusions: Cardiovascular wall motion and blood flow and their respective coupling were simultaneously imaged in mice *in vivo*. This information may provide important information for the diagnosis of cardiovascular disease as well as essential parameters for biomechanical modeling of the fluid–solid interaction between the blood and the cardiovascular wall.

Acknowledgements: This work was supported in part by the NIH (1R01HL098830).

References:

[1] Pernot et al.: ECG–Gated, Mechanical and Electromechanical Wave Imaging of Cardiovascular Tissues *In Vivo*. Ultrasound Med. Biol., 33(7), pp. 1075–1085, 2007.
[2] Luo et al.: Myocardial Elastography at Both High Temporal and Spatial Resolution for the Detection of Infarcts. Ultrasound Med. Biol., 33(8), pp. 1206–1223, 2007.
[3] Luo et al.: Pulse Wave Imaging of Normal and Aneurysmal Abdominal Aortas *In Vivo*. IEEE Trans. Med. Imaging, 28(4), pp. 477–486, 2009.
[4] Edvardsen et al.: Interaction between Left Ventricular Wall Motion and Intraventricular Flow Propagation in Acute and Chronic Ischemia. Am. J. Physiol.–Heart Circul. Physiol., 289(2), pp. H732–H737, 2005.
[5] Watanabe, et al.: Computer Simulation of Blood Flow, Left Ventricular Wall Motion and Their Interrelationship by Fluid–Structure Interaction Finite Element Method. JSME Int. J. Ser. C, 45(4), pp. 1003–1012, 2002.
[6] Luo and Konofagou: A Fast Normalized Cross–Correlation Method for Motion Estimation. IEEE Trans. Ultrason. Ferroelectr. Control, 57(6), pp. 1347–1357, 2010.

059 **ARF–DRIVEN ASSESSMENT OF *IN VIVO* MYOCARDIAL CYCLIC STIFFNESS VARIATION.**

Richard Bouchard[1], Stephen J. Hsu[1], Mark L. Palmeri[1], Ned C. Rouze[1], Gregg E. Trahey[1].*
[1]Duke University, Durham, NC, USA.

Background: A noninvasive means of assessing myocardial elasticity would be of tremendous value in diagnosing cardiac disease, which often manifests itself as changes in tissue stiffness. Acoustic radiation force (ARF)–driven techniques have demonstrated their ability to discern elastic properties of soft tissue. For the purpose of myocardial elasticity imaging, a novel ARF–based imaging technique, the displacement ratio rate (DRR) method, was developed. The advantages of this new method are that it requires a relatively small temporal (<1ms) and spatial (tenths of mm^2) sampling window and appears to be independent of ARF excitation intensity. The DRR method relies on the rate of change of (ARF–induced) displacement ratios (e.g., calculated by dividing the response in a compliant medium by the response in a stiff medium) to discern relative differences in shear wave velocities (and related stiffness metrics) between media. Using this new technique, it is possible to analyze changes in stiffness in a robust fashion (i.e., intensity independence and improved sampling) and consequently reassess stiffness changes of mid–myocardial tissue through the cardiac cycle in a more quantitative manner than has previously been reported previously [1].

Aims: 1) Development of a novel, on–axis approach (i.e., the DRR method) to more robustly assess stiffness variation and 2) assessment of myocardial stiffness variation through the cardiac cycle.

Methods: The basis/performance of the DRR method was first investigated through numerical and phantom imaging results. This technique was then implemented in a single *in vivo* canine study, during which time data were acquired through the full cardiac cycle by imaging via thoracotomy (i.e., directly on the exposed epicardium). These data were then compared to results obtained by acoustic radiation force impulse (ARFI) imaging and ARF–driven shear wave velocimetry, with the latter being used as the gold standard. For each experimental trial, twenty acquisitions (obtaining DRR, velocimetry and ARFI imaging data) were obtained at even intervals through nearly two complete heartbeats. These data were then analyzed offline and registered with a matched ECG trace.

Results: Velocimetry results estimate a range of shear wave velocities from 0.8 to 2.1 m/s through the cardiac cycle, with the highest velocities observed during systole and lowest observed during diastole for the *in vivo* canine study. DRR method and ARFI imaging results predict a similar cyclic variation. If a basic shear wave elasticity model is assumed, such a velocity result would suggest a period of increased stiffness during systole (when compared to diastole). Figure 1b presents traces of estimated shear wave velocity (blue square) and DRR stiffness rankings (green dot) through the cardiac cycle. The ECG trace (a) indicates the sample points/durations of the aforementioned estimates.

Figure 1:

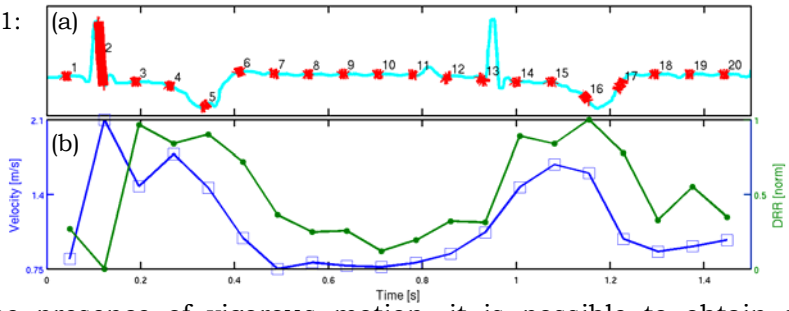

Conclusions: Even in the presence of vigorous motion, it is possible to obtain reliable velocimetry estimates throughout the cardiac cycle. Despite drawbacks of the DRR method (e.g., sensitivity to noise) and ARFI imaging (e.g., dependence on excitation intensity and unstable displacement ratio), both techniques offered a similar cyclic stiffness variation to that predicted by shear wave velocimetry with increased stiffness suggested during systole (when compared to diastole). Given the reduced temporal/spatial sampling requirements of these two on–axis approaches, both show promise in future *in vivo* myocardial elasticity investigations.

Acknowledgements: This work has been supported by NIH R37–HL096023. We thank the Ultrasound Unit of Siemens Healthcare for in–kind support.

References:

[1] Hsu SJ, Bouchard RR, Dumont DM, Wolf PD, Trahey GE: *In Vivo* Assessment of Myocardial Stiffness with Acoustic Radiation Force Impulse Imaging. Ultrasound Med. Biol., 33(11), pp. 1706–1719, 2007.

* *indicates Presenter*

092 **BREAST CANCER DIAGNOSIS USING NONLINEAR ELASTICITY IMAGING: SOME INITIAL RESULTS.**

S. Goenezen[1], Z. Sink[1], A.A. Oberai[1], J.–F. Dord[1], P.E. Barbone[2], J. Jiang[3], T.J. Hall[3].*
[1]Rensselaer Polytechnic Institute, Troy, NY, USA; [2]Boston University, Boston, MA, USA; [3]University of Wisconsin–Madison, Madison, WI, USA.

Background: Recent *ex–vivo* measurements of breast tissue samples have revealed that both benign and malignant tumors exhibit elevated linear elastic modulus. However, malignant tumors tend to stiffen at a faster rate with overall applied strain when compared with benign tumors [1]. This opens the possibility of using images of nonlinear elastic parameters for distinguishing malignant and benign tumors.

Aims: The goal of this study is to determine whether nonlinear elasticity images can be used to differentiate benign and malignant breast tumors.

Methods: Displacement data from ten patients (five fibroadenomas and five invasive ductal carcinomas) were used. The details of the study as well as the associated compliances are described in [2]. A freehand compression technique was used to induce displacements with maximum overall strain in the range of 20%. The displacements were obtained using a guided–search block–matching algorithm described in [3]. Displacement estimates were obtained on a 200*200 micron grid and were down–sampled by a factor of four for the modulus reconstructions. For the modulus reconstruction, an incompressible plane stress model was assumed, and two deformation fields, one at an overall strain of about 1% and another at a strain of about 12%, were utilized. An exponential strain energy density function with two parameters, the shear modulus at small strain and a nonlinear parameter that quantified the level of strain hardening, was used. The inverse algorithm is described in [4]. The shear modulus distribution was determined up to a multiplicative parameter using the small deformation displacement field, and, thereafter, the nonlinear parameter was determined up to an additive constant using the large deformation displacement field. Total Variation Diminishing (TVD) regularization was used for the shear modulus and the nonlinear parameter. B–mode ultrasound and linear elastic modulus images were used to locate the extent of the tumor. Once the tumor location was determined, average values of the linear shear modulus and the nonlinear parameter were evaluated.

Results: The following trends were observed and quantified: (1) The contrast in the linear elastic modulus between the tumor and the background was about the same for benign and malignant tumors. (2) The contrast in the nonlinear parameter between the tumor and the background for malignant tumors was significantly greater. The Figure1a and b represent material reconstructions for fibroadenoma (FA), whereas Figure 1c and d are from an invasive ductal carcinoma (IDC). Mu is the shear modulus and gamma is the nonlinear parameter. One can observe that gamma is much larger for IDC than for FA within the tumor.

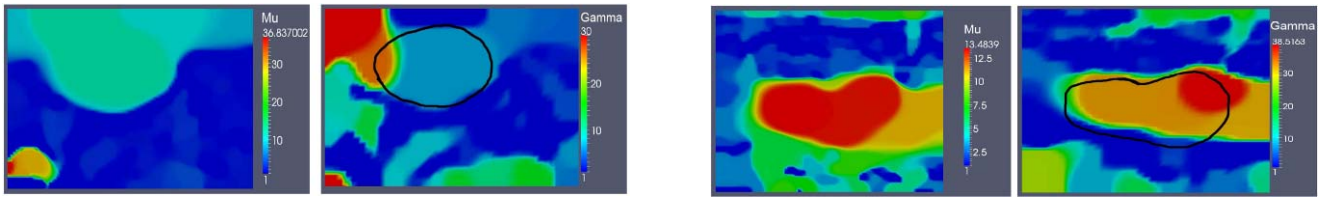

Figure 1: (a) (b) (c) (d)

Conclusions: Using a small set of data, an initial attempt was made to test the utility of nonlinear elasticity imaging in diagnosing malignant breast tumors. Encouraging results were obtained that confirmed that with increasing overall applied strain, malignant breast tumors stiffen more steeply than benign breast tumors. Further work involves generating three–dimensional images, the use of more accurate material models and better understanding of the role of regularization.

Acknowledgements: We acknowledge the support of NIH Grants R01CA100373, R21CA133488 and R01CA140271.

References:

[1] O'Hagan, JJ and Samani, A: Measurements of the Hyperelastic Properties of 44 Pathological Ex Vivo Breast Tissue Samples. Physics in Medicine and Biology, 54, pp. 2557–2569, 2009.
[2] Burnside ES, Hall TJ, Sommer AM, et al.: Using Ultrasound Strain Imaging to Distinguish Benign and Malignant Solid Breast Masses. Radiology, 245(2), pp. 401–410, 2007.
[3] Jiang J and Hall TJ: A Generalized Speckle Tracking Algorithm for Ultrasonic Strain Imaging using Dynamic Programming. Ultrasound Med Biol, 35(11), pp. 1863–1879, 2009.
[4] NH Gokhale, PE Barbone and AA Oberai: Solution of the Nonlinear Elasticity Imaging Inverse Problem: The Compressible Case. Inverse Problems, 24 045010, 2008.

100 **LATERAL MOTION COMPENSATION IN ULTRASOUND STRAIN IMAGING.**

Mok–Kun Jeong[1], Sung–Jae Kwon[1], Myung–Ki Park[1], Moo–Ho Bae[2], Dong–Kuk Shin[3]*
[1]Electronic and Communication Engineering Departments, Daejin University, Pocheon, Gyeonggi, KOREA; [2]Electronic Engineering Department, Hallym University, Chuncheon, Gangweon, KOREA; [3]Medison Research Institute, Seoul, KOREA.

Background: In strain imaging based on manual palpation, the compressed tissue in the human body undergoes 3–D displacements. To reduce the amount of computation, current ultrasound strain imaging systems produce strain images by estimating 1–D displacements along the direction of the scan line (axial). Thus, displacements, if any, perpendicular to the scan line direction (lateral) increase signal decorrelation, incurring errors in the estimated displacements. Lateral displacements are estimated using an autocorrelation method and are used to improve the strain image quality.

Aims: Among 3–D motion, the motion in the elevation direction does not significantly affect the axial displacement estimation because the ultrasound beam resolution in that direction is relatively low. So the motion in the lateral direction is mainly responsible for errors in estimating the displacement in the axial direction. Thus, our goal is to reduce errors in estimating axial displacements by taking into account lateral motion.

Methods: Displacements in the axial direction are estimated by applying an autocorrelation method to complex data obtained by demodulating the pre– and post–compression ultrasound signals. Following compensation of axial motion using the estimated axial displacements, what remains is a dataset with lateral motion only. A 1–D data sequence is formed by taking samples in the dataset at the same depth and collecting them in the lateral direction. The data sequence is converted into an analytic signal, which is complex, by the use of 1–D spatial Hilbert transform. Lateral displacements are estimated by applying an autocorrelation–based displacement estimation technique to the analytic signal. Chen et al. [1] took a 2–D frequency domain approach, followed by phase–based zero–crossing detection. The estimated lateral displacement information is applied to the original scan lines to produce new lateral–motion–compensated scan lines using linear interpolation [2]. With the original and the new scan lines that have been compensated for axial and lateral motions available, the estimation of axial displacements was performed again to obtain compensated estimates. Experiments were carried out to confirm the algorithm. A 10 mm diameter cylindrical inclusion five times stiffer than the background was embedded in a homogeneous phantom. Under external compression, the vicinity of the inclusion underwent significant lateral motions. Ultrasound data were acquired by applying 1% compression using a clinical scanner (Accuvix V10, Medison) with a linear array transducer (L15–12).

Results: Figure 1a shows strain images before and Figure 1b after compensation of lateral motion. The strain image after lateral motion compensation shows a more uniform background area than the strain image before lateral motion compensation. The maximum lateral displacement in the background was found to be 2.17 scan lines (0.43 mm). An SNR improvement of 12.7 dB was achieved in the background region to the right of the inclusion.

Conclusions: The axial and lateral displacements are finely estimated from the analytic signal obtained through the use of Hilbert transform. Experiments on a phantom demonstrate that the strain image quality is improved after lateral motion compensation.

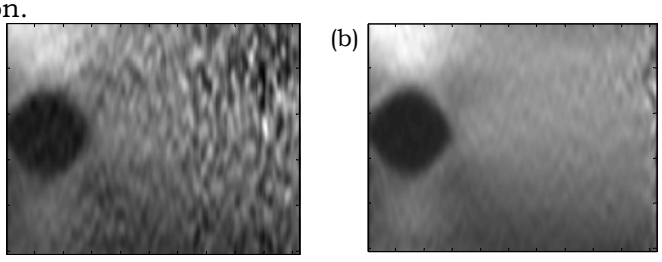

Figure 1: (a) Strain image before lateral motion compensation and (b) strain image after lateral motion compensation.

Acknowledgements: This work was supported by Medison.

References:

[1] X. Chen, M. J. Zohdy, Y. Emelianov, and M. O'Donnell: Lateral Speckle Tracking Using Synthetic Lateral Phase. IEEE Trans. UFFC, Vol. 51, No. 5, pp. 540–550, 2004.
[2] E. Konofagou and J. Ophir: A New Elastographic Method for Estimation and Imaging of Lateral Displacements, Lateral Strains, Corrected Axial Strains and Poisson's Ratios in Tissues. UMB, Vol. 24, No. 8, pp. 1183–1199, 1998.

* *indicates Presenter*

103 **TISSUE MICRO–MOTION IN HUMAN ERECTOR SPINAE AND QUADRICEPS MUSCLES OBSERVED *IN VIVO* USING ULTRASOUND ELASTOGRAPHY TECHNIQUES.**

James R. Fox[1], Helene M. Langevin[1], Cathryn Koptiuch[1]*
[1]University of Vermont, C–448 Given, Burlington, VT 05405, USA.

Background: Ultrasound based elastography techniques provide, in their first order, a local assessment of tissue displacement. These measures can, depending on the physical and computational parameters used in capturing and processing the data, provide very high resolution displacement maps from sequential radiofrequency (RF) data capture, often on the order of microns. We have been using these techniques to describe both axial and lateral connective tissue displacements in response to various mechanical inputs including acupuncture and passive trunk motion. We have observed that when time–sequenced RF data are collected over a stationary target field, there is a repeatable and predictable structure to the signal that can be modified by the orientation of the transducer with respect the underlying muscle orientation. This signal displays a fairly typical frequency and frequency/amplitude content for each orientation.

Aims: To quantify and describe the low frequency micro–motions observed in the erector spinae and quadriceps muscles.

Methods: Sixteen subjects, (Male:9, Mean Age:34, Mean BMI:25.8; Female:7, Mean Age:34, Mean BMI:23.6) were tested. An ultrasound scanner (Terason, Model 3000) with a 5–12MHz, 7.5MHz center frequency, transducer was used. The cineloop frame rate was 25fps. For measurements of the erector spinae, subjects were positioned prone on a table. The L2–3 interspace was identified by manual palpation. The ultrasound transducer was positioned 1.9cm lateral to the midline, centered on the L2–3 interspace, oriented parallel to the spine and held in place with a clamp. Additional measures were made after rotating the transducer 35, 45, 70, and 90 degrees from this orientation. The subject was instructed to complete a normal inhalation and then hold his/her breath for the duration of a 10 second data collection. For quadriceps measurement, the subject was positioned supine on a table. The transverse midpoint of the muscle was located using ultrasound imaging 15cm proximal to the knee. The RF data were used to determine lateral displacement using standard elastography cross–correlation techniques within a 10mm wide by 1mm deep zone located at the junction of the muscle and the deep fascia. An FFT of the lateral displacement data using a 250 point Hann window was determined.

Results: The FFT revealed a typical low frequency content with dominant peaks near 4Hz, the magnitude of these peaks varying with the transducer orientation with respect to the underlying muscle. Figure 1 shows the composite FFT data for all 16 subjects showing the differences in frequency content of lateral displacement signals derived from the erector spine. A similar pattern was observed in the rectus femoris muscle.

Conclusions: The data suggest an interesting relationship between the small, low frequency lateral micro–motions observable using ultrasound elastography and the directionality of the ultrasound transducer orientation. It is speculated that there may be a relationship of this motion to a phenomenon of muscle vibrations that emit a detectable sound and that can be quantified using acoustic myography techniques, or may be transducer induced as in vibrography.

Acknowledgements: This project was funded by NCCAM RO1–AT003479.

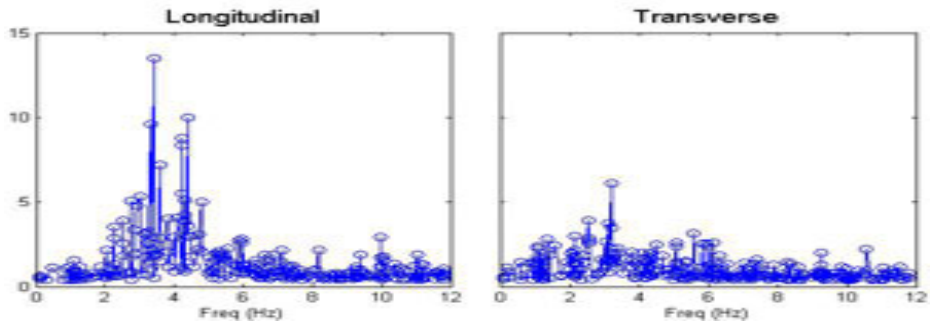

Figure 1: Composite FFT's of all subjects for longitudinal and transverse orientations of the ultrasound transducer.

* *indicates Presenter*

107 **REAL–TIME GRAPHICS PROCESSING UNIT BASED ULTRASOUND ELASTOGRAPHY.**

N.P. Deshmukh[1], H. Rivaz[1], P.J. Stolka[1], H. Kang[1], G.D. Hager[1], M.E. Alaf[2], E.M. Boctor[1,3].*
[1]Johns Hopkins University, Baltimore, MD, USA; [2]Johns Hopkins Medical Institutions, Baltimore, MD, USA; [3]Johns Hopkins Medicine, Baltimore, MD, USA.

Background: Elastography involves imaging the mechanical properties of tissue and has numerous clinical applications [1]. With the quasi–static elastography approach, tissue strain is generated by compressing the tissue and taking the pre– and post–compression ultrasound (US) images under freehand palpation. Real–time elastography has numerous applications e.g. in the detection of cancer tumors, ablation monitoring, etc. The graphics processing unit (GPU) hardware frees the CPU on an US machine to perform other useful tasks, and it is cheap and requires low maintenance compared to an array of clusters. There are other real–time implementations based on DSP/FGPA processors, but these systems need specialized hardware. GPU processors can be connected via PCI express slot available on most modern systems which eases portability and allows use on the existing hardware. It is easier to program GPUs than DSPs and FGPAs. The performance of GPUs in terms of floating point computation is better than FGPAs [2,3].

Aims: Real–time implementation of normalized cross–correlation (NCC) and Analytic Minimization/Dynamic Programming (AM/DP) elastography on the GPU to facilitate the development of a cheap and compact system that is easily deployable in an operating room. A speed comparison of NCC and AM/DP with their corresponding serial implementation has been shown.

Methods: NCC elastography involves cross–correlation of small windows in pre– and post–compression images. The number of output strain samples is equal to these search windows. This essentially means we get data–independence for the output strain, so we can parallelize cross–correlation computation of these small windows. These windows are chosen along the radiofrequency (RF) lines, which is along the direction of compression [4]. DP elastography involves fast optimization of the cost function for finding the minimum displacement along the RF lines. DP elastography calculates integer displacement cost function. For sub–integer displacement, AM elastography is used. In serial implementation of AM/DP, computation of cost function is done from left to right in the lateral direction of image pairs and computation of cost function for a RF–line takes the weighted cost function from the previous RF–line as input. In parallel implementation, AM/DP is individually applied to each of the RF lines on different cores of the GPU with parallelization of some intermediate steps to get the strain output [5].

Results: In this work, a speed of 285fps (frames per second) for the parallel NCC algorithm was obtained compared to 30fps for the serial NCC algorithm on C, for an RF image of 641 samples and 71 RF lines. For the parallel AM/DP algorithm on the GPU, a speed of 5fps compared to 0.5fps was obtained for the same serial implementation of AM/DP on C function in Matlab, for an RF image of 1040 samples and 256 RF lines. Figures 1 and 2 show output from NCC and AM/DP elastography. The vertical artifacts in Figure 2 occur due to the parallel version of AM/DP algorithm not taking input from previous RF lines.

Figure 1: Elastogram output from NCC elastography.

Figure 2: Elastogram output from AM/DP elastography.

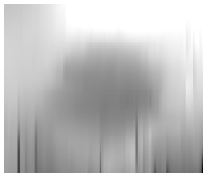

Conclusions: We attain an approximately 10 times improvement in the running time of NCC and AM/DP elastography methods compared to their serial implementations. The parallel implementation of AM/DP elastography generates artifacts (which are not present in the serial implementation [5]) which will be focus of the future research.

Acknowledgements: This work was supported by NCI SPORE Grant P50CA58236.

References:

[1] Ophir et al.: Elastography: A Quantitative Method for Imaging the Elasticity of Biological Tissues. Ultrasonic Imaging, Vol. 13, Is. 2, pp. 111–134, April 1991.
[2] D.B. Thomas et al.: Double–Precision Floating–Point Performance of Computational Devices: FGPAs, CPUs and GPUs. ACM/SIGDA International Symp. on Field-Programmable Gate Arrays, pp. 63–72, 2009.
[3] Miaoqing et al.: Accelerating Double Precision Floating–Point Hessenberg Reduction on FPGA and Multicore Architectures. Proc. of 2010 SAAHPC'10, Knoxville, TN, USA, (in press), 2010.
[4] N Deshmukh et al.: GPU–Based Elasticity Imaging Algorithms. MICCAI–GRID Workshop, pp. 45–54, 2009.
[5] Rivaz H et al.: Real–Time Regularized Ultrasound Elastography. IEEE Trans. Medical Imaging, (in press).

* *indicates Presenter*

035 **SHEAR WAVE ELASTOGRAPHY OF THE KIDNEY: PRE–CLINICAL STUDY ON A KIDNEY FIBROSIS MODEL AND CLINICAL FEASABILITY STUDY ON 70 HUMAN RENAL TRANSPLANTS.**

Jean–Luc Gennisson[1], Nicolas Grenier[3], Regis Hubrecht[3], Lionel Couzy[3], Yahsou Delmas[3], Marc Derieppe[1], Sébastien Lepreux[3], Aline Criton[2], Jeremy Bercoff[2], Mickaël Tanter[1].*
[1]Institut Langevin–Ondes et Images, ESPCI ParisTech, CNRS UMR7587, INSERM U979, Paris, FRANCE; [2]Supersonic Imagine, Aix en Provence, FRANCE; [3]Service de Néphrologie, Hôpital Pellegrin, Bordeaux, FRANCE.

Background: An increasing number of patients is affected by chronic kidney disease (CKD) world while with ensuing end–stage renal disease (ESRD). A change in global approach to CKD from costly treatment of ESRD to more aggressive primary and secondary prevention is imperative. This improvement needs a better understanding of mechanisms underlying renal scarring and a development of specific therapies to slow the progression and development of modern diagnostic tools to characterize these underlying processes. The number of patients with ESRD underestimates CKD has probably grown by more than a factor 50 in the last ten years due to initiation factors as hypertension, diabetes, hyperlipidemia, obesity or smoking.

Aims: In this work, the Supersonic Shear Imaging technique (SSI) was proven to be able to provide a quantitative follow up of kidney fibrosis on rats. Then, the technique was adapted on curved probes and proposed to map the *in vivo* viscoelastic properties of human renal transplants and compared with biopsy.

Methods: The SSI technique is based on the radiation force induced by a conventional ultrasonic probe, to generate a planar shear wave deep into tissues. Then shear wave propagation throughout the medium is caught in real time thanks to an ultrafast ultrasound scanner (5000 frames/s). Lastly, a time of flight algorithm applied on these data allows computing a map of the shear wave velocity of the kidney. A follow–up study for 8 weeks on a model of glomerulosclerosis induced by L–Name on 50 rats has been conducted in order to investigate the accuracy of the technique. Quantitative maps of the kidney cortex were performed with an 8MHz linear probe. On human renal transplants, quantitative maps of the cortex elasticity were produced for each patient with a 2.5MHz curved array.

Results: In the animal study, the results show an increase of the elasticity of the cortex of the kidney in time with a Young's modulus ranging from 9 to 25kPa. Results are compared to histological measurement as proteinuria and or quantification of fibrosis with trichrome. On human renal transplants, three groups were studied: a control group, subjects with an early or late nonfunctional transplant. The results obtained using a curved ultrasonic probe show an 8cm depth by 10cm width map of the Young's modulus for the 70 patients. Elasticity varies between groups from 9 to 50kPa. Results were compared to histology and showed a good agreement between fibrosis markers and Young's modulus.

Conclusions: Here we have demonstrated the feasibility of inducing shear waves using the supersonic shear imaging technique *in vivo* in rats and human kidneys. The good reproducibility and accuracy of the shear elasticity are discussed. The elasticity was proved to be clearly related to kidney fibrosis. As fibrotic process is responsible for the development of most CKD, noninvasive identification and follow–up of this process could improve renal prognosis if adapted targeted therapies can be applied.

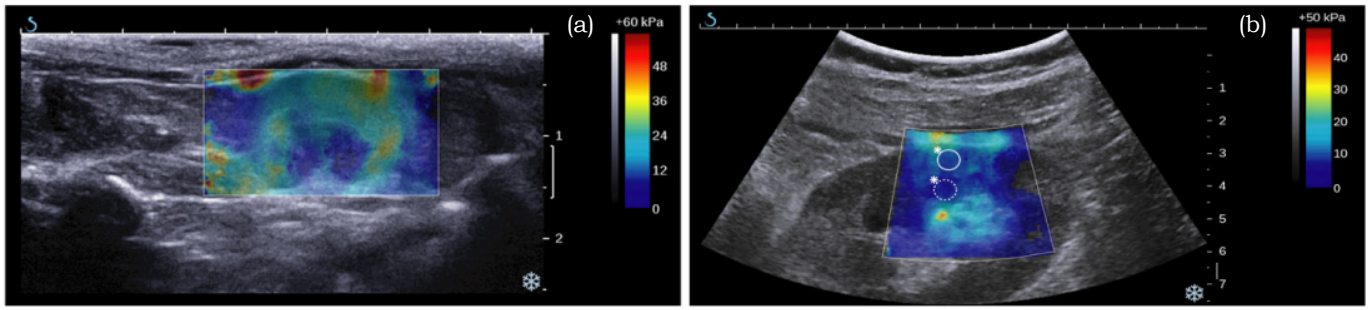

Figure 1: Ultrasound imaged in gray scale and elasticity mapping in color of: (a) a pathological rat kidney after 4 weeks of diet inducing renal fibrosis; (b) a human renal transplant from the control group. Vertical axes are in cm and the color scale in kPa.

004 **IMAGING TISSUE MECHANICAL PROPERTIES BY TRACKING HIGH AMPLITUDE SHEAR WAVES GENERATED VIA TRANSIENT NEEDLE PERTURBATION.**

Ryan J. DeWall[1,2], Tomy Varghese[1,2] and Ernest L. Madsen[1].*
[1]Medical Physics, [2]Biomedical Engineering Departments, University of Wisconsin–Madison, 1111 Highland Ave., Madison, WI, USA.

Background: Abdominal ablation procedures provide a minimally invasive alternative to surgical resection for some hepatic tumors. Ultrasound imaging is often used for needle guidance because of its real–time imaging capabilities. However, traditional ultrasound imaging has been shown to be a poor modality for monitoring ablation procedures because of the unpredictable variation in the echogenic properties of ablated and untreated tissue. Small displacement of the radiofrequency (RF) needle or microwave antenna has been used to generate strain images, which have been shown to delineate ablated volumes. However, strain is not an inherent mechanical property of tissue. Measurement of Young's Modulus provides more quantitative information. Shear wave tracking techniques such as acoustic radiation force imaging (ARFI) can be used to quantify shear wave velocity (SWV), which is proportional to Young's Modulus [1].

Aims: We propose using transient perturbation of the RF needle or microwave antenna to generate shear waves and determine SWV in the ablated and surrounding untreated tissue. This was validated in phantoms and tested *ex vivo*.

Methods: Two gelatin–oil dispersion phantoms were used in this study. Phantom 1 contained a stiff ellipsoid (E = 28.0kPa, SWV = 3.06m/s) bonded to a 1.6mm diameter stainless steel rod in a soft background (7.8kPa, SWV = 1.61m/s). Phantom 2 was similar but also contained a partially ablated region (15.2kPa, SWV = 2.25m/s). A piezoelectric actuator provided a 100 micron perturbation to the rod. The resulting shear waves were tracked using an Ultrasonix SonixTOUCH scanner and an L14–5/38 transducer. A GUI developed using the Texo SDK facilitates high frame rate tracking of the shear waves. Four tracking locations (~0.3mm spacing) were sequentially scanned at a frame rate of 2600Hz for a single perturbation. For the proceeding perturbation, the next four locations were sequenced. This process was repeated across the face of the transducer. The time–to–peak tracking method was used to generate SWV images. Finite element analysis (FEA) models of the phantoms were compared to the phantom results. The technique was then tested *ex vivo* on ablations created in bovine liver tissue.

Results: Our results show good boundary demarcation between the ellipsoid and the surrounding background in Phantom 1 (Figure 1). SWV in ROIs in the ellipsoid (two averaged, black ROIs in Figure 1) and background (two averaged, white ROIs in Figure 1) were 3.13 and 1.57m/s, respectively. Good boundary demarcation was also shown in Phantom 2. SWV in the ellipsoid, partially ablated region and surrounding background were 3.23, 2.06, and 1.52m/s, respectively. FEA and phantom results showed good agreement. SWV reconstructions *ex vivo* overestimated the SWV in the ablated volumes but provided overall good delineation of the ablated region from the surrounding untreated tissue.

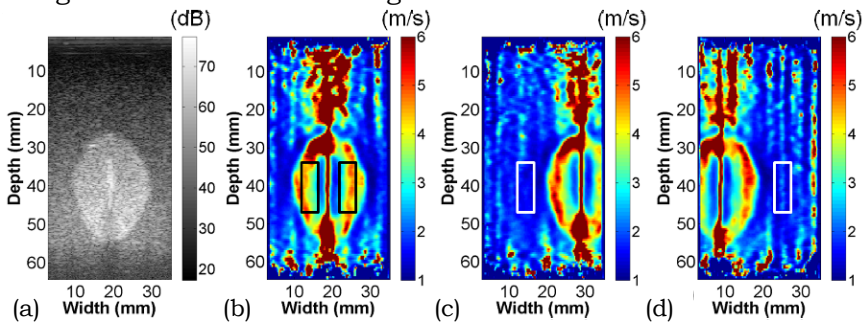

Figure 1: a) B–mode and (b–d) shear wave velocity images from Phantom 1.

Conclusions: These results show the feasibility of generating and tracking shear waves using transient electrode perturbation. Good boundary delineation was observed, and differences between ablated and partially ablated regions were detectable.

Acknowledgements: This work is supported in part by NIH grants R01 CA112192–04, R01 CA112192–S103 and T32 CA09206–31.

References:

[1] Palmeri ML, Wang MH, Dahl JJ, Frinkley KD, and Nightingale KR: Quantifying Hepatic Shear Modulus *In Vivo* using Acoustic Radiation Force. UMB, 34(4), pp. 546–58, 2008.

* *indicates Presenter*

007 **A NEW METHOD FOR THE ACQUISITION OF STRAIN IMAGE VOLUMES.**

RJ Housden[1], C Uff[2], L Chen[1], AH Gee[1], GM Treece[1], RW Prager[1], JC Bamber[2].*
[1]Engineering Department, University of Cambridge, Cambridge, England, UK; [2]Institute of Cancer Research, Sutton, Surrey, England, UK.

Background: 3D axial strain imaging is potentially useful for producing a complete picture of the anatomy and accurately measuring the volume of stiff or soft inclusions. Currently, there are two approaches to quasistatic 3D strain imaging. The Frame Sequence method uses a conventional 2D probe applying a continuous axial oscillatory motion to produce a sequence of 2D axial strain images distributed in 3D space [1]. Pairs of images are compared sequentially and a quality–weighted spatial averaging process [2] displays the best data at each 3D location. This method has been evaluated but has the practical difficulty of achieving adequate elevational frame density in a hand controlled motion and the requirement of some means to track the probe motion, such as a position sensor. The alternative Volume Pair method records two or more overlaid volumes with a small change in pressure between them and then compares one volume to the next [3,4]. However, this method is also difficult in clinical practice because the single freehand compression must be carefully applied to ensure high quality strain data.

Aims: To develop a variation on the frame sequence method that overcomes its practical limitations.

Methods: The method uses a GE RSP6–12 mechanically–swept 3D probe interfaced to a Dynamic Imaging Diasus ultrasound machine. The probe gradually sweeps out a volume, recording several frames at each step of the motor, while a continuous axial up and down motion is applied by hand. The resulting data set is similar to a standard frame sequence recording, but the probe controls the elevational motion, ensuring adequate frame density. Also, the method relies on a continuous axial motion and quality–weighted averaging of multiple frames at each step, rather than a single carefully controlled compression, to produce good data. Comparisons were made to volume pair data recorded using the RSP6–12.

Results: We have performed numerous scans using the two methods: quantitative comparisons, using average SNR_e over many small kernels, have shown that the new method produces higher quality data. Typical strain images are shown below. In Figure 1, the scanning subject is a stiff inclusion in a CIRS elasticity QA phantom (model 049). The new method is also effective *in vivo*, as shown in Figure 2. The scan using the new method was acquired with minimal effort, whereas the volume pair result required a more careful scanning technique and multiple attempts to achieve the correct compressive motion.

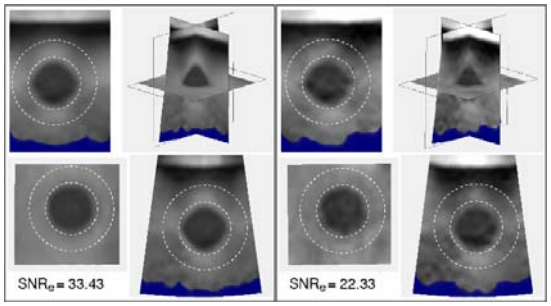

Figure 1: Three orthogonal views and a 3D view of a CIRS elasticity QA phantom. The left images show the new method; the right are from a volume pair scan. Average SNR_e values are calculated in the 3D region indicated by the dashed line.

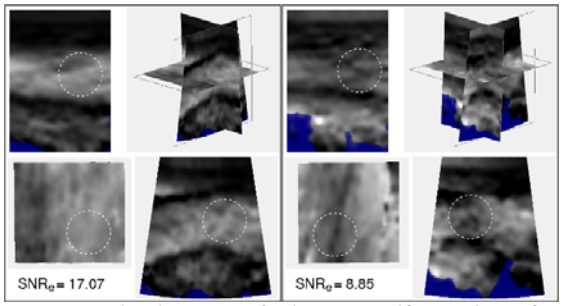

Figure 2: An *in vivo* scan of a human calf muscle. Left: the new method; right: volume pair. In both figures, the blue areas at the bottom mask regions of low quality strain data.

Conclusions: We have developed a new technique for acquisition of axial strain image volumes. Our experience is that while the volume pair approach occasionally produces very high quality images, the new method more reliably produces images of useful quality. Also, it requires a much less careful scanning technique to achieve this quality, making it an attractive option for clinical scanning. The method is currently under clinical evaluation for assisting resection of brain tumours.

Acknowledgements: This work was supported by EPSRC grant number EP/E030882/1.

References:

[1] Lindop J, Treece G, et al.: 3D Elastography using Freehand Ultrasound. UMB, 32, pp. 529–545, 2006.
[2] Lindop J, Treece G, et al.: An Intelligent Interface for Freehand Strain Imaging. UMB, 34, pp. 1117–1128, 2008.
[3] Treece G, Lindop J, et al.: Freehand Ultrasound Elastography with a 3–D Probe. UMB, 34, pp. 463–474, 2008.
[4] Bharat S, Fisher T, et al.: Three–Dimensional Electrode Displacement Elastography using the Siemens C7F2 *four*Sight Four–Dimensional Ultrasound Transducer. UMB, 34, pp. 1307–1316, 2008.

008 **ELASTICITY IMAGING USING HARMONIC EXCITATION, ULTRAFAST IMAGING AND PLANAR INVERSION OF THE WAVE EQUATION.**

R. Zahiri Azar[1,2], K. Dickie[1], C. Chung[1], A. Baghani[2], S.E. Sacludean[2], L. Pelissier[1].*
[1]Ultrasonix Medical Corporation, Richmond, CANADA; [2]University of British Columbia, Vancouver, BC, CANADA.

Background: Harmonic excitation of soft tissue followed by the inversion of the governing wave equation in steady–state is commonly used in magnetic resonance elastography to image the absolute values of tissue elasticity [1]. Harmonic motion imaging with conventional ultrasound typically requires either a small area of interest or long acquisition time [2]. To image elasticity, ultrasound elastography has focused mainly on the imaging of the propagation of transient waves with ultrafast scanners [3].

Aim: To measure harmonic motion with ultrafast ultrasound and to solve for the absolute values of the elasticity and the loss modulus from the governing wave equation.

Methods: Experiments were performed on a commercial elasticity phantom (Model 049, CIRS Inc., VA, USA) which contains several spherical inclusions with different diameters and elasticity values. An external harmonic exciter was mounted on top of the phantom to vibrate it continuously. The SonixTOUCH ultrasound machine (Ultrasonix Medical Corp., Richmond, Canada) was used to image the propagation of mechanical waves. Similarly to [3], plane wave transmits using all elements followed by parallel acquisition of pre–beamformed data from all channels were used to achieve high frame rates (up to 20kHz depending on the imaging depth). The Texo software was used to program the SonixTOUCH to transmit plane waves at 5kHz. The SonixDAQ was used to acquire the pre–beamformed echo signals from up to 40mm depth for 128 channels for 250 transmits (i.e 50ms). Pre–beamformed data were then transferred to a PC for off–line processing. Parallel beamforming was employed to reconstruct the radiofrequency (RF) frames from the channel data. Axial displacement images were estimated from these reconstructed RF frames using normalized cross–correlation (W=1mm and ΔW=50%) with cosine fitting for sub–sample estimation. The complex wave image at the excitation frequency was extracted from the displacement data using temporal Fourier analysis. Finally, the planar Algebraic Helmholtz Inversion of the wave equation [1] was used to estimate the absolute value of the elasticity from the complex wave image.

Results: The phantom Young's moduli of 29kPa and 6kPa for the background and the soft inclusion were estimated to be 32kPa and 9kPa, respectively. The experimental results for excitation frequency of 200Hz for the softest inclusion are shown in Figure 1.

Conclusions: The results show that the absolute value of elasticity can be reliably imaged in steady–state with ultrasound. Inversion of the wave equation in steady–state offers several advantages over transient waves. Temporal filtering can be employed to extract the frequency of interest from displacement data [2]. Also, spatial filtering can be used to remove unwanted wavelengths from the wave image [1]. Further investigations are required to compare the results with transient elastography.

Acknowledgements: The authors would like to acknowledge Dr. Ralph Sinkus, Dr. Ingolf Sack and Dr. Sebastian Papazoglou for their valuable feedback on the wave inversion algorithms.

References:

[1] S. Papazoglou, U. Hamhaber, J. Braun and I. Sack: Algebraic Helmholtz Inversion in Planar Magnetic Resonance Elastography. Physics in Medicine and Biology, Vol. 53, pp. 3147–3158, 2008.
[2] A. Baghani, A. Brant, S. Salcudean, R. Rohling: A High Frame Rate Ultrasound System for the Study of Tissue Motions. IEEE Trans. Ultrason., Ferroelectric, Frequency Control, (in press).
[3] Bercoff J, Chaffai S, Tanter M, Sandrin L, Catheline S, Fink M., Gennisson J, and Meunier M: *In Vivo* Breast Tumor Detection using Transient Elastography," Ultrasound in Medicine and Biology, 29, pp. 1387–1396, 2003.

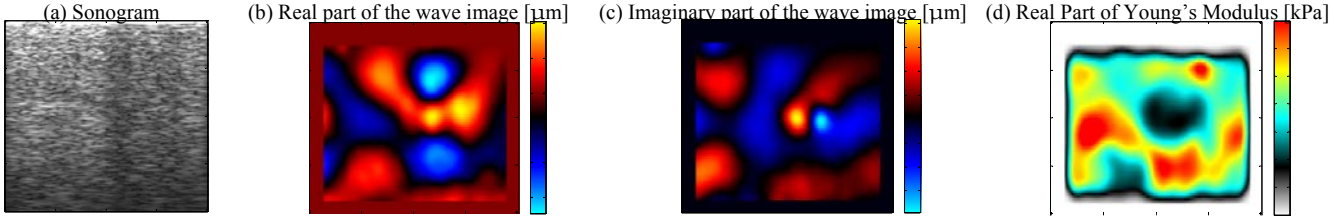

Figure 1: (a) Sonogram generated from beamformed RF frame, (b) estimated real part and (c) imaginary part of the wave image, and (d) estimated real part of the complex modulus image of the elasticity phantom with soft inclusion at 200Hz.

* *indicates Presenter*

029 ***IN–VIVO* EVALUATION OF UTERINE ABNORMALITIES BASED ON ULTRASOUND SALINE INFUSED SONOHYSTEROGRAPHY STRAIN IMAGING.**

Eenas A. Omari[1,2], Tomy Varghese[1,2], Mark A. Kliewer[3].*
[1]Medical Physics, [2]Biomedical Engineering, [3]Radiology Departments, University of Wisconsin–Madison, 1111 Highland Ave., Madison, WI, USA.

Background: More than 60% of uterine abnormalities are due to abnormal uterine bleeding, caused either due to benign conditions such as leiomyomas, endometrial polyps, adenomyosis or malignant endometrial cancers [1]. Since clinical treatment for these conditions is very different, it is very important to make a correct diagnosis.

Aims: Saline infused sonohysterography is currently used to evaluate and enhance visualization of the endometrium but lacks the ability to differentiate between different masses. Since uterine masses have different stiffness characteristics than the surrounding background, we show the feasibility of using ultrasound strain imaging to determine variation in the stiffness of the uterine masses.

Methods: Radiofrequency (RF) data were acquired on 8 patients using a Siemens Antares ultrasound system with an EC9–4 transvaginal ultrasound transducer during a saline infused sonohysterography procedure at the University of Wisconsin Hospital and Clinics. During the procedure, saline was injected into the uterus, to push apart the walls of the uterine cavity, providing the deformation required for strain imaging. Strain images were estimated using a two–dimensional multilevel hybrid algorithm for ultrasound sector array transducers which estimates displacement slopes using least squares estimation [2].

Results: Strain images estimated using the two–dimensional multilevel hybrid algorithm provide additional new information that supplement current clinical B–mode diagnostic imaging. Stiffer masses, such as fibroids, are clearly differentiated on the strain images, which appear to be darker when compared to the normal uterine tissue. Figure 1a shows a B–mode image, currently used clinically, and Figure 1b shows a strain image obtained by processing the pre– and post–compressed B–mode and RF echo signals. The strain image in Figure 1b indicates an area where a fibroid is present and its border is defined.

Conclusions: Ultrasound saline infused sonohysterography based strain imaging can be used to determine variations in the stiffness of uterine masses *in–vivo*. Our results demonstrate the feasibility of improving clinical diagnosis based on strain imaging. Further evaluation is required with additional patient data to evaluate additional uterine pathologies.

Acknowledgements: This work is funded by NIH grant 5R21CA140939.

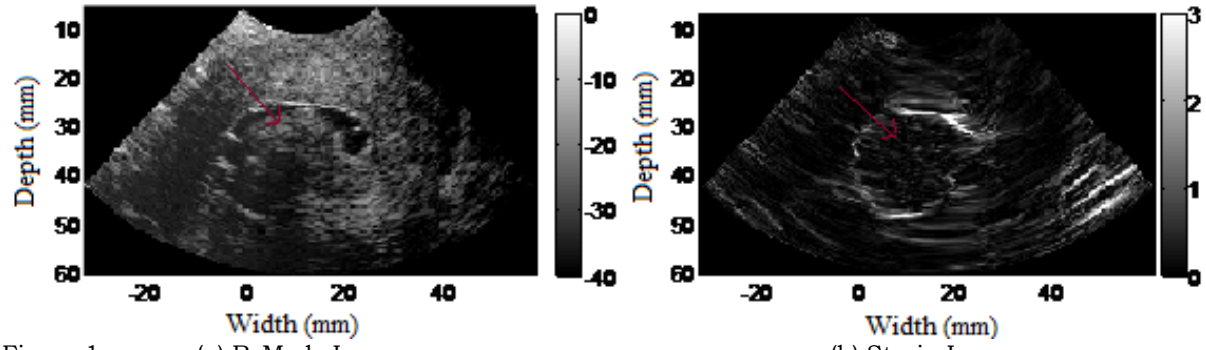

Figure 1: (a) B–Mode Image (b) Strain Image

References:

[1] Spencer, CP and MI Whitehead: Endometrial Assessment Re–Visited. Br J Obstet Gynaecol, pp. 623–632, 1999.
[2] Chen, Hao and Tomy Varghese: Multilevel Hybrid 2D Strain Imaging Algorithm for Ultrasound Sector/Phased Arrays. Medical Physics, 36, No. 6, pp. 2098–2106, 2009.

* *indicates Presenter*

032 **ON THE PROPAGATION OF GUIDED ELASTIC WAVES IN THIN PLATES FOR QUANTITATIVE SHEAR WAVE ELASTOGRAPHY OF THE CORNEA AND THE SKIN.**

Thu–Mai Nguyen[1], Jean–Luc Gennisson[1], David Touboul[3], Philippe Humbert[4], Jeremy Bercoff[2], Mathias Fink[1], Mickaël Tanter[1].*

[1]Institut Langevin Ondes et Images, ESPCI ParisTech, CNRS UMR 7587, INSERM ERL U979, Paris, FRANCE; [2]SuperSonic Imagine, Aix en Provence, FRANCE; [3]Centre Hospitalo–Universitaire de Bordeaux, FRANCE; [4]Centre Hospitalo–Universitaire de Besançon, FRANCE.

Background: Quantitative measurements of skin and cornea biomechanical properties have many applications in medicine. In ophthalmology, it could lead to a better diagnosis of pathologies or monitoring of treatments. In dermatology, it could help skin lesion removal monitoring. In the framework of Supersonic Shear Imaging (SSI), these organs are characterized by their complex sub–wavelength geometry (thin plate) that strongly influences the shear wave propagation.

Aims: The aim of this work is to refine and use the SSI technique to quantitatively map in real time cornea and skin elasticity. In this study, a method for the quantification of elastic modulus in these tissues is proposed. The shear wave dispersion induced by the guided propagation in such thin layers is estimated and fitted to the analytical dispersion curve derived from the leaky Lamb Wave theory.

Methods: The SSI technique consists of generating a shear wave by ultrasonic radiation force and imaging its propagation through the medium at a high frame rate (20kHz). For infinite media, shear wave velocity is then linked to Young's modulus. In cornea and skin layers, the high–frequency shear wave (from 500 to 2000Hz) is guided similarly to a Lamb wave, with plate thickness (<1mm) close to its wavelength. Experimental dispersion curves have been confronted to numerical studies. First, experiments were conducted *in vivo* on skin and *ex vivo* on porcine corneas. Secondly, finite element (FE) simulations were performed to obtain numerical dispersion curves in plates with known thickness and elasticity. Furthermore, theoretical dispersion equations were derived by numerically solving the propagation equation.

Results: Dispersion curves obtained *in vitro* on phantoms and *in vivo* are consistent with analytical calculations. Least mean squares fitting of curves enables recovering a quantitative assessment of elasticity (standard deviation <10%). Quantitative measurements of the shear modulus have been obtained *in vivo* in dermis and hypodermis using a linear probe (15MHz, 256 elements). On the cornea, UV–induced cross–linking (UVA CXL) an ophthalmologic treatment has been assessed *ex vivo*; an increase of 50% of the shear modulus has been measured after treatment. Corneal elasticity changes have also been observed while increasing the intra–ocular pressure (IOP) by steps of 4mmHg.

Conclusions: In this study, it has been shown that the SSI technique can be applied at high frequency to estimate local stiffness in complex geometries, such as cornea and skin, which strongly influence shear wave propagation. Quantification has been retrieved by numerically establishing the dispersion equation as a function of elasticity and thickness. The efficiency of elasticity monitoring for UVA CXL and IOP measurement is evaluated. Finally, *in vivo* feasibility was demonstrated on healthy volunteers.

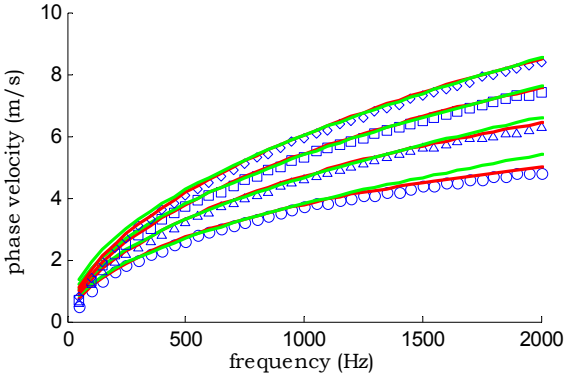

Figure 1: Dispersion curve for a plate immersed in water (thickness = 1mm), for different shear moduli (64, 144, 256 and 400 kPa) obtained by FE simulation (blue). These curves are conforming to the numerical (red) and analytical equations (green).

* *indicates Presenter*

039 **A CORRELATION TOMOGRAPHY OF COMPLEX SHEAR WAVE FIELD IN SOFT SOLIDS.**

Stefan Catheline[1], Thomas Gallot[1], Philippe Roux[1], Javier Brum[1], Carlos Negreira[2].*
[1]Grenoble University & CNRS, LGIT, Grenoble, FRANCE; [2]Science University, LAU, Montevideo, URUGUAY.

Background: Shear waves in a soft solid can be focalized using time–reversal (TR) methods [1]. The shear velocity, directly related to the elasticity of the medium, can be extracted from the TR field.

Aims: This study proposes to perform quantitative imaging of the mechanical properties inside a soft solid where a diffuse elastic field is present.

Methods: Shear waves are created by finger impacts all over the surface of the solid. One component of the vectorial field inside the solid is measured by ultrasonic techniques developed in elastography. Inspired from Green's function retrieval methods, the TR field is computed from cross–correlation of this random–like displacement signal. One point is chosen as a virtual source where the spatio–temporal refocusing is observed. Thus the method allows focalization of shear wave everywhere inside the solid without any source embedded in the solid.

Results: The local shear velocity is then deduced from the TR field. Finally, a two dimensional velocity map of a bi–layer medium is performed as shown in Figure 1.

Conclusions: Extracting elastic parameter in soft solids from a diffuse elastic field can be potentially useful in the human body where muscle activities create permanently erratic shear waves. Inspired by seismology [2], this technique would be a passive shear wave speed tomography for soft tissues.

Acknowledgements:

References:

[1] S. Catheline, N. Benech, X. Brum, and C. Negreira: Time Reversal of Elastic Waves in Soft Solids. Phys.Rev.Letter, 100, 064301, 2008.
[2] M. Campillo and A. Paul: Long–Range Correlations in the Diffuse Seismic Coda. Science, 299, pp. 547–549, 2003.

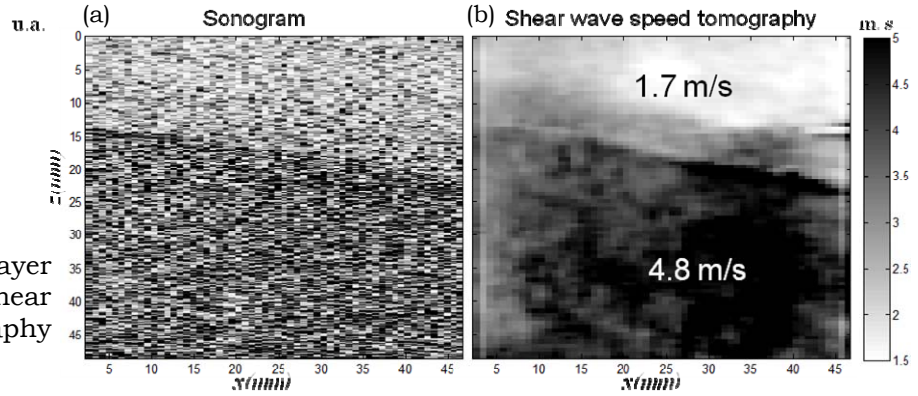

Figure 1: (a) Sonogram of a 2–layer phantom. (b) The shear wave speed tomography image.

* *indicates Presenter*

036 ***IN–VIVO* TIME REVERSAL ELASTOGRAPHY: A PASSIVE CORRELATION TOMOGRAPHY.**

Thomas Gallot[1], Stefan Catheline[1], Philippe Roux[1], Javier Brum[1], Carlos Negreira[2].*
[1]Grenoble University & CNRS, LGIT, Grenoble, FRANCE; [2]Science University, LAU, Montevideo, URUGUAY.

Background: Time Reversal experiments allow focalization of waves in soft solids [1]. The mechanical properties of the medium can be extracted from the refocusing field. Furthermore, correlation of noise–like signals is a recent method to extract information from multiple scattered wave fields [2].

Aims: In this work, the Time Reversal experiment becomes passive yielding to an *in–vivo* tomography of shear waves.

Methods: Heartbeats, breathing and muscle activity, the human body presents natural sources of vibration creating a complex shear wave field. Indeed, the shear wave noise inside soft tissue is measured by ultrasonic techniques developed in elastography. The particle motions estimated along lines or planes inside the medium can be used as artificial stars for time reversal experiments. In another language, Green's functions can be recovered from noise correlations which results in a totally passive imaging technique.

Results: The physiological noise is demonstrated in this work to be useful for *in–vivo* quantitative elasticity imaging in the liver. In comparison to a sonogram (Figure 1a), quantitative imaging of the shear speed in the liver region is presented (Figure 1b). Good correspondence is found between the two images at the interface between abdominal muscle and the liver, around *z*=10mm. The average shear wave speed in muscle and liver, 1.2m/s and 3.5m/s respectively, is in quantitative agreement with other studies [3,4].

Conclusions: This i*n–vivo* experiment demonstrates the feasibility of passive elastography. Future applications will focus on moving organs like the heart where elastography with active methods is not achievable.

References:

[1] Benech et al.: 1–D Elasticity Assessment in Soft Solids from Shear Wave Correlation: The Time–Reversal Approach. IEEE Trans. Ultrason. Ferroelectr., 56 (11), pp 2400–2410, 2009.
[2] M. Campillo and A. Paul: Long–Range Correlations in the Diffuse Seismic Coda. Science, 299, pp. 547–549, 2003.
[3] J.L. Gennisson et al. : Human Muscle Hardness Assessment During Incremental Isometric Contraction Using Transient Elastography. J. Biomech., 38(7), pp. 1543–1550, 2005.
[4] Muller et al.: Quantitative Viscoelasticity Mapping of Human Liver Using Supersonic Shear Imaging: Preliminary *In Vivo* Feasibility Study. Ultrasound in Med. & Biol., 35(2), pp. 219–229, 2009.

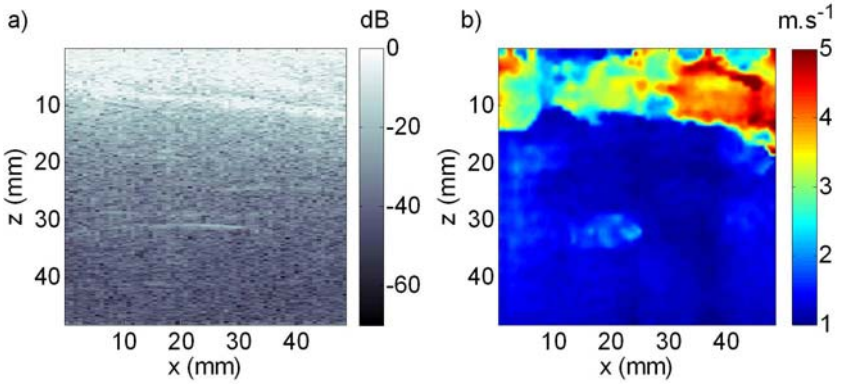

Figure 1: a) Sonogram of a liver region, the interface between belly muscle and the liver is visible around *z*=10mm.
b) The passive shear wave speed tomography from the correlation width shows the same interface and the shear speed values are in agreement with literature [3,4].

* *indicates Presenter*

062 **PRELIMINARY ASSESSMENT OF SHEARWAVE™ ELASTOGRAPHY FEATURES IN PREDICTING BREAST LESION MALIGNANCY.**

D Cosgrove[1], C Doré[2], R Hooley[3], E Mendelson[4], L Barke[5], A Cossi[6], B Cavanaugh[7], L Larsen[8].*
[1]Imperial College, Hammersmith Hospital, London, England, UK; [2]London, England, UK; [3]Yale Medical Center, Yale, CT, USA; [4]Northwestern Medical Center, Chicago, IL, USA; [5]Sally Jobe Breast Center, Denver, CO, USA,: [6]Boston Medical Center, Boston, MA, USA; [7]Thomas Jefferson University, Philadelphia, PA; USA, [8]University of Southern California, Los Angeles, CA, USA.

Background: Shear wave elastography (SWE) provides a quantitative measurement of tissue stiffness with high spatial resolution and may improve characterization of breast masses.

Aims: To evaluate the reproducibility of SWE and impact of adding SWE [1] features to the BI–RADS® classification of breast masses from the first 1000 cases in a prospective multicenter trial.

Methods: SWE studies were performed on a on a prototype of the Aixplorer system (Supersonic Imagine, Aix–en–Provence, France). A subset of 192 breast lesions (42.71% malignant) was analyzed. Reproducibility of SWE images and measurements was assessed; logistic regression analysis was performed to predict the pathology findings. SWE features were added to the ultrasound BI–RADS to generate models that were challenged by comparing the areas under the ROC curves (A_z), and the sensitivity and specificity scores.

Results: In the preliminary analysis, intra–operator reproducibility of SWE size ($R \geq 0.93$) and mean elasticity ($R=0.88$) measurements were in near–perfect agreement. Using the best three–variable model (BIRADS + elasticity shape + maximum elasticity), the A_z increased from 0.77 to 0.93 specificity increased from 61.8% to 87.3%, although sensitivity decreased from 92.7% to 87.8%. Adding more variables did not effect further improvements.

Conclusions: In this ongoing study, SWE provided reproducible information (elasticity values and SWE mapping) that improved the characterization of breast lesions. These features are directly linked to the characteristics of SWE: local quantification and millimeter resolution. Further evaluation of the study is in progress.

Acknowledgements: The BE1 Collaborative Group study was sponsored by Supersonic Imagine and comprised centers in the USA and Europe. Their support and participation is gratefully acknowledged.

References:

[1] Tanter M, Bercoff J, Athanasiou A, Deffieux T, Gennisson JL, Montaldo G, Muller M, Tardivon A and Fink M: Quantitative Assessment of Breast Lesion Viscoelasticity: Initial Clinical Results using Supersonic Shear Imaging. Ultrasound Med Biol, 34(9), pp. 1373–86, 2008.

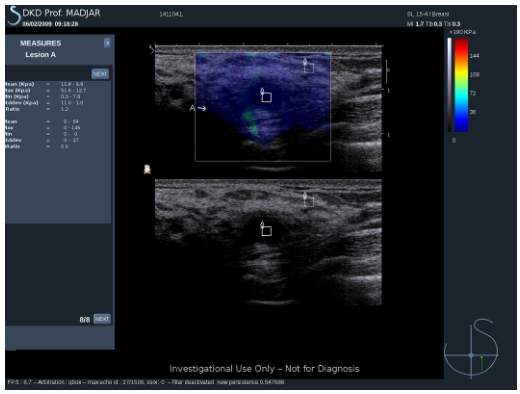

Figure 1: This suspicious lesion was classified as BI–RADS 4B on B–mode but SWE showed low kPa values (around 50kPa) so was reclassified as BI–RADS 3. Biopsy showed fibrocystic change only.

009 **AXIAL SHEAR STRAIN FEATURE FOR DIFFERENTIATING BREAST LESIONS.**

Haiyan Xu[1,2], Min Rao[1], T Varghese[1,2], S Baker[1], AM Sommer[1], TJ Hall[1], GA Sisney[3], ES Burnside[3].*
[1]Medical Physics Department, [2]Electrical and Computer Engineering Department, [3]Radiology Department, University of Wisconsin–Madison, Madison, WI 53705, USA.

Background: Ultrasound–based axial strain imaging has been used to aid in distinguishing benign from malignant breast masses, based on the stiffness and size–ratio (ratio of mass dimensions on the strain image to that on the B–mode image). The desmoplastic scirrhous reaction evoked by infiltrating cancers also tend to make these masses become firmly attached to background tissue and are thereby less mobile during applied deformations when compared to benign masses like fibroadenomas. We utilize the variations in the bonding between different breast masses for characterization.

Aims: The feasibility of using the normalized axial shear strain feature to differentiate between benign and malignant breast masses utilizing ultrasound radiofrequency (RF) data acquired *in–vivo* on patients scheduled for biopsy is evaluated. The normalized axial shear strain area feature estimates the degree of bonding of breast masses to background tissue and may provides improved differentiation of benign from malignant breast masses leading to improved breast cancer diagnosis [1,2].

Methods: *In–vivo* RF data were acquired using a Siemens SONOLINE Antares real–time clinical scanner equipped with a VFX13–5 linear array transducer at the University of Wisconsin–Madison Breast Center. Free–hand palpation with deformation up to 10% was utilized to acquire pre– and post–deformation RF data to generate ultrasound axial strain and axial shear strain images. The axial strain and the axial component of shear strain are generated using a two–dimensional cross–correlation algorithm. Axial shear strain values normalized to breast mass dimensions, applied strain and strain contrast were utilized to estimate feature values for differentiating benign from malignant masses. In this study, we compare *in–vivo* feature values of 8 malignant tumors and 33 fibroadenomas using axial shear strains to that obtained from biopsy results which are considered the diagnostic standard to evaluate the feasibility of our approach.

Results: Our results indicate that the normalized axial shear strain area (NASSA) feature is significantly larger for malignant masses when compared to fibroadenomas. These results corroborate *in-vivo* results reported by Thittaikumar et al. [1], on 15 benign and 15 malignant masses. Axial shear strain values greater than a specified threshold along with correlation coefficient values greater than 0.75, are overlaid on the corresponding B–mode images and utilized for diagnosis. A scatter plot of the shear strain area feature indicates the ability to differentiate benign from malignant breast masses. Based on results obtained using a linear classifier, the area under the receiver operator characteristic curve was 0.996, showing the potential of this feature to noninvasively differentiate breast masses.

Conclusions: Axial shear strain images may provide additional information which along with currently utilized axial strain and B–mode images may improve differentiation of benign and malignant breast masses and may reduce unnecessary biopsy thereby reducing patient morbidity.

Acknowledgements: This work is supported by Komen grant BCTR0601153 and NIH–NCI grants 5R21CA140939 and R01CA112192–S103.

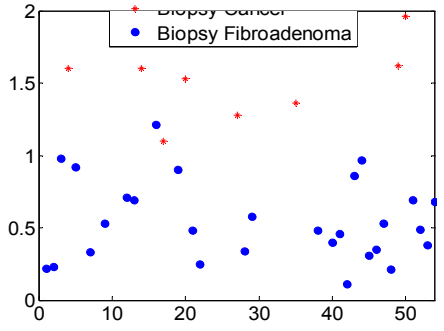

Figure 1: Scatter plot of NASSA values for 41 patients (8 malignant, 33 benign fibroadenomas)

References:

[1] Thitaikumar, A., Mobbs, L., Kraemer–Chant, C., Garra, B., and Ophir, J.: Breast Tumor Classification using Axial Shear Strain Elastography: A Feasibility Study. Phys Med Biol; 53(17), pp. 4809–4823, 2008.
[2] Xu, H, Rao, M, Varghese, T, Sommer, A, Baker S, Hall TJ, Sisney G.A. Burnside, B.: Ultrasound Med Biol, (in press), 2010.

* *indicates Presenter*

018 **ARFI IMAGING OF HUMAN PROSTATE *IN VIVO*: INITIAL FINDINGS FROM 20 PATIENTS.**

Liang Zhai[1], Stephen Rosenzweig[1], Thomas Polascik[2], Wen–Chi Foo[3], Vladimir Mouraviev[2], John Madden[3], Mark L. Palmeri[1] and Kathy R. Nightingale[1].*

[1]Biomedical Engineering Department, Duke University, Durham, NC, USA; [2]Duke Prostate Center and Division of Urologic Surgery, Surgery Department; [3]Pathology Department, Medicine Department, Duke University Medical Center, Durham, NC, USA.

Background: Elasticity imaging techniques have shown promise for guiding clinical procedures such as needle biopsy and focal therapy [1]. Yet, challenges have been reported associated with achieving uniform compression on the prostate. Acoustic radiation force impulse (ARFI) imaging is an elasticity imaging method that uses remotely generated, focused acoustic beams to interrogate tissue stiffness [2], which can overcome this problem. By monitoring tissue displacement response to impulse acoustic radiation force, relative stiffness among structures inside the soft tissue can be inferred based on the resultant displacement amplitudes in ARFI images. Previously, we have demontrated the capability of ARFI imaging to resolve various prostatic structures in excised prostate specimens [3]. In this work, we performed a pilot study on 20 patients to investigate the feasibility of ARFI prostate imaging *in vivo*.

Aims: The goal of this study is to investigate the feasibility of ARFI imaging to visualize the internal structures and prostate cancer (PCa) in human prostate *in vivo*.

Methods: Twenty patients were consented under an IRB approved protocol and imaged in Duke Medical Center. A modified Siemens Antares™ scanner and a 3D wobbler, end–firing, transrectal probe, EV9F4 was used to acquire *in vivo* ARFI data. ARFI excitation pulses used a center frequency of 4.0 MHz, focal depth of 20 mm, F/# 2.9 and duration of 100 μs. Tracking beams used 4:1 parallel–receive techniques to reduce acquisition time. Each 2D ARFI imaging plane consisted of 55 pushing locations, and the entire 3D volume of the prostate was acquired using 50 2D planes with 1.8 degree increments. The *in vivo* study was performed at the beginning of the prostatectomy surgery when the patient was anesthetized. The prostate was imaged again after it was surgically removed, and compared to the *in vivo* ARFI images to explore potential stiffness differences of prostatic tissue under the two conditions. During histological analysis, pathologies and anatomic structures were identified in each histological slide. These slides were then digitized and assembled together to recontruct the volume of each prostate. Finally, the reconstructed histological volumes were registered to the 3D ARFI data to identify various prostate structures in ARFI images.

Results: Compared to the matched B–mode images, ARFI images portray prostate structures with higher contrast. Similar stiffness contrast was observed among prostate tissues in registered *in vivo* and *ex vivo* ARFI images. Zonal anatomy was visualized. PCa was shown to be stiffer than the normal surrounding tissue in the peripheral and transitional zones. Initial data suggest that prostate cancer with higher Gleason's scores seems to be better visualized in ARFI images.

Conclusions: This on–going pilot study demonstrates that prostatic structures such as zonal anatomy, BPH and focal PCa lesions can be visualized in ARFI images. As such, this technology has the potential to provide improved image guidance for prostate needle biopsy and focal therapy.

Acknowledgements: The authors would like to thank Siemens Healthcare, Ultrasound Business Unit for their technical support. This work is supported by NIH R01EB002132, NIH R01CA114075, NIH R01CA142824 and DOD PCRP W81XWH–08–10132.

References:

[1] Konig K, Scheipers U, Pesavento A, Lorenz A, Ermert H, Senge T: Initial Experiences with Real-Time Elastography Guided Biopsies of the Prostate. J Urol., 174, pp. 115–117, 2005.

[2] Nightingale K, Palmeri M, Nightingale R, Trahey G: On the Feasibility of Remote Palpation using Acoustic Radiation Force. JASA, 110(1), pp. 625–634, 2001.

[3] Zhai L, Madden J, Foo W, Palmeri M, Mouraviev V, Polascik T, Nightingale K: Acoustic Radiation Force Impulse Imaging of Human Prostate *Ex Vivo*. Ultrasound Med. Biol., 36(4), pp. 576–588, 2010.

074 **ELECTRODE DISPLACEMENT BASED STRAIN IMAGING FOR MONITORING *IN–VIVO* OPEN–SURGERY THERMAL ABLATION THERAPIES.**

N Rubert[1], S Bharat[1], RJ Dewall[1], A Andreano[2], C Brace[2], J Jiang[1], L Sampson[2], T Varghese[1].*
[1]Medical Physics Department, [2]Radiology Department, University of Wisconsin–Madison, Madison, WI, USA.

Background: Radiofrequency (RF) ablation therapy is being increasingly used to non–invasively destroy hepatic tumors. Convenient, cost–effective imaging for monitoring the extent of thermal ablation is critical for the success of this technique. Ultrasound B–mode images are widely used for monitoring the placement of the ablation electrode when performing RF ablation procedures. However, B–mode images are not reliable for displaying the extent of the thermal ablation zone. The thermal ablation does have elevated stiffness, making imaging modalities which display tissue mechanical properties attractive for monitoring the extent of the ablation zone.

Aims: The aim of this study is to assess the ability of two–dimensional electrode displacement based strain imaging to accurately monitor the extent of thermal ablations.

Methods: Open abdominal RF ablation procedures (n=13) were performed on porcine animal models. In each animal three or four RF ablations were created, a maximum of one in each lobe of the liver. Strain imaging using electrode displacement was performed within ten minutes of each ablation procedure. Manually applied minute displacements (< 1mm) of the unconstrained end of the ablation electrode were used to displace the ablated region bonded to the active end of the electrode. A Siemens Antares clinical (Siemens Medical Solution, USA, Inc., Issaquah, WA) real–time scanner equipped with a 10 MHz center frequency linear array transducer (VFX 13–5), was used to record RF data as the ablation electrode was displaced. For gross pathology measurements, the livers were excised following the RF ablations and each thermal ablation zone was sliced through the assumed imaging plane using a commercially available meat slicer. The recorded RF data were used to create electrode displacement strain images off line. Manual contouring of the ablated region was performed by three of the authors, along with an automated segmentation algorithm in order to determine the extent of the thermal ablation zones. The depiction of the thermal ablation zone in the strain images was compared to gross pathology measurements for cross–sectional area comparisons using linear regression analysis.

Results: Manual cross–sectional area measurements from strain images of these ablation zones and areas measured using automated segmentation were correlated with areas measured on histopathology images using linear regression. For each individual and the automated segmentation, the correlation coefficient was found to be R = 0.824, R = 0.901, R = 0.465 and R = 0.828, respectively. The linear regression was also performed after averaging together the areas measured manually yielding a correlation coefficient of R = 0.894.

Conclusions: This study further demonstrates that electrode displacement based strain imaging is capable of providing high contrast images from a widely available commercial ultrasound system which may be used to assess the extent of thermal ablation zones.

Acknowledgements: This work was funded by NIH–NCI Grants R01 CA112192–04 and R01 CA112192–03S1. Ryan DeWall is also supported in part by NIH Grant T32 CA09206–31.

References:

[1] N. Rubert, S. Bharat, R. J. DeWall, et al.: Electrode Displacement Strain Imaging of Thermally Ablated Liver Tissue in An *In Vivo* Animal Model. Medical Physics, Vol. 37, No. 3, 2010.

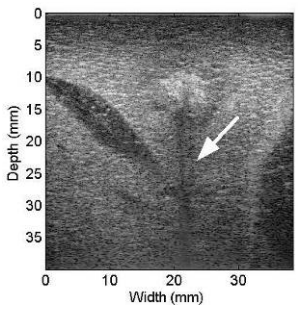

Figure 1: B-mode image of thermal ablation. Arrow indicates shadowing from ablation electrode.

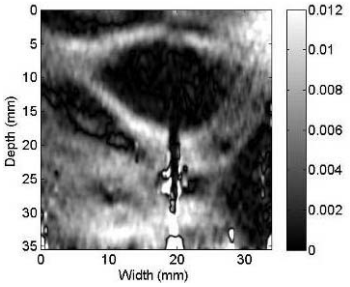

Figure 2: Corresponding Strain Image.

* *indicates Presenter*

028 **STRAIN RATIO IN REAL TIME SONOELASTOGRAPHY OF THE PROSTATE AS A SEMI–QUANTITATIVE MEASUREMENT TOOL: IMPACT ON PROSTATE CANCER DETECTION.**

*D Junker[1], F Aigner[1], T De Zordo[1], F Pedross[1], G Schaefer[1], G Mikuz[1], W Horninger[1], W Jaschke[1], F Frauscher[1]. Presented by A Lebovici[1]**

[1]Medical University Innsbruck, Innsbruck, AUSTRIA.

Background: Prostate cancer (PCa) has increased tissue stiffness (higher cell density) than the normal surrounding tissue under compression [1]. Real time sonoelastography (RTE) allows assessment of tissue elasticity of the prostate and, therefore, can demonstrate PCa as a hard area [2].

Aims: To assess the value of semi–quantitative strain–ratio measurement of tissue elasticity to differentiate benign stiff areas of the prostate, i.e. fibrosis or prostatitis, from malignant stiff areas and thereby reduce the number of biopsy cores with its related costs and complications.

Methods: Sixty–nine men were included in this study. All patients had elevated prostate specific antigen (PSA) serum levels and were scheduled for prostate biopsy. Tissue elasticity was assessed with real time sonoelastography using a Hitachi ultrasound machine (Hitachi EUB 8500, Tokyo, Japan), capable of color coding hard areas, i.e. blue. Prostate cancer has decreased tissue elasticity due to its high cell density. The uroradiologists biopsied up to 5 core samples from stiff outer gland areas of the prostate targeted by RTE. The degree of stiffness of a hard outer gland area was quantified with strain ratio, a semi–quantitative measurement tool integrated in the ultrasound machine and displayed on the left side of the screen. The strain ratio is calculated by comparing the suspicious stiff area with the area that shows the lowest stiffness in the same slice. Furthermore, each biopsy core was reviewed by a pathologist and reported as either cancer with an assigned Gleason score or as benign tissue.

Results: Overall, 104 hard prostate outer gland areas were measured using RTE with strain ratio values and were histologically analyzed. We divided the obtained values in 3 groups. Group A, with values between 0 and 40, showed a cancer detection rate of 19%. Group B, with values between 41 and 80, showed a cancer detection rate of 25%. Group C, with values > 80, showed a cancer detection rate of 36%. Cancer–negative hard areas histology revealed prostatitis, adenomyomatosis, atrophia or hyperplasia.

Conclusions: A hard lesion of the prostate with an assigned high strain ratio value has a higher chance to be malignant. Nevertheless, in our study we found a considerable number of PCa in the low strain ratio value group. It was not possible to calculate a strain ratio cut off value level ruling out PCa and decreasing the number of false positive findings on RTE and therefore reducing biopsy cores with its related costs and complication.

Figure 1

References:

[1] Krouskop TA, Wheeler TM, Kallel F, Garra BS, Hall T: Ultrason Imaging, 20(4), pp. 260–74, Oct 1998.

[2] Pallwein L, Aigner F, et al.: Prostate Cancer Diagnosis: Value of Real–Time Elastography. Review. Abdominal Imaging, 33(6), pp. 729–35, Nov–Dec 2008.

** indicates Presenter*

104 **THORACOLUMBAR FASCIA SHEAR PLANE MOTION IN CHRONIC LOW BACK PAIN.**

HM Langevin[1,2], JR Fox[1], C Koptiuch[1], NA Bouffard[1].*
[1]Neurology Department, [2]Orthopedics and Rehabilitation Department, University of Vermont, Burlington, VT, USA.

Background: Connective tissue is increasingly recognized as an important potential contributor to chronic musculoskeletal pain including low back pain [1]. The thoracolumbar fascia in humans is composed of several layers of dense connective tissue separated by layers of loose connective tissue allowing the dense layers to glide past one another. The dense layers correspond to the aponeuroses of muscles with different directions of pull: longitudinal for latissimus dorsi and erector spinae and transverse for internal/external obliques and latissimus dorsi. During passive trunk flexion/extension, shear plane motion can be observed with B–scan ultrasound between the dense connective tissue layers within the thoracolumbar fascia. We hypothesized that this shear plane motion could be quantified using ultrasound elasticity imaging techniques. We further hypothesized that this shear plane motion would be reduced in human subjects with chronic low back pain of greater than 12 months duration (LBP) compared with control subjects without low back pain (No–LBP).

Aims: To quantify the relative motion of the connective tissue layer closest to the muscle relative to the connective tissue immediately superficial to it in both a normal group and a chronic low back pain group of subjects.

Methods: So far, we have tested 128 subjects (73 with LBP and 55 with No–LBP). Groups were frequency matched for age, sex and body mass index. Subjects were placed prone on a motorized articulated table capable of inducing passive flexion/extension of the back standardized with respect to rate and range. An ultrasound cineloop was collected over a 10 second period of a 15 degree flexion/extension at 0.5Hz. The ultrasound transducer was placed longitudinally 2cm lateral to the midline at the level of the L2/3 interspace. Ultrasound data were collected using a Terason 3000 ultrasound machine equipped with a 10MHz linear array transducer. The cineloop frame rate was 25fps. The ultrasound radiofrequency (RF) data were collected and analyzed for displacement using elasticity imaging cross–correlation techniques [2,3]. We quantified the motion between the connective tissue layers closest to muscle relative to the connective tissue layers immediately superficial to it, identifying this as the perimuscular shear plane. Two rectangular regions of interest (ROI) were identified on each ultrasound B–scan image. These ROIs measured 10mm wide and 2mm deep and were located superior and inferior to the perimuscular shear plane. Total lateral displacement was determined within these ROIs over the period of the flexion portion of one cycle of the table. Relative motion of tissue between the two ROIs was determined by integrating the area under the curve of the difference in the time based displacement history.

Results: Preliminary analyses suggest that male subjects with LBP (but not females) had on average ~20% less perimuscular shear plane motion than subjects without LBP. Mean±SE % lateral shear strain was 56.7±27.5 vs. 70.2±25.2 for LBP and No–LBP respectively ($p<0.01$). We also found a negative correlation between % lateral shear strain and total body fat ($r=-0.42$, $p<.02$), % body fat ($r=-0.39$, $p<.02$) and trunk fat ($r=-0.37$, $p<.05$) in males with LBP but not in female subjects.

Conclusions: These preliminary findings suggest that thoracolumbar fascia shear plane motion may be related to LBP and/or trunk fat distribution in males. The significance of the observed gender differences in shear plane motion is currently unknown. Further testing and analyses are examining the specific role played by LBP independent of trunk fat. Possible explanations for reduced thoracolumbar shear plane motion during passive trunk flexion in LBP include abnormal patterns of trunk muscle activity and decreased fascia mobility due to fibrosis.

Acknowledgements: This work was supported by NCCAM Research Grant RO1–AT003479.

References:

[1] Langevin HM, Stevens–Tuttle D, Fox JR, et al.: Ultrasound Evidence of Altered Lumbar Connective Tissue Structure in Human Subjects with Chronic Low Back Pain. BMC Musculoskelet Disord, 10:151, 2009.
[2] Ophir J, Alam SK, Garra B, et al.: Elastography: Ultrasonic Estimation and Imaging of the Elastic Properties of Tissues. Proc Inst Mech Eng [H], 213, pp. 203–233, 1999.
[3] Konofagou E, Ophir J.: A New Elastographic Method for Estimation and Imaging of Lateral Displacements, Lateral Strains, Corrected Axial Strains and Poisson's Ratios in Tissues. Ultrasound Med Biol, 24, pp. 1183–99, 1998.

* *indicates Presenter*

024 **A FEASIBILITY STUDY OF CALIBRATING OPTICAL STRAIN ELASTOGRAMS WITH BIOMECHANICAL TESTING.**

Hazel Marie[1], Susheel Vadde[1], Harish Kukatla[1], Shalini Gadapa[1], Yong Zhang[1], John R. Sullins[1].*
[1]Youngstown State University, Meshell Hall, One University Plaza, Youngstown, OH, 44555, USA.

Background: There are two fundamental approaches in imaging elastic properties of soft tissue:

1) A direct method that estimates absolute elasticity (Young's modulus) from observed tissue displacement [1];
2) An indirect method that computes a strain elastogram from which relative property variations can be examined [2].

The second method has the advantage in that it avoids the numerical difficulties associated with solving an ill–posed inverse problem that often plague the direct method. However, the indirect method does not provide absolute elasticity values that may be desirable in certain clinical settings.

Aims: The aim of this study is to find an alternative approach that infers absolute elasticity information from a relative strain elastogram. This is accomplished through the calibration of an optical strain image with biomechanical tensile testing results.

Methods: Specimen of Mesenchymal Stromal Cells (MSC) treated rabbit tissues were subjected to the force–extension tensiometric tests. During a test, a sample went through a complete deformation cycle (linear, plastic and post–rupture stages). Video sequences of tissue deformation were captured using a SONY HD camcorder (Figure 1). A robust optical flow algorithm was used to compute a flow image between two adjacent frames that quantifies the tissue deformation. A strain elastogram was obtained by convolving the flow images with a weighted gradient filter. A strain elastogram is shown in Figure 2. The pixel–level property heterogeneity can be observed.

Results: To facilitate elastogram calibration, we defined an "elastographic strain" by taking the average of all pixel values in an elastogram. The "elastographic strain" of a video sequence that captured both linear and plastic deformations of a specimen (more than 5000 frames) was plotted against the stress data in Figure 3. The stress–strain curve derived from the "elastographic strain" matched almost perfectly with that of the tensile test. The Young's modulus values estimated from the first linear segment of stress–strain curves are: 666kPa (tensile test) and 691kPa (elastogram). The Young's modulus values estimated from the second linear segments are: 672kPa (tensile test) and 690kPa (elastogram).

Conclusions: A preliminary study has shown that a strain elastogram can yield much more information when calibrated properly with a tensile test. One promising application is that a calibrated elastogram using a finite element model will enable us to assess wound healing effect on a much finer scale.

Acknowledgements: This work was partially supported by Ohio Board of Regents Research Incentive Grant #34241, Youngstown State University URC Grant 08–#8, and St. Elizabeth Health Center.

References:

[1] F. Kallel and M. Bertrand: Tissue Elasticity Reconstruction using Linear Perturbation Method. IEEE Trans. on Medical Imaging, Vol. 15, pp. 299–313, 1996.
[2] J. Ophir, E. I. Cespedes, H. Ponnekanti, Y. Yazdi, and X. Li: Elastography: A Quantitative Method for Imaging the Elasticity of Biological Tissues. Ultrasonic Imaging, Vol. 13, pp. 111–134, 1991.

Figure 1: A video frame of a specimen during a tensile test.

Figure 2: An optical strain elastogram that shows property heterogeneity.

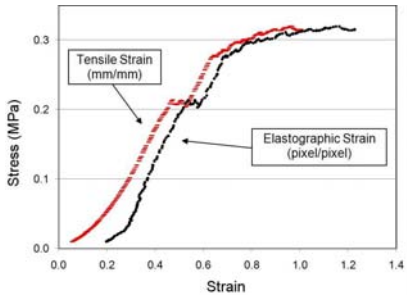

Figure 3: Stress–strain curves from the tensile test and the strain elastogram.

005 **QUANTIFYING STORAGE MODULUS OF HUMAN HEPATIC CANCERS WITH *EX VIVO* DYNAMIC COMPRESSION TESTING.**

Ryan J. DeWall[1,2], Shyam Bharat[1], Tomy Varghese[1,2], Meghan E. Hanson[3] and Mark A. Kliewer[3].*
[1]Medical Physics, [2]Biomedical Engineering, [3]Radiology Departments, University of Wisconsin–Madison, 1111 Highland Ave., Madison, WI, USA.

Background: Manual palpation has long been used by physicians to qualitatively detect the presence of diseases such as cancer. Recently, ultrasound elastography has provided several diagnostic techniques that quantify this mechanical information, which may complement traditional B–mode imaging in the clinic. Quasistatic electrode displacement approaches have shown good boundary demarcation of abdominal ablations on strain images [1]. Shear wave tracking techniques such as acoustic radiation force imaging (ARFI) and 1D transient elastography have been used to reconstruct Young's Modulus in small regions of interest (ROIs) in the liver, which may be used as a noninvasive diagnostic alternative to biopsy to detect liver fibrosis [2,3]. However, few studies have quantified the elasticity of human hepatic pathologies using *ex vivo* mechanical tests. These data will provide complementary information while diagnosing diseases using new elastographic techniques.

Aims: Our aim is to dynamically test human hepatic cancers and surrounding liver tissue to quantify the storage modulus (E'). The impact of strain hardening on the underlying contrast is also evaluated to determine the potential benefits of pre–compression in delineating lesions using elastography techniques.

Methods: Liver samples were obtained from the UW Pathology Lab and dynamically tested using an EnduraTEC ELF 3220 (Bose Corporation, EnduraTEC Systems Group, Minnetonka, MN). Samples were obtained from patients who underwent surgical resection at the University of Wisconsin Hospital and Clinics (Madison, WI). All protocols and procedures for this study were approved by the University of Wisconsin Institutional Review Board. One cubic centimeter samples were dynamically tested with 1–6% pre–compression and 2, 3 and 4% amplitudes (e.g. 1% pre–compression with 2% amplitude is tested from 1–3% compression). Testing frequencies of 1, 10, 20 and 30 Hz were used for each test. For each specimen tested we measured E', the elastic portion of the compression cycle.

Results: Table 1 shows the pathologies obtained thus far in this study, including hepatocellular carcinoma (HCC), colon metastases (Mets), rectal mets, gastrointestinal (GIST) mets and cirrhosis. Our results indicate that some of the cancers are significantly stiffer than surrounding background tissue. In particular, some colon mets and the GIST met tested were significantly stiffer than the surrounding background. HCCs were approximately the same stiffness as the surrounding background. Strain hardening was observed, particularly in the colon mets and neuroendocrine met samples.

Pathology	E' (kPa)	N
Normal	3.3 ± 1.3	14
HCC	3.5 ± 1.5	2
Colon Mets	23.1 ± 23.0	7
Rectal Mets	30.9	1
GIST Mets	4.3	1
Neuroendocrine Mets	3.9	1
Cirrhosis	13.7 ± 6.8	2

Table 1: E' for 1–3% Dynamic Compression Test (1Hz Frequency)

Conclusions: These results present E' obtained from mechanical testing of pathologic and normal liver samples through a range of pre–compression values. Some cancers were significantly stiffer than the surrounding background, indicating that elastographic techniques may be a useful diagnostic tool in these cases. However, some cancers were approximately the same stiffness as the surrounding background (e.g. HCCs). Strain hardening was also observed with some cancers, which suggests that pre–compression may increase the contrast between the cancer and surrounding background.

Acknowledgements: This work is supported in part by NIH grants R01 CA112192–04, R01 CA112192–S103 and T32 CA09206–31.

References:

[1] Rubert N et al.: Electrode Displacement Strain Imaging of Thermally–Ablated Liver Tissue in an *In Vitro* Animal Model. Med Phys, 37(3), pp. 1075–82, 2010.
[2] Sandrin L et al.: Transient Elastography: A New Noninvasive Method for Assessment of Hepatic Fibrosis. UMB, 29(12), pp. 1705–13, 2003.
[3] Palmeri ML, Wang MH, Dahl JJ, Frinkley KD, and Nightingale KR: Quantifying Hepatic Shear Modulus *In Vivo* using Acoustic Radiation Force. UMB, 34(4), pp. 546–58, 2008.

* *indicates Presenter*

030 **QUANTIFICATION OF THE VISCOELASTIC CHARACTERISTICS OF THE UTERUS AND ASSOCIATED PATHOLOGIES.**

Eenas A Omari[1,2], MZ Kiss[1], T Varghese[1,2], MA Kliewer[3], JM Harter[4], EM Hartenbach[5].
[1]Medical Physics, [2]Electrical and Computer Engineering, [3]Radiology, [4]Pathology, [5]Obstetrics and Gynecology Departments, University of Wisconsin–Madison, 1111 Highland Ave., Madison, WI, USA.

Background: Abnormal uterine bleeding is the number one cause of gynecological visits, bleeding is caused either due to benign conditions such as leiomyomas, endometrial polyps, adenomyosis or malignant endometrial cancers [1]. Ultrasound saline infusion based strain imaging, a minimally invasive alternative to hysteroscopy or uterine biopsies, is currently being investigated to be used to distinguish between different masses that cause abnormal bleeding.

Aims: In order to characterize uterine masses *in vivo* using ultrasound saline infusion based strain imaging, it is important to determine the effectiveness of differentiating between the stiffer (fibroids) and softer (endometrial polyps) masses that cause uterine bleeding. Quantification of the complex modulus is investigated in this research.

Methods: Normal and abnormal uterine tissue is obtained from hysterectomies performed at the University of Wisconsin Hospital and Clinics. A mechanical testing system (MTM), EnduraTEC model 3200 ElectorForce (ELF), is used to evaluate sections of uterine masses with dimensions of approximately one cubic centimeter to determine the Young's storage modulus. Dynamic testing is performed with compression ranges of 2%, 3% and 4% in amplitude over a frequency range 1–30 Hz.

Results: Results are obtained for 5 normal uterine tissue samples and 3 uterine fibroids. The Young's storage modulus at the lowest frequency of the mechanical testing (1Hz) and a percent strain (2–4%) for normal uterine tissue is approximately 29.7kPa with standard deviation of 2.2kPa, and the loss modulus is 8.8kPa with standard deviation of 1.6kPa. The Young's storage modulus for fibroid uterine tissue was found on average to be 97.2kPa with 6.5kPa standard deviation, and the loss modulus is 3kPa with standard deviation of 1.6kPa, using the same pre–compression and similar cyclic deformation. Table 1 lists the storage modulus (E') and loss modulus (E") for normal uterine tissue and fibroid extracted from uterine tissue.

Patient	E' (kPa)	E" (kPa)	Patient	E' (kPa)	E" (kPa)
Normal 1	27.2	8.1	Fibroid 1	90.7	28.8
Normal 2	29.9	6.7	Fibroid 2	103.7	32
Normal 3	31.7	10.2	Fibroid 3	97.3	30.1
Normal 4	27.8	8.7			
Normal 5	31.9	10.4			

Table 1: E' and E" for 1 to 4% Dynamic Compression Test (1Hz frequency)

Conclusions: We show that fibroids are significantly stiffer when compared to normal uterine tissue. Further mechanical testing will be performed on normal and different abnormal uterine tissue, such as polyps, fibroid and cancerous, as they become available.

Acknowledgments: This work is funded by NIH grant 5R21CA140939.

References:

[1] Spencer, CP and MI Whitehead: Endometrial Assessment Re–Visited. Br J Obstet Gynaecol, pp. 623–632, 1999.

034 **NONLINEAR SHEAR MODULUS QUANTIFICATION BY COMBINING STATIC AND DYNAMIC ELASTOGRAPHY.**

Heldmuth Latorre–Ossa[1], Jean-Luc Gennisson[1], Emilie De Brosses[1], Mickaël Tanter[1].*
[1]Institut Langevin–Ondes et Images, ESPCI ParisTech, CNRS UMR7587, INSERM U979, Paris, FRANCE.

Background: The assessment of mechanical properties of soft media is enjoying a growing interest in the field of medical imaging as pathologies are often correlated with a local change in stiffness. To date, advanced techniques in this field have been concentrating on the estimation of the second order elastic modulus (the shear modulus, μ). However, it could be useful to study additional tissue mechanical properties such as shear nonlinearity (the third order elastic modulus, A) in order to have more accurate tissue characterization.

Aims: The goal of acoustoelasticity experiments [1] is to retrieve the nonlinear shear modulus (A) in soft solids by applying uniaxial stress (σ) at the medium's surface. In quasi–incompressible soft solids, this theory is governed by the following equation: $\rho V_S^2 = \mu_0 - \sigma(A/12\mu_0)$, where μ_0 is the material shear modulus at $\sigma = 0$, V_S is the shear wave speed and ρ is the medium density. Here, we propose a method combining static elastography (uniaxial quasi–static compressions) and dynamic elastography (Supersonic Shear Imaging (SSI) technique) to compute the 2D stress map of the medium which is subsequently used to calculate the nonlinear shear modulus.

Methods: Two tissue mimicking phantoms (2% Agar – 5% Gelatin) containing a soft (2% A – 3%G) and hard inclusion (2% A – 8% G) are axially compressed in steps of 0.1 mm from 0 to 5 mm. Firstly, at each compression step, the SSI technique allows quantitatively mapping the Young's modulus of the medium. Shear waves are generated directly inside the medium through ultrasonic radiation force and caught by using an ultrafast ultrasound scanner (5000 frames/s). Then, a time of flight algorithm is employed to estimate the shear wave speed which is directly related to the Young's modulus (E) by the well known equation $E \approx 3\mu = 3\rho V_S^2$. Sets of ultrasonic raw–data are acquired before and after uniaxial compression to compute the axial 2D strain map (ε). Next, the stress (σ) map is retrieved according to Hooke's equation ($\sigma = E.\varepsilon$) and can be also used to stepwise crawl up the stress–strain curve. Lastly, the acoustoelasticity theory in soft media [1] is applied to map the nonlinear shear modulus A, by knowing the stress variation as a function of the shear modulus at each compression step.

Results: Tissue 2D strain and stress maps were successfully calculated for both phantoms. Experimental results were compared to numerical simulations and showed good accordance. Figure 1 presents the results for the phantom with a soft inclusion: the shear modulus (a), the cumulative strain (b) and the cumulative stress (c) after 1 mm compression. Figure 1(d) presents the nonlinear shear modulus for the same phantom where the nonlinear shear modulus had a mean value of -70 ± 4 kPa and 82 ± 23 kPa for the inclusion and its surrounding media respectively. For the phantom with a hard inclusion, the nonlinear shear modulus had a mean value of -8 ± 7 kPa for the inclusion and 40 ± 9 kPa for its surrounding media.

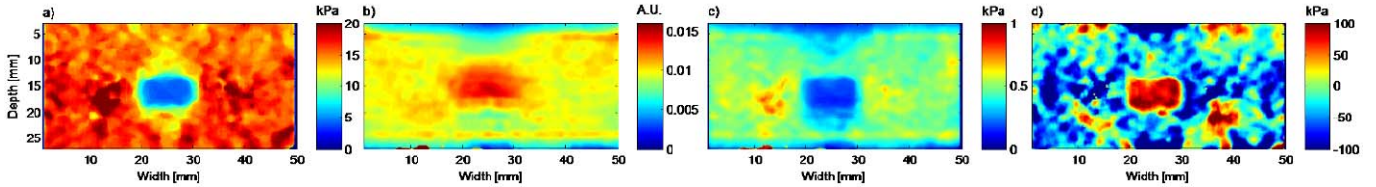

Figure 1: (a) shear modulus, (b) cumulative strain map and (c) cumulative stress map after 1 mm compression, (d) nonlinear shear modulus (A) after 5 mm compression.

Conclusions: Results show that for applied stress, the elasticity of biological tissues is linked to nonlinearity. The quantification of the nonlinear shear modulus could play a key role in improving the clinical diagnosis of tissue pathologies. Although we have proved capability to quantify stress and shear nonlinearity in phantoms, it is necessary to carry out *in vivo* studies to validate the obtained results. In addition to the nonlinear shear modulus, knowing the stress distribution could be an important factor to better understand mechano-transduction processes (processes of genes activation in cells due to applied stress) *in vivo* [2].

References:

[1] Gennisson J.L., Rénier M., et al.: Acoustoelasticity in Soft Solids: Assessment of the Nonlinear Shear Modulus with the Acoustic Radiation Force. J. Acoust. Soc. Am., 122 (6), pp. 3211–3219, 2007.
[2] E. Brouzés, E. Farge: Interplay of Mechanical Deformation and Patterned Gene Expression in Developing Embryos. Current Opinion in Genetics and Development, 4, pp. 367–374.

* *indicates Presenter*

075 **ULTRASOUND ELASTICITY IMAGING OF HUMAN POSTERIOR TIBIAL TENDON.**

Liang Gao[1], Chris Geffre[1], John Szivek[1], Mihra S. Taljanovic[1], L. Daniel Latt[1], Russell S. Witte[1].*
[1]University of Arizona, Tucson, AZ, USA

Background: Posterior tibial tendon dysfunction (PTTD) leads to a progressive flatfoot deformity that is accompanied by pain [1] and decreased gait efficiency [2]. PTTD is exceedingly common, affecting 3.3% of women over the age of 40 [3]. There is a continuum of disease from tendon inflammation to irreversible tendon degeneration. Due to the pain that is experienced in the inflamed tendon, it is often difficult to clinically differentiate an inflamed tendon from one that has undergone degenerative change. Inflamed tendons are treated with immobilization and rest, whereas, those that have undergone irreversible degenerative change are treated with surgery [1]. Ultrasound elasticity imaging (UEI) allows for the noninvasive characterization of the mechanical properties of soft tissue structures, such as tendon. It is hypothesized that UEI will yield different load–deformation curves for normal and degenerated tendons. This technique can then be applied to tendons of unknown degenerative status to help avoid needless surgery or futile prolonged immobilization.

Aims: The goal of this study was to demonstrate feasibility of UEI to noninvasively map the mechanical properties of human tendon using a controlled, *ex vivo* preparation. We implemented a 2D phase–sensitive cross–correlation speckle tracking algorithm [4] to determine the mechanical properties of the human posterior tibial tendon under controlled external force. Our long term goal is to compare normal and dysfunctional posterior tibial tendons and further refine UEI as a diagnostic tool for PTTD.

Methods: The posterior tibial tendon from a normal human cadaver was partially dissected at one end and connected to a mechanical testing system (MTS 810, Eden Prairie, MN). The MTS applied a force through a Labview™ interface (National Instruments). The system also recorded the force and stroke during the stretch. The movement of the tendon was simultaneously measured in real time at a frame rate of 80Hz using a clinical ultrasound scanner (Zonare Medical Systems) and a 14MHz linear array (L14–5). Displacement at each pixel was obtained using the raw RF data and a 2D phase sensitive cross–correlation algorithm between ultrasound frames. A weighted least–squares spline method [5] was also used to improve tracking performance. Based on the axial and lateral displacements and external force, mechanical properties of the tendon, such as stiffness (k) and Young's modulus (λ), were estimated.

Results: In the B–mode ultrasound movies, the posterior tibial tendon can be easily distinguished from surrounding soft tissue and bone. 2D displacement and strain maps were calculated both parallel and perpendicular to the tendon axis, providing enhanced contrast of the tendon during the stretch sub–regions inside the tendon (Figure 1a) were chosen for further analysis. Based on the slope of the tendon force–displacement curve and geometry of the tendon, k and λ were calculated (Figure 1b). The average k and λ for one tendon were approximately 30N/mm and 200MPa at small load (<100N) and strain (<2%), consistent with average estimates of the MTS and within range of published values for human tendons.

Conclusions: This study demonstrated the feasibility of using ultrasound to noninvasively track mechanical properties of the posterior tibial tendon. We are now preparing for *in vivo* human studies to compare normal tendons with those associated with PTTD. UEI could be an effective noninvasive tool for comparing normal and dysfunctional tendons and specifically the diagnosis of PTTD.

Figure 1: (a) 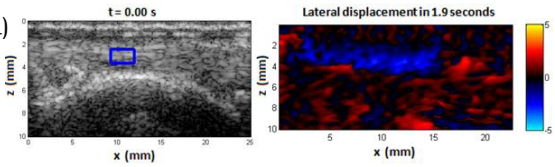

(b) 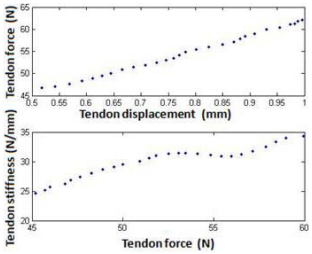

Acknowledgements:
Zonare Medical Systems; Advanced Research Institute for Biomedical Imaging (ARIBI); the Technology Research Initiative Fund (TRIF).

References:

[1] Deland, J.T.: Adult–Acquired Flatfoot Deformity. Jou. of the Am. Acad. of Orth. Surg., 16(7), pp. 399–406, 2008.
[2] Ness, M.E., Long, J., Marks, R., and Harris, G.: Foot and Ankle Kinematics in Patients with Posterior Tibial Tendon Dysfunction. Gait Posture, 27(2), pp. 331–9, 2008.
[3] Kohls–Gatzoulis, J., Woods, B., Angel, J.C. and Singh, D.: The Prevalence of Symptomatic Posterior Tibialis Tendon Dysfunction in Women over the Age of 40 in England. Foot Ankle Surg, 15(2), pp. 75–81, 2009.
[4] M.A. Lubinski, S.Y. Emelianov and M. O'Donnell: Speckle Tracking Methods for Ultrasonic Elasticity Imaging using Short–Time Correlation. IEEE Trans. Ultrason., Ferroelect., Freq. Contr., Vol. 46, No. 1, pp. 82–96, 1999.
[5] R.S. Witte, K. Kim, S–W. Huang, B.J. Martin, M. O'Donnell: Least–Squares Spline for Reducing Tracking Error in Muscle Strain Imaging. Proceedings of ITEC, 2007.

096 **FREQUENCY DEPENDENCE IN PHASE WAVE SPEEDS RECOVERED FROM INTERFERENCE PATTERNS MADE WITH ARC DATA.**

Ashley Thomas[1], Kui Lin[1], Joyce R. McLaughlin[1], Christopher R. Hazard[2], Kai Thomenius[2], Zaegyoo Hah[3], Kevin J. Parker[3], Deborah J. Rubens[4].*

[1]Rensselaer Polytechnic Institute, Troy, NY, USA; [2]GE Global Research, Niskayuna, NY, USA; [3]University of Rochester, Rochester, NY, USA; [4]University of Rochester Medical Center, Rochester, NY, USA.

Background: Acoustic radiation crawling wave sonoelastography (ARC) is an extension of traditional crawling wave sonoelastography, where two mechanical point or line sources oscillate at nearby frequencies on either side of the image plane, thereby inducing a moving interference pattern of shear waves [1,2]. The gain in using two different frequencies is that a moving interference pattern can be imaged, where the speed of the interference pattern is a fraction of the shear wave speed. The interference pattern data is used to produce the targeted biomechanical shear wave speed image. Images of excised prostate glands match histology slides of the same cross section well [3]. In ARC sonoelastography, the excitations at opposite sides of the imaging region are made using acoustic radiation force.

Aims: The goal is to identify inclusions in phantoms and to exhibit the frequency dependence of the phase wave speed of interference patterns made from ARC data.

Methods: Two distinct displacement data sets are obtained using a specially programmed GE Logiq 9 ultrasound machine. An interference pattern is created synthetically by repeating and delaying one of the data sets and adding it to the other. By varying the delay times, the dominant frequency content in the interference pattern can be changed. We utilize ARC displacement data that has been obtained for a phantom with a circular inclusion. We create several interference patterns, varying the dominant frequency. Then we recover the phase wave speed of each interference pattern using two methods: (1) a local arrival time method and (2) an L^1 minimization 2D phase unwrapping method [3].

Results: In this presentation, we will image the phase wave speed recovered from interference patterns with varying dominant frequencies. In addition, we will plot the mean inclusion phase wave speed as a function of frequency and exhibit best–fit for several viscoelastic models. In Figure 1, we show phase wave speed images recovered from synthetic interference patterns at two different frequencies using the local arrival time method. The mean inclusion wave speed for frequency, f = 277.7Hz, is 3.6m/s, and the mean inclusion wave speed for frequency, f = 416.6Hz, is 3.9m/s.

Conclusions: Phantoms are successfully imaged with ARC data, and frequency dependency matches are obtained with both fractional and linear solid models.

Acknowledgements: The authors acknowledge partial funding from NIH Grant No. R01AG029804, ONR and NPSC. Data were collected at the University of Rochester using GE equipment. This work was performed at IPRPI, the Inverse Problems Center at Rensselaer Polytechnic Institute.

References:

[1] Z. Wu, L.S. Taylor, D.J. Rubens and K.J. Parker: Sonoelastographic Imaging of Interference Patterns for Estimation of the Shear Velocity of Homogeneous Biomaterials. Phys. Med. Biol., 49, pp. 911–922, 2004.

[2] J.R. McLaughlin, D. Renzi, K.J. Parker and Z. Wu: Shear Wave Speed Recovery Using Moving Interference Patterns Obtained in Sonoelastography Experiments. J. Acoust. Soc. Am., 121(4), pp. 2438–2446, 2007.

[3] K. Lin, J. McLaughlin, A. Thomas, K. Parker, B. Castaneda and D.J. Rubens: Two–Dimensional Shear Wave Speed and Crawling Wave Speed Recoveries from *In Vitro* Prostate Data. Submitted J. Acoust. Soc. Am., 2010.

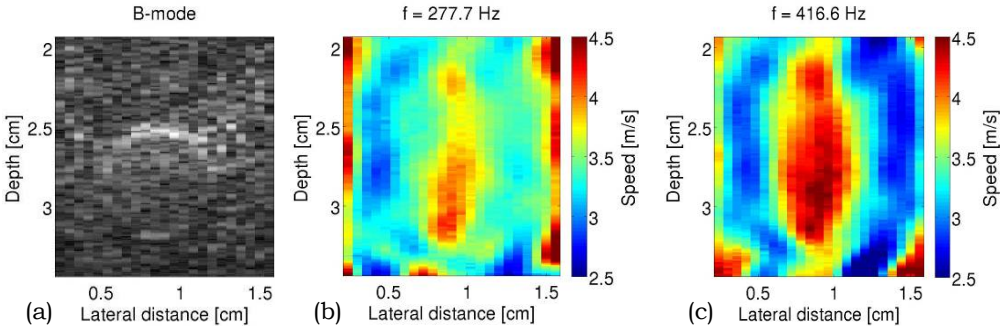

Figure 1: (a) B–mode image of a phantom; (b) and (c) phase wave speeds computed for two different frequencies. Each frequency content data set is obtained from a different delay/add sequence.

* *indicates Presenter*

097 **NEW COMBINATION OF ARC DATA: IMAGING SHEAR MODULI AND MATCHING PHANTOM RECOVERY FREQUENCY DEPENDENCE TO VISCOELASTIC MODELS.**

K Lin[1], A Thomas[1], JR McLaughlin[1], CR Hazard[2], K Thomenius[2], Z Hah[3], KJ Parker[3], DJ Rubens[4].*
[1]Rensselaer Polytechnic Institute, Troy, NY, USA; [2] GE Global Research, Niskayuna, NY, USA; [3]University of Rochester, Rochester, NY, USA; [4]University of Rochester Medical Center, Rochester, NY, USA.

Background: In the acoustic radiation crawling wave sonoelastography (ARC), the excitations at opposite sides of the imaging region are made using acoustic radiation force instead of mechanical vibrations in the traditional crawling wave sonoelastography [1,2]. As an alternative to finding the phase wave speed from an interference pattern of shear waves measured, the frequency dependent complex shear modulus can be obtained from a novel combination of two single component displacement data sets generated from the two separate excitations on either side of the image plane in ARC.

Aims: We aim to establish a constructive combination of the two displacement data sets measured in ARC and reconstruct images of complex shear modulus by a stable PDE solver. The goal is to obtain best fits of the frequency dependence of the viscoelastic shear stiffness parameters for two viscoelastic models.

Methods: Two displacement data sets are generated by two separate sources at opposite sides of image plane in a phantom with a circular inclusion. A specially programmed GE Logiq 9 ultrasound machine is utilized for data acquisition. The time trace from each data set is synthetically extended by delaying and adding with a 12 points' window. The frequency content of each data set is then extracted from the Fourier Transform of the extended time traces and combined together to reconstruct the complex modulus with a first order convergent linear complex PDE solver and a 2D phase unwrapping algorithm [3]. The viscoelastic shear stiffness parameters in the fractional element model and the standard linear solid model are calculated by a least–square fit to the reconstructed complex shear modulus.

Results: Images of complex shear modulus from ARC displacement data in a phantom with 6mm diameter inclusion are presented for increasing frequencies and the averaged absolute value of complex modulus inside the inclusion is plotted to exhibit a consistent pattern of frequency dependence. The fitted viscoelastic shear stiffness parameters are also plotted against frequencies with a similar pattern. For the two complex shear modulus reconstruction images shown below, the averaged modulus inside the inclusion is 3.4998kPa for frequency f = 66.6Hz and 10.9714kPa for frequency f = 125Hz.

Conclusions: From a novel combination of ARC displacement data sets, stable recovery of complex shear modulus is achieved, and the fit of the frequency dependence of the viscoelastic shear stiffness parameters is established for the fractional element model and standard linear solid model.

Acknowledgements: We acknowledge partial funding from NIH Grant No. R01AG029804. This work was performed at the Inverse Problem Center at Rensselaer Polytechnic Institute, GE Global Research and University of Rochester.

References:

[1] Z. Wu, L. S. Taylor, D. J. Rubens and K. J. Parker: Sonoelastographic Imaging of Interference Patterns for Estimation of the Shear Velocity of Homogeneous Biomaterials. Phys. Med. Biol., 49, pp. 911–922, 2004.
[2] J. R. McLaughlin, D. Renzi, K. J. Parker and Z. Wu: Shear Wave Speed Recovery using Moving Interference Patterns Obtained in Sonoelastography Experiments. J. Acoust. Soc. Am., 121(4), pp. 2438–2446, 2007.
[3] K. Lin, J. McLaughlin, A. Thomas, K. Parker, B. Castaneda and D. J. Rubens: Two–Dimensional Shear Wave Speed and Crawling Wave Speed Recoveries from *In Vitro* Prostate Data. J. Acoust. Soc. Am. (submitted), 2010.

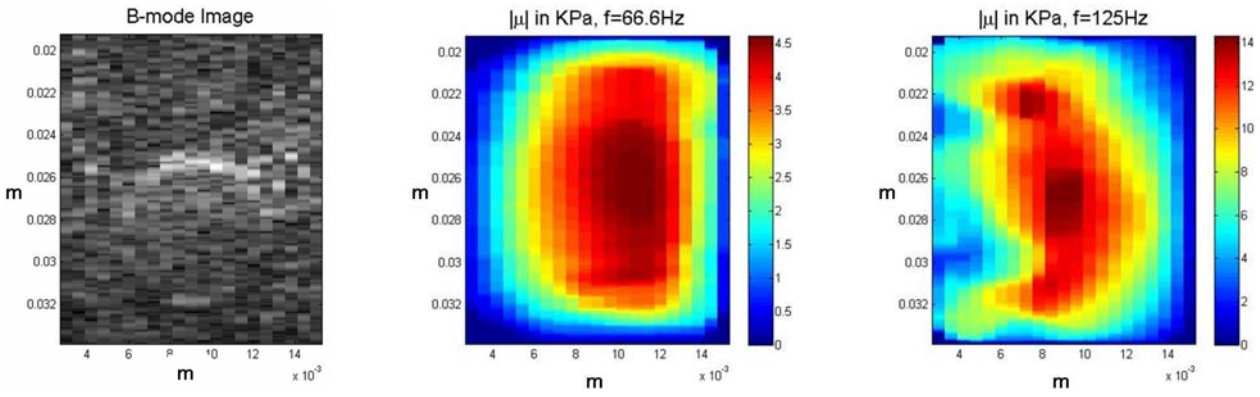

006 **A NORMALIZATION ALGORITHM FOR AXIAL–SHEAR STRAIN ELASTOGRAPHY.**

Lujie Chen[1], R. James Housden[1], Graham M. Treece[1], Andrew H. Gee[1], Richard W. Prager[1].*
[1]University of Cambridge, Cambridge, England, UK.

Background: Recently, there has been interest in correlating the slip pattern of a suspicious lesion to its malignancy. Some evidence suggests that the slip pattern is better characterized by the axial–shear strain than the axial strain [1]. While the difference between the two is simply the direction of the gradient in the same axial displacement field, the two images have very different properties that impact on visualization. For example, unlike the axial strain where the absolute value is of interest, the shear strain is more useful when visualized as a signed quantity. This creates a problem when taking a time average on a sequence of shear strain fields recorded with both compression and relaxation: the signed values from the different strain directions may cancel, resulting in a loss of information. Furthermore, the majority of data values in a shear strain field are close to zero, which makes it difficult to extract sufficient information to compensate for the variations in probe motion.

Aims: To develop a normalization method for axial–shear strain imaging.

Methods: An axial strain field can be normalized by fitting a two–dimensional (2D) function to the axial strain data. The function $s = a(1+by)(1+cx)$ (y and x denote the axial and lateral directions respectively, a, b and c are found by least–squares regression) allows for typical stress variation in the axial and lateral directions [2]. We propose that the same function, s, can also be used to normalize the shear strain field: $\varepsilon'_{yx}(x,y) = \arctan[\varepsilon_{yx}(x,y)/s(x,y)]$, where ε_{yx} is the raw shear strain and ε'_{yx} is the normalized shear strain. The advantages of this procedure are threefold. Firstly, all data are bounded within the range $[-\pi/2, \pi/2]$, so a display range can be selected with ease. Secondly, since s embodies an estimate of the axial and lateral stress variation, ε'_{yx} is compensated accordingly to produce a relatively uniform background. Thirdly, the sign of s is a reliable indicator of the probe's motion (compression or relaxation). Dividing ε_{yx} by s makes the sign of ε'_{yx} independent of this motion.

Results: Several phantom and *in vivo* data sets were tested. Figure 1 shows a sample analysis from a brain scan, which comprises 50 shear strain fields. The axial strain image, Figure 1b, suggests that the tumour is stiffer than the surrounding tissue, subsequently confirmed by histology. The raw shear strain images, Figures 1d–f, indicate that there is a slip boundary around the tumour, but there is no clear contrast between the tumour and the background. Better contrast is evident in the normalized shear strain image, Figure 1c. A dark upper left quadrant slip pattern, indicated in Figure 1c, is further evidence of a stiff inclusion. It is stable in the normalized shear strain images but not in Figures 1d–f. With normalization, the sign of the shear data is determined by a property of the tissue and not the probe motion.

Conclusions: The proposed normalization method for axial–shear strain facilitates automatic selection of the display range, compensates for variations in the probe motion, preserves the signed values during time averaging and is able to decouple certain slip patterns inherent to tissue properties from those induced by the probe motion.

Acknowledgements: We would like to thank Dr. Christopher Uff for providing the *in vivo* data set. This work was funded by Translation Award 081511/Z/06/Z from the Wellcome Trust.

References:

[1] A. Thitai Kumar, J. Ophir, and T.A. Krouskop: Noise Performance and Signal–to–Noise ratio of Shear Strain Elastograms. Ultrasonic Imaging, Vol. 27, pp. 145–165, 2005.

[2] J.E. Lindop, G.M. Treece, A.H. Gee, and R.W. Prager: An Intelligent Interface for Freehand Strain Imaging. Ultrasound in Medicine and Biology, Vol. 34, No. 7, pp. 1117–1128, 2008.

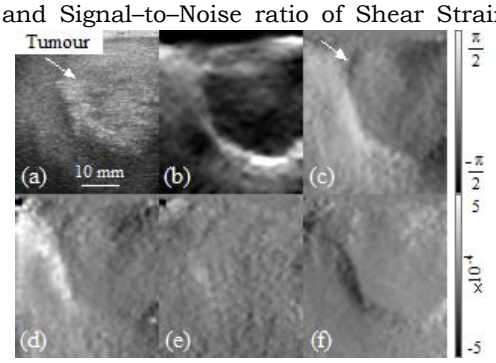

Figure 1: Results for the *in vivo* brain scan. (a) B–mode image, (b) normalized axial strain and (c) normalized shear strain at frame 30 of 50. Raw shear strain at (d) frame 20, (e) frame 30 and (f) frame 40. The axial and shear strain images were obtained under a progressive time average of ten frames.

* *indicates Presenter*

089 **LOCAL INVERSION OF THE WAVE EQUATION FOR ELASTICITY IMAGING USING FIR FILTERS.**

Ali Baghani[1], Reza Zahiri Azar[1], Septimiu E. Salcudean[1], Robert Rohling[1].*
[1]University of British Columbia, Vancouver, BC, CANADA.

Background: Local inversion of the wave equation is one of the techniques used for estimating tissue elasticity from the measured displacements [1]. The equation usually used can be written as $\mu = -\rho(2\pi f)^2 u/\Delta u$, where u is a component of the displacement or its curl, f is the frequency of excitation, ρ is the density and μ is the shear modulus. The quotient in this formula estimates the (squared) wavelength. The numerical calculation of the Laplacian Δ, is the main challenge for wavelength (or frequency) estimation.

Aims: To develop custom FIR filters to accurately perform the Laplacian operator for elasticity estimation.

Methods: Since the range of elasticity values for most soft tissues is known to be from 5–500 kPa, the range of wavelengths for each frequency of excitation can be calculated. For instance at 200 Hz, the wavelength is from 6.5–65 mm or the spatial frequency from 15.5–155/m. For a typical filter size of 15×15×3, there are 675 coefficients to be determined. These coefficients were determined by weighted least squares optimization. The error function was the sum of squared differences between the frequency response of the FIR filter and a target frequency response at a number of chosen frequencies. Inside the 15.5–155/m frequency range, the target frequency response was chosen to be the true Laplacian. The spatial variation of the displacements outside the frequency range was considered to be noise, and the target frequency response was chosen as a decaying exponential in this range. This is a simple method to deal with measurement noise. If a noise model is available from experiments, it can be incorporated in the filter design. The spatial frequency domain was sampled uniformly inside the frequency range. To reduce the size of the optimization problem, it was sampled randomly outside the frequency range. Simulations created with FEM were used to validate the designed FIR filters and compare against other methods.

Results: Figure 1a shows the true elasticity map of the simulated phantom. The background and inclusion have elasticity values of 50 and 100 kPa, respectively. Figure 1b–e show the elastograms obtained from four different methods by using the data without noise. Figure. 1f–i show the corresponding elastograms for added white Gaussian noise (SNR = 40 db). In 1b and 1f, the simple 3 point finite difference formula was used (filter size=3×3×3). In 1c and 1g, a truncated Laplacian of Gaussian was used (filter size=15×15×3). In 1d and 1h, the local frequency estimator (LFE) was used with 7 filter banks [2]. In 1e and 1i the designed FIR filter was used (filter size=15×15×3).

Conclusions: Although the finite difference formula gives accurate estimates in the absence of noise (Figure 1b), other methods are needed when dealing with measurement noise in ultrasound data. The Laplacian of Gaussian (Figure 1c and 1g) gives consistent results in the presence of noise. However, the absolute values of elasticities are biased. LFE filters (Figure 1d and 1h) produce lower bias. Custom designed FIR filters (Figure 1e and 1i) give consistent results in the presence of noise and recover the elasticity values correctly.

Acknowledgements: This research was supported by Natural Sciences and Engineering Research Council (NSERC).

References:

[1] T.E. Oliphant: Direct Methods for Dynamic Elastography Reconstruction: Optimal Inversion of the Interior Helmholtz Problem. Ph.D. dissertation, Mayo Graduate School, 2001.
[2] A. Manduca, et al: Visualization of Tissue Elasticity by Magnetic Resonance Elastography. Lecture Notes in Computer Science, Volume 1131, pp. 63–68, 1996.

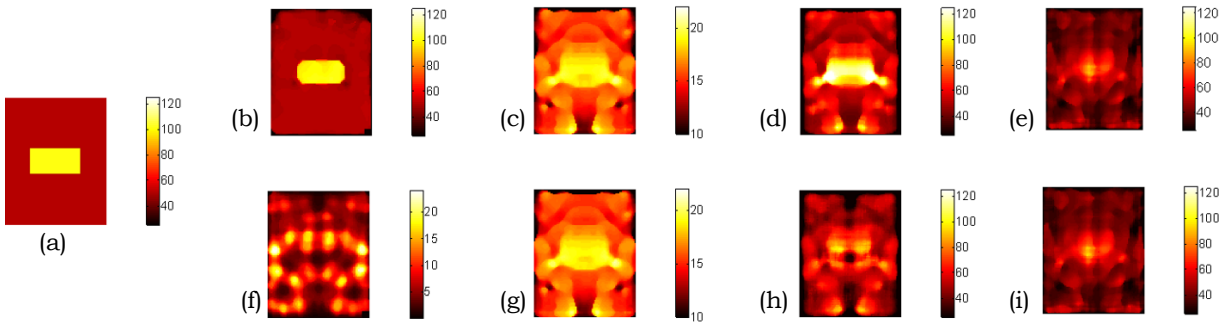

Figure 1: (a) Original distribution of elasticity, (b)–(i) reconstructed elastograms using different methods (see text).

033 **INVERSE PROBLEMS IN DYNAMIC ELASTOGRAPHY: THEORETICAL, EXPERIMENTAL AND NUMERICAL ANALYSIS.**

Thomas Deffieux[1], Jean–Luc Gennisson[1], Benoit Larrat[1], Mathias Fink[1], Mickaël Tanter[1].*
[1]Institut Langevin–Ondes et Images, ESPCI Paris Tech, CNRS UMR 7587, INSERM ERL U979, Paris, FRANCE.

Background: Dynamic elastography imaging techniques allow quantitative estimation of elasticity thanks to analysis of shear waves propagating in a medium. The possibilities raised by such quantitative techniques are particularly important for diagnostic purposes, especially for liver fibrosis staging or breast cancer screening. In dynamic elastography, a force is first applied to generate a shear wave; its propagation is then imaged and analyzed. By inverting the wave equation or computing the shear wave propagation velocity, it is possible to retrieve the shear modulus of the medium. Among those techniques, we can distinguish Magnetic Resonance Elastography (MRE), which uses an external mechanical vibrator with a Magnetic Resonance Imaging (MRI) system to generate and acquire in 3D a complex monochromatic shear wave in its steady state, and Shear Wave Imaging (SWI), which uses acoustic radiation force and an ultrafast ultrasound scanner to generate and image a transient plane shear wave. The two approaches can lead to two natural inversion strategies, the 3D local wave equation in MRE and the 1D time of flight estimation in SWI made possible by plane shear wave generation.

Aims: The goal of this study is to compare both approaches in terms of inverse problems to highlight their strengths and drawbacks.

Methods: Using a theoretical framework based on the Cramer–Rao Lower Bound and probability theory, the statistical properties of both inversions are derived and explicated in terms of SNR, bias and resolution. Experimental measurements of displacement fields in a calibrated phantom are performed and used as input and control for the theory. Numerical simulations are also performed to investigate the heterogeneous case (with spherical inclusions) and the link between SNR, bias and resolution.

Results: *In vitro* displacements SNRs were found higher in SWI (16dB) than in MRE (10dB) as well as reconstructed elasticity maps SNRs (37dB versus 25dB, respectively). The theoretical frameworks allow a good prediction of the noise and resolution behavior for both approaches and is validated by experiments and simulations. The SWI approach allows getting higher resolution (500µm) for a given SNR than what is possible in MRE (2mm) for much shorter acquisition times.

Conclusions: The plane wave assumption, made possible in SWI, allows a more robust inverse problem than the full wave equation inversion. Its general benefits seem to overcome its limitation for experimental noise levels in the tested cases.

042 **INCREASE IN SPATIAL RESOLUTION OF LATERAL MODULATION IMAGING.**

Chikayoshi Sumi[1], Kunio Shimizu[1], Yuuki Takanashi[1].*
[1]Sophia University, 7-1, Kioicho, Chiyodaku, Tokyo, JAPAN.

Background: A number of ultrasonic (US) displacement/velocity measurement methods have been extensively developed for measurements of blood flow, tissue motion and strain [1]. Lateral modulation (LM) methods have also been reported using steered, crossed beams, and these methods permit measurements of displacement vectors [1]. LM echo imaging has almost the same lateral resolution as axial resolution [2]. The beamforming is also used for US microscope, acoustical radiation force imaging (ARFI), high intensity focus ultrasound (HIFU) treatment etc by us. Another new beam steering method using only a steering angle (ASTA) [3] is also proposed. The measurements achievable are also used for reconstructing mechanical properties of living tissues (breast, liver, heart, blood) (e.g., [4]).

Aims: For the improvement of measurement accuracy and imaging quality by increasing a spatial resolution of echo signals, our previously proposed virtual source is used [5]. The new virtual source uses an arbitrary position ahead of the physical array elements as a virtual source position. Regular or random scattering media (material) or holes like point acoustical sources can be used as virtual sources. Moreover, the new Method A is also proposed for LM and ASTA, in which low frequency spectra are disregarded for increasing the instantaneous frequencies [3]. In conjunction, the spectral division method (Method B) [3] is also proposed for obtaining simultaneous equations in multidimensional autocorrelation and Doppler methods [1]. As a version of ASTA, a non–steering beam is used together with the rotation of a coordinate system (Method C) [3]. Simultaneous B–mode imaging can also be performed. Recall that for LM, non–symmetric arbitrary steering angles can also be used. For LM and ASTA, when beamforming is preformed, after receiving echo signals for a beamforming or after obtaining synthesized steering beams, by rotating the coordinate in the spatial or frequency domain, the axial, lateral and elevation frequencies can also be controlled (Method D) [3]. For LM, this rotation also allows the use of non–symmetric steering angles with 1D displacement measurement methods (Method E) [3].

Methods: An US linear array type transducer was used (US element pitch, 0.2mm; US frequency, 7.5MHz). Experiments were performed using the same agar phantom (40 (axial)×96 (lateral)×40 (elevation) mm^3) which was described previously [2,5]. The concentrations of the agar in the stiff cylindrical inclusion (dia.=10mm, depth=19mm) and in the surrounding region were 6.0 and 3.0%, respectively. The relative shear modulus obtained was 3.29. The phantom was compressed in a lateral direction. A rectangular ROI 13.7 (axial) × 13.2 (lateral) mm was centered on the inclusion. With LM and ASTA, the same parabolic modulation was performed as described in [2]. The lateral modulation frequency achieved was 3.75MHz. For Method C, a plane wave transmission was also performed.

Results: For virtual sources at depths of 1.0 to 9.0mm, LM was achieved. The lateral resolutions were evaluated for various depths using a lateral shape of 2D autocorrelation function. The lateral widths of main lobes revealed that the virtual source yielded higher uniform lateral resolutions than the physical sources [5]. Also new Methods A to E worked well. Specifically for Method C, statistics of displacement vectors (magnitudes and angles) measured and shear moduli reconstructed in the inclusion were evaluated. For instance, for a rotation of 45°, the order of accuracies were, LM > Method C > Method B (ASTA) > Method C with a plane wave >> a conventional beamforming (e.g., means of displacement magnitudes, about 0.85mm vs SDs, 0.019; 0.020; 0.037; 0.057; 1.208 mm).

Conclusions: The virtual source proposed mitigated the physical and electrical limitations for using smaller US array elements and a smaller pitch such that both high lateral resolution and high echo SNR were obtained. New methods A to E were also effective. Method C yielded a larger bandwidth than a beam steering with instantaneous frequencies determined geometrically. However, because the beam steering allows yielding a higher axial frequency than Method C, Method D may yield more accurate results. Moreover, Method C also allowed no use of a spherical focusing for a transmission. Thus, a use of Method C will yield a more accurate 3D displacement vector measurement than conventional 3D beamforming.

References:

[1] C. Sumi: IEEE Trans. UFFC, 55, pp. 24–43, 2008.
[2] C. Sumi, et al.: IEEE Trans. UFFC, 55, pp. 2607–2625, 2008.
[3] C. Sumi: Utilization of an Ultrasonic Beam Steering Angle. Rep Med Imag (in press).
[4] C. Sumi: Relative Shear Modulus Reconstruction with No Geometrical Artifact. Acoust Sci Tech (in press).
[5] C. Sumi, et al.: Effective Ultrasonic Virtual Sources Which Can Be Positioned Independently of Physical Aperture Focus Positions. Rep Med Imag (in press).

091 **BANDPASS SAMPLING OF HIGH FREQUENCY TISSUE MOTION.**

H Eskandari[1], O Goksel[1], S E Salcudean[1], R Rohling[1].*
[1]University of British Columbia, Vancouver, BC, CANADA.

Background: Quantitative characterization and inversion of the wave equation requires a high frequency excitation. Given the low frame rate of standard ultrasound systems, it is not possible to perform dynamic elastography on a large ROI. Based on the conventional sampling theorem, the minimum sampling frequency to avoid aliasing is twice the maximum frequency in the signal.

Aims: The objective of this work is to introduce the idea of bandpass sampling (BPS) for dynamic elastography to enable sampling of high frequency tissue motion using the conventional settings of a low frame rate ultrasound system.

Methods: A bandpass signal may still be recovered when sampled at a rate lower than the Nyquist rate [1]. As illustrated in Figure 1, when a bandpass signal is sampled at a lower sampling rate, the spectrum is repeatedly shifted to the baseband frequencies. With the appropriate choice of the sampling frequency, spectrum overlaps can be avoided, and the signal can be accurately recovered. With a spectral bandwidth of B and a center frequency of f_c, the allowable bandpass sampling frequency (f_s) falls in the range $max\{2B, (2f_c+B)/(m+1)\} < f_s < (2f_c-B)/m$, where m is a positive integer indicating the minimum number of half–shifts $f_s/2$ required to project the original spectrum to the baseband [1]. Since even a single spectral line will exhibit a non–zero bandwidth after sampling, the finite observation time imposes additional guard–bands on f_s.

Results: Simulations have been performed by modeling tissue deformation with the finite element method. These deformations were then used in the Field II software package to simulate the radiofrequency (RF) data, assuming standard settings of the ultrasound systems. Also, the experimental set–up and the elasticity reconstruction algorithm in [2] have been used to collect tissue–mimicking phantom data. A phantom with a hard inclusion was vibrated at 120Hz, and RF frames were collected at 50Hz. As expected from the theory of bandpass sampling, the original spectrum could be observed at 20Hz. The motion tracking data and the elasticity estimation results indicate that the reconstruction was accurate when compared to the case where a higher sampling frequency (i.e. 334Hz) was chosen (Figure 2).

Conclusions: Bandpass sampling has not been previously explored for dynamic elastography. Using bandpass sampling, it is feasible to use conventional beamforming on diagnostic ultrasound systems to perform high frequency dynamic elastography. Bandpass sampling is simpler to implement on ultrasound machines, compared to beam interleaving techniques. However, one of the limitations of bandpass sampling is the lower SNR due to low–frequency noise and tissue motion (e.g. respiratory) which will be studied in future work.

Acknowledgements: The authors would like to thank NSERC for funding this work.

References:

[1] W. M. Waters and B. R. Jarrett: Bandpass Signal Sampling and Coherent Detection. IEEE Trans. on Aerospace and Electronic Systems, Col. AES–18, No. 6, pp. 731–736, Nov. 1982.
[2] H. Eskandari, S. Salcudean, R. Rohling, and J. Ohayon: Viscoelastic Characterization of Soft Tissue from Dynamic Finite Element Models. Physics in Medicine and Biology, Vol. 53, No. 22, pp. 6569–6590, Nov. 2008.

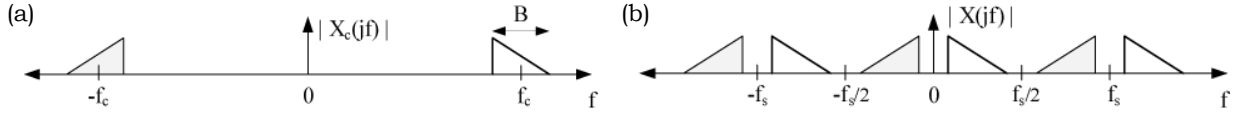

Figure 1: (a) The original spectrum of a bandpass signal and (b) the spectrum after bandpass sampling at a low sampling rate (fs).

Figure 2: Phantom displacements at 120Hz when sampled at (a) 334Hz and (b) 50Hz and the reconstructed elasticity at the same sampling rates (c) and (d).

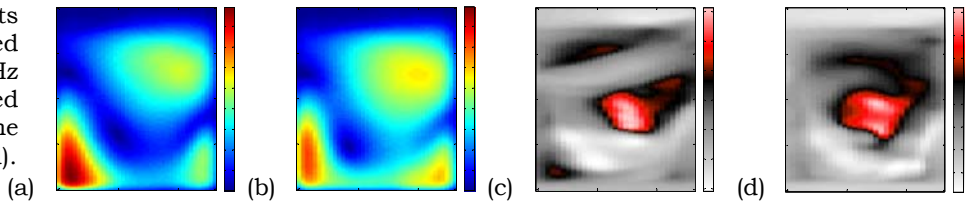

* *indicates Presenter*

049 **A FAST GPU BASED 3D ULTRASOUND DEFORMATION SIMULATION FOR BENCHMARKING MOTION TRACKING ALGORITHMS.**

Ted G. Fisher[1], Timothy J. Hall[1].*
[1]School of Medicine and Public Health, University of Wisconsin–Madison, Madison, WI, USA.

Background: Simulated ultrasound data has been used for many years to investigate different spatio–temporal sampling problems and motion tracking techniques. Field II is commonly used but is quite time consuming unless a computing cluster is used [1]. Alternate methods [2] have been performed with good success, but when presented with a volume of scatterers, these methods take considerable computation time as well. The complexity of these simulations, and the associated long computational time, is not needed for day to day testing of motion tracking algorithms. The use of a graphics processing unit (GPU) has the potential to greatly speed up the simulation process by taking advantage of the parallel nature of the problem.

Aims: The aim of this project is to create a fast method of simulating pre– and post–deformation volumes of ultrasound data in order to test how well different tracking strategies perform under different motion.

Methods: Using CUDA (Nvidia, Santa Clara, CA, USA) we are able access the memory and computing power of the CUDA–enabled GPU. With this, we are able to run thousands of threads executing concurrently in order to do massively parallel computations. To simulate a typical 3D ultrasound radiofrequency (RF) signal, a volume of data was first populated with random numbers representing the scattering function at that point, T(x,y,z). The scattering field is then deformed by applying a 3x3 transform matrix on each coordinate effectively mapping the old coordinates to new coordinates: (x,y,z) -> (x',y',z'). Each coordinate is independent of neighboring coordinates (homogenous media) which leads to parallel computation. Using this method, different compressions, expansions and shears can be applied. To determine the value of the scattering function at these deformed coordinates, T(x',y',z'), cubic spline interpolation [3] of the original scattering function is used. These new values of the scattering function represent the scattering function values of deformed volume at the original grid coordinates, T'(x,y,z). To simulate an RF signal, we convolve the two volumes of data with a pre–calculated ultrasound 3D PSF. The initial implementation assumes separability of the PSF(x,y,z) = PSF(x) * PSF(y) * PSF(z) [4]. The elevation and lateral PSFs are represented by Gaussian curves with different widths while the axial PSF is represented by a modulated Gaussian pulse. By modeling as such, we are assuming a linear, spatial–shift-invariant system. Assuming PSF separability simplifies the calculations and makes the algorithm much more parallel.

Results: Using an Nvidia GTX 260 video card, deforming a 1024x256x64 grid takes about 10ms or 1640Mpixels/s. Using the cubic spline interpolation to regrid the data takes about 14ms or 1200Mpixels/s. The 3D convolution takes on average 100ms, or 16.4Mpixels/s. Overall, it takes around 2 seconds to simulate the 2 volumes of ultrasound data ($3.3 * 10^6$ points combined). This includes time to copy data to and from the CPU, as well as any other CPU time (generating the random numbers, etc).

Conclusions: The use of a GPU is quite advantageous in the acceleration of simulations. With the simulation code written for the GPU, there is an order of magnitude acceleration as compared to C++ code and two orders of magnitude when compared to Matlab code for doing comparable computations. We are currently limited to 2048 points in any of the three directions due to the CUDA limitations on texture references. Being able to rapidly change the types of deformations or the size of the PSF of the ultrasound pulse will help with testing of how different motion tracking strategies perform in different situations.

Acknowledgements: We gratefully acknowledge the support from NIH grants T32–009206 and R21CA133488.

References:

[1] Jensen J, Nikolov S: Fast Simulation of Ultrasound Images. Proceedings the IEEE Ultras Symp in Puerto Rico, Oct 2000.
[2] Rao M, Varghese T, Zagzebski JA: Simulation of Ultrasound Two-Dimensional Array Transducers using a Frequency Domain Model. Med Phys, Vol. 35, pp. 3162–9, 2008.
[3] Ruijters D, ter Haar Romeny B, Suetens P: Efficient GPU–Based Texture Interpolation using Uniform B–Splines. Journal of Graphics Tools, Vol. 13, No. 4, pp. 61–69, 2008.
[4] Kallel F, Ophir J: Three–Dimensional Tissue Motion and its Effect on Image Noise in Elastography. IEEE Trans on Ultra Ferro and Freq Control, Vol. 44, pp. 1286–96, 1997.

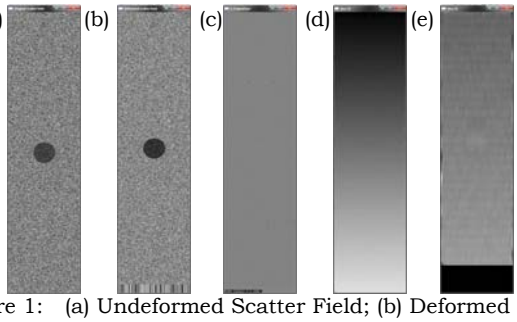

Figure 1: (a) Undeformed Scatter Field; (b) Deformed Scatter Field, Plane 2% Uniaxial Strain; (c) Deformed RF Plane; (d) Sample Axial Displacements from Motion Tracking; (e) Sample Axial Strain from Motion Tracking Displacements.

061 **A COUPLED SPECKLE TRACKING ALGORITHM FOR ELASTICITY IMAGING: INITIAL *IN VIVO* EXPERIENCE.**

Jingfeng Jiang[1] and Timothy J. Hall[1].*
[1]Medical Physics Department, University of Wisconsin–Madison, Madison, WI 53705, USA.

Background and Aims: In ultrasound strain imaging, tissue displacements along the insonification (axial) direction are often measured to assess "relative stiffness", while the displacements perpendicular (lateral) to the ultrasound beam, necessary for accurate motion tracking, are typically discarded because of their poor accuracy. However, for many more advanced elasticity imaging applications such as modulus inversion, temperature imaging through measurements of thermal expansion and shear strain imaging, all components of the displacement vector become essential. Furthermore, the efficacy of these advanced elasticity imaging techniques are largely dependent on the quality of both axial and lateral displacement estimates. Our objective of this study is to improve the speckle tracking accuracy for both axial and lateral directions using conventional ultrasound echo data acquired with standard clinical ultrasound equipment and with freehand scanning.

Methods: The proposed coupled speckle tracking technique involves three steps: (a) estimating the initial displacement and strain using a regularized speckle tracking method [1]; (b) shifting and stretching the post–deformation kernel locally using sample–level displacement and axial strain estimates assuming local tissue incompressibility; and (c) performing coupled sub–sample estimation to obtain high quality axial and lateral displacements. In the first step, a regularized speckle tracking algorithm [1] is used to significantly reduce the occurrence of large tracking errors due to "false correlation peaks" that are also known as "peak hopping" errors [2]. The second step uses the information of "sample–level" displacements and estimated axial strains of Step 1 to locally compensate for apparent motion and, further, for deformations both corresponding to the search kernel on the target radiofrequency (RF) frame. In this step, we explicitly assume that the object being imaged is incompressible under the plane stress condition. In the third step, based on the linear system theory of medical ultrasound [3], we fit iso–contours/surfaces (2D/3D) of the estimated correlation functions to ideal ellipses and ellipsoids to obtain their centers (i.e. the true correlation peaks in sub–sample accuracy).

Results: Computer simulation results show that the method greatly reduces the standard deviations of tracking errors. For high strain cases, such reductions are up to a factor of 2 and 10 under 5% of uni–axial compressions for lateral and axial displacements, respectively. From *in vivo* breast lesion data investigated, we found high quality lateral displacements and shear strains can be estimated for large accumulative compressions (up to 15% frame–average strain).

Conclusions: A novel coupled speckle tracking algorithm along with its theoretical basis is presented. Overall, our initial results demonstrated that this conceptually and computationally simple method could be used to improve displacements for ultrasound–based quasi–static elasticity imaging with current clinical equipment. In the near future, we plan to further investigate the use of this novel speckle tracking algorithm in conjunction with more advanced elasticity imaging techniques such as nonlinear modulus inversion [4].

Acknowledgements: This study was supported in part by NIH grants R21CA133488 and R01CA140271.

References:

[1] J. Jiang and T. Hall: A Generalized Speckle Tracking Algorithm for Ultrasonic Strain Imaging using Dynamic Programming. Ultrasound in Medicine and Biology, Vol. 35, pp. 1863–1879, 2009.
[2] W.F. Walker and G.E. Trahey: Fundamental Limit on Delay Estimation using Partially Correlated Speckle Signals. IEEE Transactions on Ultrasonics, Ferroelectrics, and Frequency Control, Vol. 42, pp. 301–308, 1995.
[3] J. Meunier and M. Bertrand: Ultrasonic Texture Motion Analysis: Theory and Simulation. IEEE Transactions on Medical Imaging, Vol. 14, pp. 293–300, 1995.
[4] A.A. Oberai et al.: Linear and Nonlinear Elasticity Imaging of Soft Tissue *In–Vivo*: Demonstration of Feasibility. Physics in Medicine and Biology, Vol. 54, pp. 1191–1207.

* *indicates Presenter*

019 **A MODEL–BASED APPROACH TO INTRAVASCULAR ULTRASOUND ELASTOGRAPHY.**

Michael S. Richards[1], Marvin M. Doyley[1].*
[1]Electrical and Computer Engineering Department, University of Rochester,Rochester, NY, USA.

Background: Cardiovascular disease and, in particular atherosclerosis, is the cause of approximately 1 in 3 deaths in the United States [1]. The study of arterial plaque mechanics is essential to the detection and monitoring of vulnerable plaque. Intravascular ultrasound (IVUS) is a common diagnostic tool used in the monitoring of the disease and IVUS elastography is method in development for studying plaque mechanics [2].

Aims: Our work aims to develop and characterize a minimally constrained, inverse reconstruction algorithm to quantify the shear modulus (μ) of arterial tissue imaged with IVUS. Unlike previous treatments, our algorithm uses a total variation regularization penalty rather than parametric lumping to ensure the problem is well posed.

Methods: We conducted simulation and phantom studies to evaluate the performance of our model-based inversion technique. We obtained multiple displacement estimates for various applied pressures that were used simultaneously as input to the image reconstruction algorithm. The inverse algorithm seeks to find a shear modulus distribution that yields predicted displacement fields, under the appropriate boundary conditions, that match the measured fields [3].

Results: Reconstruction results show good agreement with true shear modulus distributions (up to a multiplicative constant). Figure 1 shows an example finite element model simulation in which a soft plaque (μ=5 kPa) is present in a hard background (μ=15 kPa) with a harder cap at the lumen boundary (μ=20 kPa). Figure 2 shows the reconstruction result when only the radial displacement component of the "measured" field is used in the reconstruction. Figure 3 shows the improvement in the reconstruction when the angular (lateral) displacement estimates are also used in the reconstruction.

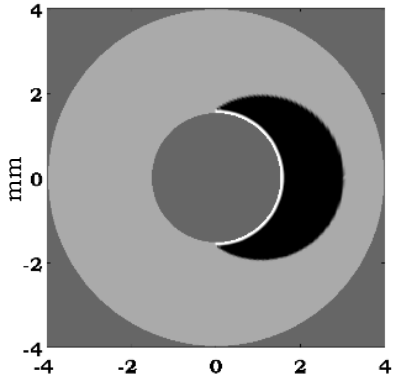

Figure 1: Shear modulus (μ) distribution in forward simulation.

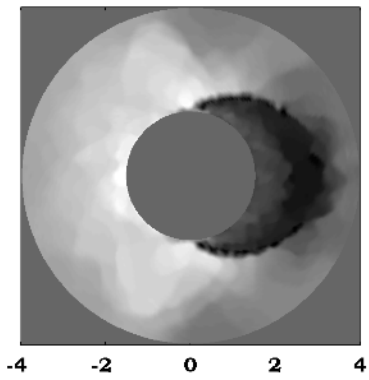

Figure 2: Reconstructed modulus distribution using only radial displacement information.

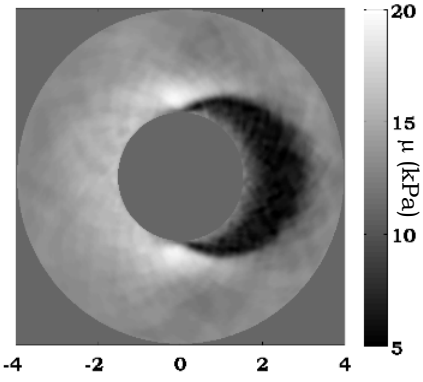

Figure 3: Reconstructed modulus using both radial and lateral displacement components.

Conclusions: The feasibility of a minimally constrained reconstruction algorithm is shown with a high degree of accuracy. Results show that, if available, reconstructions are improved with lateral displacement information.

Acknowledgements: This work is funded by the National Heart and Lungs Research grant R01 HL088523.

References:

[1] D. Lloyd–Jones, R. Adams, M. Carnethon et al.: Heart Disease and Stroke Statistics – 2009 Update: A Report from the American Heart Association Statistics Committee and Stroke Statistics Subcommittee. Circulation, Vol. 119, No. 3, pp. e21–181, Jan 27, 2009.
[2] C.L. de Korte and A.F. van der Steen: Intravascular Ultrasound Elastography: An Overview. Ultrasonics, Vol. 40, No. 1–8, pp. 859–65, May, 2002.
[3] M.S. Richards, P.E. Barbone, and A.A. Oberai: Quantitative Three–Dimensional Elasticity Imaging from Quasi–Static Deformation: A Phantom Study. Phys Med Biol, Vol. 54, No. 3, pp. 757–79, Feb 7, 2009.

020 **RF–BASED 2D STRAIN IMAGING IN THE NORMAL AND DISEASED ABDOMINAL AORTA.**

RGP Lopata[1,2], HHG Hansen[3], GW Schurink[4], CL de Korte[3], EMH Bosboom[1,2], FN van de Vosse[1,2].*
[1]Eindhoven University of Technology, Eindhoven, The NETHERLANDS; [2]Maastricht University Medical Center, Maastricht, The NETHERLANDS; [3]Radboud University Nijmegen Medical Center, Nijmegen, The NETHERLANDS; [4]General Surgery Department, Maastricht University Medical Center, Maastricht, The NETHERLANDS.

Background: An abdominal aortic aneurysm (AAA) is a local dilatation of the aorta. In general, patients with an AAA are asymptomatic, but AAA rupture leads to death in most cases. CT and MR scans can be used to estimate growth and to perform wall stress analysis using Finite Element Modeling. Ultrasound is used to estimate AAA diameter and growth. Vascular elastography might provide insight in the strain distribution over the aortic wall [1] and its mechanical properties and give indications for rupture risk.

Aims: The aim of this study was to determine the feasibility of mechanical characterization of the vessel wall by performing 2D radio frequency (RF) based strain imaging on both healthy and diseased human aortas.

Methods: RF data were acquired from five healthy volunteers' aortas and one patient's aorta diagnosed with AAA. The healthy aortas were imaged in both transverse and longitudinal planes with an Esaote MyLab 70 ultrasound system equipped with an RF–interface and a linear array probe (center frequency (f_c) = 7MHz, sampling frequency (f_s) = 50MHz). To allow sufficient penetration, the AAA was imaged with a curved array transducer (f_c = 3.5MHz). Data were acquired during a fixed period of 6s at a moderate frame rate (f_r) of 20–25Hz. For four subsequent heartbeats, an iterative RF–based strain algorithm was used with a resolution of 200μm axial x 1 RF-line to estimate the 2D displacement field [2]. A total of 140–160 images was analyzed for each subject. In the transverse images, ellipses ranging from the lumen/aorta boundary to the outer aorta interface were defined and tracked over the cardiac cycle, resulting in the radial (R) and circumferential (C) displacements. In the longitudinal view, a square region aligned with the vessel orientation was tracked, yielding the radial and longitudinal (L) strains. The strain was calculated using a 5 x 11 2D least squares strain estimator (LSQSE).

Results: Results for the healthy volunteers showed a peak cumulative systolic strain over an inter–quartile range of 5.0 – 13.5% (R), 7.2 – 9.1% (C) and 0.1 – 6.5% (L) in the upper wall. The strain curves were reproducible for consecutive cardiac cycles. The use of ellipsoids resulted in a direct projection of the axial and lateral displacements in the radial and circumferential directions. In the AAA patient, strain was measured in the wall with the aneurism and thrombus. Results showed a relatively low peak cumulative strain of 0.6 – 1.0% (R) and 0.4 – 2.4% (C) in the wall with the aneurism and 0.9 – 1.5% (R) and 3.3 – 4.3% (C) in the thrombus.

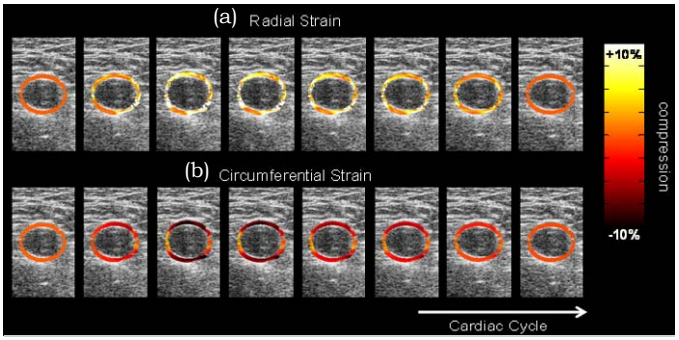

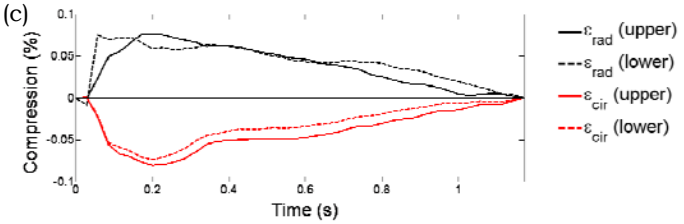

Figure 1: Radial (a) and circumferential (b) strain in a transverse ultrasound image of the aorta during the cardiac cycle and corresponding strain curves.

Conclusions: RF–based 2D strain imaging of the normal and diseased aorta is feasible. A large group of AAA patients will be examined to investigate the reproducibility and sensitivity of the method. Improvement of transverse image quality is required to enhance strain estimation precision. Considering the complex geometry of the aneurysms, extension of the technique to 3D is recommended.

References:

[1] Fromageau J, et al.: Non–Invasive Vascular Ultrasound Elastography Applied to the Characterization of Experimental Aneurysms and Follow–Up after Endovascular Repair. Phys Med Biol, 53, pp. 6475–6490, 2008.
[2] Lopata RGP, et al.: Methodical Study on the Measurement of Strain in Deforming Structures with Large Shearing and Rotational Movement using RF–Based 1D and 2D Strain Estimation. IEEE UFFC, 57(4), pp. 855–865, 2010.

* *indicates Presenter*

021 **4D CARDIAC STRAIN IMAGING USING RF–DATA IN YOUNG CHILDREN.**

RGP Lopata[1,2], MM Nillesen[3], JM Thijssen[3], L Kapusta[3], CL de Korte[3].*
[1]Eindhoven University of Technology, Eindhoven, The NETHERLANDS; [2]Maastricht University Medical Center, Maastricht, The NETHERLANDS; [3]Radboud University Nijmegen Medical Center, Nijmegen, The NETHERLANDS.

Background: Congenital heart diseases, such as valvular aortic stenosis, may result in severe hypertrophy and fibrosis of the heart. Quantification of tissue contractility is required to monitor the progression of such disease. In recent years, 3D (+t) strain imaging techniques have been applied to echocardiographic data to assess 3D strain. Several studies on speckle tracking [1,2] and image registration [3] have been reported, but only few groups attempt raw ultrasound radiofrequency (RF) based strain imaging.

Aims: In this study, a 2D (+t) RF–based strain estimation method [4,5], was extended to 3D and applied to 3D (+t) RF data acquired in young children.

Methods: Eight young, healthy children were imaged (age 6 – 14 years). RF data were acquired with a Philips iE33 3D ultrasound system, equipped with a pediatric X7 probe. ECG–gated acquisition was used to obtain full volume 3D RF data of the left ventricle over one cardiac cycle at a relatively low frame rate of 38–51Hz. An iterative, 'free–shape' 3D displacement estimation algorithm was used to estimate the axial, lateral and elevational displacements simultaneously (resolution of 0.5mm by 1.25ºx1.25º). The heart muscle was segmented by drawing ellipses manually in several short–axis and long–axis views and fitting a 3D ellipsoid. The points on this 3D ellipsoid were tracked in time using the 3D displacement fields, thereby projecting the axial, lateral and elevational displacements in the radial (R), longitudinal (L) and circumferential (C) directions. Strains were calculated by applying a 5x11x11 3D LSQSE in the RLC directions.

Results: Preliminary results revealed the applicability of the 3D strain estimation technique on full volume 3D RF data. The technique enabled 3D strain images of all three strain components. The average strains for all children in the lateral wall were R = 32 ± 13% (infero–lateral) and R = 41 ± 15% (antero–lateral), C = -11 ± 4% (antero–lateral) and C = -9 ± 2% (infero–lateral), L = -17 ± 6% (antero–lateral) and L = -14 ± 5% (infero–lateral). In the septum, strains were found to be R = 16 ± 14% (antero–septal) and R = 13 ± 9% (infero–septal), C = -11 ± 4% (antero–septal) and -17 ± 1% (infero–septal) and L = -16 ± 3% (antero–septal) and L = -13 ± 3% (infero–septal). Strains in the anterior and inferior wall seemed underestimated. In these regions, the direction of the ultrasound beam is parallel to the myocardial wall. This results in a lower image quality. Besides, in these regions, the radial strain contains mostly lateral displacement and strain information, which is of lower quality due to the lack of phase information and resolution. Unfortunately, the field of view and image quality were not always sufficient to image the entire left ventricle.

Conclusions: RF–based 3D strain imaging can be used to estimate 3D strain within the left ventricular wall. The combination of RF–based strain imaging and segmentation [6] might result in a fully automated technique, revealing both geometry and function.

Acknowledgements: The support of the Dutch Technology Foundation (STW) and Philips Medical Systems.

References:

[1] Chen X, Xie H, Erkamp R, et al.: 3–D Correlation–Based Speckle Tracking. Ultrason Imag, 27, pp. 21–36, 2005.
[2] Crosby J, Amundsen BH, Hergum T, Remme EW, Langeland S, Torp H: 3–D Speckle Tracking for Assessment of Regional Left Ventricular Function. Ultrasound Med Biol, 35, pp. 458–471, 2009.
[3] Elen A, Choi HF, Loeckx D, et al.: Three–Dimensional Cardiac Strain Estimation using Spatio–Temporal Elastic Registration of Ultrasound Images: A Feasibility Study. IEEE Trans Med Imag, 27, pp. 1580–1591, 2008.
[4] Lopata RGP, Nillesen MM, Gerrits IH, Thijssen JM, Kapusta L, de Korte CL: 4D Cardiac Strain Imaging: Methods and Initial Results. IEEE International Ultrasonics Symposium, New York, NY, USA, pp. 872–875, 2007.
[5] Lopata RGP, Hansen HHG, Nillesen MM, Thijssen JM, de Korte CL: Methodical Study on the Measurement of Strain in Deforming Structures with Large Shearing and Rotational Movement using RF–Based 1D and 2D Strain Estimation. IEEE Ultrasonics, Ferro–Electrics & Frequency Control, 57(4), pp. 855–865, 2010.
[6] Nillesen MM, Lopata RGP, Gerrits IH, et al.: Segmentation of the Heart Muscle in 3–D Pediatric Echocardiographic Images. Ultrasound Med Biol, 33, pp. 1453–1462, 2007.

003 **SEGMENTAL DISPLACEMENT AND STRAIN ANALYSIS OF LEFT VENTRICULAR DEFORMATIONS.**

Chi Ma[1], Hao Chen[2], Tomy Varghese[1], P.S. Rahko[3], A.F. Kelly[3].*
[1]Medical Physics, [3]Cardiovascular Medicine Section, University of Wisconsin–Madison, Madison, WI, USA; [2]Emory University, Atlanta, GA, USA.

Background: Echocardiography is used routinely for assessing regional myocardial function. Clinical diagnosis based on visually assessed wall motion scoring and evaluation of wall thickening is semi–quantitative, image quality dependent and heavily weighted by operator experience. Tissue Doppler has also been utilized. However, due to limitations in Doppler–derived velocity and strain indices, there has been renewed interest in using B–mode based strain and strain rate measurements. Cardiac elastography using [1-4] radiofrequency (RF) echo signals can provide more accurate two–dimensional (2D) strain information than B–mode image data, provided data are acquired at sufficient frame rates.

Aims: To evaluate and compare B–mode and RF based speckle tracking for cardiac elastography using cardiac segmental analysis.

Methods: Cardiac ultrasound RF data along the parasternal short–axis views were acquired from 7 healthy volunteers from 20–30 years of age using GE Vivid 7 System with a 2.5 MHz phased array transducer under an approved Institutional review board protocol. A multilevel hybrid 2D strain imaging algorithm for sector/phased array [5] was used for displacement and strain estimation for both RF and B–mode data sets. Displacement and strain analysis was performed using both regional and global analysis based on 6 segments within the short–axis view as illustrated in Figure 1. The estimated local displacement and strains were averaged within each segment over the cardiac cycle. Global displacement and strain were computed over all six segments. Finally, the mean displacement and strain along with the standard error (error bars) were plotted and compared over the cardiac cycle.

Results: Plots of the mean axial displacement and strain in segment 1 along with error bars are shown in Figures 2 and 3, respectively. Both plots indicate the significant under estimation of displacement and strain obtained using B–mode instead of RF speckle tracking. Error bars denote the standard error and indicate the variability in the estimates over segment 1. Note the similar pattern of the displacement and strain over 4 cardiac cycles. Similar results are obtained over all the segments and over different volunteers. Speckle tracking using RF data is also more sensitive as shown in Figures 2 and 3.

Conclusions: Preliminary results demonstrate the ability to compare different processing techniques using segmental and global analysis for the displacement and strain distributions over the cardiac cycle. These results demonstrate the potential of comparing normal values generated over the cardiac cycle on volunteers to data acquired on patients with coronary artery disease or cardiomyopathy to determine strain features for identifying pathological changes.

Acknowledgements: This work was supported by NIH grants 5R21EB010098 and R01CA112192.

References:

[1] E. Konofagou, J. D'Hooge, J. Ophir: Ultrasound Med Biol, Vol. 27, No. 4, pp. 475–82, 2002.
[2] T. Varghese, JA Zagzebski, PS. Rahko, CS Breburda: Ultrason Imaging, 25(1), pp. 1–16, 2003.
[3] S. Langeland, J. D'hooge, T. Claessens, et al.: IEEE Trans Ultrason Ferroel Freq Cont, 51(11), pp. 1537–46, 2004.
[4] RG. Lopata, MM. Nillesen, CN. Verrijp, et al.: Phys Med Biol, Vol. 55, No. 4, pp. 963–79, 2010.
[5] H. Chen and T. Varghese: Med. Phys., Vol. 36, No. 6, pp. 2098–2106, 2009.

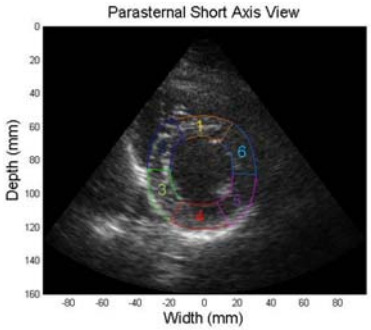

Figure 1: Segmental analysis of the left ventricular wall

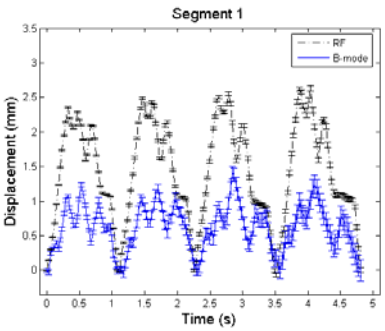

Figure 2: Mean displacement for segment 1

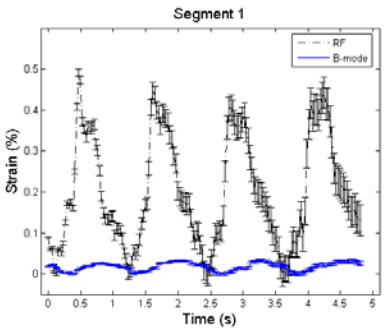

Figure 3: Mean axial strain for segment 1

* *indicates Presenter*

022 **METHOD FOR MINIMIZING THE EFFECT OF CATHETER ECCENTRICITY IN INTRAVASCULAR ULTRASOUND ELASTOGRAPHY.**

Shayin Jing[1], Michael S. Richards[1], Marvin M. Doyley[1].*
[1]Electrical and Computer Engineering Department, University of Rochester, Rochester, NY, USA.

Background: Each year, over 750,000 Americans experience an acute coronary syndrome or sudden cardiac death when a life–threatening atherosclerotic plaque ruptures in the later stages of coronary atherosclerosis [1]. To determine the propensity of atherosclerotic plaque rupture, we need to know the mechanical properties of the atherosclerotic plaque. One method that intravascular ultrasound (IVUS) elastography visualizes the radial strain is by performing cross–correlation analysis on radio frequency (RF) echo frames obtained at different intraluminal pressures. Although radial strain correlates well with the intrinsic tissue, artifacts will occur when the vessel and catheter coordinate systems are misaligned.

Aims: The goal of this presentation is to describe a mapping method that we have developed for reducing the effect of catheter eccentricity [2].

Methods: In this work, we modeled the catheter eccentricity problem as a simple translation between two polar coordinate systems. Note that by knowing the radial and circumferential displacement, we can derive a closed form expression that can be used to map the displacement fields measured in one coordinate system (i.e., the catheter) to the other coordinate system (i.e., the vessel coordinate system). To demonstrate the algorithm, we conducted simulation studies with the displacement field obtained from different eccentric locations.

Results: Figure 1 shows radial strain elastograms obtained when the catheter was at different locations in an elastically homogeneous vessel, before and after coordinate systems were realigned. Strain artifacts are apparent in the elastograms computed in the catheter coordinate system, which was minimized by mapping the displacement field to the vessel coordinate system before computing radial strain. Figure 2 shows radial strain elastograms obtained for different IVUS catheter locations in an elastically inhomogeneous vessel model. Again, artifacts incurred when radial strain was computed in the catheter coordinate system; however, we circumvented this problem by computing strain in the vessel coordinate system.

Figure 1: (a) radial strain of an elastically homogeneous vessel observed from the vessel coordinate system; (b) strain elastogram calculated from measured displacement field with catheter 3mm off center; (c) strain elastogram calculated from correct displacement field.

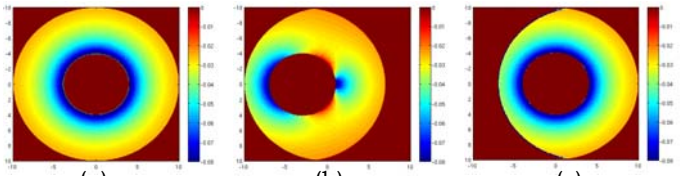

Figure 2: (a) radial strain of an elastically inhomogeneous vessel with respect to the vessel center; (b) strain elastogram calculated from measured displacement field with catheter 3mm off center; (c) strain elastogram calculated from correct displacement field.

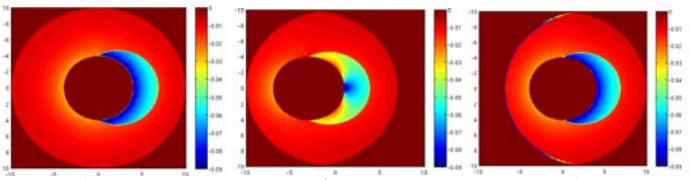

Conclusions: We can reduce artifacts incurred from catheter eccentricity by mapping radial displacements measured in the catheter coordinate system to the vessel coordinate system using knowledge of radial and circumferential displacement obtained from a non–rigid image registration method.

Acknowledgements: Work is funded in part by the National Heart and Lungs Research Grant R01 HL088523.

References:

[1] Howard M. Loree, Roger D. Kamm, et al.: Effects of Fibrous Cap Thickness on Peak Circumferential Stress in Model Atherosclerotic Vessels. Circulation Research, 71, pp. 850–858, 1992.
[2] Chris L. de Korte, E. Ignacio Cespedes, et al.: Influence of Catheter Position on Estimated Strain in Intravascular Elastography. IEEE UFFC, 46, pp. 616–625, 1999.

* *indicates Presenter*

023 **PLAQUE VISUALIZATION WITH A COMBINED B–MODE/ARFI/DOPPLER REAL–TIME IMAGING SYSTEM: TEMPORAL AND SPATIAL STABILITY.**

Joshua R. Doherty[1], Douglas M. Dumont[1], Jeremy J. Dahl[1], Jason D. Allen[1], Gregg E. Trahey[1].*
[1]Duke University, Durham, NC, USA.

Background: Acoustic radiation force impulse (ARFI) imaging has shown to be useful in non–invasively characterizing the mechanical properties of vascular tissue [1]. To that end, it has been hypothesized that radiation force can be used *in vivo* to detect carotid artery plaques and, more importantly, differentiate between hard and soft regions of plaque tissue. Shown to play an important role in the onset of ischemic events, the identification of more vulnerable, soft lipid filled plaques compared to harder, calcified plaque regions would help clinicians better diagnose a patient's risk of stroke [2]. In order to assess the clinical viability of ARFI methods in characterizing carotid plaques, it is necessary to establish the temporal and spatial stability of plaque visualization using such methods.

Aims: To investigate the temporal and spatial stability of ARFI imaging in the visualization of *in vivo* plaques by developing a real–time combined B–mode/ARFI/Doppler imaging system that produces temporally and spatially co–registered depictions of cardiovascular elasticity with blood flow.

Methods: A novel sequence was developed to acquire multiple frames of co–registered B–mode, ARFI and Doppler data. Implemented on a conventional Siemens ultrasound scanner (Issaquah, WA), the carotid arteries of normal and atherosclerotic subjects with moderate (50–69%) stenosis were scanned. Combined B–mode/ARFI/Doppler In–phase Quadrature demodulated radiofrequency data were collected across several heartbeats and at various angles. To assess temporal stability, the consistency of ARFI displacements from beat–to–beat as well as across the cardiac cycle was investigated. Plaque visualization and artifacts within the field of view were evaluated as a function of transducer location and angle to assess spatial stability.

Results: A real–time imaging system capable of capturing B–mode/ARFI/Doppler in a single frame at a rate of 40 ms/frame was developed for visualizing vascular tissue *in vivo* (Figure 1). Temporal sequences of vascular ARFI images showed excellent correspondence with B–mode and Doppler depictions. The measured ARFI displacements of vascular tissue were temporally stable but dependent upon transducer location.

Conclusions: We have developed a B–mode/ARFI/Doppler imaging system capable of rendering real–time images of carotid artery plaques *in vivo*. Investigations of the temporal and spatial stability of ARFI measurements suggest that the ability of ARFI imaging to characterize mechanical properties of plaque (i.e. distinguish hard vs. soft plaque regions) is a function of transducer location and angle. As such, with the ability to measure ARFI displacements throughout the cardiac cycle, over several heartbeats and at multiple locations or angles, we believe the identification of potentially vulnerable lipid cores in plaque tissue is improved using this real–time diagnostic tool.

Acknowledgements: This work is supported by NIH Grants R01–HL075485.

References:

[1] Dahl, J.J, Dumont, D.M., Allen, J.D. Miller, E.M., and Trahey, G.E.: Acoustic Radiation Force Impulse Imaging for Noninvasive Characterization of Carotid Artery Atherosclerotic Plaques: A Feasibility Study. Ultrasound in Med. Biol., Vol. 35:5, pp. 707–716, May 2009.

[2] Redgrave, J.N., Lovett, J.K., Gallagher, P.J. and Rothwell, P.M.: Histological Assessment of 526 Symptomatic Carotid Plaques in Relation to the Nature and Timing of Ischemic Symptoms: The Oxford Plaque Study. Circulation, Vol. 113:19, pp. 2320–2328, May 2006.

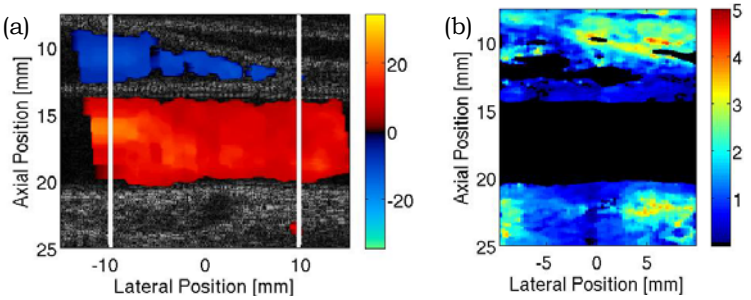

Figure 1: Captured single frame image, showing co-registered B–mode with (a) color Doppler (cm/s) and (b) ARFI displacement (μm) taken from a sequence acquired at a triplex frame rate = 40ms/frame of a carotid artery (lower) and jugular vein (upper) in a normal subject.

* *indicates Presenter*

037 **NON–INVASIVE MULTI–ANGLE STRAIN IMAGING IN PULSATING VESSELS.**

Hendrik HG Hansen[1], Michiel Keijts[1,2], Richard GP Lopata[3,4], Tim Idzenga[1], Chris L de Korte[1].*
[1]Clinical Physics Laboratory, Radboud University Nijmegen Medical Center, Nijmegen, The NETHERLANDS; [2]Electrical Engineering Department, Eindhoven, Eindhoven University of Technology, The NETHERLANDS; [3]Biomedical Engineering Department, Maastricht University, Maastricht, The NETHERLANDS; [4]Biomedical Engineering Department, Eindhoven University of Technology, Eindhoven, The NETHERLANDS.

Background: Radial and circumferential strain images of transverse cross–sections of vessels are scarcely reported, mainly because it also requires a precise estimation of the lateral strain. Lateral strains are more challenging to estimate due to the lower resolution and the lack of phase information. We have shown recently [1] that projection of axial displacements acquired at multiple beam steering angles enables a precise estimation of lateral, radial and circumferential strains. However, the method has only been tested using quasi–static phantoms, thus interframe motion artifacts were not present.

Aims: This study investigates the performance of the projection technique in recordings of a pulsating phantom mimicking an atherosclerotic vessel and in acquisitions of carotid arteries *in vivo.*

Methods: A two–layered phantom (see Figure 1) was constructed by freeze–thawing a 10% polyvinyl–alcohol solution with 2% silica–carbon (SiC) particles. The outer layer was freeze–thawed four times, the softer inner layer (plaque) once. The phantom was placed in a water tank and connected to a pump that provided a pulsating (1Hz) water flow of 400ml/min resulting in a pressure wave between 2 and 19mmHg. Radio frequency (RF) data of the phantom were recorded during 3 seconds using a modified Medison Accuvix V10 that sequentially stored data from beam steering angles of -26°, 0° and 26°. The data were acquired at a frame rate of 129Hz (43Hz/beam steered angle) using an L5–13 linear transducer (center frequency (f_c) = 8.5MHz, sampling frequency (f_s) = 61.6MHz). Displacements were iteratively calculated using 2D cross–correlations. Next, radial and circumferential displacements were derived with projection (multi–angle acquisition) and without projection (conventional 0° acquisition) [1]. The corresponding strains were derived using nine–point least squares strain estimators. Cumulative strain images of the phantom with and without projection were constructed for a pressure increase of 15mmHg by cumulating subsequent strain images (pressure steps between images <1.5mmHg). Also, the correlation of the mean strain curves for subsequent pressure cycles was determined. This was performed separately for three regions of interest (see Figure 1). Additionally, 3 seconds of RF data of healthy carotid arteries (n=3) were obtained using the same equipment. Cumulative strain images for the diastolic phase were determined, and the 25–75% range of the strain values over the entire vessel wall was calculated.

Results: Figure 1 shows that the projection method improves the radial and circumferential strains also in a pulsating vessel. Especially the precision in regions dominated by lateral information increased (f.i. the 3 and 9 o'clock regions in the radial strain images). The increase in precision was also reflected in the 25–75% range values for the *in vivo* data, under the assumption that a healthy vessel wall has an approximately homogeneous strain distribution. The range decreased radially from [-4%, 4%] without projection to [-0.8%, 2%] with projection, and circumferentially from [-8%, 3%] to [-4%, -0.3%]. The reproducibility of the strain curves was very high, the correlation coefficient for the three regions remained above 0.97 for both strain components when using projection.

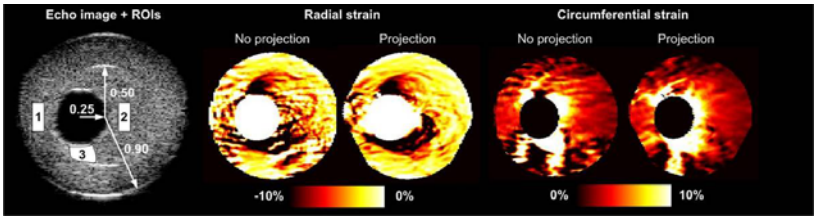

Figure 1

Conclusions: Non–invasive multi–angle strain imaging enables a reproducible and improved estimation of radial and circumferential strains for transverse cross–sections in pulsating (~1Hz) vessels.

Acknowledgements: The support of the Dutch Technology Foundation (STW) is acknowledged and the authors would like to thank Medison for the development of the automatic multi–angle carotid scanning mode.

References:

[1] H.H.G. Hansen, R.G.P. Lopata and C.L. de Korte: Full 2D Displacement Vector and Strain Tensor Estimation For Superficial Tissue Using Beam Steered Ultrasound Imaging. Phys. Med. Biol., (55), pp. 3201–3218, 2010.

* *indicates Presenter*

045 **INTRAVASCULAR ULTRASOUND ELASTOGRAPHY OF CORONARY ARTERIES: A PRE– AND POST–ATHERECTOMY STUDY.**

Younes Majdouline[1], Yoshifumi Saijo[2], François Destrempes[1], Jacques Ohayon[3], Guy Cloutier[1].*
[1]Laboratory of Biorheology and Medical Ultrasonics, University of Montréal Hospital Research Center (CRCHUM), Montréal, Québec, CANADA; [2]Medical Engineering and Cardiology Department, Institute of Development, Aging and Cancer, Tohoku University, Aobaku, Sendai, JAPAN; [3]Laboratory TIMC–DynaCell, UJF, CNRS UMR 5525, In[3]S, Grenoble, FRANCE.

Background: Pathological diagnosis of atherosclerotic coronary plaques aims to prevent thrombosis prone rupture of the artery wall, which can induce an acute ischemic syndrome. Elastography by intravascular ultrasound (IVUS) is a useful technique because plaque components such as lipid, fibrosis and calcification can be directly assessed by the difference in tissue deformations. In a recent preliminary study, we performed *in vivo* vascular elastography corroborated by histology [1]. A global image rotation compensation improving the quality of elastograms was used.

Aims: In this work, we evaluated the potential of IVUS elastography to investigate the difference in mechanical properties of the artery wall before and after catheter–based atherectomy.

Methods: A robust algorithm known as the Lagrangian Speckle Model Estimator [2] was applied to *in vivo* data obtained from 11 arteries (different patients) before and after directional coronary atherectomy (DCA). Before elastogram calculation, the pre–processing included the detection of the vessel wall and global IVUS catheter rotation compensation [1,3]. Instantaneous strain histograms were plotted at peak–flow (i.e., maximum wall compression). The peak–compression strain was estimated as the peak of the histogram (as in Figure 1), and this value was used for statistical analysis over the whole database.

Results: Analyses revealed a significant difference in radial deformations between pre– and post–atherectomy data. Peak–compression strains were higher in the artery before DCA (unpaired t–test, $p < 0.003$), which may be indicative of lipid pool and connective tissue removal during the intervention.

Conclusions: This study showed that the peak–compression strain may be indicative of the presence of soft lipid pools in patients with unstable angina referred for intervention. The difference in elasticity of the arterial wall before and after DCA shows the potential of IVUS elastography to differentiate mechanical properties of the atherosclerotic plaque and, therefore, may also evaluate the risk of rupture.

Acknowledgments: Financial support was obtained by a joint international initiative of NSERC Strategic grant program of Canada (#STPGP–381136–09) and ANR of France (MELANII project # 09–BLANC–0423).

References:

[1] Fromageau J., Saijo Y., Maurice R.L., Roy Cardinal M.H., Cloutier G.: IVUS Elastography of Complex Human Coronary Plaques Treated by Directional Atherectomy: Technical Issues and Preliminary Clinical Results. 2nd MICCAI Workshop on Computer Vision for Intravascular and Intracardiac Imaging, pp. 88–95, 2008.
[2] Maurice R.L., Ohayon J., Finet G., Cloutier G.: Adapting the Lagrangian Speckle Model Estimator for Endovascular Elastography: Theory and Validation with Simulated Radio–Frequency Data. J. Acoust. Soc. Am., 116 (2), pp. 1276–1286, 2004.
[3] Roy Cardinal M.H., Meunier J., Soulez G., Maurice R.L., Therasse E., Cloutier G.: Intravascular Ultrasound Image Segmentation: A Three–Dimensional Fast–Marching Method Based on Gray Level Distributions. IEEE Trans. Med. Imag., 25(5), pp. 590–601, 2006.

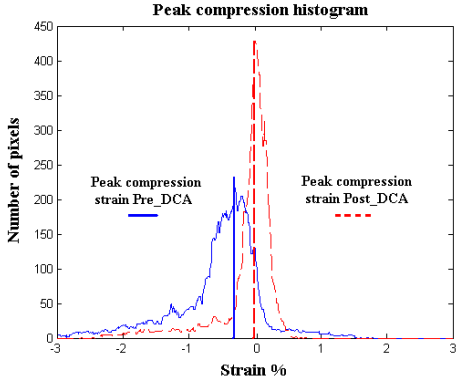

Figure1: Example of a radial strain histogram at peak compression. Pre–DCA (solid line) Post–DCA (dashed line)

* *indicates Presenter*

043 **QUANTIFYING THE IMPACT OF SHEAR WAVELENGTH ON SHEAR WAVE SPEED ESTIMATION.**

ML Palmeri[1], NC Rouze[1], MH Wang[1], X Ding[1], KR Nightingale[1].*
[1]Duke University, Durham, NC, USA.

Background: The propagation speed of shear waves (c_T) resulting from focused, impulsive acoustic radiation force excitations can be estimated in soft tissues to reconstruct the tissue's shear stiffness (μ) using the relationship $c_T = \sqrt{\mu/\rho}$ under the assumption of constant density ($\rho = 1.0 g/cm^3$) in a linear, elastic, isotropic solid. Using *a priori* information about the shear wave propagation direction relative to the excitation beam, shear wave positions through time can be determined using dynamic displacement metrics, such as time–to–peak (TTP) displacement [1] or correlation–based methods [2].

Aims: The purpose of this work is to evaluate the impact that spatial shear wavelength has on the accuracy and precision of shear wave speed (SWS) estimates.

Methods: Finite element method (FEM) models were used to simulate the dynamic tissue response associated with impulsive (50–500μs), 3D axisymmetric Gaussian excitations with varying widths (0.25–1.0cm -6dB widths) in linear, isotropic, elastic media (μ = 0.3–8kPa). 0.3 x 0.3 x 0.3mm^3 elements were used in a quarter–symmetry mesh solved with an explicit, time–domain solver (LS–DYNA, Livermore Software Technology Corp., Livermore, CA). The excitations were extended to asymmetric Gaussians and complex 3D distributions associated with two commercial transducers; the Siemens CH4–1 (focus at 49mm, 2.2MHz) and the VF10–5 (focus at 20mm, 6.7MHz). The impact of ultrasonic tracking, and more specifically, displacement estimation bias and jitter, were evaluated using Field II [3] simulations with a fixed 10kHz pulse repetition frequency. Experimental validation of the CH4–1 and VF10–5 results were performed using tissue–mimicking phantoms (Computerized Imaging Reference Systems, Norfolk, VA) with shear stiffnesses ranging from 1.4–16.0kPa. The Lateral TTP algorithm was used for the SWS reconstructions [1]. Spatial shear wavelengths were defined as the -6dB width from the peak displacement for the monophasic shear waves resulting from the impulsive excitations. Axial excitation gradients were considered negligible for the depth of analysis in this study (i.e., the focal depth).

Results: TTP displacements were directly related to the excitation duration (T_{rad}), excitation beamwidth (σ) and density (ρ) of the material, and inversely related to the shear stiffness (μ), following the relationship $TTP = M(\sigma,\rho)/\mu + T_{rad}$, where $M(\sigma,\rho)$ is a proportionality constant. TTP displacements at the focal point ranged from 0.8–3.9ms (μ = 8.0–0.3kPa, T_{rad} = 50μs, σ = 1.0cm), demonstrating that for more compliant media, the TTP responses were dominated by the mass of the excited material ($M(\sigma,\rho)$). The measured –6dB spatial shear wavelengths (λ_T) were directly related to the input -6dB excitation beamwidth (σ) by the relation $\lambda_T = K\sigma$, $K = 1.0 \pm 0.01$; K was independent of μ and T_{rad}.
While the mean SWS estimates in different stiffness media were not significantly affected by λ_T ($p > 0.05$), their standard deviations significantly decreased from ± 0.50kPa to ± 0.01kPa (i.e., improvement of 98%, $p < 0.05$) in a μ = 1kPa medium as σ increased from 0.25-1.0cm. These differences were statistically insignificant (0.50–0.45kPa, $p > 0.05$) in the stiffer media (μ > 8kPa).

Conclusions: Spatial shear wavelengths are independent of the excitation duration, but are directly modulated by the 3D spatial extent of the excitation beam. Larger shear wavelengths provide greater periods to estimate TTP metrics in fixed PRF imaging configurations, reducing the variability of the shear wave speed estimates, particularly in softer media. Smaller shear wavelengths, however, are advantageous in the context of using smaller reconstruction kernels to generate shear stiffness images with high spatial resolution. This study held the peak excitation amplitude constant; the effects of changing the resultant displacement magnitudes in response to varying the aperture sizes of linear arrays that would occur when experimentally modulating excitation beamwidths are being explored.

Acknowledgements: This work was supported by NIH grants R01 EB002132 and R01 CA124824. We thank Siemens Healthcare, Ultrasound Business Unit, Mountain View, CA for their system support.

References:

[1] Palmeri ML, Wang MH, Dahl JJ, Frinkley KD, Nightingale KR: Quantifying Hepatic Shear Modulus *In Vivo* using Acoustic Radiation Force. Ultrasound Med. Biol., 34(4), pp. 546–558, 2008.
[2] McLaughlin J and Renzi D: Using Level Set Based Inversion of Arrival Times to Recover Shear Wave Speed in Transient Elastography and Supersonic Imaging. Inverse Problems, 22, pp. 707–725, 2006.
[3] Jensen JA and Svendsen NB: Calculation of Pressure Fields from Arbitrarily Shaped, Apodized, and Excited Ultrasound Transducers. IEEE Trans. Ultrason., Ferroelec., Freq. Contr., 39, pp. 262–267, 1992.

040 **INTERNAL INDENTATION FOR DIRECT MODULUS ESTIMATION**

J Vappou[1], E Konofagou[1].*
[1]Ultrasound and Elasticity Imaging Laboratory, Columbia University, New York, NY, USA.

Background: Harmonic Motion Imaging (HMI) is a Focused–Ultrasound (FUS)–based method that consists of applying a low–frequency oscillatory force (typically 10–500Hz) using a FUS transducer and simultaneously estimating the resulting displacements using an ultrasound imaging transducer [1]. At high acoustic intensity, HMI can be used for tumor ablation and monitoring of the displacements during the ablation process [2]. At low acoustic intensity, HMI can be used as an elasticity imaging method where a sinusoidal force is applied and the resulting displacements are measured. A low–intensity HMI–based method has been previously proposed to estimate quantitatively viscoelastic properties of soft tissues [3]. However, it is based on shear wave propagation and suffers from significant limitations commonly encountered in shear wave–based methods, in particular, strong attenuation due to diffraction and inaccuracy in highly non–uniform media. In this study, we propose to use a novel approach where the highly localized nature of the applied force and the knowledge of the magnitude of this force are used to regionally estimate the elasticity of the tested medium. Such a protocol has strong similarities with mechanical indentation, one significant difference being that HMI allows for internal, noninvasive testing.

Aims: There are two aims in this study: 1) to develop a HMI–based method that allows quantitative measurement of local elasticity based on the principle of indentation and 2) to evaluate the accuracy of the method in a finite–element and phantom framework.

Methods: An HMI–based experimental protocol was used, combining a FUS transducer (4.5MHz) that generates an oscillatory force at the focus and an imaging transducer (phased array, 3.3MHz) with high lateral resolution and high frame rate (≈ 200–400Hz) obtained by reducing the sector size to a limited ROI around the focal region. The axial displacement is estimated by cross–correlation within the whole image, during the application of the force. Spatial derivatives of the displacement are calculated offline. An HMI modulus (E_{HMI}) was defined based on the knowledge of both magnitude and distribution of the applied force and on the measured strains.
Finite–Element Study: The problem was first simulated using the finite element (FE) method in order to evaluate its accuracy. For this purpose, 8 numerical phantoms were generated, the Young's modulus varying from 1kPa to 100kPa. The actual force measured experimentally was implemented within the FE model and E_{HMI} was compared to the input Young's modulus E.
Phantom Study: E_{HMI} measurements were performed on 6 polyacrylamide phantoms (concentrations from 15–40%, f=10Hz) that were also tested by rheometry for validation purposes (dynamic shear tests, f= 1-10Hz, ε = 0.5%).

Results: Excellent correlation was found between E_{HMI} and the actual Young's modulus E in the finite element study (r^2 = 0.995). The robustness of the proposed method was also demonstrated by showing that boundary conditions, geometry, heterogeneity have a negligible effect on the measured E_{HMI}. This numerical study also shows that the proposed method has a resolution of about the lateral size of the focus (approx. 1mm). Very good correlation (r^2 = 0.925) and reproducibility were found in the polyacrylamide phantom study.

Conclusions: The method proposed here has similarities with indentation techniques that are conventionally used for mechanical testing. Here, the indentation is internal thanks to the use of focused ultrasound, allowing us to perform *in vivo*, noninvasive internal measurements that are not feasible with mechanical indentation. The quantitative nature of the proposed method has been demonstrated in this study through the measurement of E_{HMI} in both simulations and experiments.

Acknowledgements: The study was funded in part by NIH R21EB008521 and NIH R01 HL098830.

References:
[1] Maleke et al.: Ultrason. Imaging, Vol. 28, No. 3, pp. 144–158, 2006.
[2] Maleke et al.: IEEE Trans. Biomed. Eng., Vol. 57, pp. 7–11, Jan. 2010.
[3] Vappou et al.: Phys. Med. Biol., Vol. 54, pp. 3579–3595, Mar. 2009.

050 **SHEAR STRAIN ELASTOGRAPHY USING OPTICAL COHERENCE TOMOGRAPHY (OCT) AS A MEANS OF GENERATING CONTRAST.**

A Grimwood[1], L Garcia[2], JC Bamber[2], J Holmes[3], P Woolliams[4], P Tomlins[4], Q Pankhurst[1].*

[1]Royal Institution of Great Britain, London, England, UK; [2]Institute of Cancer Research, Sutton, Surrey, England, UK; [3]Michelson Diagnostics Ltd., Orpington, Kent, England, UK; [4]National Physical Laboratory, Teddington, Middx, England, UK.

Introduction: A technique using optical coherence tomography (OCT) to image total shear strain within a sample is employed, generating useful contrast between regions of different Young's Modulus. Experimental results and finite element simulations are presented for a phantom model of a surface lesion comprising a silicone rubber test object with a well-bonded inclusion ~10 times stiffer than its surroundings. Close agreement between simulated and experimental data is demonstrated.

Background: Total shear strain elastograms have been produced for micron–scale displacements imaged using OCT. The elastograms generate useful contrast between a stiff surface inclusion and surrounding tissue in phantom models. The phantom was actuated using a controlled, repeatable method comprising a magnetizable implant and an external magnet. Elastograms obtained under repeatable conditions such as these could potentially limit inter–observer variation in diagnoses from histopathology. They may also prove useful where evaluation of cancer relies on qualitative measures such as the ABCD rule (asymmetry, border, colour, diameter).

Aims: Demonstration of a technique for imaging total shear strain in OCT is described. Useful contrast is derived from the shear strain elastograms. The experimental results are supported by finite element simulations. Finally, potential refinements and applications of the technique are discussed.

Methods: A silicone rubber tissue phantom containing an embedded 0.79 mm magnetizable implant was imaged under OCT. Using normalized cross–correlation, a displacement map was formed from B–scans taken prior to and during actuation of the implant. The strain field generated by this localized, non–uniform stress was estimated from displacement data using a least–squares strain estimator. Total shear strain elastograms were thus produced depicting an inclusion in the phantom ~10 times stiffer than its surroundings (268.5 ± 31kPa and 36.7 ± 7kPa, respectively).

Results: Total shear strain elastograms are shown in Figure 1. These depict the magnitude of total shear strain in two phantoms: one with a stiff surface inclusion, the other without. The pictures inset are comparable elastograms obtained from finite element simulations.

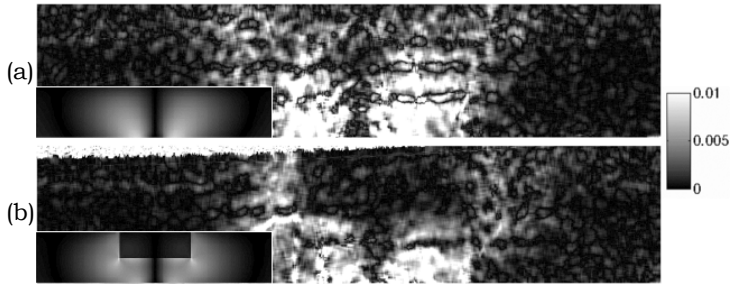

Figure 1: Elastograms depicting magnitude of shear strain in experimental phantoms with: (a) no inclusion and (b) a stiff inclusion (upper centre). Insert images show corresponding finite element elastograms. Color scale is absolute strain.

Conclusions: Useful contrast is generated by the attenuation of shear strain through the stiff inclusion. Horizontal banding artifacts are visible; however, these could conceivably be mitigated in the future through changes to image processing. Additionally, the method of actuation could be replaced by a less invasive technique in the future, such as surface indentation, to facilitate *in–vivo* sampling. OCT is a real–time imaging modality with a resolution of >10μm and a depth penetration in tissue of ~2mm, making it potentially well–suited to elastographic measurements of small skin–surface lesions.

Acknowledgements: Research funded by an EPSRC CASE Studentship with financial contribution from industrial sponsors Michelson Diagnostics Ltd. Support from NPL Biophotonics Dept. and ICR Elastogrpahy Team gratefully acknowledged.

055 **NUMERICAL EVALUATION OF CORRELATION BASED 3D SPECKLE TRACKING FOR CARDIAC ULTRASOUND ELASTICITY IMAGING.**

S. Tripathy[1,2], M. A. Simon[2], K. Kim[1,2,3].*
[1]The Center for Ultrasound Molecular Imaging and Therapeutics, [2]Cardiovascular Institute, [3]Bioengineering Department, University of Pittsburgh, Pittsburgh, PA, USA.

Background: Noninvasive functional assessment of myocardium is critical for the diagnosis and prognosis of various cardiac and cardiovascular diseases such as myocardial infarction. Ultrasound elasticity imaging (UEI) based on speckle tracking (ST) has been shown to be an effective tool for functional assessment of the myocardium with limitations [1,2]. The local elastic property changes of the infarct area are reflected on the strain map. Due to complex geometry and contraction of a heart, 3D ST is needed. Recently, correlation–based 3D ST was developed to reduce the large de–correlation due to out–of–plane motion of the tissue [3]. In this study, a two chamber finite element (FE) model is developed to evaluate and establish the efficacy of 3D UEI to identify the infarct area.

Aims: (1) Develop a numerical myocardial infarct 3D UEI model based on FE simulations. (2) Identify the infarct region from the strain map more accurately than 2D UEI.

Methods: A two chamber cardiac FE model was developed. A cavity pressure driven quasi–static deformation problem was set up. The tissue was considered linearly elastic (Young's modulus, E = 150kPa) and incompressible (Poisson's ratio, μ = 0.495). Four–noded tetrahedral hybrid elements with linear interpolation were used. A small spherical hard inclusion, E = 2MPa, was used to model the infarct area as shown in Figure 1a. The full heart cycle was divided into 15 linear time–steps. A 2D phased array centered at 2MHz with a band–width of 50% at 6dB was simulated to generate 3D US radio frequency (RF) data. Both 2D and 3D ST were performed on the US RF data.

Results: Figure 1 plots the radial, circumferential and elevational displacements from FE simulation as well as 2D and 3D ST estimates for a single elevational slice. A clear improvement (compared to the FE results) is observed for the 3D ST maps. Figure 1 also compares all 6 components of the strain tensor for the FE and the 3D ST estimates. Since the 2D UEI assumes in–plane strain, there are only 3 strain components. The infarct region as marked in the B–mode image (Figure 1a) can be clearly and more accurately identified using the 3D ST strain maps compared to 2D ST.

Conclusions: Strong decorrelation in 2D ST due to out–of–plane motion in cardiac application can be addressed by 3D ST. Since 3D ST considers the elevational plane motion as well, more accurate displacement and strain estimates are also obtained as observed in this numerical study. It was shown that the 3D UEI is able to identify the infarct region more closely than 2D ST. From quantitative analysis of the results, the improvement was about 60–80% for some areas with large out–of–plane motions.

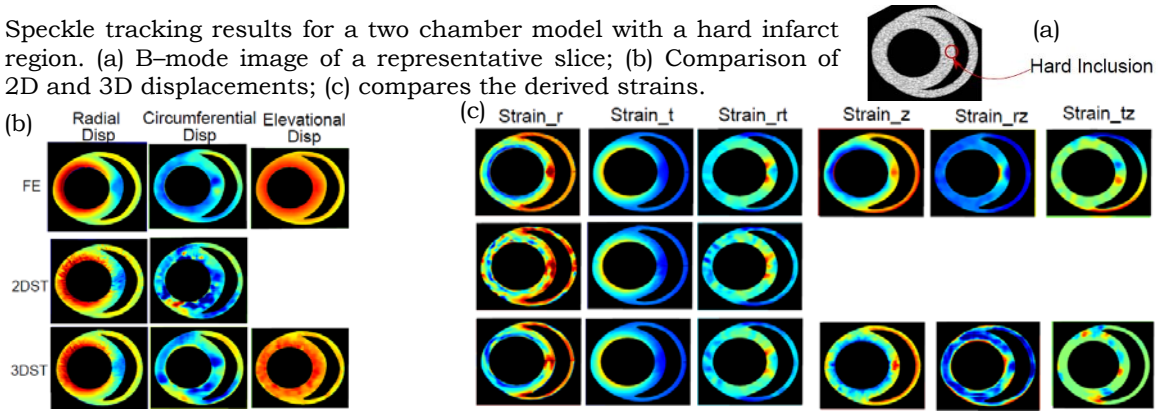

Figure 1: Speckle tracking results for a two chamber model with a hard infarct region. (a) B–mode image of a representative slice; (b) Comparison of 2D and 3D displacements; (c) compares the derived strains.

Acknowledgements: The project was partly funded by Grant Number KL2 RR024154 from the National Center for Research Resources (NCRR), a component of the National Institutes of Health (NIH) and NIH Roadmap for Medical Research, and its contents are solely the responsibility of the authors and do not necessarily represent the official view of NCRR or NIH.

References:

[1] J. Ophir, et al.: Ultrasound Imaging, 13, pp. 111–134, 1991.
[2] A. R. Skovoroda, et al.: IEEE UFFC, 41(3), pp. 302–313, 1994.
[3] X. Chen, et al.: Ultrasonic Imaging, 27(1), pp. 21–36, 2005.

* *indicates Presenter*

015 **TRANSTHORACIC ACOUSTIC RADIATION FORCE IMPULSE IMAGING OF CARDIAC FUNCTION.**

David P. Bradway[1], Stephen J. Hsu[2], Patrick D. Wolf[1], Gregg E. Trahey[1].*
[1]Duke University, Room 136 Hudson Hall, Box 90281, Durham, NC, 27708, USA; [2]Siemens Healthcare, Ultrasound Business Unit, 22010 SE 51st Street Issaquah, WA, 98029, USA.

Background: The Acoustic Radiation Force Impulse (ARFI) imaging method was previously shown capable of visualizing myocardial stiffness in real–time [1]. Cyclic variation in ARFI–induced displacements reflected the changing mechanical properties of the heart through the heartbeat, matching the timing and behavior of cardiac strain rate and ECG [2].

Aims: Apply transthoracic cardiac ARFI imaging methods in studies of left ventricular function in human subjects and animal models. Evaluate available ultrasound probes for transthoracic cardiac use.

Methods: Transthoracic ARFI imaging was used to examine function of the left ventricular free wall in human subjects and animal models at Duke University and Synecor, LLC. A Siemens ACUSON Antares™ ultrasound scanner (Siemens Healthcare, Ultrasound Business Unit) that was modified for research was used in these studies. For all studies, matched global ECG was acquired, and for the canine study shown in Figure 1, LV pressure and volume measurements were also acquired using a Millar catheter (Millar Instruments, INC). A Siemens VF10–5 transducer was used for the results shown here and for other initial feasibility studies. Other probes were tested under various imaging configurations.

Results: Images of a canine LV free wall are shown in Figure 1. The traditional M–mode (Figure 1a) displays contraction and relaxation of the myocardial wall through the cardiac cycle. The LV wall thickening and relaxation are coincident with the QRS complex and T wave in the global ECG (Figure 1d). Figure 1b displays an M–mode ARFI image at the same time and location. A mask has been used to blank the left ventricle and regions of tissue that were poorly tracked. Simultaneous pressure and volume measurements from a Millar catheter placed in the LV are shown in Figure 1e and f. ARFI–induced displacements (Figure 1c) fall with the onset of ventricular systole (Figure 1d), the corresponding rise in ventricular pressure (Figure 1e), and drop in volume (Figure 1f). Displacements (Figure 1c) rise at the T wave (Figure 1d) through passive filling (Figure 1f) as the ventricular pressure drops (Figure 1e).

Conclusions: Transthoracic cardiac ARFI imaging has been shown suitable for non–invasive evaluation of LV function.

Acknowledgements: This work has been supported by NSF Graduate Research Fellowship and NIH grant #5R37HL096023. We thank Siemens Healthcare Ultrasound Business Unit for technical and in-kind support.

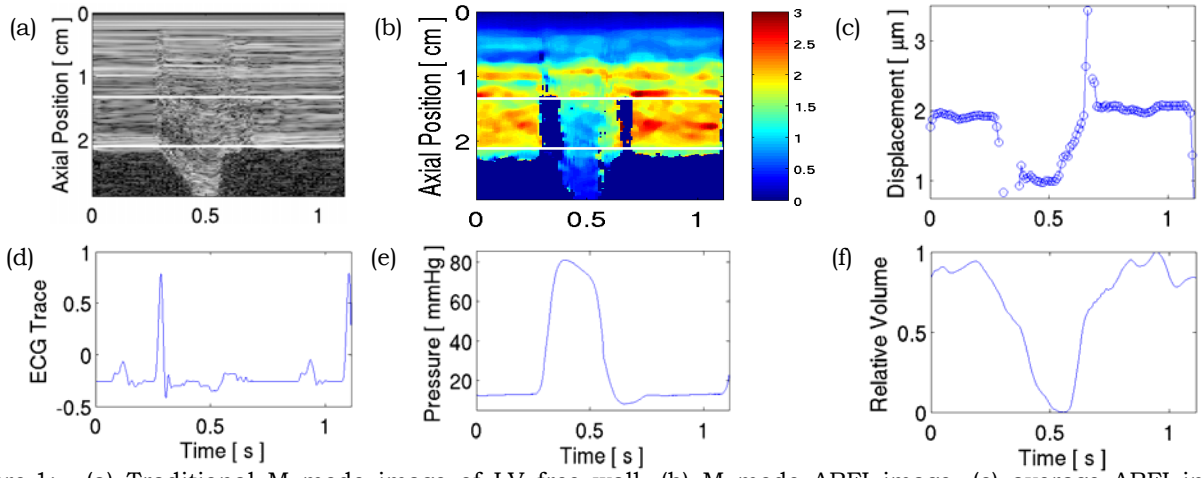

Figure 1: (a) Traditional M–mode image of LV free wall, (b) M–mode ARFI image, (c) average ARFI–induced displacement in ROI, (d) global ECG, (e) LV pressure, and (f) volume through a single cardiac cycle. The axial ROI is marked with white lines on (a) and (b). The ARFI–induced displacement (b) image and (c) plot reflect cyclic activity in the LV free wall.

References:

[1] DP Bradway, SJ Hsu, BJ Fahey, JJ Dahl, T Nichols, GE Trahey: Transthoracic Cardiac ARFI: A Feasibility Study. Proc IEEE Ultrason Symp, pp. 448–451, 2007.

[2] SJ Hsu, RR Bouchard, DM Dumont, CW Ong, PD Wolf, GE Trahey: Novel Acoustic Radiation Force Impulse Imaging Methods for Visualization of Rapidly Moving Tissue. Ultrason Imaging, 31(3), pp. 183–200, July, 2009.

* *indicates Presenter*

064 ***EX VIVO* FEASIBILITY OF HARMONIC MOTION IMAGING OF HUMAN BREAST TUMORS.**

Elisa E. Konofagou[1,2], Caroline Maleke[1].*
[1]Ultrasound and Elasticity Imaging Laboratory, Biomedical Engineering Department, Columbia University, New York, NY, USA; [2]Radiology Department, Columbia University, New York, NY, USA.

Background: In this presentation, a feasibility study of Harmonic Motion Imaging (HMI) [1–3] for human tumor detection, localization and characterization *ex vivo* is presented. HMI is a technique that uses an amplitude–modulated (AM) focused beam to induce a localized vibration at the focus and thus map the underlying mechanical properties of the vibrated tissue [4].

Aims: The capability of HMI to differentiate between benign, malignant and normal breast tissues is examined.

Methods: Seventeen (n=17) post–surgical human breast specimens (5 benign (fibroadenomas), 9 malignant (4 invasive ductal carcinomas, 3 ductal carcinomas *in situ* and 2 invasive lobular carcinomas) and 3 normal) were collected approximately 30 minutes after excision and prior to histopathology. Specimens were imaged using sonography or mammography prior to HMI. The HMI system was used to generate an oscillatory radiation force using an AM (10–30Hz) force transducer (4.5MHz; Imasonic) and a pulse–echo transducer (7.5MHz; Panametrics) that acquired radiofrequency (RF) frames during application of the radiation force. For 2D HMI, the transducer assembly was moved in a 2D raster–scanning fashion at a step size equal to 1mm in the lateral and elevational directions using a computer–controlled positioner (Velmex Inc., Bloomfield, NY, USA). The scan planes were adapted based on the specimen's size. The acoustic intensity (I_{sppa}) was equal to 31.4W/cm^2 with a duration of 0.2s at each point. In order to determine the optimal AM frequency, a linear chirp test within the range of 10–30Hz was applied to investigate the optimal vibration frequency for the highest mechanical contrast between the tumor and the surrounding regions. A 1D cross–correlation technique was applied on the acquired RF signals to estimate the resulting displacement.

Results: HMI was capable of accurately detecting, mapping and localizing tumors of varying size (4x2 to14x22mm^2) with excellent agreement with sonography and mammography findings. An unpaired Student t–test with a 90% confidence interval was performed to determine whether different breast pathologies could be differentiated based on the HMI images. Normal breast tissues could be differentiated from both benign and malignant tumors at high statistical significance ($p < 0.005$). The benign tumors experienced a lower average displacement compared to the malignant masses but at lower statistical significance ($p = 0.008$). Thus, the HMI images could categorize different tumor types based on their relative stiffness. However, HMI could not differentiate between different malignant types ($p>0.1$).

Conclusions: The results presented here show that HMI could detect, map, localize and characterize breast tumors *ex vivo*. Normal, benign and malignant tumors could be accurately mapped and differentiated with HMI displacements lower in the benign relative to malignant tumors. HMI may thus serve as a reliable technique for noninvasive localization and characterization of breast tumors.

Acknowledgements: This work was supported in part by the National Institutes of Health (1R21EB008521).

References:

[1] Maleke C., Pernot, M. and Konofagou E.E.: A Single–Element Focused Transducer Method for Harmonic Motion Imaging. Ultrason. Imaging, Vol. 28, No. 3, pp. 144–158, 2006.
[2] Maleke C. and Konofagou E.E.: Harmonic Motion Imaging for Focused Ultrasound (HMIFU): A Fully Integrated Technique for Sonication and Monitoring of Thermal Ablation in Tissues. Phys. Med. Biol., Vol. 53, No. 6, pp. 1773–1793, 2008.
[3] Maleke C and Konofagou EE: *In Vivo* Feasibility of Real–Time Monitoring of Focused Ultrasound Surgery (FUS) using Harmonic Motion Imaging (HMI). IEEE Trans. Biomed. Eng., Vol. 57, pp. 7–11, 2010.
[4] Vappou J., Maleke, C. and Konofagou, E.E.: Quantitative Viscoelastic Parameters Measured by Harmonic Motion Imaging. Phys. Med. Biol., 54(11), pp. 3579–94, 2009.

* *indicates Presenter*

001 **PARAMETRIC ANALYSIS OF AXIAL SHEAR STRAIN IMAGING ON ELLIPSOIDAL MASSES.**

Haiyan Xu[1,2], Tomy Varghese[1,2].*
[1]Medical Physics Department, [2]Electrical and Computer Engineering Department, University of Wisconsin–Madison, Madison, WI 53705, USA.

Background: Axial shear strain patterns and parametric analysis around circular inclusion/background interfaces was previously reported by Thittaikumar et al. [1]. Several investigators have also demonstrated the potential to utilize normalized axial shear strain area features for distinguishing benign from malignant breast tumors under *in–vivo* imaging conditions [2,3].

Aims: Parametric evaluation of shear strain features generated using finite element analysis (FEA) software to examine feasibility of utilizing different axial shear strain features for differentiating benign from malignant tumors is evaluated for different mass shapes and asymmetric mass locations. The impact of parameters such as stiffness variations, tumor dimensions and shape, applied deformation and asymmetric location of masses is studied [1].

Methods: Two–dimensional finite element simulations of both spherical [1] and ellipsoidal masses embedded within a uniform background were utilized for axial shear strain analysis. Different degrees of bonding at the mass/background interface were characterized using friction coefficient values ranging from 0.01 to 100 denoting loosely bonded to firmly bonded masses [1]. Axial shear strain images were estimated from the gradient of the displacement with quasi–static deformation varied from 1% up to 10% of the model dimensions. Other mechanical modeling aspects, such as stiffness ratios between the inclusion and background, mass dimensions and shape and positioning of the masses within the background were also controlled to identify the contribution of each parameter to the shear strain patterns and corresponding impact on breast lesion differentiation. Axial shear strain areas were normalized to the mass dimensions, percentage of applied deformation and the strain contrast to determine features that can be utilized to discriminate between benign and malignant masses [1]. The normalized threshold percentage was also varied in order to determine optimal values for breast mass differentiation.

Results: Our results indicate that the normalized axial shear strain area feature is significantly larger, while the normalized mean shear strain value is smaller for firmly bonded masses when compared to loosely bonded ones [1-3]. Higher stiffness ratios (>1) between the inclusion and background improve the discrimination. The differentiation performances are identical for different symmetric mass shapes as well as for small applied deformations. However, larger applied deformations (>3%) reduce the discrimination performance at lower values of the friction coefficients. Variations in the normalized shear strain areas and mean values were also observed for asymmetric positioning of ellipsoidal masses at lower friction coefficients.

Conclusions: Finite element results demonstrate the feasibility of utilizing both the area and mean of normalized axial shear strain feature to differentiate benign from malignant masses based on their bonding to background tissue. Potential sources of errors with the use of these features occur for loosely bonded inclusions at larger applied deformations or for asymmetric masses (Figure 1).

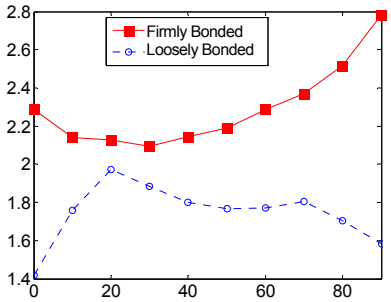

Figure 1: Plot showing the impact of varying the location of asymmetry on the Normalized axial–shear strain area between the loosely bonded (■) and firmly bonded (○) ellipsoidal inclusions.

Acknowledgements: This work is supported by Komen Grant BCTR0601153 and NIH–NCI grants 5R21CA140939–02 and R01CA112192–S103.

References:

[1] Thitai Kumar, A., Krouskop, T.A. Garra, B.S. and Ophir, J.: Visualization of Bonding at an Inclusion Boundary using Axial Shear Strain Elastography: A Feasibility Study. Phys Med Biol, 52(9), p. 2615–2633, 2007.
[2] Thitai Kumar, A., Mobbs, L., Kraemer–Chant, C., Garra, B., and Ophir, J.: Breast Tumor Classification using Axial Shear Strain Elastography: A Feasibility Study. Phys Med Biol; 53(17), pp. 4809–4823, 2008.
[3] Xu, H, Rao, M, Varghese, T, Sommer, A, Baker S, Hall TJ, Sisney G.A. Burnside, B.: Ultrasound Med Biol, (in press), 2010.

011 **THE FINITE DIFFERENCE MODEL OF SHEAR WAVE PROPAGATION IN VISCOELASTIC TISSUE.**

Gang Cheng[1], Xiaodong Han[1], Wei Tan[1], Christopher R. Hazard[2]*
[1]GE Global Research, Shanghai, Pudong District, CHINA; [2]GE Global Research, Niskayuna, NY, USA.

Background: Shear modulus and viscosity are two parameters related to tissue health. In the past two decades, researchers have used several different methods to measure the viscoelastic properties of tissue. One of the major approaches is quantitative shear wave elastography. This method estimates the shear modulus by pushing the tissue in order to generate a propagating shear wave and then detects the resulting displacements of the tissue as that shear wave travels. Several modalities (MRI [1], CT [2] or ultrasound [3]) have been used to measure tissue deformation and to validate mechanical models of viscoelastic tissue.

Aims: This research aims to set up a model based method to estimate tissue viscoelasticity based on shear wave propagation. A finite difference model (FDM) has been developed to simulate shear wave propagation in a viscoelastic tissue after being pushed by an acoustic radiation force. The FDM model can be used by an inverse solver to estimate tissue viscoelasticity through iterative searching.

Methods: An FDM of shear wave propagation in isotropic viscoelastic tissue was used to simulate the shear wave induced displacements in materials with varied viscoelastic parameters. The following equations characterize the model of the shear wave propagation that we used:

$$\begin{bmatrix}\sigma_x\\ \sigma_z\\ \sigma_{xz}\end{bmatrix}=\frac{E}{1-\nu^2}\cdot\begin{bmatrix}1 & \nu & 0\\ \nu & 1 & 0\\ 0 & 0 & \frac{1-\nu}{2}\end{bmatrix}\cdot\begin{bmatrix}\varepsilon_x\\ \varepsilon_z\\ \varepsilon_{xz}\end{bmatrix}+\frac{\eta}{2}\cdot\begin{bmatrix}1 & -1 & 0\\ -1 & 1 & 0\\ 0 & 0 & 2\end{bmatrix}\cdot\begin{bmatrix}\dot{\varepsilon}_x\\ \dot{\varepsilon}_z\\ \dot{\varepsilon}_{xz}\end{bmatrix},\quad \rho\cdot\alpha_i=\sum_j\frac{\partial\sigma_{ij}}{\partial x_j}+P_i\,,$$

Where, σ is stress vector, ε is strain vector, E is Young's modulus, η is viscosity, ν is Poisson's ratio, a_i is the external acceleration, ρ is the material density and P_i is the acoustic radiation body force. In real world application, there is also considerable background motion or drifting caused by the vibrations in the environment. We assume that the frequency of the drifting vibration is lower than the frequency of the shear wave displacement. A linear function can then be used to approximately fit the background drift [4]. The FDM model has been implemented in Matlab. The model simulates the shear wave shape over time for a given acoustic pushing pulse. To validate the model, a modified GE LOGIQ9 ultrasound system generates acoustic radiation force and detects the shear wave on customized phantoms. The output of the model is compared with experimental data to evaluate the performance of the model.

Results: Figure 1 shows that there is reasonable agreement between the shear wave simulation and the measurement results at the two locations. The Young's modulus used in the FDM was 19kPa and the viscosity was 3.8Pa s. The background drift was also incorporated into the model to allow for better matching of the results.

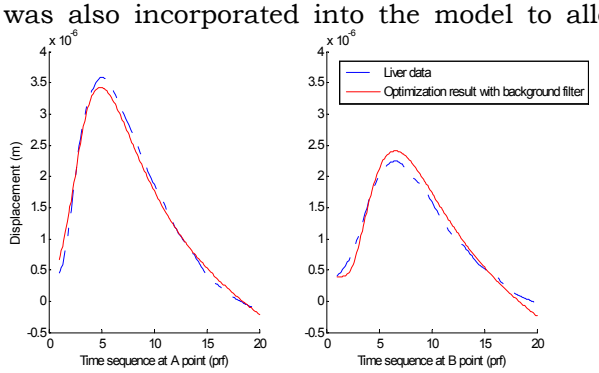

Figure 1: The result after iterative optimization

Conclusions: The FDM with incorporated background drifting can accurately represent the tissue displacements caused by the shear wave propagation after a radiation force push. Using this model, researchers can optimize the parameters of radiation force based systems and analyze the associated errors.

References:

[1] A. Manduca, T. E. Oliphant, M. A. Dresner, et al.: Medical Image Analysis, (4), pp. 237–254, 2001.
[2] Shi Hongjian, Farag, AA.m Fabmi, Rachid, Chen Dongqing: IEEE Transactions on Biomedical Engineering, (3), pp. 978–984, 2008.
[3] M.L. Palmeri, M.H. Wang, J.J. Dahl, K.D. Frinkley, K.R. Nightingale: Ultrasound in Medicine and Biology, (4), pp. 546–558, 2008.
[4] K. Nightingale, D. Stutz, R Bentley, G Trahey: IEEE Ultrasonics Symposium Proc., pp. 525–528, 2002.

* *indicates Presenter*

012 **FINITE ELEMENT SIMULATION OF SHEAR WAVE PROPAGATION INDUCED BY A VCTE PROBE.**

Stéphane Audière[1,2], Maurice Charbit[1], Elsa Angelini[1], Veronique Miette[2], Jennifer Oudry[2], Laurent Sandrin[2].*

[1]Institut Telecom, Telecom ParisTech, CNRS LTCI, 46 rue Barrault, 75013, Paris, FRANCE; [2]Echosens, Research and Development Department, 153 avenue d'Italie, 75013, Paris, FRANCE.

Background: The Fibroscan® (Echosens, Paris, France) device based on vibration–controlled transient elastography (VCTE) is used to non–invasively assess liver stiffness correlated to the hepatic fibrosis. Stiffness is quantified by measuring the velocity of a low–frequency shear wave traveling through the liver, which is proportional to the Young's modulus E. It has been demonstrated that E is highly correlated with liver fibrosis stage as assessed by liver biopsy.

Aims: To study the emergence of two shear waves with different velocity detected with the Fibroscan® on *in vivo* liver cases; simulations with finite element models (FEM) on a 3D anatomical model of liver and ribs can help understand this propagation pattern. Indeed, the shape and direction of the shear wave front induced by the Fibroscan® probe in the liver are not entirely known.

Methods: Liver elasticity measured by Fibroscan® ranges between 2–75kPa and corresponds to a shear wave velocity range of 0.8–5m/s. The shear wave is mechanically induced by the displacement of a piston controlled with a single period 50Hz sinusoid pulse. We have considered a FEM approach to solve the generalized Maxwell viscoelastic model for propagation in the liver and an isotropic model with damping (loss factor or Rayleigh model) for propagation in a phantom. The first simulation step consisted of validating the model parameterization for 2D simulations. We verified that the Young's modulus injected in the model generated the proper shear wave velocity [1]. An algorithm was then developed to derive Young's modulus values from simulated strain rate images. The second step consisted of simulating an experiment setup feasible with the Fibroscan® to compare results extracted from simulated and real strain–rate images. A cylindrical copolymer–in–oil phantom was used to mimic liver tissues. The axisymmetric geometry enabled the use of a 2D model. The last step consisted of simulating the shear wave generation and propagation induced by a piston hitting a 3D model: phantom or liver model, created from the surface mesh models distributed by the IRCAD (Strasbourg, France). Simulation results presented in this work use the COMSOL Multiphysics software tool to solve the partial differential equations associated with the transient analysis with a FEM method. COMSOL Multiphysics running on desktop computational resources provides sufficiently accurate results for wave propagation problems.

Results: For the first step, simulation of shear wave propagation is validated with Young's modulus measurement differences in agreement with the Fibroscan®'s accuracy. The viscoelastic model simulation reports a viscosity index that has little influence on the wave propagation, along depth and time. For the second step, preliminary results suggest that Rayleigh model is suitable to approach experimental results. For the last step, preliminary results are encouraging. Observations showed that the shear wave front is first spherical and then progressively deforms during propagation, according to the geometry of the liver.

Conclusions: This study reveals encouraging results regarding the feasibility to use FEM simulations to understand the behavior of different tissue types and organs for Fibroscan® scanning. 3D simulations design will be improved using a complete thoracic and abdominal anatomy, to study potential sources of aberrant propagation patterns and velocity measures.

References:

[1] Laurent Sandrin, et al.: The Role of the Coupling Term in Transient Elastography. J. Acoust. Soc. Am., 115, 73, 2004.

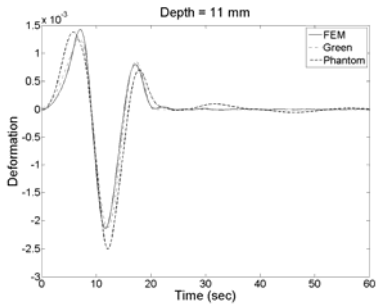

Figure 1: Amplitude of the deformation at 11mm depth: comparison between simulated data by FEM, the Green's functions and experience.

* *indicates Presenter*

080 **EFFECT OF BOUNDARY CONDITIONS ON THE PERFORMANCE OF POROELASTOGRAPHY TECHNIQUES IN COMPLEX SIMULATED MEDIA.**

Anuj Chaudhry[1], Ginu Unnikrishnan[2] , JN Reddy[2], Raffaella Righetti[1].*
[1]Electrical and Computer Engineering [2]Mechanical Engineering Departments, Texas A&M University, College Station, TX, USA.

Background: Many biological tissues behave as spatially and temporally complex composite materials due to their high fluid content. Pathological conditions and related therapies may significantly alter fluid transport mechanisms in tissues. Poroelastography is a modality for imaging the temporal behavior of tissues that can be modeled as poroelastic media, under sustained loading [1]. While several types of poroelastographic images may be used to depict the temporal behavior of a tissue, internal and external boundary conditions may affect the resulting temporal strain distributions and have important implications on the quality of the resulting poroelastographic images.

Aims: In this study, we assess the performance of poroelastography techniques for imaging the behavior of non–homogeneous poroelastic media under two different loading conditions: stress relaxation (material is subjected to a constant strain) and creep (material is subjected to a constant stress).

Methods: A simulation study was carried out using in–house FE poroelastic simulation software [2] combined with ultrasound simulation routines. Two types of complex media were simulated: a cubical 2–layer medium and a cubical medium containing a cylindrical inclusion. Different permeability ($1.95*10^{-14}$÷$1.95*10^{-6}m^4/N*s$), Young's modulus (1.74÷1.74∗10kPa) and Poisson's ratio contrasts (0.05÷0.45) between the underlying matrixes of the background and the target were considered. The performance of poroelastography techniques (both axial strain and effective Poisson's ratio) was quantified in terms of contrast–to–noise ratio (CNR), contrast transfer efficiency and sensitivity.

Results: The results of this study show that, in general, image quality of both axial strain and effective Poisson's ratio poroelastograms is a complex function of time, which depends on the geometry of the medium and the contrast between the material properties of the background and the material properties of the target. According to our results, the boundary conditions affect the performance of poroelastographic images both of axial strain and effective Poisson's ratio poroelastograms. Figure 1a shows elastographic CNR as a function of time for a simulated medium containing a cylindrical inclusion having different permeability properties with respect to the background (but the same elastic modulus and Poisson's ratio) subjected to two different loading conditions. Figure 1b shows a set of temporal axial strain elastograms corresponding to the stress relaxation (top) and the creep (bottom) cases shown in Figure 1a.

Conclusions: The results of this study suggest that internal and external boundary conditions may have a significant impact on the performance of poroelastography techniques. Experiments are currently undergoing to corroborate these simulation findings.

Acknowledgements: This work is supported by Texas Engineering Experiment Station and Texas A&M University, College Station, TX.

References:

[1] Righetti R, Ophir J, Krouskop TA.: A Method for Generating Permeability Elastograms and Poisson's Ratio Time–Constant Elastograms. Ultras. Med. Biol., vol. 31(6), pp. 803–816, 2005.
[2] Unnikrishnan, GU, Unnikrishnan, VU, Reddy, JN: Tissue–Fluid Interface Analysis Using Biphasic Finite Element Method. Comp. Meth. Biomech. Biomed. Eng., Vol. 12(2), pp. 165–172, 2009.

Figure 1: (a) (b)

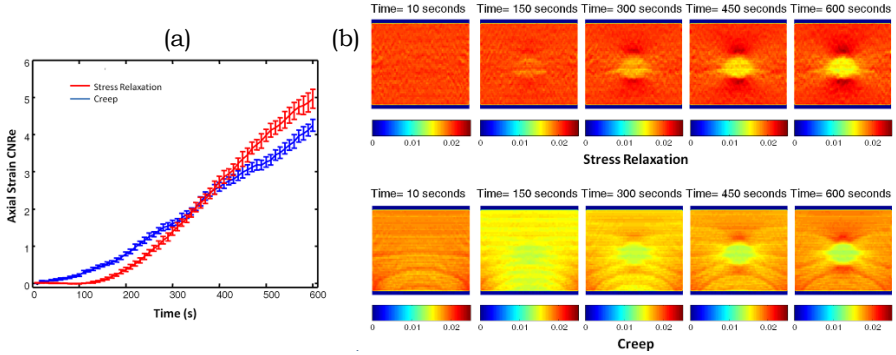

* *indicates Presenter*

093 **FEM SIMULATION OF HARMONIC TISSUE EXCITATION FOR PROSTATE ELASTOGRAPHY.**

O Goksel[1], S E Salcudean[1].*
[1]University of British Columbia, Vancouver, BC, CANADA.

Background: Prostate elastography can provide valuable information for diagnosis and treatment planning of prostate cancer. Both transrectal excitation [1] and abdominal excitation [2] have been used to generate mechanical waves in the prostate. Recently, transperineal excitation during magnetic resonance elastography [3] has also been used. Optimizing the location and frequency of mechanical excitation for prostate elastography will help improve imaging quality and patient comfort.

Aims: To compare the effectiveness of producing waves in the prostate using transperineal and transrectal excitation.

Methods: An anatomical model of the prostate region was obtained by meshing the contours, segmented from MR images, using Computer Graphics Algorithms (CGAL) software. This model includes the pubic bone, the prostate and part of the bladder. Harmonic excitations were modeled by vibrating a mesh node on the skin for transperineal excitation and vibrating the mesh nodes within the model of a transrectal ultrasound probe for transrectal excitation (Figure 1). The finite element method (FEM) was used with linear–elasticity and linear–geometry assumptions. Dynamic steady–state solutions within the region of interest were obtained using Ansys©. The tissue mechanical properties for the prostate and the surrounding tissue were set according to [2], with the Poisson's ratio set to 0.499. Tissue viscosity was modeled using Rayleigh damping model with a structural damping coefficient of 10^{-4}. The surface of the pubic bone is used as a zero displacement boundary condition. Sinusoidal excitations were applied in 0.5Hz increments from 5 to 100Hz, a typical range for dynamic elastography, at an amplitude of 1mm for transperineal compression and 0.2mm for transrectal antero–posterior compression. Wave penetration into different sections of the prostate was studied by observing wave amplitudes at three mesh nodes, located at the apex, the mid–gland and the base of the prostate, as seen in Figure 2.

Results: Wave propagation degrades with increased frequency of excitation as expected. Resonances observed at lower frequencies are the result of standing waves due to the higher wave penetration. Amplitude distributions along transverse and sagittal prostate cross–sections (Figure 3) are shown at two typical excitation frequencies for each method: 45Hz for MR elastography [3] and 5Hz for TRUS vibro–elastography (Figure 4).

Conclusions: The present simulation framework for dynamic prostate elastography can be used to study and later optimize elastography imaging. More sophisticated models with a larger anatomical extent and non–linear elasticity formulation will increase the realism of the simulation, enabling a comparison and validation of these simulations. Our results simply estimate the wave distribution patterns for different excitations. In the future, inverse problem algorithms will be evaluated based on such simulations.

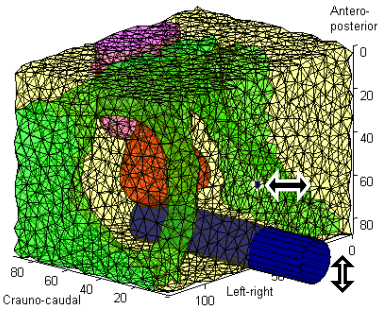

Figure 1: Our prostate region model.

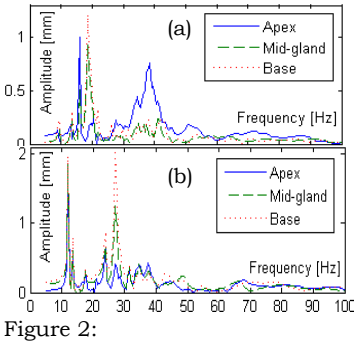

Figure 2: Oscillation amplitudes at the apex, mid–gland and base for (a) transperineal and (b) transrectal excitation.

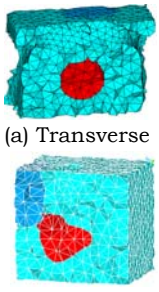
(a) Transverse

(b) Sagittal

Figure 3: Two mesh cross–sections as a reference for Figure 4.

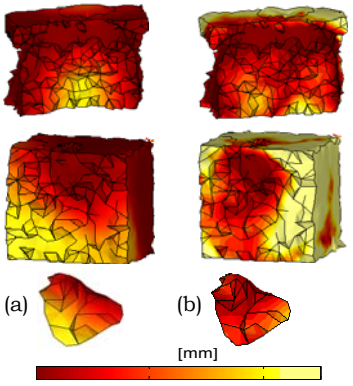

Figure 4: Demonstrates amplitudes for (a) transperineal excitation, 45Hz, and (b) transrectal excitation, 5Hz.

References:

[1] SE Salcudean, D French, S Bachmann, R Zahiri-Azar, X Wen, and WJ Morris: Viscoelasticity Modelling of the Prostate Region Using Vibro–Elastography. MICCAI, pp. 389-396, 2006.
[2] J Kemper, R Sinkus, J Lorenzen, C Nolte–Ernsting, A Stork, and G Adam: MR Elastography of the Prostate: Initial *In–Vivo* Application. Fortschr Röntgenstr, 176, pp. 1094–1099, 2004.
[3] RS Sahebjavaher, R Sinkus, SE Salcudean: Transperineal Prostate MRE at 3T. Proc ITEC, p. 33, 2010.

* *indicates Presenter*

084 **ALGORITHMS FOR QUANTIATIVE NONLINEAR ELASTICITY IMAGING IN THREE DIMENSIONS.**

S Goenezen[1], J–F Dord[1], PE Barbone[2], AA Oberai[1].*
[1]Rensselaer Polytechnic Institute, Troy, NY, USA; [2]Boston University, Boston, MA, USA.

Background: Linear elastic properties are useful in that they may be used to distinguish different tissue types. However, confining elasticity imaging to linear material properties limits its ability in classifying tissue types. For example, stress–strain curves from experimental compression tests in *ex–vivo* breast tissue samples indicate that at small strains both benign and malignant tumors tend to have a higher elastic modulus when compared with surrounding tissue [1]. However, with increasing strain (15%), benign breast tumors stiffen less than malignant breast tumors. This mechanical behavior can be captured with a nonlinear material parameter within an appropriate constitutive model, and images of this parameter may be used to improve breast cancer diagnosis. Recently we have developed an algorithm (assuming incompressible plane stress hypothesis) that accomplishes this by imaging the linear and nonlinear elastic parameters of tissue using quasi–static displacement data measured at two different levels of overall strain [2].

Aims: In quantitative elasticity images, the absolute values of the elastic parameters are obtained (as opposed to values relative to a reference region). Quantitative images are useful as they allow the possibility of monitoring the progression of a disease or a treatment plan and for inter–patient comparisons. Our goal is to develop an algorithm for generating quantitative linear and nonlinear elasticity images in three dimensions for incompressible materials. We accomplish this by extending our algorithms to three dimensions and by incorporating force measurements.

Methods: We solve the inverse problem of determining the linear and nonlinear elastic property distribution iteratively. We utilize a quasi–Newton method to minimize the difference between predicted and measured displacement fields as well as the difference between measured and predicted force. The overall computational cost of this algorithm is significantly reduced by employing the adjoint method and a novel material property continuation strategy. We model tissue as an incompressible isotropic hyperelastic solid. We present a new strain energy density function that has an exponential stress–strain response. In order to handle the incompressibility constraint, we augment the finite element formulation with a stabilizing term that prevents the appearance of the spurious pressure modes and the accompanying displacement locking observed in standard finite element schemes [3].

Results: We validate our inverse problem solution strategy with noisy, synthetic displacement data, obtained by solving forward problems for a given material parameter distribution. We assess the robustness and the accuracy of the algorithm for different noise levels (white Gaussian). Figure 1 shows the shear modulus reconstruction at zero strain (a) and the nonlinear parameter reconstruction at large strain (b) computed for synthetic data with 3% white Gaussian noise. The exact inclusion to background ratio for both material parameters is 5:1. The shear modulus here is known only up to a multiplicative factor.

Conclusions: We have developed a robust, accurate and efficient approach for solving the inverse nonlinear elasticity problem in three dimensions. In order to generate quantitative images, we have included force data in our inversion strategy. The key ingredients of our approach are an adjoint based gradient calculation, a material continuation strategy and a stabilized finite element method that avoids the pitfall associated with the incompressibility constraint.

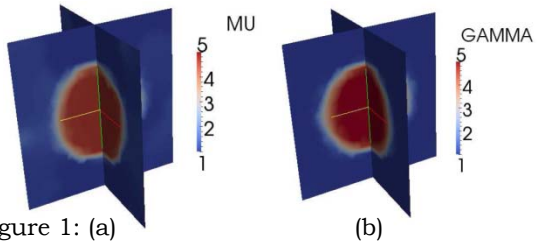

Figure 1: (a) (b)

Acknowledgements: We acknowledge the support of the NIH through grants R21CA133488 and R01CA140271.

References:

[1] O'Hagan, JJ and Samani, A: Measurements of the Hyperelastic Properties of 44 Pathological *Ex Vivo* Breast Tissue Samples. Physics in Medicine and Biology, 54, pp. 2557–2569, 2009.
[2] NH Gokhale, PE Barbone and AA Oberai: Solution of the Nonlinear Elasticity Imaging Inverse Problem: The Compressible Case. Inverse Problems, 24 045010, 2008.
[3] Klaas O, Maniatty A and Shephard MS: A Stabilized Mixed Finite Element Method for Finite Elasticity: Formulation for Linear Displacement and Pressure Interpolation. Computer Methods in Applied Mechanics and Engineering, 180 (1–2), pp. 65–79, 1999.

* *indicates Presenter*

085 **A DIRECT ALGORITHM FOR TIME–HARMONIC ELASTICITY IMAGING WITH MULTIPLE SOURCES.**

Yixiao Zhang[1], Assad A. Oberai[1], Paul E. Barbone[2], Isaac Harari[3].*
[1]Rensselaer Polytechnic Institute, Troy, NY, USA; [2]Boston University, Boston, MA, USA; [3]Tel Aviv University, Ramat Aviv, ISRAEL.

Background: In dynamic elasticity imaging, the response of tissue to a time–dependent excitation is measured and utilized to determine the spatial distribution of its viscoelastic parameters by solving an inverse problem. Several methods have been developed to solve this problem. These include the algebraic inversion method, where the solution is reduced to solving an algebraic problem, methods based on the time of arrival of a front and those based on interpreting the wave equation as a partial differential equation (PDE) for the shear modulus (see [1,2] for a review).

Aims: Our long-term goal is to develop an accurate, robust and fast method for determining the viscoelastic properties of tissue. Here we consider the model problem of the time–harmonic wave equation and develop and test a method for determining the real and imaginary components of the shear modulus. In particular, this method accounts for multiple measurements and uses these to overcome practical issues, such as noise and data limitations from experimental restrictions.

Methods: As a starting point, we consider the Adjoint–Weighted equations (AWE) for the inverse heat conduction problem. A finite element implementation of these equations is stable and accurate [3]. Further, it accounts for multiple measurements in a straightforward manner. For the time–harmonic wave equation, we develop the complex counterpart of this formulation. To improve the contrast of shear modulus in normal and abnormal tissues in the presence of noise, we append to it the total variation diminishing (TVD) regularization that penalizes jumps in the solution without penalizing their steepness. This is particularly useful in recovering localized regions of increased stiffness. We test the method using synthetic displacement fields produced by solving the forward problem. We also test the method on ultrasound measured experimental data involving a tissue–mimicking phantom.

Results: Applying the method to a single measured displacement field yields poor recovery. Small errors in boundary conditions tend to be amplified and propagated into the domain. Using multiple measurements ameliorates this issue somewhat. Adding TVD regularization further improves the reconstructions by preserving the edges of inclusion. With this method, we can successfully detect the abnormal region of different shear modulus from the background.

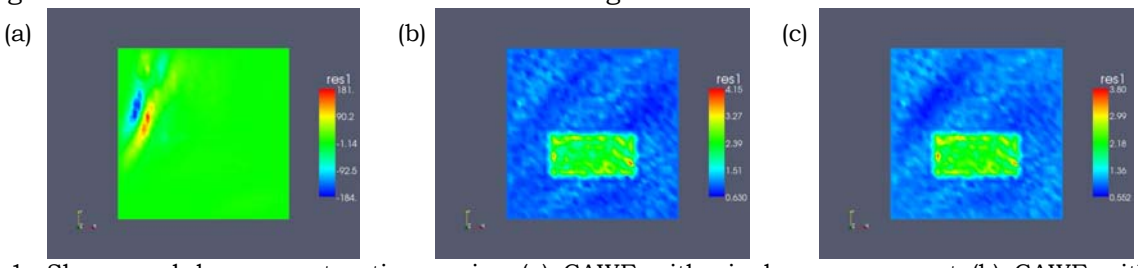

Figure 1: Shear modulus reconstructions using (a) CAWE with single measurement (b) CAWE with multiple measurements and (c) Regularized CAWE with multiple measurements.

Conclusions: We have developed and implemented an accurate, robust and fast algorithm for determining the spatial distribution of the viscoelastic properties of tissue. This method relies on solving the time–harmonic wave equation for the complex shear modulus and utilizes a stable finite element method to do so. It utilizes multiple measurements for better estimates of material properties. The extension of this method for the time–harmonic viscoelastic equations is underway.

Acknowledgements: This work has been supported by the NIH through the grant NIH RO1 AG029804. The authors thank J. R. McLaughlin and A. M. Maniatty at Rensselaer Polytechnic Institute for helpful discussions and Kevin J. Parker's team at the University of Rochester for tissue–mimicking phantom data.

References:

[1] Greenleaf, J.F., Fatemi, M. and Insana, M.: Selected Methods for Imaging Elastic Properties of Biological Tissues. Annual Review of Biomedical Engineering, 5 (1), pp. 57–78, 2003.
[2] Barbone, P.E. and Oberai, A.A.: Review of the Mathematical and Computational Foundations of Biomechanical Imaging, chapter in Computational Modeling in Biomechanics. Springer Netherlands, pp. 375–408, 2010.
[3] Barbone P.E., Oberai A.A., and Harari I.: Adjoint–Weighted Variational Formulation for Direct Solution of Inverse Heat Conduction Problem. Inverse Problems, 23, pp. 2325–2342, 2007.

094 **MESH ADAPTATION FOR IMPROVING INVERSE–PROBLEM RECONSTRUCTION.**

O Goksel[1], H Eskandari[1], S E Salcudean[1].*
[1]University of British Columbia, Vancouver, BC, CANADA.

Background: The use of the finite element method (FEM) to model deformation for a known elasticity distribution is often called the forward problem (FP), while recovering such elasticity parameters from observed displacements is referred to as the inverse problem (IP) [1]. Various approaches were proposed in the literature for the estimation of viscoelastic tissue parameters from static or dynamic observations. However, the spatial resolution of such recovery is limited by the resolution of the FEM mesh employed. Furthermore, due to the high computational cost, only a limited number of nodes can be used in the IP.

Aims: To improve the effective resolution of the IP by adapting meshes to the observed displacements. This generates problem–specific meshes that fit the geometry even at a coarse mesh resolution.

Methods: This work presents a simulation study of the effect of the FEM mesh on the IP of elasticity. For the simulations, a 10x10cm^2 phantom with a 4x4cm^2 inclusion was meshed using 6–node triangular elements. The Young's modulus of the inclusion and the substrate were 20kPa and 10kPa, respectively. The bottom of the phantom was fixed. A sinusoidal axial excitation was applied to the top of the phantom, which was free to slide laterally. The displacements at multiple frequencies (10,20,…,50Hz) were simulated using the FEM on a fine mesh, seen in Figure 1a. The observed displacements were then used to estimate the underlying Young's modulus (E) distribution [1]. A known density of 1g/cm^3 and zero damping were assumed. A technique for adapting meshes to given spatial functions (e.g., strain images) was presented in [2], where vertex positions and their triangulation are optimized such that the difference between an image and its mesh–discretized approximation is minimized. This yields meshes that tend to naturally align the element faces to the image gradients. In this work, this mesh adaptation technique is applied to the meshes for the IP in order to improve elasticity reconstruction. For this purpose, axial strain images, which are simulated using a quasi–static compression in the FP, are used. The mesh adaptation aims to minimize the variance of the axial strain within each mesh element, aligning the mesh with the underlying elasticity distribution and, hence, improving the corresponding IP reconstruction.

Results: Using meshes that accurately delineate the inclusion, a high–quality reconstruction was possible (for example, see Figure 1b). However, the unknown E distribution is not necessarily delineated well by any arbitrary mesh (Figure 1c,g,k), which can yield inaccurate reconstructions (Figure 1d,h,l). When these meshes are aligned to an axial strain image of the phantom using [2], resulting in the meshes shown in Figure 1e,i,m, the corresponding elasticity reconstructions using the IP improve drastically (Figure 1f,j,n). An enhanced reconstruction contrast is observed, in particular at the axial boundaries that were resolved given only the axial strain image for mesh adaptation.

Conclusions: The FEM IP can recover the viscoelastic parameters, but it is limited by the discretization provided by the mesh. Axial strain images are used in this work to condition the meshes for the IP. Other displacement–derived information can also be used to further improve meshes used in the IP.

References:

[1] H Eskandari, SE Salcudean, R Rohling, and J Ohayon: Viscoelastic Characterization of Soft Tissue from Dynamic Finite Element Models. Physics in Medicine and Biology, 53(22), pp. 6569–6590, 2008.
[2] O Goksel, SE Salcudean: Image–Based Variational Meshing. IEEE Transactions in Medical Imaging (in press).

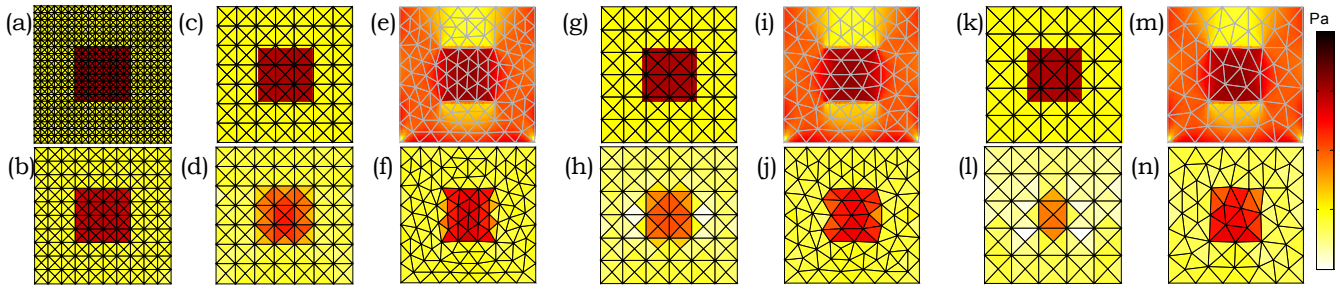

Figure 1: (a) A fine mesh for simulating the FP and (b) a successful Young's modulus reconstruction using the IP with a coarse, inclusion–compliant mesh. (c,g,k) Three other coarser meshes that are not aligned with the inclusion and (d,h,l) their corresponding IPs. (e,i,m) The same three meshes now adapted to the axial strain image, which is here computed from the FP and (f,j,n) the corresponding improved IP reconstructions.

* *indicates Presenter*

038 **ULTRASOUND ELASTICITY IMAGING IN THE DETECTION OF INTESTINAL FIBROSIS AND EDEMA/INFLAMMATION IN RATS AND HUMANS WITH CROHN'S DISEASE.**

J.M. Rubin[1], R.W. Stidham[2], P.D.R. Higgins[2], J. Xu[3], L.A. Johnson[2], M. Zhang[1], D. Moons[4], B. McKenna[4], K. Kim[3,5,6].*

[1]Radiology Department, [2]Internal Medicine Department, [4]Pathology Department, University of Michigan, Ann Arbor, MI 48109, USA; [3]University of Pittsburgh Cardiovascular Institute, [5]Bioengineering Department, [6]The Center for Ultrasound Molecular Imaging and Therapeutics, University of Pittsburgh, Pittsburgh, PA 15261, USA.

Background: Intestinal fibrosis and edema in Crohn's disease result from cycles of inflammation and healing and are rarely identified prior to onset of clinical symptoms. Inflammation and fibrosis can be very difficult to distinguish *in vivo*. They often occur together, but they are treated very differently: inflammation with powerful anti–inflammatory agents; fibrosis with surgery. Hence, methods for distinguishing intestinal fibrosis and inflammation are needed. Ultrasound elasticity imaging (UEI) has been proposed as a potential means of making this distinction [1]. Our previous work has shown that UEI can differentiate fibrotic from normal intestine in rodents using a 2,4,6 trinitrobenzenesulfonic acid (TNBS) enema model that correlates with histopathology in resected intestine from Crohn's patients [1].

Aims: To determine if UEI can differentiate acutely inflamed from chronically fibrotic bowel in our rat model. In addition, to demonstrate that UEI can differentiate between normal and fibrotic bowel in human Crohn's patients.

Methods: Female Lewis rats were exposed to TNBS enemas for 48 hours (acute inflammation, N=5) or weekly x 6 weeks (chronic fibrosis, N=5) vs. phosphate–buffered saline (PBS) enemas for 6 weeks (normal controls, N=3). UEI was performed shortly before intestinal harvest. Ultrasound radiofrequency (rf) data were acquired during controlled deformation of each rat's abdomen using an L10–5 transducer on a Zonare Z–1 scanner (Zonare Ultrasound, Mountain View, CA 94043). Strain estimates were obtained using a 2D correlation–based phase–sensitive speckle tracking algorithm. To account for differences in deforming force, all strain measurements were normalized to the average strain in normal untreated bowel in each image. Resected bowel segments were evaluated with histopathology, real–time polymeraze chain reaction and Western blot for evidence of inflammation and fibrosis. In addition, we studied 4 human subjects with known Crohn's disease within a week prior of surgical resection of involved bowel. The project was approved by the University of Michigan Institutional Review Board, and informed consent was obtained from each subject or his/her parents. A prior computed tomogram or magnetic resonance scan identified the involved loops of bowel in advance of the UEI study. Again, using a Zonare Z–1, rf data were collected during freehand deformations of the abnormal loops along with normal adjacent loops. The transducer used depended on the patient's body habitus. Normalized strain images were then produced in the manner described above. After resection of the bowel, a Young's modulus estimation was performed using a piston elastometer (Artann Laboratories, Inc., Lambertville, NJ 08530).

Results: In the rat model, UEI demonstrated significantly different normalized strains in fibrotic bowel (0.43 ± 0.09, $p<0.001$) and inflamed bowel (0.57 ± 0.11, $p<0.007$) compared to PBS treated bowel (0.84 ± 0.035). Normalized UEI strain ratios of fibrotic and inflammatory bowel UEI strain ratio differences reached statistical significance, $p=0.041$. Histopathologic comparison of normal, inflamed and fibrotic tissue revealed consistent changes in fibrosis and inflammation. Alpha–smooth muscle analysis by western blot analysis also supports this fibrotic and inflammatory animal model. In humans, the results of elasticity imaging strain of normal (-6.10 ± 3.10) and abnormal (-2.60 ± 0.96) bowel significantly differed, $p=0.05$. UEI strains were highly correlated with Young's Modulus estimates in normal (0.80 ± 0.12) and abnormal (2.12 ± 0.53) resected bowel specimens (corr. coef., $r = 0.86$).

Conclusions: Based on these studies, it appears that UEI can distinguish between acutely inflamed and fibrotic bowel in a rat model, and further UEI can distinguish between abnormal fibrotic and normal bowel in human Crohn's patients.

Acknowledgements: NIH R21 DK081123–01A.

References:

[1] Kim K, Johnson LA, Jia C, Joyce JC, Higgins PDR, Rangwalla S, Rubin JM: Non–Invasive Ultrasound Elasticity Imaging (UEI) on Crohn's Disease. UMB, 34, pp. 902–912, 2008.

068 **CONTRAST DIFFERENCES IN ULTRASOUND B–MODE AND STRAIN IMAGES OF BRAIN TUMORS – PRELIMINARY RESULTS**

Tormod Selbekk[1,2], Reidar Brekken[1,2], Ole Solheim[2,3], Geirmund Unsgaard[2,3].*
[1]SINTEF, Trondheim, NORWAY; [2]The Norwegian University of Science and Technology, Trondheim, NORWAY; [3]St. Olav Hospital, Trondheim University Hospital, Trondheim, NORWAY.

Background: Ultrasound is used in brain tumor surgery for anatomical orientation and resection control. Several groups have reported the use of ultrasound strain imaging techniques for imaging brain tumors [1–3]. These initial reports suggest that the elastograms can be used for intraoperative imaging of brain tumors and may serve as a useful adjunct to conventional B–mode images. However, differences in image contrast between strain images and conventional ultrasound have not been previously investigated.

Aims: The study aims to investigate differences in image contrast between ultrasound B–mode and strain images of brain tumors with well–defined borders (meningiomas/metastases) and diffuse infiltrating tumors (low–grade gliomas, WHO grade I, II).

Methods: Ultrasound data have been acquired during surgery of 12 patients with brain tumors diagnosed as meningiomas or metastases (N=4) or as low–grade astrocytomas (N=8). The data were acquired with a Vingmed System 5 scanner (GE Vingmed, Horten, Norway) using a flat linear 10MHz transducer, with the probe held motionless on dura during acquisition. Strain images were generated by a previously published method [4] enabling imaging of strain induced by arterial pulsation. At a user selected depth, the average intensity and strain magnitude (window size approx. 1x1 mm) were calculated and displayed for the whole image width for a selected image frame. The maximum and minimum levels closest to the ultrasound visible tumor border were registered and used for calculation of contrast between normal tissue and tumor tissue for the two image modalities. Contrast is being defined as the difference in amplitude level between the two areas divided by the sum of the amplitude levels. The paired–samples T–test were used for statistical analyses.

Results: Image contrast for regions in tumor tissue and normal tissue were calculated for both B–mode ultrasound and ultrasound strain images (Figure 1). There are no significant differences in contrast between B–mode and strain for meningiomas and metastases, i.e. tumors with well–defined borders (P=0.29). For low–grade astrocytomas, which are diffuse infiltrating tumors, the contrast in the strain images is significantly higher than the contrast in B–mode images (P<0.001).

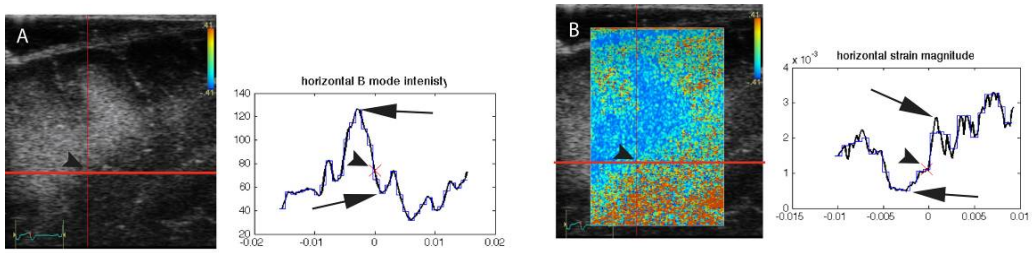

Figure 1:
B–mode intensity in the lateral direction for (A) a given depth and (B) equivalent strain magnitude. Tumor border marked with short arrows, levels used to calculate contrast marked with long arrows.

Conclusions: The observed difference in contrast in the two tumor groups might be related to the difference in pathology and biomechanical properties of brain tissue with diffuse tumor cell infiltration. The results imply that ultrasound strain imaging may have the potential to provide additional information about tissue pathology for diffuse infiltrating tumors compared to conventional B–mode imaging. A limitation of the study is the low number of cases, and work is in progress to include more data.

Acknowledgements: The work has been financed by the National Centre for 3D Ultrasound in Surgery at St. Olavs Hospital, Trondheim, Norway and the independent research foundation SINTEF.

References:

[1] Selbekk T, Brekken R et al.: Tissue Motion and Strain in the Human Brain Assessed by Intraoperative Ultrasound in Glioma Patients. Ultrasound Med Biol, 36 (1), pp. 2–10, 2010.
[2] Scholz M, Lorenz A et al.: Current Status of Intraoperative Real–Time Vibrography in Neurosurgery. Ultraschall Med, 28 (5), pp. 493–497, 2007.
[3] Chakraborty A, Berry G et al.: Intra–Operative Ultrasound Elastography and Registered Magnetic Resonance Imaging of Brain Tumours: A Feasibility Study. Ultrasound, 14 (1), pp. 43–49, 2006.
[4] Selbekk T, Bang J, Unsgaard G: Strain Processing of Intraoperative Ultrasound Images of Brain Tumours: Initial Results. Ultrasound in Medicine & Biology, 31 (1), pp. 45–51, 2005.

* *indicates Presenter*

072 **DOUBLE PUSH ARF ASSESSMENT OF MUSCULAR MECHANICAL PROPERTIES IN A DOG MODEL OF DMD WITH MYOSTATIN VARIATION.**

Mallory R. Scola[1], Joe N. Kornegay[1], and Caterina M. Gallippi[1].*
[1]The University of North Carolina at Chapel Hill, Chapel Hill, NC, USA.

Background: Duchenne muscular dystrophy (DMD) is an X–linked recessive disorder that is caused by a mutation in the gene for dystrophin leading to a loss of the dystrophin protein from the muscle cell membrane. Muscle inflammation, necrosis and fibrosis occur as a result of the dystrophin deficiency leading to severe and progressive loss of muscle mass and function. The golden retriever muscular dystrophy (GRMD) model has a naturally–occurring dystrophin gene mutation and progressive phenotypic features analogous to those seen in DMD. Myostatin, a member of the TGF-β family, is a negative regulator of muscle growth. It has been proposed that reduction or elimination of myostatin could promote muscle growth and indirectly compensate for muscle degradation in DMD.

Aims: This work investigates the use of Double Push ARF for delineating differences in muscle composition caused by a variation in the myostatin gene in the context of a dog model of DMD.

Methods: Imaging was performed *in vivo*, in planes transverse (Tr) and parallel (Par) to muscle fibers, on the rectus femoris (RF) and cranial sartorius (CS) muscles of three golden retriever–whippet cross littermates with the following genotypes: (1) GRMD normal/myostatin normal (control), (2) GRMD/myostatin heterozygote null (Mstn+/-), and (3) GRMD/myostatin normal (Mstn+/+). ARF imaging was performed using a modified Siemens SONOLINE Antares™ imaging system and a VF7–3 transducer (Siemens Medical Solutions USA, Inc. Ultrasound Division). A double excitation (DP ARF) method was employed; with two 300 cycle impulses administered in the same ROE separated by 0.8ms and followed by 4:1 parallel receive tracking [1]. Displacements were compared by calculating marginal peak displacements (MPD), given by $\%MPD = [PD_1 - (PD_2 - D)]/PD_1$ where PD_1 is the peak displacement achieved by the first push, PD_2 is the peak displacement achieved by the second push, and D is the displacement at the time of the second push.

Results: The RF muscle of the control (Tr: 0.82%± 0.10, Par: 0.84%±0.19) experienced higher MPDs than both the GRMD/Mstn+/+ (Tr: 0.74% ± 0.12, Par: 0.81%±0.12; $p<0.02$, paired t–test) and the GRMD/Mstn+/-(Tr: 0.71% ± 0.18, Par: 0.73%±0.08; $p<0.02$). Similarly, the CS muscle of the control (Tr: 0.79%± 0.08, Par: 0.81%±0.07) experienced higher MPDs than the CS of the GRMD/Mstn+/+(Tr: 0.70% ± 0.09, Par: 0.79% ± 0.08; $p<0.02$) and the GRMD/Mstn+/-CS (Tr: 0.76% ± 0.07, Par: 0.80%±0.06; $p<0.02$). Additionally, in the control RF 0.93% and 2.40% of values fell below an empirically derived threshold of 0.7%, in the transverse and parallel planes respectively, while 8.76% and 12.80% of values in the GRMD/Mstn+/+ and 18.88% and 14.97% of values in the GRMD/Mstn+/- were below the threshold. In the CS, 0.84% and 0.05% of values in the control, 10.78% and 4.43% in the GRMD/Mstn+/+, 2.12% and 3.45% of values in the GRMD/Mstn+/- were below the threshold. These values suggest increased stiffness and fibrous deposition in the GRMD/Mstn+/+ and GRMD/Mstn+/- RF and CS and are consistent with increased FS Signal intensity observed in MRI images of the RF and CS of the GRMD/Mstn+/+ and GRMD/Mstn+/- dogs.

Conclusions: This work demonstrates the feasibility of noninvasive DP ARF imaging for monitoring therapy in individuals affected by DMD.

Acknowledgements: This work was supported by 1 U24 NS059696–01A1 (NIH–NINDS/NIAMS), National Center for Canine Models of DMD (NCDMD), Joe N. Kornegay (PI) and Integrated Biomedical Research Training Program.

References:

[1] R.H. Behler, T.C. Nichols, E.P. Merricks, and C.M. Gallippi: Comparison of Multiple Beam Sequences in Arterial ARFI Imaging. 2008 IEEE International Ultrasonics Symposium Proceedings, Beijing, China, pp. 2003–2008, October 2008.

069 **BREAST ELASTOGRAPHY: EXPERIENCE OF 800 CASES.**

E Fleury[1].*
[1]CTC Genese Medicina Diagnóstica, São Paulo/SP, BRAZIL.

Background: Elastography is a noninvasive tool for assessing the rigidity of the lesion, assuming that malignant lesions are more rigid than benign ones [1]. However, it is observed in clinical practice that breast elastography reproduces faithfully the pattern of stiffness of the lesion shown by histology. That is, mucinous and papillary carcinomas tend be displayed as softer on elastography, while schirrous carcinomas tend to be displayed as hard.

Aims: To correlate elastographic studies of breast lesions with the histological results.

Methods: This study compares findings by elastography with results of 834 percutaneous biopsies of breast lesions from 01/01/2009 to 01/01/2010. The elastographic studies were performed using a Sonix SP (Ultrasonix Medical Corporation, Vancouver, Canada) ultrasound system with a 5–14 MHz multifrequency linear probe. For the elastography study, special software was used for the Ultrasonix system, version 2.6. The elastographic classification used a four–point scale according to the color variation during compression and after decompression of the ROI. A score of 1 was assigned to lesions presenting the same color spectrum of the peripheral breast tissue. A score of 2 was assigned to lesions that after decompression presented variation to lighter strains of more than 50% of the mass area when compared to the image acquired during compression. A score of 3 was assigned to lesions presenting color variation of less than 50% of the lesion area (between 10 and 50%) after decompression. Finally, a score of 4 was assigned to the lesions presenting no relevant color variation during compression and after decompression of the parenchyma, appearing blue in both images. Scores 1, 2 and 3 were considered negative and score 4 positive. The lesions were divided according to their histology, as benign or malignant lesions. The malignant lesions were subdivided into soft (i.e. mucinous and papillary carcinomas) and hard (i.e. schirrous carcinoma) [2,3].

Results: The sensitivity, specificity and diagnostic accuracy of elastography were respectively 85.3, 94.0 and 92.1 (151 true positive, 621 true negative, 40 false positive and 26 false negative). Of the 834 breast lesions, 657 (78.8%) were benign lesions and 177 (21.2%) were malignant. Of the 177 malignant lesions, 26 (14.7%) were included in the subgroup of soft lesions (false negative: 8 scored as 2 and 18 as 3). The other 151 were included in the subgroup of hard lesions (true positive). When applied to malignant lesions, the Chi–squared test with type 2x2 contingency tables to determine association between histopathologic results and elastographic scores revealed an association among results with a p–value of less than 0.001. For this calculation, scores of 2 and 3 were considered soft (false negative results) and a score of 4 (true positive results) as hard, while subgroup 1 lesions were hard and subgroup 2 lesions soft. The false–negative results were shown to be more strongly influenced by histological type of lesion than by size or patient age.

Conclusions: This study demonstrates that there is strict correspondence of histological types of breast lesions with the elastographic study.

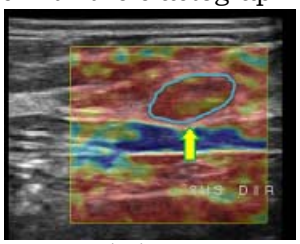

Figure 1: Score 2 lesion on elastography, with soft color on MORE than 50% of the lesion. Histology: typical fibroadenoma.

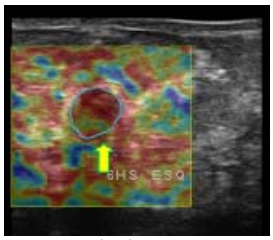

Figure 2: Score 3 lesion on elastography, with soft color on LESS than 50% of the lesion. Histology: phylloid tumor.

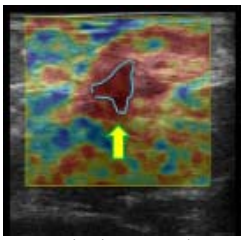

Figure 3: Score 4 lesion on elastography, with hard color on all the lesion. Histology: invasive ductal carcinoma (schirrous carcinoma).

References:

[1] EFC Fleury, D Roveda Jr., JC Fleury, MCA Queiroz, S Piato: Elastrography: Theory into Clinical Practice. Breast J, 15(5), p. 546, Sept 2009.
[2] EFC Fleury, JC Fleury, S Piato, D Roveda Jr.: New Elastographic Classification of Breast Lesions During and after Compression. Diagn Interv Radiol, 15(2), pp. 96–103, Jun 2009.
[3] EFC Fleury, JC Fleury, VM Oliveira, JF Rinaldi, D Roveda Jr.: Proposal for the Systematization of the Elastographic Study of Mammary Lesions through Ultrasound Scan. Rev Assoc Med Bras, 55(2), pp. 192–6, Mar 2009.
[4] EFC Fleury, JF Rinaldi, S Piato, JC Fleury, D Roveda Jr.: Appearance of Breast Masses on Sonoelastography with Special Focus on the Diagnosis of Fibroadenomas. Eur Radiol, 19(6), pp. 1337–46, Jun 2009.

* *indicates Presenter*

026 **DOES THE ELASTOGRAPHY/B–MODE LENGTH RATIO PREDICT BREAST CANCER TUMOR GRADE?**

Richard G. Barr[1], Joseph R. Grajo[2], Cynthia Peterson[1].*
[1]Southwoods Radiology Consultants, 250 DeBartolo Place, Youngstown, OH, USA; [2]University of South Florida, 12901 Bruce B Downs Blvd, MDC 41, Tampa, FL, USA.

Background: The length of breast cancers appears larger on ultrasound elastography than on B–mode imaging with length change ratios of 1.0 to 3.5 [1,2]. We observed that the ratio appeared to correlate with aggressiveness of the tumor.

Aims: To determine if the length change ratio of breast cancers on ultrasound elastography corresponds to tumor grade.

Methods: Elastography (E) was performed on 134 patients undergoing breast biopsy. Compression elastography was performed using a 10 or 13 MHz probe of a Siemens Antares ultrasound machine. Biopsies were performed with a 14 gauge biopsy needle. In patients with a pre–malignant or malignant diagnosis, the pathology reports were reviewed for staging. If the tumor was excised, the grading was based on the surgical specimen. In order to calculate an E/B ratio, the largest dimension of a lesion was measured on the sonogram and mirrored on the elastogram automatically by the US system at the time of clinical examination. The mean E/B–mode ratio of the tumor was calculated for each pathology, categorized by biopsy or surgery. The E/B–mode ratio of the tumor was compared to Scharf–Bloom–Richardson (SBR) grade and intraductal carcinoma grade using Pearson correlation coefficient.

Results: The average patient age was 63.69 years (range 36–95). Mean E/B–mode ratios were calculated for this single–reader study. Ratios varied with pathology: 1.168 with low grade (SD 0.188), DCIS 1.344 (SD 0.353), IDC 1.460 (SD 0.40), lobular 1.506 (SD 0.482) (Table 1). The E/B–mode ratio as compared to the tumor grade in IDC using one–tailed Pearson correlation coefficient ($p < 0.05$) was 0.078. The EI/B–mode ratio as compared to the SBR grade in IDC using one–tailed Pearson correlation coefficient ($p < 0.05$) was significant at 0.040 [3].

Conclusions: The E/B–mode ratio correlated with the aggressiveness of a tumor.

Average E/B Ratio	Pathology	Standard Deviation
1.168	Low grade	0.188
1.344	DCIS	0.353
1.460	IDC	0.40
1.506	Lobular CA	0.482

Table 1: Average E/B Ratios for Varying Tumor Grades

References:

[1] Hall T, Zhu Y, Spalding C: *In Vivo* Real–Time Freehand Palpation Imaging. Ultrasound in Medicine and Biology, Volume 29, pp. 427–435, 2003.
[2] Garra BS, Cespedes EI, Ophir J, Spratt SR, Zuurbier RA, Magnant CM, Pennanen MF.: Elastography of Breast Lesions. Radiology, 202(1), pp. 79–86, 1997.
[3] Barr, Richard G: Elasticity of the Breast: Initial Results. Ultrasound Quarterly, 26(2), pp. 61–66, 2010.

101 **AXIAL–SHEAR STRAIN ELASTOGRAPHY FOR BREAST LESION CLASSIFICATION: INITIAL RESULTS FROM RETROSPECTIVE *IN VIVO* DATA.**

Arun K. Thittai[1], Jose–Miguel Yamal[2], Louise M. Mobbs[3], Christina M. Kraemer–Chant[3], Srinivasa Chekuri[1], Brian S. Garra[3] and Jonathan Ophir[1].*

[1]Diagnostic and Interventional Imaging Department, The University of Texas Medical School, Houston, TX, USA; [2]Biostatistics Division, The University of Texas School of Public Health, Houston, TX, USA;[3]Radiology Department, Fletcher Allen Health Care, Burlington, VT, USA.

Background: The image depicting the axial–shear strain has been referred to as axial–shear strain elastogram (ASSE) [1]. The normalized axial–shear strain area (NASSA) near the inclusion/background boundary has been shown as a feature that can identify the boundary bonding conditions [1]. Results from the initial feasibility study that evaluated the potential of this feature to differentiate between fibroadenomas and malignant tumors in the breast were encouraging [2]. However, the initial feasibility study was restricted to a limited number of *in vivo* cases without a detailed statistical analysis.

Aims: The aim of this work was to investigate the potential of NASSA feature for breast lesion classification into fibroadenomas and cancers. This retrospective study consisted of previously acquired data from sonographic *in vivo* cases, with biopsy results as the reference standard.

Methods: We used previously acquired *in vivo* digital radiofrequency (RF) data of breast lesions that were originally acquired for evaluating standard axial elastograms. This retrospective study had an IRB approval from University of Texas Health Science Center–Houston. A total of 33 biopsy–proven malignant tumors and 30 fibroadenoma cases were included in the study that involved 3 observers blinded to the BIRADS® ultrasound scores. The observers outlined the lesions on the sonograms. The ASSE was automatically segmented and color overlaid on the sonogram, and the NASSA feature from ASSE was computed semi–automatically (see Figure 1). Receiver operating characteristic (ROC) curves were then generated, and the area under the curve (AUC) was calculated for each observer and compared. A logistic regression classifier was built to compare the improvement in the AUC when using BIRADS plus ASSE scores as opposed to BIRADS scores alone.

Results: BIRADS score ROC had an AUC of 0.88 (95% CI = 0.81 – 0.96). In comparison, the average of the AUC for all the three observers using ASSE feature alone was 0.85. However, the AUC increased to 0.96 (average of 3 observers) when BIRADS score and ASSE feature were combined (see Figure 3). The corresponding scatter plot of NASSA vs. BIRADS score is shown in Figure 2.

Conclusions: The results demonstrate that ASSE has the potential to improve the standard BIRADS–based breast lesion classification of fibroadenoma and malignant tumors.

Acknowledgements: Data used in this study were acquired previously for projects supported by NIH Program Project grants P01–CA64597 and P01–EB02105–13. The current work was supported by NIH grant R21–CA135580. The authors would also like to thank the observers Elaine Khalil, MD, Karen Ophir, BS, RDMS and Rhoda Reading, BS, RDMS, RVT, RT, who volunteered their time to participate in the study.

References:

[1] Thitai Kumar A, Krouskop TA, Garra BS and Ophir J: Visualization of Bonding at an Inclusion Boundary using Axial-Shear Strain Elastography: A Feasibility Study. Phys. Med and Biol., 52, pp. 2615–2633, 2007.

[2] Thitai Kumar A, Mobbs LM, Kraemer–Chant CM, Garra BS and Ophir J. Breast Tumor Classification using Axial Shear Strain Elastography: A Feasibility Study. Phys. Med. Biol., 53, pp. 4809–4823, 2008.

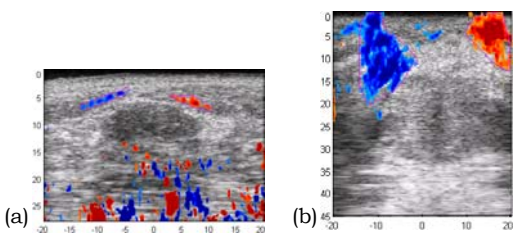

Figure 1: Examples showing the axial–shear strain region of interest as a color–overlay on top of corresponding sonogram of (a) fibroadenoma and (b) cancer. Notice that the axial–shear strain area (outlined for convenience) due to the cancer were bulkier compared to the slim ones due to the fibroadenoma.

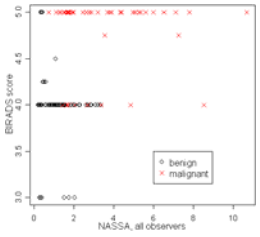

Figure 2: Scatter plot of BIRADS vs. NASSA scores. Note that the combination of both axes gives better separation of fibroadenoma (o) and cancer (x) compared to any one axis.

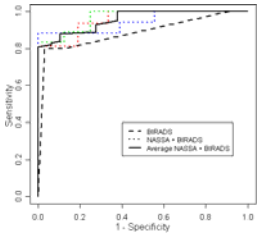

Figure 3: ROC Curves of the logistic regression model scores, using predictors NASSA + BIRADS for the three observers, compared to BIRADS alone.

* *indicates Presenter*

063 **BREAST FAT: SHEAR-WAVE ELASTICITY MEASUREMENTS.**

D Cosgrove[1], R Hooley[2], E Mendelson[3], L Barke[4], A Cossi[5], B Cavanaugh[6], L Larsen[7].*
[1]Imperial College, Hammersmith Hospital, London, England, UK; [2]Yale Medical Center, Yale, CT, USA; [3]Northwestern Medical Center, Chicago, IL, USA; [4]Sally Jobe Breast Center, Denver, CO, USA; [5]Boston Medical Center, Boston, MA, USA; [6]Thomas Jefferson University, Philadelphia, PA; USA, [7]University of Southern California, Los Angeles, CA, USA.

Background: The fatty tissue of the breast is commonly used as a reference for assessing relative strain, but its normal variation has not been documented.

Aims: To measure the elasticity of breast fat using shear wave elastography (SWE) in women of different ages.

Methods: SWE was performed on 1000 women in the multicenter BE1 study of breast masses; measurements of the subcutaneous fat adjacent to the lesion in kPa were made using SWE on a prototype of the Aixplorer system (Supersonic Imagine, Aix–en–Provence, France). The values were compared with the patients' age and with the type of pathology (benign or malignant).

Results: The mean age of the patients was 52.1 (SD ±14.8, range 21.2–95.3). The mean elasticity value was 14.0kPa (SD ±10.3, range 0.03–122.7). The mean values ranked against the patients' age by decade were: 20–30: 11.6; 30–40: 12.1; 40–50: 14; 50–60: 14.3; 60–70: 15.5; 70–80: 14.2; >80: 17kPa. Fat in the patients with benign masses had a mean elasticity of 13.1kPa while in the malignant group, the mean value was 15.6kPa.

Conclusions: This is the first quantitative assessment of the stiffness of breast fatty tissue. The elasticity varied little with age or pathology, supporting the use of fat stiffness as a comparator.

Acknowledgements: The BE1 Collaborative Group study was sponsored by Supersonic Imagine and comprised centers in the USA and Europe. Their support and participation is gratefully acknowledged.

References:

[1] Tanter M, Bercoff J, Athanasiou A, Deffieux T, Gennisson JL, Montaldo G, Muller M, Tardivon A and Fink M: Quantitative Assessment of Breast Lesion Viscoelasticity: Initial Clinical Results using Supersonic Shear Imaging. Ultrasound Med Biol, 34(9), pp. 1373–86, 2008.

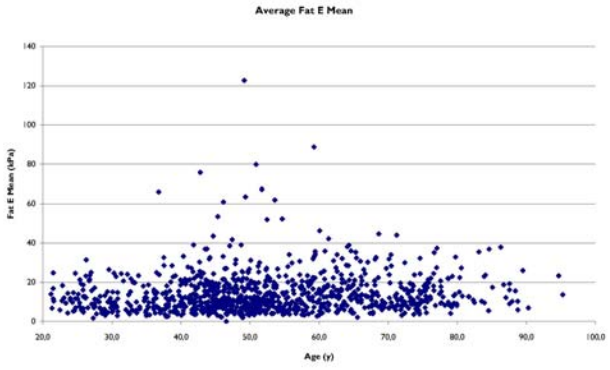

Figure 1: Scatterplot of mean SWE values of breast fat in kPa versus patient age.

106 **STRAIN ESTIMATION USING KALMAN FILTER: SIMULATION AND CLINICAL RESULTS FOR MONITORING ABLATIVE THERAPY.**

H Rivaz[1], U Hamper[2], M Choti[2], GD Hager[1], EM Boctor[1].*
[1]Johns Hopkins University, Baltimore, MD, USA; [2]Johns Hopkins Medical Institutes, Baltimore, MD, USA.

Introduction: In this abstract, we first introduce a method to calculate strain images from displacement images using Kalman filter. We show the results of the method on simulated data. We also show the results of the analytic minimization (AM) method (another work submitted to this conference) with the Kalman filtering strain estimation on ablation monitoring in patient trials. The strain estimation technique along with the radiofrequency (RF) data of the patient trials can be downloaded from http://www.cs.jhu.edu/~rivaz/UltrasoundElastography/.

Aims: (1) Develop a method for strain estimation from displacement which reduces the noise and retains the sharp boundaries. (2) Use elastography in clinical trials of monitoring ablative therapy of liver cancer.

Methods: Strain estimation requires spatial derivation of the displacement field. Since differentiation amplifies the signal noise, least squares regression techniques are commonly used to obtain the strain field. Adjacent A–lines are usually processed independently in strain calculation. However, the strain value of each pixel is not independent from the strain value of its neighboring pixels. The only exception is the boundary of two tissue types with different mechanical properties where the strain field is discontinuous. We use the prior of piecewise strain continuity via a Kalman filter to improve the quality of strain estimation. Let $z_{i,j}$ be the noisy strain estimate (obtained by least squares regression of the displacement image). Let the ground truth strain value be $\varepsilon_{i,j}$. Let $r_{i,j}$ be the Gaussian process noise and $s_{i,j}$ be the Gaussian measurement noise to be removed. We have $\varepsilon_{i,j} = \varepsilon_{i,j-1} + r_{i,j}$ (model) and $z_{i,j} = \varepsilon_{i,j} + s_{i,j}$ (measurement) [1]. Let $\hat{\epsilon}^{-}_{i,j}$ (note the super minus) and $\hat{\epsilon}_{i,j}$ be respectively *a priori* and *a posteriori* strain estimates at step *j*, and let their variances be respectively p^{-} and p. The time update equations will be [1] $\hat{\epsilon}^{-}_{i,j} = \hat{\epsilon}_{i,j-1}$ and $p^{-}_{i,j} = p_{i,j-1} + \sigma^2_r$ where σ^2_r is the variance of the process noise r. The measurement update equations will be

$$\hat{\epsilon}_{i,j} = \hat{\epsilon}^{-}_{i,j} + \frac{p^{-}_{i,j}}{p^{-}_{i,j} + \sigma^2_s}(z_{i,j} - \hat{\epsilon}^{-}_{i,j}) \qquad p_{i,j} = (1 - \frac{p^{-}_{i,j}}{p^{-}_{i,j} + \sigma^2_s})p^{-}_{i,j}$$

and where σ^2_r is the variance of the measurement noise s [1,2].

Results: Simulation results are shown in Figure 1. Results of 1 patient trial (out of 7) are shown in Figure 2.

Conclusions: The proposed strain estimation technique produces smooth images that preserve sharpness across boundaries. The strain estimation method works in real time.

References:

[1] G. Welch and G. Bishop: An Introduction to the Kalman Filter. UNC TR 95–041, pp. 1–16, 1995.
[2] Rivaz H, Boctor E, Choti M, Hager G: Real–Time Regularized Elastography. IEEE Trans. Med. Imaging (in press).

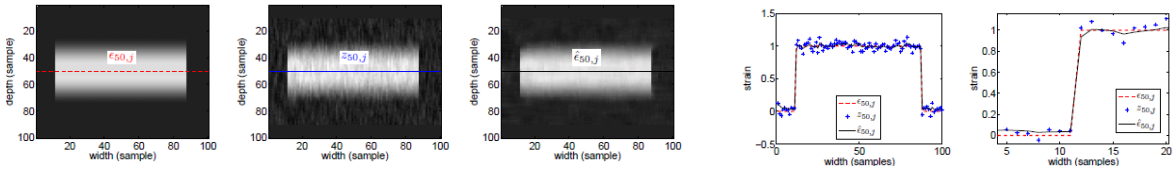

(a) Ground Truth Strain (b) Strain without KF (c) Strain with KF (d) Strain Estimate (e) Strain Estimates

Figure 1: Simulation results. KF refers to Kalman filter. The ground truth ε (a) is not known. In (b), the strain estimate z is obtained by linear regression (i.e. least squares differentiation). In (c), noisy estimates of image (b) are used to generate a smooth strain image.

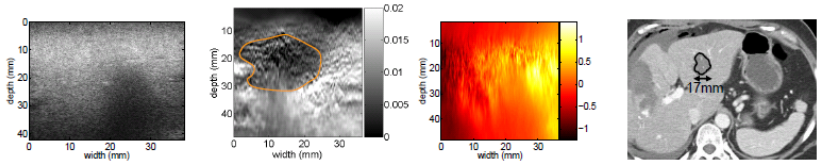

(a) B–Mode Patient 1 (b) Axial Strain (c) Lateral Displacement (d) CT Patient 1

Figure 2: First patient trial of monitoring RF ablation using ultrasound elastography. The delineated lesion in the intra–operative strain image corresponds to the CT image which is obtained two weeks after the surgery.

* *indicates Presenter*

070 **PROSTATE ELASTOGRAPHY: INITIAL EXPERIENCE AND CLINICAL PERSPECTIVE.**

E Fleury[1]*.

[1]CTC Genese Medicina Diagnóstica, São Paulo/SP, BRAZIL.

Background: The diagnosis of prostate cancer is challenging when a patient has an increase in PSA [1]. Currently, the option is in these cases for diagnosis is the sextant biopsy of the prostate and, in cases of re–biopsy, the saturation biopsy. However, in our practice, we have not found significant variation in the diagnosis of cancer by increasing the number of cores per biopsy. As prostate cancer usually does not present as a true mass on ultrasound, we believe that it may be difficult to introduce the elastography as an auxiliary tool in the clinical diagnosis. Currently, it seems there is no consensus on the usefulness of elastography as an auxiliary method to ultrasound for diagnosis of prostate cancer [2].

Aims: To demonstrate the initial results of prostate elastography and its clinical applicability.

Methods: This study compares 2 groups: Group 1 (25 patients) without elastographic study and Group 2 (25 patients) with elastographic study in the period from 01/07/2009 to 01/01/2010. All patients had transrectal sextant biopsies (12 samples). The elastographic studies were performed using a Sonix SP (Ultrasonix Medical Corporation, Vancouver, Canada) US system with a 5–9 MHz multifrequency endocavitary probe. For the elastography study, special software was used for the Ultrasonix system, version 3.0.2 (Beta1), upgraded to the commercial version 2.6. We used a two point score for elastographic classification, where 1 corresponds to soft lesions and 2 to rigid lesions based on color variation. The lesions were divided according to their histology as benign or malignant [3,4].

Results: Results showed 16 (32%) malignant lesions: 8 malignant lesions in Group 1 (1 appeared as a mass on B–mode) and 8 malignant lesions in Group 2 (2 appeared as a mass on B–mode). Of the malignant lesions seen on the elastographic study, 2 appear as a hard mass, 1 as diffuse hard tissue on the right lobe and the other 5 as false negative results. All false positive results corresponded to areas of greater rigidity in the peripheral zone of prostate, the location where the cancers usually appear. Adenomatous masses and cysts (7 lesions) were correctly classified as soft. There was no statistically significant difference between the two groups in the diagnosis of prostate cancer ($p<0001$). The sensitivity, specificity and diagnostic accuracy of elastography were respectively 37.5, 70.5 and 60.0 (3 true positive, 12 true negative, 5 false positive and 5 false negative).

Conclusions: This initial study demonstrates that elastography has limited application in the clinical diagnosis of prostate cancer due to low sensitivity and specificity. We think it has potential use to guide prostate biopsies to regions where there is more rigid tissue, reducing the number of cores and the consequent morbidity from saturation biopsy, without impairing its sensitivity.

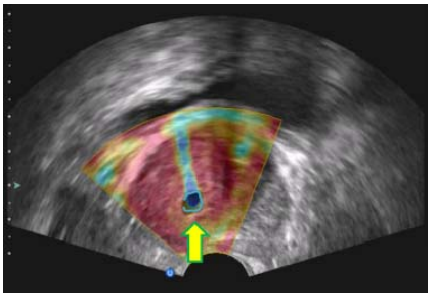

Figure 1: Small anechoic mass on the right lobe appears as soft on the elastogram, compatible with cyst, Confirmed on biopsy.

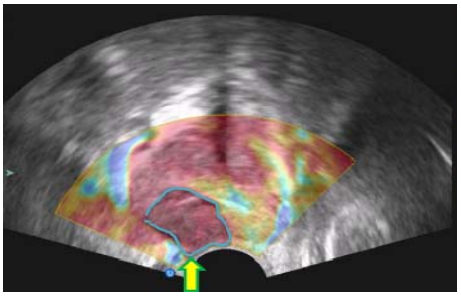

Figure 2: A mass on the right lobe of the prostate appears as hard on the elastogram. Confirmed as an adenocarinoma by histology.

References:

[1] NB Delongchamps, GP Haas: Saturation Biopsies for Prostate Cancer: Current Uses and future Prospects. Nat Rev Urol, 6(12), pp. 645–52, Dec 2009.

[2] DT Ginat, SV Destounis, RG Barr, B Castaneda, JG Strang, DJ Rubens: US Elastography of Breast and Prostate Lesions. Radiographics, 29(7), pp. 2007–16, Nov 2009.

[3] EFC Fleury, JC Fleury, S Piato, D Roveda Jr.: New Elastographic Classification of Breast Lesions During and After Compression. Diagn Interv Radiol, 15(2), pp. 96–103, Jun 2009.

[4] EFC Fleury, JC Fleury, VM Oliveira, JF Rinaldi, D Roveda Jr.: Proposal for the Systematization of the Elastographic a Study of Mammary Lesions through Ultrasound Scan. Rev Assoc Med Bras, 55(2), pp. 192–6, Mar 2009.

087 **PROSTATE MECHANICAL IMAGING: CLINICAL RESULTS.**

V Egorov[1], N Sarvazyan[1], RE Weiss[2], M Ankem[2], JW Slaton[3], LA Mynderse[4], PR Sieber[5], MD Efros[6], M Patel[1], AP Sarvazyan[1].*

[1]Artann Laboratories, 1459 Lower Ferry Rd, Trenton, NJ 08618, USA; [2]The Division of Urology, Robert Wood Johnson Medical School/University of Medicine and Dentistry of New Jersey, New Brunswick, NJ 08901, USA; [3]Minneapolis VA Medical Center, One Veterans Dr, Minneapolis, MN 55417, USA; [4]Department of Urology, Mayo Clinic, Rochester, MN 55905, USA; [5]Urological Associates of Lancaster, 2106 Harrisburg Pike, Lancaster, PA 17601, USA; [6]Accumed Research Associates, 1305 Franklin Avenue, Garden City, NY 11530, USA.

Background: Mechanical imaging [1] yields tissue elasticity map and provides quantitative characterization of a detected pathology. The changes in surface stress patterns as a function of applied load provide information about the elastic composition and geometry of the underlying tissue structures [2]. In an earlier clinical study with 168 patients, we have evaluated the PMI capability in prostate visualization and assessment of prostate size and nodularity. In 84% of the cases, the PMI device was able to reconstruct 2D/3D images of the prostate [3].

Aims: The objective of this study was the clinical assessment of the imaging capability, evaluation of safety and ease of use of novel Prostate Mechanical Imager (PMI) in multi–site clinical study.

Methods: The PMI shown in Figure 1 is an electronic palpation device that includes a probe with two pressure sensor arrays, motion tracking system and an electronic unit providing data acquisition from the pressure sensors and communication with a touch–screen computer. It visualizes real time 2D pressure patterns from the prostate surface and provides integration of the pressure patterns into 3D prostate elasticity image (Figure 2). This clinical study was performed at five clinical sites where the PMI device was used by five urologists. The study population included adult males with digital rectal examination (DRE) detected abnormalities and scheduled TRUS–guided biopsy or prostatectomy.

Figure 1: Prostate Mechanical Imager.

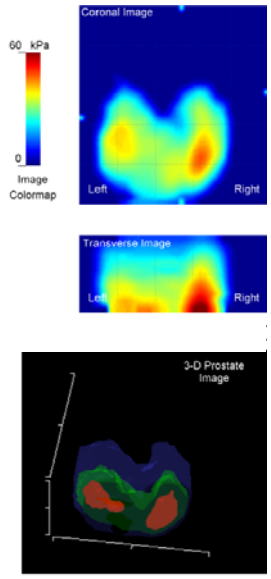

Blue Surface Level: 15kPa
Green Surface Level: 30kPa
Red Surface Level: 45kPa

Figure 2: PMI 2D and 3D Elasticity Images of the Prostate.

Results: There were 56 patients with the average age of 65, ranging from 43–80 years, and with the average PSA score of 4.7, ranging from 0.25–16.2. Based on the independent readers' review of the PMI images, the PMI provided prostate image in 55 of the 56 examined patients, and, for all of those cases, the PMI visualized the prostate abnormality. There was agreement between DRE and PMI in determinations regarding the presence of an abnormality in 89% of the studied cases. No safety concerns or side effects associated with the PMI examination procedure were found in any of the five sites. All participating investigators rated the PMI as reasonably easy to use.

Conclusions: This multi–site clinical study has demonstrated the capability of this novel PMI technique to produce elasticity images of prostate in 98% of examined patients. The PMI has demonstrated th e capability to be used as an aid in visualizing and documenting abnormalities of the prostate that were initially identified by DRE.

Acknowledgements: The work was supported by the National Cancer Institute, grant R44CA082620.

References:

[1] A Sarvazyan:. Mechanical Imaging: A New Technology for Medical Diagnostics. Int. J. Med. Inf., 49, pp. 195–216, 1998.
[2] V Egorov, S Ayrapetyan, A Sarvazyan: Prostate Mechanical Imaging: 3–D Image Composition and Feature Calculations. IEEE Trans. Medical Imaging, 25(10), pp. 1329–1340, 2006.
[3] R Weiss, V Egorov, S Ayrapetyan, N Sarvazyan, A Sarvazyan: Prostate Mechanical Imaging: A New Method For Prostate Assessment. Urology, 71(3), pp. 425–429, 2008.

* *indicates Presenter*

056 **DETECTION OF LAYERS OF ALIGNED COLLAGEN IN HUMAN CERVICAL TISSUE USING ULTRASOUND.**

Lisa M. Reusch[1], Janelle Anderson[1], Lindsey Carlson[1], Carolyn Pehlke[2], Mark A. Kliewer[3], Josephine Harter[4], Jeremy J. Dahl[5], Mark L. Palmeri[5], Kevin Eliceiri[2], Helen Feltovich[1,6], Timothy J. Hall[1].*
[1]Medical Physics, [2]Laboratory for Optical and Computational Instrumentation, [3]Radiology, [4]Pathology Departments, University of Wisconsin–Madison, Madison WI, USA; [5]Biomedical Engineering, Duke University, Durham, NC, USA; [6]Maternal Fetal Medicine, Intermountain Healthcare, Park City, UT, USA.

Background: Spontaneous preterm birth rates have not changed in a century despite extensive research [1]. Collagen alignment in the cervix contributes to cervical strength and undergoes rearrangement long before gross changes (shortening, softening) can be seen, thus understanding cervical microstructure is paramount to understanding cervical dysfunction [2,3]. A quantitative assessment of these changes in women has been challenging due to a lack of noninvasive technology sophisticated enough to interrogate the microstructure of the cervix.

Aims: Our goal is to develop quantitative ultrasound techniques to reliably assess collagen alignment, as shown in Figure 1. We acquired quantitative ultrasound (QUS) and acoustic radiation force impulse (ARFI) data from human cervical tissue to measure backscatter properties and shear sound speeds. We corroborated our ultrasound findings with multiphoton optical microscopy and curvelet transform analysis (CTA) to quantify the collagen alignment.

Methods: Hysterectomy specimens were scanned with a Siemens Acuson S2000 ultrasound machine using a prototype intracavity transducer (Siemens Medical Solutions USA, Malvern, PA, USA). Radio frequency (RF) data were acquired with the endocervical canal parallel to the transducer face. Transmit and receive angles were changed through electronic control to assess anisotropic acoustic propagation. ARFI measurements were collected at steering angles of 0º, ±20º and ±40º, and displacements were estimated using a cross–correlation method. Shear sound speeds are estimated from the time–to–peak values. Backscattered data were collected for steering angles between $\pm$40º. Power spectra were computed for each angle in selected regions of interest. Data from a phantom with spherical scatterers were used for system calibration. Lastly, the tissue was sectioned with a vibrotome for second harmonic generation (SHG) imaging. Semi–automatic stitching of the images created a comprehensive image. Distinct collagen layers were delineated both with visual inspection and with CTA.

Results: For positive steering angles, power spectra of the backscattered RF signals from the cervix were higher at normal incidence (beams perpendicular to tissue) than beams steered to large angles. Backscattered power from both the control phantom and cervix decreased with increasing steering angle. The difference in power was larger from the cervix, which is consistent with scattering from an aligned structure (e.g. collagen). At negative steering angles, the power spectra are similar to that at normal incidence. We attribute this to an aligned structure, which is angled with respect to the transducer. Additionally, both ARFI imaging and shear wave measurements show clear evidence of layers of differing alignment consistent with the backscatter results. SHG and CTA identified regions of interest consistent with both visual assessment of collagen alignment and ultrasound results.

Conclusions: We show QUS and ARFI results that are consistent with CTA of SHG images of the cervix. Ongoing studies aim to quantify collagen alignment as it changes throughout pregnancy as early detection of microstructural changes may open pathways to novel interventions for preterm delivery.

Acknowledgements: NIH R21HD061896.

References:

[1] C. Y. Spong: Obstetrics and Gynecology, Vol. 110, pp. 405–415, 2007.
[2] D. Parry: Biophys Chem, Vol. 29, pp. 195–209, 1988.
[3] M. Mahendroo, et al.: Mol Endocrinol, Vol. 13, pp. 981–992, 1999.

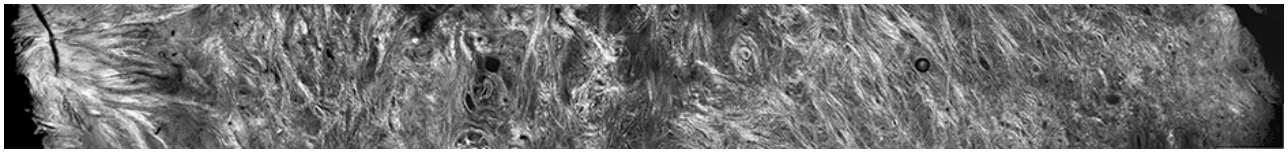

Figure 1: We detect the alignment of collagen within layers in this SHG image of cervix using ultrasound. The cervical canal is on the right and the ectocervix (outer edge) is on the left.

060 **ELASTICITY RECONSTRUCTION WITH DUAL TRANSDUCER MOTION TRACKING.**

JM Abeysekera[1], A Baghani[1], H Eskandari[1], R Rohling[1].*
[1]University of British Columbia, Vancouver, BC, CANADA.

Background: High quality motion estimation is critical to the inverse problem of solving for tissue elasticity. It is desirable to obtain motion estimates in more than one dimension to reduce the amount of assumptions needed to solve the inversion problem. Motion estimation in ultrasound is highly accurate along the beam axis; however, estimation accuracy suffers in other directions due to an order of magnitude difference in the sample spacing. Orienting two transducers orthogonally and into the same scan plane (dual transducer method) has been proposed for providing improved 2D motion estimates by using the estimate along the beam axis of each transducer [1]. While improved motion estimation has been demonstrated, the impact of the technique for reconstructing elasticity has not yet been explored.

Aims: In this work, elasticity images are obtained from motion tracking estimates using the dual transducer technique.

Methods: We created a model of a 3D block (5x5x5cm^3) with a spherical inclusion (1cm diameter) and used ANSYS FEA software to determine the displacement field for a 100Hz harmonic excitation. The displacements were applied to randomly distributed scatterers (40 per mm^3) at eight evenly spaced time steps covering one period of excitation. Radiofrequency (RF) data were acquired using Field II© with a simulated linear array transducer (L14–5, f = 7.2MHz, pitch = 0.3048mm). Three motion estimation techniques were applied to evaluate the performance of the proposed technique; 2D tracking, 2D tracking with angular compounding and 2D tracking with dual transducers.

Results: Multiple reconstruction approaches were applied to solve for elasticity values. Inversion using dynamic finite elements accurately found the location of the inclusion for both the FEA and dual transducer motions, but not for 2D tracking and 2D tracking with angular compounding (Figure 1b–e). Comparing the FEA and dual transducer results shows CNR_e values of 60.1dB and 51.2dB, respectively. Another technique based on the equations of motion and using FIR filters to reconstruct elasticity was able to more accurately solve Young's modulus values; however it contained significantly more artifacts, obscuring the inclusion. For the FIR filter method, the CNR_e values for the FEA, 2D tracking, angular compounding, dual transducer motion data were found to be 9.73dB, 4.59dB, 19.96dB and 32.69dB, respectively.

Conclusions: Quantitative estimation of Young's modulus values using dual transducer motion estimation has been studied in this work. The proposed method shows promise for accurately reconstructing elasticity values using different inversion techniques.

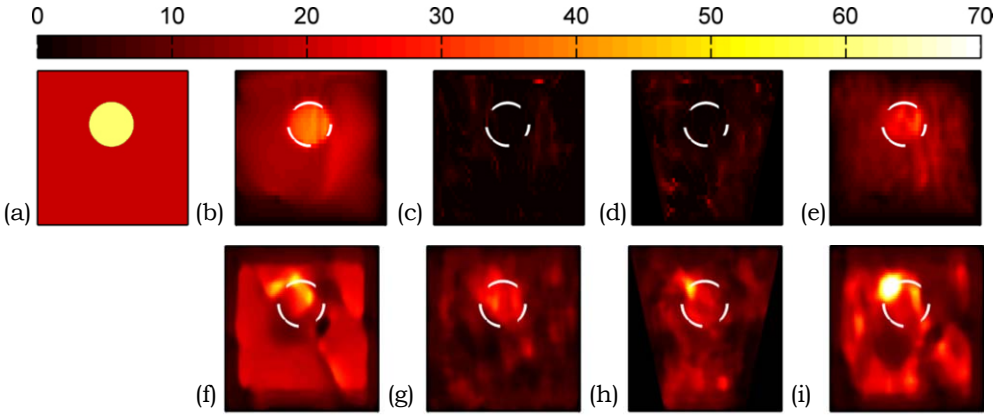

Figure 1: The true (a) Young's modulus distribution (kPa) and the reconstructed distributions using finite elements (b–e) and FIR filters (f–i). The columns represent reconstruction from different motion data: (left–to–right) ANSYS FEA, 2D tracking, angular compounding and dual transducer. The true location of the inclusion boundary is shown in white.

Acknowledgements: This research was supported by NSERC.

References:

[1] Abeysekera JM, Rohling R: Improved 2D Motion Tracking for Elastography using Dual Transducers. Proc. of 8th ITEC, p. 77, 2009.

* *indicates Presenter*

066 **FREQUENCY DOMAIN EXTRACTION OF VISCOELASTIC PROPERTIES USING ACOUSTIC RADIATION FORCE.**

Samuel M. Frew[1], Ali Baghani[1], Hani Eskandari[1], Reza Zahiri Azar[1], Septimiu E. Salcudean[1].*
[1]University of British Columbia, Vancouver, BC, CANADA.

Background: The acoustic radiation force (ARF) of focused ultrasound provides a way of displacing a viscoelastic medium at internal, localized positions. Together with the ability of ultrasound to monitor the displacement, it gives a method for recovering the local viscoelastic parameters. This has application in the diagnosis of various medical conditions, including cancers and organ fibrosis.

Aims: This work aims to demonstrate the feasibility of a new frequency–domain method to recover the elasticity, viscosity, and power–law parameters of gelatin media from ARF-induced displacements.

Methods: The parameter inversion approach uses a force–displacement transfer function obtained from the relaxation response of the medium to an ARF push. Relaxation of axial displacement is monitored at the focal depth of the push. Assuming the relaxation corresponds to the negative step response of a linear system, a frequency–domain transfer function is computed. In this study, a parametric mass–spring–damper model is fitted to the transfer function over a range of frequencies with the goal of obtaining a relative elasticity and frequency–dependent relative viscosity. We expect the frequency dependency to be due to a reported power–law relationship, $\eta = \eta_c \omega^n$, where η is viscosity, η_c is the consistency index, ω is angular frequency and n is the flow index [1]. A SonixMDP ultrasound platform (Ultrasonix Medical Corp., Richmond, Canada) was used to apply an ARF sequence to three homogenous phantoms (A, B and C) with different gelatin concentrations (1.5, 2.0 and 2.5wt%, respectively). The sequence consisted of a 5ms pushing period followed by a 30ms relaxation–tracking period. The sequence was repeated five times to analyze the consistency of the results. For each phantom, the relative elasticity was extracted from the low frequency asymptote of the transfer function and compared with values predicted by an empirical formula in the literature relating elasticity to gelatin concentration [2]. Relative viscosity and the flow index were obtained using the transfer function and the proposed models.

Results: The results are depicted in Figure 1. The transfer functions and the derived parameters were consistent over repeated experiments. The relative elasticity values increased with gelatin concentration, and closely matched predicted results (Figure 1c), with a maximum error of 2.9%. The relative viscosity values were consistent over the five sequences at frequencies from approximately 100–300Hz. Overall values increased with gelatin concentration. The elasticity has a greater dependency than viscosity on gelatin concentration, as expected for the low gelatin concentrations used here [1]. For all phantoms, relative viscosity decreased with frequency over 100–300Hz, as expected from the reported power–law relationship (Figure 1d). Fitting the power–law to the averaged experimental data over 100–300Hz gave flow indices of -0.36, -0.11 and -0.20 for phantoms A, B and C, respectively.

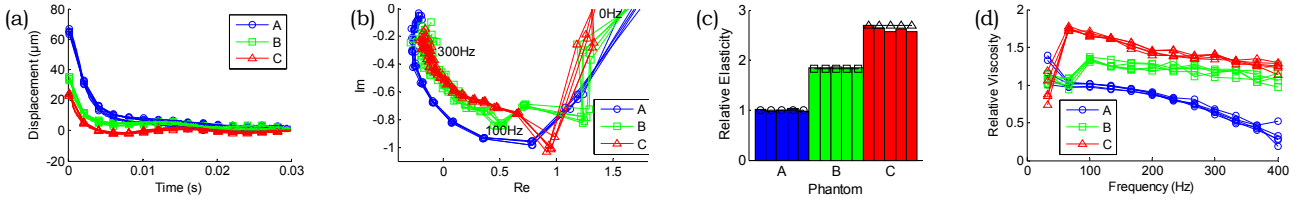

Figure 1: Results for phantoms A–C over the five sequence repetitions: (a) relaxation responses; (b) Nyquist plots of the transfer functions, with each normalized by the absolute value of the 100Hz component; (c) relative elasticity, with empirically predicted values indicated by the black marked lines; (d) relative viscosity versus frequency.

Conclusions: The extracted relative elasticity values gave a close match to empirical predictions. The relative viscosity values were consistent over multiple trials and showed the expected decrease with frequency due to the power–law. Both result sets exhibit good contrast between phantoms. The results show the feasibility of this frequency–domain method of recovering viscoelastic parameters from an ARF–generated tissue response and indicate it has potential for tissue classification applications. Further work is required to apply the method to more complex phantoms and assess its limitations.

Acknowledgements: This work was funded by NSERC.

References:

[1] H. Eskandari, S.E. Salcudean, and R. Rohling: Viscoelastic Parameter Estimation Based on Spectral Analysis," IEEE Trans. Ultrason., Ferroelect., Freq. Contr., Vol. 55, No. 7, pp. 1611–1625, July 2008.
[2] T.J. Hall, M. Bilgen, M.F. Insana and T.A. Krouskop: Phantom Materials for Elastography. IEEE Trans. Ultrason., Ferroelect., Freq. Contr., Vol. 44, No.6, pp. 1355–1365, November 1997.

073 **CORTICAL ELASTICITY MEASUREMENT DURING ULTRASOUND–GUIDED KIDNEY BIOPSY: AN *EX–VIVO* STUDY.**

Grant H. Kruger[1,2], Jonathan M. Rubin[3,4], Dae Woo Park[3,5], Ashish Hinger[3], James Hamilton[6], Paul Gottschalk[6] and William F. Weitzel[3].*

[1]Mechanical Engineering, [2]Anesthesiology, [3]Internal Medicine, [4]Radiology, and [5]Biomedical Engineering Departments, University of Michigan, Ann Arbor, Michigan, USA; [6]Epsilon Imaging, Inc., Ann Arbor, Michigan, USA.

Background: Percutaneous biopsy is performed in many areas of medicine, including kidney and liver diseases, to obtain important diagnostic information that would otherwise not be available. An estimated 50,000 renal biopsies are performed annually in the United States alone, of which 1–2% result in serious complications. Ultrasound imaging is commonly used to guide this procedure. We describe a method and results to non–invasively determine tissue shear modulus by measuring the propagation velocity of a shear wave (S–wave) induced through tissue excitation by the biopsy needle. Shear modulus may also be determined using acoustic radiation force imaging (ARFI) methods. However, this information is already accessible at the time of biopsy since the needle induces an S–wave, which can be monitored using traditional ultrasound hardware. The biopsy induced S–wave amplitude may also be several orders of magnitude greater than ARFI, thereby improving signal–to–noise ratio. Thus, in addition to the histology sample, clinicians may gather diagnostic information from tissue surrounding the biopsy site.

Aims: Determine the shear modulus of renal cortical tissue by measuring the propagation velocity of a biopsy needle initiated S–wave using ultrasound imaging.

Methods: High frame rate ultrasound imaging (>200 Hz) of bovine kidney during biopsy was performed using a 128 element 7 MHz linear array. The 2s recording buffer was manually frozen immediately after the biopsy device was fired. Regions of interest (ROIs) were placed at known locations along the S–wave path. A correlation–based, phase–sensitive speckle–tracking algorithm automatically measured tissue displacement perpendicular (along the ultrasound beam) to the direction of S–wave propagation at these ROIs. The location of the peak cross–correlation between the ROI signals provided a measure of the propagation delay, and, hence, the wave velocity could be determined. Tissue specimens (3mm dia. x 5mm) were tested on a micro–elastometer to compare to the ultrasound results.

Results: Figure 2 shows a) B–mode image including ROIs (biopsy needle entry vertical on right side of image) and b) instantaneous longitudinal tissue velocity image corresponding to B–model image (lighter/red indicate higher velocities away from the transducer). The S–wave propagation is from right to left. Figure 2(c) shows the temporal plot of tissue velocity recorded at the ROIs. A velocity of 2.19 m/s was measured with a standard deviation of ±0.39m/s as the ROIs were moved over the scan area. Assuming a tissue density of 1g/cm^3, these velocities relate to a shear modulus of 15 ± 6kPa. We are currently validating these results using a micro–elastometer.

Conclusions: Encouraging results supporting the feasibility of *in–vivo* renal cortical elasticity measurements using ultrasound scans taken during biopsy were obtained. Additionally, the ground work for future experiments was developed to assess the accuracy of this method. The technique offers the potential for additional diagnostic information of a larger volume of kidney tissue than the histological sample without significant hardware or procedural modifications.

Acknowledgements: Epsilon Imaging (Ann Arbor, MI, USA) for the use of their ultrasound machine and analysis software, as well as Artann Laboratories, Inc. (Lambertville, NJ, USA) for the use of their micro–elastometer. This work was supported in part by NIH grant DK 62848.

Figure 1

Figure 2

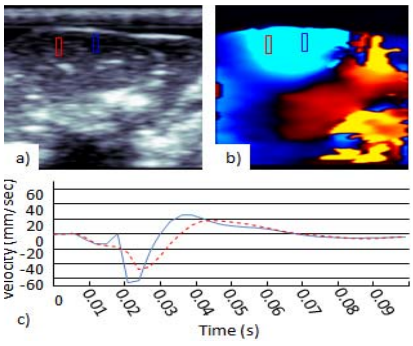

* *indicates Presenter*

078 **HIGH FRAME RATE 2D WAVE IMAGING ON CONVENTIONAL ULTRASOUND USING SECTOR SUBDIVISION, DELAY COMPENSATION, AND ANGULAR COMPOUNDING.**

R. Zahiri Azar[1,2], A. Baghani[2], S.E. Sacludean[2], R. Rohling[2].*
[1]Ultrasonix Medical Corporation, Richmond, CANADA; [2]University of British Columbia, Vancouver, CANADA.

Background: High frame rate motion estimation has proven to be critical for studying the propagation of mechanical waves in tissue [1]. Conventional ultrasound systems are based on line by line acquisition of the echo signals, introducing a fundamental trade off between the acquisition rate and the number of scan lines in the imaging plane. With a trade off of long acquisition time or additional hardware overhead, techniques such as synchronization [2,3], multi–line acquisition [4] and ultrafast imaging [1] have been used to increase the imaging frame rate.

Aim: To develop a system based on conventional ultrasound that images both axial and lateral components of periodic tissue motion at high frame rate (>1000Hz) in a short acquisition time (<1 sec).

Methods: A custom pulse sequencer has been developed to accomplish this task. The sequencer acquires the radiofrequency (RF) signals from the tissue while it is being vibrated continuously with a periodic mechanical exciter. To increase the acquisition rate, the sequencer divides the imaging area into several smaller areas, herein referred to as sectors, each containing a few scan lines. Each sector is acquired multiple times at a high rate before moving on to the next sector until all the sectors are acquired. To reconstruct the 2D motion vectors, the sequencer acquires RF signals from the region of interest using multiple steering angles. Following the data acquisition, 1D motion along the beam direction is estimated from these acquired RF signals for all steering angles. To eliminate the acquisition delays introduced in the sequencer, the intra– and inter–sector delays in displacement data are compensated in the frequency domain for the frequency of interest (i.e. excitation frequency) using a recently introduced phase correction algorithm [5]. 2D motion vectors are then reconstructed from these delay compensated 1D motion, each estimated along different beam directions. Finally, by assuming incompressibility, modulus images are estimated from these 2D motion vectors using least squares inversion of the governing wave equation in 2D.

Results: To quantitatively study the performance of the system, experiments were performed on a commercial elasticity phantom (Model 049, CIRS Inc., VA, USA) with spherical soft and hard inclusions. The phantom was excited at 200Hz using an external mechanical exciter mounted on top of it and imaged using the proposed system implemented on a SonixRP ultrasound machine (Ultrasonix Medical Corp., Richmond, Canada). In the sequencer, the total number of scan lines was set at 128, the sector size was set at 8 (128/8=16 sectors), the number of observations for each sector was set at 20, the number of steering angles was set at two (±10 degrees), and the acquisition depth was set at 5cm, for a pulse repetition frequency of 10kHz. This resulted in an acquisition rate of 1250Hz (10,000/8) and total acquisition time of 128×20×2×0.1ms = 512ms (≈ overall refresh rate of 2 modulus images per second). Once the RF data were acquired, they were processed as mentioned above to reconstruct the high frame rate motion vectors and modulus images. At the frame rate of 1250Hz, the phantom Young's moduli of 29kPa, 6kPa, and 54kPa for the background, the soft inclusion and the hard inclusion were imaged and estimated to be 30kPa, 11kPa, and 53kPa, respectively.

Conclusions: For a periodic excitation, the proposed system estimates 2D motion vectors and elasticity images without the need for synchronization or specialized hardware. Therefore, it provides a similar functionality to that offered by ultrafast scanners, at the expense of a lower frame rate and a higher sensitivity to motion artifacts. While the total acquisition time is increased, it is still kept within the range suitable for real time applications, with achieved rates of 2 to 5 modulus images per second.

References:

[1] M. Tanter, J. Bercoff, L. Sandrin, and M. Fink: Ultrafast Compound Imaging for 2D Motion Vector Estimation: Application to Transient Elastography. IEEE Trans. Ultrason., Ferr., Freq. Control, 49, pp. 1363–1374, 2002.
[2] A. Hadj Henni, C. Schmitt, and G. Cloutier: Three–Dimensional Transient and Harmonic Shear–Wave Scattering by a Soft Cylinder for Dynamic Vascular Elastography. Journal of the Acoustical Society of America, 124, pp. 2394–2405, 2008.
[3] S. Wang, W. Lee, J. Provost, L. Jianwen, and E. Konofagou: A Composite High–Frame–Rate System for Clinical Cardiovascular Imaging. IEEE Trans. Ultrason., Ferr., Freq. Control, 55, pp. 2221–2233, 2008.
[4] J. Dahl, G. Pinton, M. Palmeri, V. Agrawal, K. Nightingale, and G. Trahey: A Parallel Tracking Method for Acoustic Radiation Force Impulse Imaging. IEEE Trans. Ultrason., Ferr., Freq. Control, 54, pp. 301–312, 2007.
[5] A. Baghani, A. Brant, S. Salcudean, R. Rohling: A High Frame Rate Ultrasound System for the Study of Tissue Motions," IEEE Trans. Ultrason., Ferr., Freq. Control, (in press).

098 ***IN VIVO* FREQUENCY DEPENDENT SHEAR VISCOELASTIC PROPERTIES OF THE BRAIN IN NORMAL PRESSURE HYDROCEPHALUS.**

K Lin[1], JR McLaughlin[1], KJ Streitberger[2], E Weiner[2], J Hoffmann[2,3], FB Freimann[4], D Klatt[2], J Braun[2], C Sprung[4], R Klingebiel[2,5], I Sack[2].*

[1]Rensselaer Polytechnic Institute, Troy, NY, USA; [2]University Medicine Berlin, Berlin, GERMANY; [3]University of California San Francisco, San Francisco, CA, USA; [4]University Berlin, Berlin, GERMANY; [5]Neuroradiology and Radiology Insitute, Klinik im Park, Zürich, Switzerland.

Background: Normal Pressure Hydrocephalus (NPH) is a neurological disorder characterized by the abnormal enlargement of ventricles with a triad of clinical symptoms including gait disorder, dementia and urinary incontinence. Current treatment options including shunt operations can lead to a transient improvement of the clinical symptoms by draining cerebrospinal fluid (CSF) from the brain. However, a reduction or even a complete recovery of the ventricular size is often not achieved [1]. To understand the underlying mechanism that transmits relatively small CSF pressure peaks into a significant, irreversible ventricular enlargement, it is vital to obtain accurate estimation of altered biomechanical tissue properties of brain.

Aims: The goal here is to investigate the frequency dependence of the shear viscoelastic properties of the brain for NPH patients and healthy volunteers by using an enhanced magnetic resonance elastography (MRE) technique with multifrequency vibrations [2]. We aim to: (1) recover frequency dependent complex shear moduli of brain parenchyma; (2) provide accurate estimation of the shear viscoelasticity by deriving two phenomenological constants, α and μ, from a fractional element model; (3) establish a consistent pattern of the viscoelastic shear moduli between healthy persons and patients in the periventricular region and the rest of brain parenchyma.

Methods: Twenty NPH patients and twenty–-five healthy volunteers with comparable age and gender characteristics were included in the study. Measurements were performed on a standard 1.5T clinical MRI scanner (Sonata, Siemens, Erlangen, Germany). Mechanical vibrations were induced into the head by a custom–made head cradle connected via carbon–fiber piston to a remote vibration of 25, 37.5, 50 and 62.5Hz. Single out of image plane phase difference data acquisition was performed by a single–shot echo–planar motion encoding imaging sequence and the frequency dependent complex shear modulus is reconstructed from the phase difference data using the linear algebraic inversion together with a two dimensional L^1 phase unwrapping algorithm [3]. The two parameters, α and μ, from the fractional element model are then determined by a least square fit over the averaged value of the estimates of the frequency dependent complex shear modulus. The periventricular area was segmented from the brain parenchyma by a filter of 6 pixels around the ventricles, and the averaged value of complex shear modulus is computed and compared inside and outside the periventricular area.

Results: Significant decrease of cerebral viscoelasticity is observed by a reduction of α and μ in patients with NPH compared to healthy volunteers. All measured complex shear moduli were significantly decreased in patients by both real and imaginary parts. Also, there is a consistent increase of moduli with the increase of frequencies, and shear viscoelasticity is lower in the periventricular area than the rest of brain parenchyma.

Conclusions: Our study is the first to assess alternations of viscoelastic properties of brain tissue in NPH. Our reconstructions of complex shear moduli and viscoelastic parameters from the fraction element model clearly show that NPH is associated with a decrease in elasticity and thus an increase of brain tissue compliance. Multifrequency MRE is able to reveal details about the micro–mechanical connectivity of biological tissue in addition to stiffness estimation. Further studies are required to translate these initial findings into a valid model of the mechanism of disease progression in NPH.

Acknowledgements: We acknowledge NIH, ONR and German Research Foundation (Sa/901–3) for partial support of this work. This work was performed at the Inverse Problem Center at Rensselaer Polytechnic Institute and University Medicine Berlin, Campus Charité Mitte.

References:

[1] C Sprung, C Miethke, HG Schlosser, M Brock: The Enigma of Underdrainage in Shunting with Hhydrostatic Valves and Possible Solutions. Acta Neurochir Supple 95, pp. 229–235, 2005.

[2] D Klatt, et al.: Noninvasive Assessment of the Rheological Behavior of Human Internal Organs using Multifrequency MR Elastography: A Study of Brain and Liver Viscoelasticity. Phys Med Biol, 52, pp. 7281–7294, 2007.

[3] K Lin, J McLaughlin, A Thomas, K Parker, B Castaneda and D Rubens: Two–Dimensional Shear Wave Speed and Crawling Wave Speed Recoveries from *In Vitro* Prostate Data. JASA (submitted), 2010.

* *indicates Presenter*

047 **A NOVEL INSTRUMENT FOR THE VISCOELASTIC SPECTROSCOPY OF BIOMATERIALS AND TISSUE MIMICKING MATERIALS FROM 10 TO 1000 HZ.**

Cédric Schmitt[1], Anis Hadj Henni[1], Marie–Élise Tremblay[2], Mélina Hamdine[2], Marie–Claude Heuzey[2], Pierre J. Carreau[2], Guy Cloutier[1].*

[1]Laboratory of Biorheology and Medical Ultrasonics, University of Montréal Hospital Research Center (CRCHUM), Montréal, Québec, CANADA; [2]Center for Applied Research on Polymers and Composites, École Polytechnique, Montréal, Québec, CANADA.

Background: Materials mimicking biological tissue mechanical properties are intensively used to validate and improve emerging multimodality imaging techniques, which couple anatomical information (MRI, ultrasound, etc.) with elastic or viscoelastic mapping (i.e., quasi–static and dynamic elastography). Most of the proposed elastography methods apply a dynamic stress to the probed medium at frequencies typically up to 1500 Hz. However, commercial rheological instruments dedicated to measuring mechanical parameters are limited to frequencies below 200 Hz. Thus, there is a need for instruments allowing viscoelasticity measurement in a broad–band frequency range to evaluate the sensitivity and robustness of elastography imaging techniques.

Aim: Our objective was, on one hand, to introduce a novel instrument, Rheospectris, capable of measuring the complex shear modulus of biomaterials and soft tissue materials from 10 to 1000 Hz, and, on the other hand, to validate the new instrument by comparison with a commercial rheometer.

Methods: The basic principle of Rheospectris (Rheolution Inc., QC, Canada) consists of applying a transient vibration to a material sample contained in a cylindrical tube and in measuring its dynamical response. The spectral material viscoelasticity (G' and G'') is then determined from the measured sample vibrations. For validation purposes, we characterized the complex shear modulus of silicon rubber and PVA cryogel using rheometry with a Physica MCR 501 instrument (Anton Paar GmbH, Austria), between 0.1 Hz and 100 Hz and with the new Rheospectris device from 10 Hz to 1000 Hz. Statistical analyses of variance (ANOVA) were performed on storage (G') and loss (G'') moduli obtained with both instruments in the common frequency range from 10 Hz to 100 Hz.

Results: As seen in Figure 1, G' values, obtained with both instruments, are in very good agreement within the 10–100 Hz common frequency range (silicon: p = 0.399, PVA cryogel: p = 0.880) whereas poorer agreement was found for G'' (silicon: p < 0.001, PVA cryogel: p = 0.304). G' and G'' evolution given by Rheospectris over two frequency decades exhibit a stronger material viscoelastic dispersion for silicon samples compared to PVA cryogel samples. This frequency dependence, not always clearly visible from standard rheometry data (e.g., low–frequency rheometry data shown on Figure 1b), needs to be taken into consideration to understand the shear wave velocity evolution as a function of frequency in dynamic elastography techniques. Similar results as shown in Figure 1 were obtained for PVC and chitosane (not shown).

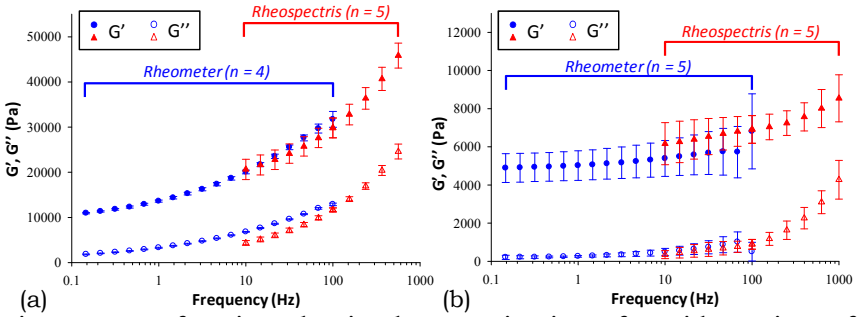

Figure 1: Storage (G') and loss (G'') moduli as a function of frequency for (a) silicon and (b) PVA cryogel samples measured using a standard rheometer and with the Rheospectris instrument. See: www.rheolution.com

Conclusions: Rheospectris is a valuable instrument for viscoelastic characterization of a wide variety of tissue mimicking materials and biomaterials currently used in elastography imaging studies. The Rheospectris instrument, contrary to rheometry devices due to technological limitations, has access to wideband complex shear moduli commonly explored in dynamic elastography.

Acknowledgment: Funding was received by a grant from the Canadian Institutes of Health Research (#MOP–84358).

* *indicates Presenter*

067 **FURTHER CHARACTERISATION OF CHANGES IN AXIAL STRAIN ELASTOGRAMS DUE TO THE PRESENCE OF SLIPPERY TUMOR BOUNDARIES. PART I: SIMULATION STUDY.**

Leo Garcia[1], Jérémie Fromageau[1], Jeffrey C. Bamber[1], Chris Uff[1].*
[1]Joint Department of Physics, Institute of Cancer Research, 15 Cotswold Road, Sutton, Surrey, SM2 5NG, England, UK.

Background: Whether a tumor is firmly attached to, or free to slip against, surrounding tissue can affect its appearance in axial and axial shear elastograms [1–4]. For example, mobile tumors are surrounded by a halo of slip–induced high strain, show changes in strain contrast with their shape and orientation [5,6] and have characteristic distributions of shear strain [7]. Exploiting these differences could aid diagnosis because some benign tumors, such as fibroadenoma in the breast, are loosely bonded and slip upon palpation. Real time detection and characterization of slippery boundaries may also aid tumor resection, where knowledge of potential planes of cleavage is useful.

Aims: We wish to further understand the effect of lesion mobility on elastograms. Here, we consider changes in axial strain only, for the case of a symmetrical model undergoing uniaxial compression, studied by characterizing changes in tumor contrast transfer efficiency (CTE) and strain contrast between the slip–induced strain contrast, both as a function of Young's modulus contrast.

Methods: Finite element analysis (FEA) was used to simulate two plane–strain tumor models, one that is equivalent to a cylindrical inclusion bonded to its surroundings and another that is free to slip with no friction. CTE values were calculated using element-based strain directly from FEA, so as to exclude slip–induced strain at the boundary. CTE is defined as the ratio (in decibels) of the mean lesion to background strain contrast to the equivalent lesion to background Young's modulus contrast [8]. Strain was also calculated by applying a gradient estimator to nodal displacements to obtain a more "realistic" elastogram with a strain halo around the mobile lesion. Mean strain values within an annulus centered on the inclusion boundary, of width equal to half the strain estimator length, were used to estimate annulus contrast, defined as $(\varepsilon_{annulus}-\varepsilon_{background})/\varepsilon_{background}$, where ε is mean absolute axial strain. We hypothesize that high positive contrast between this annulus region and the background indicates lesion mobility.

Results: Figure 1 shows CTE curves obtained from element–based strain for the two model types. The slip model has positive CTE for the case where the inclusion and the background moduli are equal, indicating image tumor contrast in the absence of stiffness contrast. In general, as described previously, mobile inclusions appear stiffer than their adhered equivalents. Note that there is a point where the "slippery" curve crosses CTE = 0 dB, i.e. where the strain contrast closely matches the Young's modulus contrast. Figure 2 shows the variation in boundary annulus contrast with inclusion stiffness. For the slip model, annulus contrast is always positive and greater than the adhered case. It increases with inclusion modulus and remains approximately constant with applied strain (not shown here).

Conclusions: The presence of a slippery tumor boundary introduces two mechanisms for generating strain contrast that are additional to that due to any modulus contrast: slip–induced strain at the inclusion boundary and deformation strain within the inclusion. Experimental study of these phenomena is presented in an accompanying abstract.

Acknowledgements: This work was supported by the Engineering and Physical Sciences Research Council, UK.

References:

[1] Maciejko et al.: Proc. of ITEC, p. 91, 2003.
[2] Krouskop et al.: Proc. of ITEC p. 120, 2004.
[3] Konofagou et al.: Ultrasonics, 38, pp. 400–404; 2000.
[4] Garcia et al.: Proc. IEEE Ultrasonics Symposium, 2010.
[5] Thitai Kumar, Ophir: Ultrasound Med. and Biol., 33(9), pp. 1463–1467, 2007.
[6] Galaz et al.: Proc. of ITEC, p. 99, 2009.
[7] Thitai Kumar et al.: Physics Med. and Biol., 52, pp. 2615–2633, 2007.
[8] Ponnekanti et al.: Ultrasound Med. and Biol., 21(4), pp. 533–543, 1995.

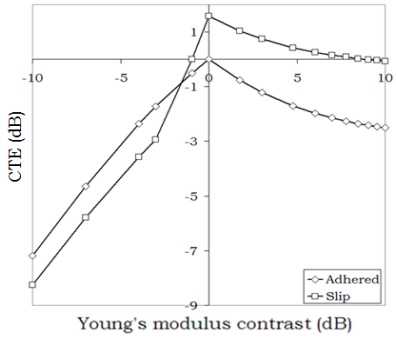

Figure 1: Contrast transfer efficiency curves for adhered and mobile inclusions.

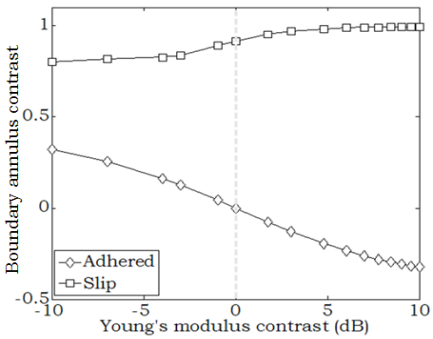

Figure 2: Variations in boundary annulus contrast with increasing inclusion Young's modulus.

* *indicates Presenter*

081 **FURTHER CHARACTERISATION OF CHANGES IN AXIAL STRAIN ELASTOGRAMS DUE TO THE PRESENCE OF SLIPPERY TUMOR BOUNDARIES. PART II: EXPERIMENTAL VERIFICATION.**

Chris Uff[1], Leo Garcia[1], Jérémie Fromageau[1], Jeffrey C. Bamber[1].*
[1]Joint Department of Physics, Institute of Cancer Research, 15 Cotswold Road, Sutton, Surrey, SM2 5NG, England, UK.

Background: Tumor mobility has implications in both diagnosis (as in breast cancer) and in surgical planning (as in neurosurgery). It has been established in Finite Element Analysis (FEA) models that a slippery boundary can affect the appearance of both normal axial strain [1] and axial shear strain [2] elastograms, but experimental data are lacking. We have presented FEA of axial strain data for slippery vs. adhered inclusions in a companion paper and here we present the experimental results.

Aims: Experimental verification of FEA studies as a precursor to translation into clinical practice.

Methods: Cuboidal gelatine phantoms with a cylindrical inclusion of differing gelatine concentrations (by weight) were manufactured, and the Young's modulus (YM) derived from stress–strain curves measured on an Instron mechanical testing device (Table 1). Bonded and slippery (water lubricated) inclusions were made for each YM contrast (C_Y). Ultrasound elastography data were acquired with a DIASUS scanner (Dynamic Imaging Ltd, UK) and a 6–12MHz linear array transducer within a mechanical 3D probe, in conjunction with Stradwin 3.8 (Cambridge University, UK) ultrasound elastography acquisition software. The transducer was connected to an Instron compression device. 1N pre–compression was applied to ensure good acoustic contact, followed by incremental compressions of 0.5% strain to generate 10 single–step elastograms. The mean strain values were calculated over regions of interest (ROI) within the inclusion (a circular ROI) and the background (an annular ROI) and the halo of high strain at the boundary of the slippery inclusions (an annular ROI). CTE was calculated as $\eta = |C_{strain}(dB)| - |C_Y(dB)|$ [3].

Results: Our slippery phantoms did not exhibit uniform slip over the whole compression cycle: the pre–compression invariably started slip, but halo contrast, inclusion strain and background strain varied locally as the compression increased, consistent with adherence occurring at points on the inclusion boundary (Figure 1). CTE curves (Figure 2), which are regarded as preliminary at present, agree in some respects with FEA studies in that the slip curve lies (on average) below the adhered curve for soft inclusions (indicating false stiffness), crosses it to become positive at zero YM contrast and stays above it for hard inclusions (also indicating false stiffness). For both types of stiff inclusion the loss of CTE with increasing modulus contrast was greater than expected, which currently remains unexplained.

% Gel Background	% Gel Inclusion	YM Contrast (dB)
8	14	4.27
8	12	2.68
8	10	1.08
14	14	0
14	12	-1.59
14	10	-3.19
14	8	-4.29

Table 1: Young's modulus of gelatine

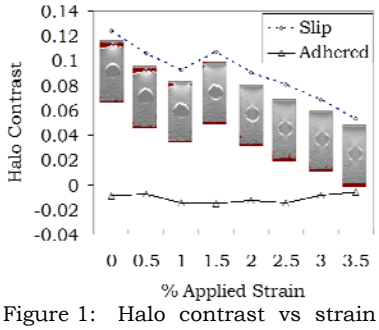

Figure 1: Halo contrast vs strain demonstrating slip–stick behaviour.

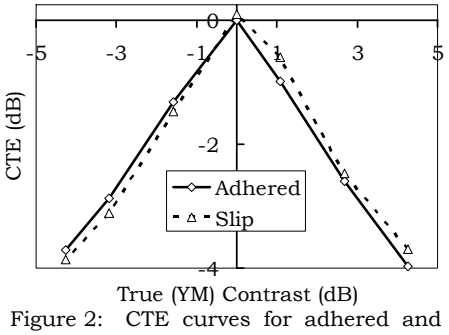

Figure 2: CTE curves for adhered and slippery inclusions.

Conclusions: The stiffening effect of a slippery boundary on both soft and hard inclusions has been observed in a phantom experiment. The difference demonstrated is, however, less than that shown by FEA, and, if these results are correct, in the clinical setting, this phenomenon is unlikely to contribute to erroneous interpretation of axial strain contrast with respect to stiffness contrast. Localized adherence on the other hand produces changes in halo, lesion and background strain patterns that may be clinically helpful. Future work may be directed towards development of phantoms that exhibit more uniform slip.

Acknowledgements: Work supported by the Engineering and Physical Sciences Research Council, UK.

References:

[1] Thitai Kumar and Ophir: Ultrasound Med. and Biol., 33(9), pp. 1463–1467, 2007.
[2] Thitai Kumar et al.: Physics Med. and Biol., 52, pp. 2615–2633, 2007.
[3] Ponnekanti et al.: Ultrasound Med. and Biol., 21(4), pp. 533–543, 1995.

* *indicates Presenter*

082 **MEASURING THE YOUNG'S MODULUS OF HUMAN BRAIN *IN VIVO* WITH REAL TIME SHEAR WAVE ELASTOGRAPHY.**

Chris Uff[1], Jeffrey C. Bamber[1], Neil L Dorward[2].*
[1]Joint Department of Physics, Institute of Cancer Research, 15 Cotswold Road, Sutton, Surrey, SM2 5NG, London, England, UK; [2]Neurosurgery Department, Royal Free Hospital, Pond St, London, NW3 2NQ, England, UK.

Background: The human brain is organised into cortex and subcortical areas. The cortex comprises a 1–2mm layer of grey matter (cell bodies) with underlying white matter (axons). The subcortical areas also have grey and white matter, the grey matter organised into large nuclei and the white matter tracts highly compacted. Previous attempts to measure the Young's modulus (YM) of human brain have resulted in values differing by more than a factor of ten (3–35kPa) [1], with a predominance of cadaver studies using a variety of methods. The few studies that differentiate between grey and white matter used subcortical regions of interest (ROIs) and found white matter to have a higher YM than grey. Shear wave elastography allows real time YM measurement *in vivo* with small ROIs.

Aims: To measure YM of human brain *in vivo* to differentiate cortical grey and white matter.

Methods: 4 patients were scanned during surgery to resect brain tumors. During the scans, areas of normal brain adjacent to the pathological areas were scanned with a SuperSonic Imagine Aixplorer™ scanner using the shear wave elastography (SWE) function. Measurements of YM were made in ROIs identified as grey and white matter from the B–mode sonograms using the Aixplorer's *Q-box* function (Figure 1).

Results: The mean Young's modulus of cortical grey matter was 31.2kPa compared to 16.3kPa for white matter (Figure 2). Identification of the different regions of the cortex was possible in high resolution sonograms.

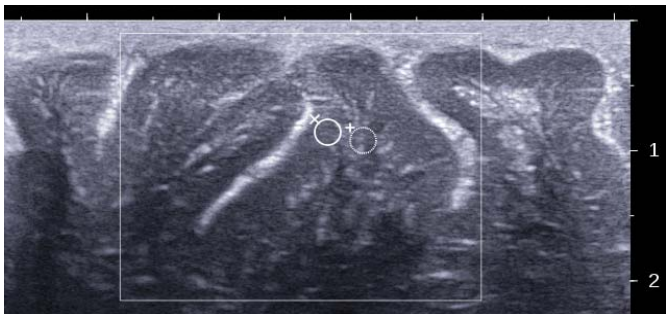

Figure 1: B–mode scan of normal brain with cortical grey (×) and white (+) matter ROIs selected.

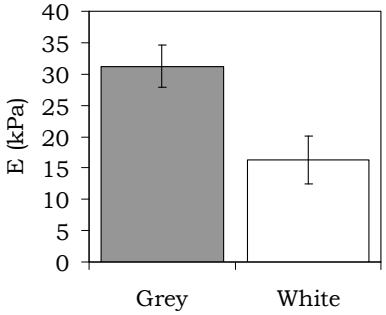

Figure 2: Grey and White matter YM measurements

Conclusions: In contrast to previous studies, we found grey matter to be stiffer than white matter. The differences between the structure of the cortex compared to the sub–cortical regions may explain this difference. It is now becoming apparent that YM varies significantly between different types of tissue in different areas of the brain; selection of appropriately small ROIs is necessary. YM anisotropy in white matter has recently been demonstrated *in vivo* in the rat [2], and future work may be directed towards developing methods of ultrasonic imaging of white matter tracts for neurosurgical intra–operative guidance.

Acknowledgements: The Aixplorer scanner was kindly loaned to the group by SuperSonic Imagine UK Ltd. This work was supported by the Engineering and Physical Sciences Research Council, UK. Ethical approval was obtained from the The National Hospital for Neurology and Neurosurgery & Institute of Neurology Joint Regional Ethics Committee (Ref: 08/H0716/92). Research and development (R&D) approval and sponsorship were obtained from the Royal Free Hospital Clinical R&D Department (Ref 7745).

References:

[1] Kruse S, Rose G: Magnetic Resonance Elastography of the Brain. Neuroimage, 39, pp. 231–237, 2008.
[2] Macé E, Cohen I: 3D *In Vivo* Brain Elasticity Mapping in Small Animals using Ultrasound. IEEE International Ultrasonics Symposium Proceedings, pp. 471–474, 2009.

* *indicates Presenter*

095 **CAN MRI ACCURATELY MEASURE TRANSIENT DISPLACEMENT WAVEFORMS? A COMPARISON WITH ULTRAFAST ULTRASOUND IMAGING.**

Rémi Souchon[1], Jean–Luc Gennisson [2], Mickaël Tanter [2], Jean–Yves Chapelon [1], Olivier Rouvière [1,3].*
[1] INSERM, U556, Lyon, FRANCE; [2] Institut Langevin–Ondes et Images, ESPCI ParisTech, CNRS UMR7587, INSERM U979, Paris, FRANCE; [3] Hospices Civils de Lyon, Lyon, FRANCE.

Background: Magnetic resonance acoustic radiation force imaging (MR–ARFI) [1] measures the peak displacement induced by an ultrasound pulse. The technique is based on the assumption that the focus is stationary during the encoding gradients. However, this hypothesis may or may not be valid depending on the time needed to reach equilibrium. A measurement of the displacement waveforms [2] may overcome this limitation. However, the ability of motion–sensitive MR sequences to accurately measure such waveforms remains to be established.

Aims: To compare transient displacement waveforms measured with MRI and those measured with an ultrafast ultrasound scanner.

Methods: Transient displacements were induced in liver samples *ex vivo* using the radiation force of a focused ultrasound transducer (2.4MHz, f#1.3, push duration 2ms), and the waveforms were measured using a motion–sensitive MR sequence [2]. The push experiment was repeated and monitored using an ultrafast ultrasound scanner (Aixplorer, Supersonic Imagine, France). The peak amplitude and the time constants of the displacement waveforms were compared.

Results: Figures 1, 2 and 3 respectively show the displacement waveforms for ultrafast ultrasound, MRI processed by deconvolution, and MRI processed with a model-based (minimization) approach. Quantitative measurements are summarized in Table 1.

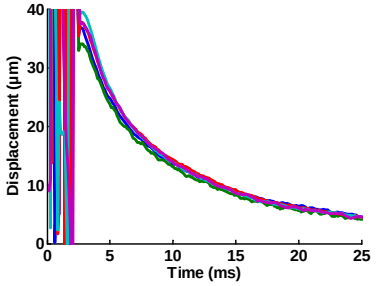

Figure 1: Displacement (Ultrafast US)

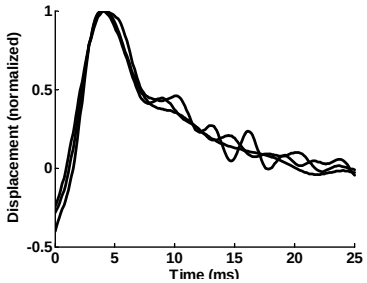

Figure 2: Displacement (MRI + deconvolution)

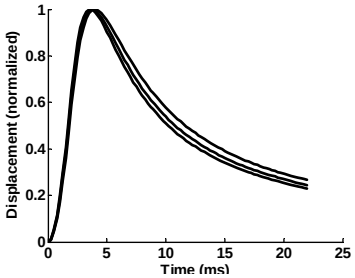

Figure 3: Displacement (MRI + model)

	Peak displacement (µm)	Time constant of decay (ms)
Ultrafast US (*N*=1)	33 – 38	5.7 – 6.7
MRI + Deconvolution (*N*=3)	26 – 40	2.6 – 3.2
MRI + Model (*N*=3)	31 – 47	8.8 – 10.2

Table 1: Summary of measurements (min–max)

Conclusions: Reasonable agreement was found between both modalities. However quantitative measurement of relaxation times appears challenging in MRI.

References:

[1] McDannold N, Maier SE: Magnetic Resonance Acoustic Radiation Force Imaging. Med Phys, 35(8), pp. 3748–3758, 2008.
[2] Souchon R et al.: Estimation of Displacement Waveforms with Transient MR Elastography. Proc 8th ITEC, 2009.

079 **A GPU–BASED–TIME CONSTANT ESTIMATOR FOR REAL–TIME ELASTOGRAPHY APPLICATIONS.**

Sanjay P. Nair[1], Xu Yang[1], Thomas A. Krouskop[2], Raffaella Righetti[1].*
[1]Electrical and Computer Engineering Department, Texas A&M University, College Station, TX, USA; [2]National Institute for Human Performance, Houston, TX, USA.

Background: New elastographic techniques such as poroelastography and viscoelasticity imaging aim at imaging the temporal mechanical behavior of tissues [1]. These techniques usually involve the use of curve fitting methods as applied to noisy strain data to estimate new elastographic parameters [2]. As of today, however, current elastographic implementations of these novel imaging methods are generally too slow and not optimized for clinical applications. Additionally, image quality performance of these new elastographic imaging techniques is still largely unknown.

Aims: The purpose of this study is to propose a new elastographic time constant (TC) estimator, which allows simultaneously imaging multiple TC elastographic parameters in real–time and with high accuracy and sensitivity.

Methods: We implemented a well studied algorithm that, to our knowledge, is new to elastographic TC estimation, which is based on the use of the Least Square Error (LSE) curve–fitting method and the Levenberg–Marquardt (LM) optimization rule as applied to noisy elastographic data. The LM algorithm is an optimization technique which is perfectly suited for solving LSE problems [3]. The algorithm is executed on a massively parallel General Purpose Graphics Processing Unit (GPGPU) to achieve real–time performance.

The performance of the new estimator is analyzed using simulations and quantified in terms of accuracy, precision, sensitivity, signal–to–noise ratio (SNR) and speed. Experiments are performed as a proof of principle of the technical applicability of the new estimator to real experimental data.

Results: Figure 1a and b show an experimental axial strain TC elastogram and an axial strain equilibrium point elastogram, respectively, obtained from a block of tofu using the new elastographic GPGPU–TC estimator. These elastograms were obtained at a final image calculation rate of 7.8 frames/s, with an improvement in computational speed up to 400 times with respect to the CPU version of the same algorithm. This estimator was also found to be up to three orders of magnitude faster than commercially available MATLAB functions [4] and previously proposed elastographic TC algorithms [1,2]. Figure 1c shows the accuracy [4] of the algorithm with respect to the true TC and equilibrium strain.

Conclusions: The results of this study demonstrate that the elastographic estimator described in this presentation can produce time constant estimates in real–time and with high accuracy (>99%) and sensitivity (< 5s). The availability of this GPU–based LM–LSE TC estimator has the potential to enable real–time monitoring of the temporal behavior of complex poroelastic tissues using ultrasound elastography.

Acknowledgements: This work is supported by Texas Engineering Experiment Station and Texas A&M University, College Station, TX. The authors would like to acknowledge Gautham Nair's assistance throughout the course of this study.

References:

[1] Righetti R, Ophir J, Krouskop TA: A Method for Generating Permeability Elastograms and Poisson's Ratio Time–Constant Elastograms. Ultras. Med. Biol., Vol. 31(6), pp. 803–816, 2005.
[2] Berry GP, Bamber JC, Armstrong CG, Miller NR, Barbone PE: Towards an Acoustic Model–Based Poroelastic Imaging Method: I. Theoretical Foundation. Ultras. Med. Biol., vol. 32(4): 547–567, 2006.
[3] Ranganathan A. The Levenberg–Marquardt Algorithm. 8th June 2004. http://www.scribd.com/doc/10093320/Levenberg–Marquardt–Algorithm.
[4] Nair, Sanjay: Performance Analysis of a New Ultrasound Axial Strain Time Constant Estimation. MS thesis Texas A&M University, 2010. Print.

Figure 1: (a) (b) (c)

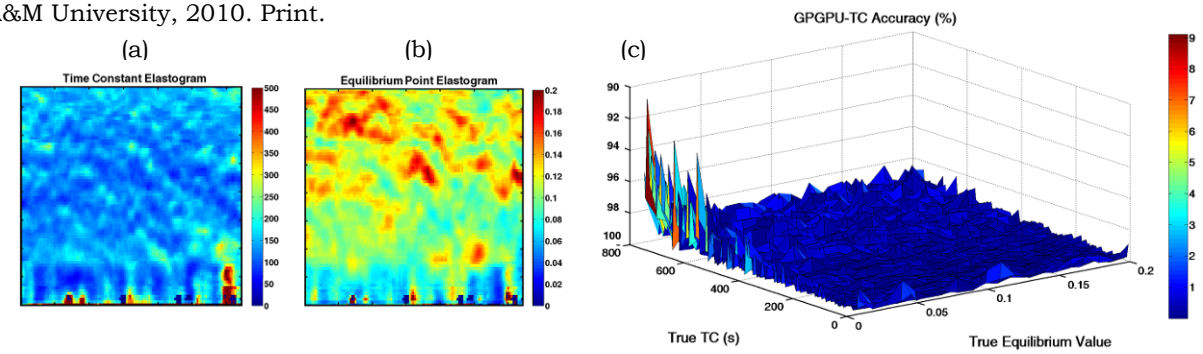

* *indicates Presenter*

058 **SYNTHESIS AND ANALYSIS OF CRAWLING WAVES GENERATED FROM RADIATION FORCE.**

Zaegyoo Hah[1], Christopher R. Hazard[2], Deborah J. Rubens[3], Kevin J. Parker[1].*

[1]Electrical and Computer Engineering Department, [3]Imaging Science Department, University of Rochester, Rochester, NY, 14627, USA; [2]GE Global Research, One Research Circle, Niskayuna, NY, 12309, USA.

Background: Conventional crawling waves (CR waves) are formed by the interference pattern of two continuous sinusoidal excitations with small frequency differences. CR waves have advantages of easy imaging using conventional color Doppler scanning and well–posed estimation of local elastic properties of tissues and lesions [1,2]. However, with radiation force from the ultrasound beam acting as the excitation source, the resulting vibration will be more pulsatile in time and space. A synthesis scheme is applied to create the sinusoidal interference and, therefore, CR waves [3] over a range of frequencies.

Aims: This presentation demonstrates the methods to generate CR waves with radiation force from ultrasonic beams and shows results of CR waves synthesized from the measurement of phantoms.

Methods: A GE Logiq 9 ultrasound system was modified to collect the data required to generate the synthetic arc wave displacement time histories. A special research scan sequence format was developed. Complex baseband demodulated data (IQ) were stored for offline processing. The sampling rate of the IQ data was 10 MHz. The duty cycle of the overall scan sequence was maintained at less than 0.5% to avoid thermal limits of the components. IQ data were processed to extract displacements shown in Figure 1. The displacements were further processed to generate CR waves. One such frame is shown in Figure 2. Two types of phantoms were made and scanned with the modified Logiq 9 system: a gelatin phantom with an inclusion, and a fatty phantom with 30–50% oil. The displacement data for each of the phantom were used to generate CR waves and further analyzed to estimate local shear speed.

Results: The Crawling Wave data are analyzed to estimate the shear wave velocity of the medium. Both a homogeneous medium and a medium with an inclusion are covered. The background medium is designed to have a shear velocity of 2–3 m/s while the inclusion has higher velocity of 4–5 m/s.

Conclusions: It is confirmed that the CR waves with displacements below 10 microns can be generated with radiation force induced by ultrasound beam. Also, the analysis of the data shows the validity of the methods in detecting the elastic properties of the tissue.

Acknowledgements: This study was partly supported by NIH grant 5 ROI AG016317 and NIH grant 5 RO1AG29804.

References:

[1] Zhe Wu, Kenneth Hoyt, Deborah J. Rubens, Kevin J. Parker: Sonoelastographic Imaging of Interference Patterns for Estimation of Shear Velocity Distribution in Biomaterials. Journal of the Acoustical Society of America, Vol. 120, No. 1, pp. 535–545, July 2006.

[2] Kenneth Hoyt, Kevin J. Parker, and Deborah J. Rubens: Real–Time Shear Velocity Imaging Using Sonoelastographic Techniques. Ultrasound in Medicine and Biology, Vol. 33, No. 7, pp. 1086–1087, 2007.

[3] Zaegyoo Hah, Young Thung Cho, Chris Hazard, Kevin Parker, Deborah Rubens: Crawling Waves from Radiation Force Excitation. Ultrasonic Imaging, special issue in honor of Dr. Wagner, in press.

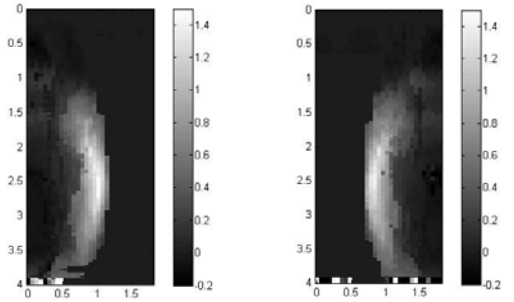

Figure 1: A frame of displacements measured with Logiq 9 system. (a) from left push, (b) from right push.

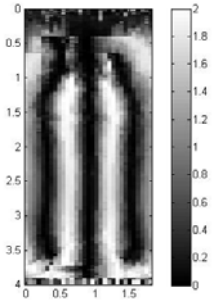

Figure 2: A frame of CR wave synthesized from left and right displacement data.

065 **A SIMULATION FRAMEWORK FOR HARMONIC MOTION IMAGING FOR FOCUSED ULTRASOUND (HMIFU) WITH *EX VIVO* VALIDATION.**

Gary Y. Hou[1], Jianwen Luo[1], Caroline Maleke[1], Jonathan Vappou[1], Elisa E. Konofagou[1,2].*
[1]Department of Biomedical Engineering, [2]Department of Radiology, Columbia University, New York, NY, USA.

Background: HMIFU is a recently developed high–intensity focused ultrasound (HIFU) therapy monitoring method with feasibilities demonstrated *in vitro* and *in vivo* [1,2]. Its principle is based on Harmonic Motion Imaging (HMI) [3], an oscillatory radiation force technique for imaging tissue mechanical properties during application of an amplitude modulated (AM) therapeutic beam used by HIFU. In this work, a theoretical framework of HMIFU is presented, comprising a customized nonlinear wave propagation model, a finite–element (FE) analysis module, and an image–formation model.

Aims: 1) Assessment of the fundamental capabilities of HMIFU in lesion localization and quantification and 2) validation of the simulation findings *ex vivo*.

Methods: The same HMI and HMIFU parameters ($I_{spta,\ HMI}$ = 231W/cm^2, $I_{spta,\ HMIFU}$ = 942W/cm^2) as in the aforementioned experimental studies were used, i.e., 4.68MHz HIFU frequency and an AM frequency of 25Hz. A HIFU–simulator [4] was modified to simulate HMIFU pressure and thermal lesion maps within a 30 x 9mm^2 target. Both fields were used as inputs into the 3D FE solver (COMSOL Multiphysics™, Burlington, MA) to compute the displacement in a linear elastic, lesion–embedded simulated phantom with the lesion Young's modulus varying between 30, 60 and 90kPa in a background of 10kPa. The radiofrequency (RF) signals were simulated in MATLAB using a linear convolutional model (f_{center}= 7.5MHz, f_{sample}= 80MHz) and then used to estimate the HMI displacements using 1D cross–correlation. Using the same parameters as in the simulations, HIFU experiments were performed on three *ex vivo* canine liver specimens with 10s, 20s, and 30s heating durations.

Results: Good agreement was found between the simulated (2.86, 5.93 and 17.5mm^2) and experimental (2.83, 6.75 and 17.9mm^2) HMIFU lesion sizes as well as focal depths of 4.8–5.2cm, 4.6–5cm, and 4.4–5.1cm in the 10s, 20s and 30s cases, respectively. For a Young's modulus ratio of 3, 6, and 9, the FE and estimated lesion–to–background HMI displacement ratios were equal to 2.42, 3.93, and 5.41, and 1.89, 3.54, and 5.04, respectively. In experiments, the HMI displacement followed a similar trend of 1.82, 3.25, and 4.20 at 10s, 20s, and 30s heating, respectively.

Conclusions: The capability for lesion characterization and quantification based on the underlying tissue mechanical properties using HMIFU was assessed using a theoretical framework, which comprised a HIFU simulator, a FE mechanical model and an image formation model. Good agreement in both lesion size and focal depth was found between the actual and estimated HMI lesion maps in both simulations and experiments. In conclusion, the reliability of the HMIFU system for lesion detection, localization and quantification using the parameters previously studied was demonstrated.

Acknowledgements: The presented work is supported by the National Institutes of Health (NIH R21EB008521). The authors wish to thank Joshua Soneson, Ph.D. at US Food and Drug Administration for providing the source codes of the HIFU Simulator Ver. 1.0.

References:

[1] Maleke C. and Konofagou E.E.: Harmonic Motion Imaging for Focused Ultrasound (HMIFU): A Fully Integrated Technique for Sonication and Monitoring of Thermal Ablation in Tissues. Phys. Med. Biol., Vol. 53, No. 6, pp. 1773–1793, 2008.
[2] Maleke C and Konofagou EE: *In Vivo* Feasibility of Real–Time Monitoring of Focused Ultrasound Surgery (FUS) using Harmonic Motion Imaging (HMI). IEEE Trans. Biomed. Eng., Vol. 57, pp. 7–11, 2010.
[3] Maleke C., Pernot, M. and Konofagou E.E.: A Single–Element Focused Transducer Method for Harmonic Motion Imaging. Ultrason. Imaging, Vol. 28, No. 3, pp. 144–158, 2006.
[4] Soneson J.: A User–Friendly Software Package for HIFU Simulation. 8th International Symposium on Therapeutic Ultrasound. AIP Conference Proceedings, Vol. 1113, pp.165–169, 2009.

* *indicates Presenter*

083 **IDENTIFICATION OF NON–LINEAR MATERIAL ELASTIC PROPERTIES OF TISSUE PHANTOMS USING A REGULARIZED INVERSION METHOD.**

JF Dord[1], S Goenezen[1], AA Oberai[1], PE Barbone[2], TJ Hall[3], J Jiang[3].*

[1]Rensselaer Polytechnic Institute, 110 8th Street, Troy, NY, 12180, USA; [2]Boston University, 110 Cummington Street, Boston, MA, 02215, USA; [3]Medical Physics Department, 1111 Highland Ave., University of Wisconsin–Madison, Madison, WI, USA.

Background: Quasistatic ultrasound elastography provides a noninvasive means to measure the displacement fields within deforming tissues, *in vivo* [1]. The measured displacement fields may then be used in an iterative inversion procedure to recover the mechanical properties of the ensonified tissues [2]. This procedure has been repeatedly demonstrated to recover and quantify linear elastic contrast. Recent studies [3] regarding the mechanical properties of tumors show that benign and malignant tissues exhibit strong non–linear behaviors, thus providing an opportunity to evaluate elastic parameters beside linear elastic modulus.

Aims: Our aim is to develop and test methodologies to reconstruct, pointwise within a region of interest, both the linear elastic shear modulus and the non–linear parameters for a model describing the mechanical behavior of ensonified tissues and tissue mimicking phantoms.

Methods: A finite element code that includes material and geometric nonlinearity was written and coupled with an optimization program. By matching observed to predicted displacement fields, the parameters defining the mechanical behavior of the tissues can be recovered using a quasi–Newton algorithm. This method allowed us to recover both the relative linear elastic modulus and the non–linear parameter defining the tissue's behavior. The noise and the imperfections in the displacement fields were handled by a regularization approach. The inverse processing requires several modeling choices that we evaluated. These included boundary conditions defining the predicted displacement, the form of the regularization function and regularization parameter, and its interaction with the optimization method. These choices were evaluated with both simulated data and phantom data. Displacement data from a tissue–mimicking phantom with well–characterized linear and non–linear elastic properties was constructed. It was imaged under continued compression up to strains of roughly 20%. Here a series of four different targets were investigated.

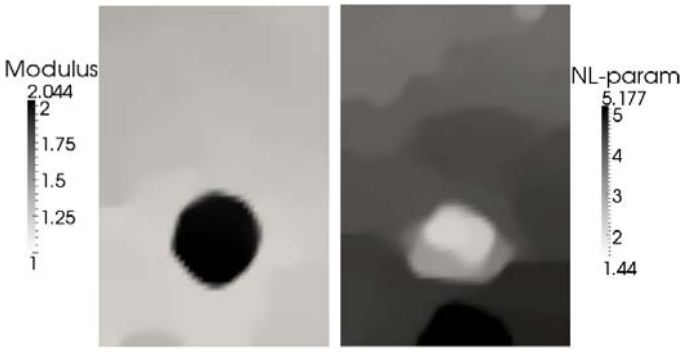

Figure 1: Modulus and non–linear parameter fields of a non–linear tissue phantom using displacements associated with 4 compression levels.

Results and Conclusions: Linear elastic reconstructions are very stable geometrically and quantitatively. The reconstructed relative linear elastic shear modulus is sensitive to even low levels (1%) of prestrain. The non–linear elastic parameter is more sensitive to noise than the linear elastic stiffness, and errors in the linear modulus reconstruction pollute the non–linear reconstructions. Future work includes extensions to 3D, incorporating pressure and/or force data, and testing on clinical data.

Acknowledgements: We acknowledge the support of NIH Grants R21CA133488 and R01CA140271.

References:

[1] J. Jiang and T.J. Hall: A Generalized Speckle Tracking Algorithm for Ultrasonic Strain Imaging Using Dynamic Programming. Ultrasound in Medicine and Biology, 35(11), pp. 1863–1879, 2009.

[2] A. Oberai et al.: Linear and Nonlinear Elasticity Imaging of Soft Tissue *In Vivo*: Demonstration of Feasibility. Physics in Medicine and Biology, 54, pp. 1191–1207, 2009.

[3] J.J. O'Hagan, A. Samani: Measurement of the Hyperelastic Properties of 44 Pathological *Ex Vivo* Breast Tissue Samples. Physics in Medicine and Biology, 54, pp. 2557–2569, 2009.

088 **IMPROVING CRAWLING WAVE DETECTION OF PROSTATE CANCER: PRELIMINARY *IN VITRO* RESULTS.**

L An[1], Z Hah[1], Y Cho[1], B Mills[1], S Mao[1], L Baxter[2], L Kushner[2], J Yao[2], J Joseph[2], DJ Rubens[2], J Strang[2], KJ Parker[1].*

[1]University of Rochester, Rochester, NY, USA; [2]University of Rochester Medical Center, Rochester, NY, USA.

Background: The crawling wave (CrW) technique [1] for local tissue shear velocity estimation was recently introduced into the sonoelastographic field. It has been applied to depict the elastic properties of biological tissues including radiofrequency ablated hepatic lesions *in vitro* [2], human skeletal muscle *in vitro* [3] and excised human prostate [4].

Aims: The objective of this study is to establish a protocol based on CrW sonoelastography to detect prostate cancer.

Methods: The whole prostate gland was obtained after radical prostatectomy and embedded in a 10.5% gelatin mold. Two vibration sources were positioned at each side of the mold with an ultrasound transducer scanning from the top of the cross–section under observation. The gland was imaged at three positions (apex, mid–gland and base) at three vibration frequencies (100, 120 and 140 Hz) with a small frequency offset between the sources. The average shear velocity estimation over three frequencies was obtained by globally selecting and averaging the highest 90% of the data ranked by correlation coefficient. The tumor regions were then segmented using a semi–automatic region–growing segmentation technique. The sites for the three cross–sections were marked, and the corresponding histological slices were obtained, which provided the ground truth of cancer distribution.

Results: Preliminary results from one cross–section are shown in Figure 1. Separation of the shear velocity values of the cancerous tissue and the normal tissue is indicated. The segmentation of the cancerous region was in approximately the same position as the outline of the tumor on the histological slice. The shear wave velocities of cancerous and non–cancerous tissues were 3.71±0.20 m/s and 2.38±0.24 m/s, respectively. The elastic contrast was 1.56, similar to the ratio found in prostate cancer by mechanical testing [5].

Conclusions: These preliminary results suggested the ability of the shear velocity estimator to distinguish prostate cancer from normal tissue and that the approach based on CrW sonoelastography can be adapted to detect prostate cancer.

Acknowledgements: This study was partly supported by NIH Grants 5 RO1 AG016317 and 5 RO1 AG29804.

References:

[1] Zhe Wu et al.: Sonoelastographic Imaging of Interference Patterns for Estimation of Shear Velocity Distribution in Biomaterials. JASA, 120(1), pp. 535–545, 2006.
[2] Kenneth Hoyt et al.: Two–Dimensional Sonoelastographic Shear Velocity Imaging. UMB, 34(2), pp. 276–288, 2008.
[3] Kenneth Hoyt et al.: Muscle Tissue Characterization Using Quantitative Sonoelastography: Preliminary Results. Proceedings of the IEEE Ultrasonics Symposium, pp. 365–368, 2007.
[4] B Castañeda et al.: Prostate Cancer Detection Using Crawling Wave Sonoelastography. SPIE, 7265, 726513, 2009.
[5] Man Zhang et al.: Congruence of Imaging Estimator and Mechanical Measurements of Viscoelastic Properties of Soft Tissues. UMB, 33, pp. 1617–1631, 2007.

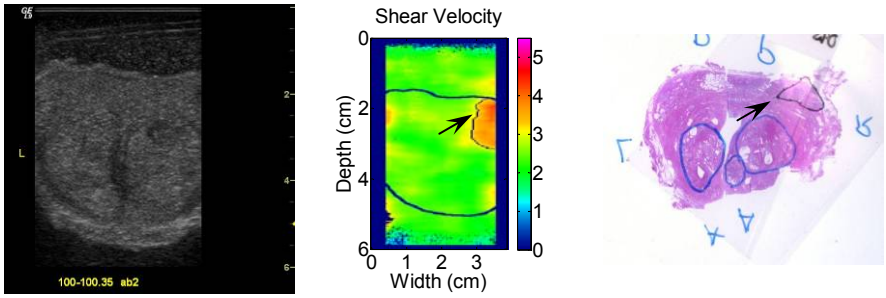

(a) (b) (c)

Figure 1: (a) B–mode (b) shear wave velocity and (c) histological images of a cross–section of a human prostate gland. (b) shows a region with elevated shear wave velocity to the posterior–right of the cross–section which corresponds to a cancerous region in (c) (black outlines indicate cancer and blue outlines indicate BPH in the histological slice). Cancer (arrow in b and c) is not seen on the gray scale (a).

* *indicates Presenter*

102 **VISUALIZATION OF HIFU–INDUCED LESION BOUNDARIES BY AXIAL–SHEAR STRAIN ELASTOGRAPHY.**

Arun K. Thittai[1], Belfor Galaz[1] and Jonathan Ophir[1].*
[1]Diagnostic and Interventional Imaging Department, The University of Texas Medical School, Houston, TX, USA.

Background: High intensity focused ultrasound (HIFU) has become a promising noninvasive technique to thermally ablate tumors lying deep in tissue. However, the extent of the thermal damage (referred to as a lesion) is difficult to quantify with current B–mode imaging techniques [1]. The desire to have a unified system for HIFU treatment and real time lesion visualization has fueled research on several ultrasound based methodologies [1]. Among them, elastography was proposed as method utilizing the fact that the HIFU lesion is stiffer than surrounding tissue [2]. Although regular axial strain elastography has shown promise in HIFU lesion core visualization, there still is a need to reliably identify the lesion boundaries. Recently, axial–shear strain elastography has been introduced as a method to visualize the boundaries of breast lesions [3]. We hypothesize that this method may also be useful in reliable HIFU lesion boundary visualization.

Aims: The aim of this study was to investigate the feasibility of reliably visualizing HIFU lesion boundaries using axial–shear strain elastograms (ASSE).

Methods: HIFU–induced lesion cases used in the present work were selected from data acquired in a previous study [2]. The samples consisted of excised canine livers with thermal lesions produced by MR–compatible HIFU system (GE Medical System, Milwaukee, WI). After thermal exposure, the samples were cast in a gelatin block for elastographic experiments performed using Diasonics Spectra II (Santa Clara, CA) Ultrasound scanner. In the present work, the radiofrequency (RF) data obtained earlier were reprocessed using a multilevel coarse–to–fine 2D block–matching algorithm. The Axial Strain and Axial–Shear Strain Elastograms (ASE and ASSE, respectively) were generated using a least squares strain estimator (LSQE) with a kernel size of ~4mm and staggered–strain estimation, respectively [3]. For each of the single lesion sample, the lesion boundaries were determined independently from the ASE and ASSE at various isointensity contour thresholds (from -2dB to -6dB), and the area of the enclosed lesion was computed. For samples with multiple lesions, the resulting ASSE was analyzed for identifying any unique axial–shear strain zones of interest.

Results: These results show that estimation of lesion area using ASSE is less sensitive to isointensity threshold selection, making this method more robust compared to ASE–based method. The ASE and ASSE, along with segmented boundary at -2dB and -6dB contour threshold, from an example HIFU lesion case is shown in Figure 1. A plot of the lesion size at other thresholds is provided in Figure 2. ASSE from a multiple lesion sample is shown in Figure 3. Observe that ASSE enables high–contrast visualization of a "thin" untreated region between the two lesions.

Conclusions: The results demonstrate that it is feasible to reliably visualize HIFU lesion boundaries using ASSE. Further, ASSE can visualize the presence of very thin untreated regions between multiple fully treated HIFU lesions.

Acknowledgements: Data used in this study were acquired previously for projects supported by NIH Program Project grants P01–CA64597 and P01–EB02105–13. The current work was supported by NIH grant R21–CA135580. The authors would like to thank the authors of the previous study [2] who acquired and archived the data that is used in the present study.

References:

[1] Zheng X, Vaezy S: An Acoustic Backscatter–Based Method for Localization of Lesions Induced By High–Intensity Focused Ultrasound. Ultras. Med Biol, 36(4), pp. 610–22, 2010.
[2] Righetti R, Kallel F, Stafford RJ, Price RE, Krouskop TA, Hazle JD and Ophir J: Elastographic Characterization of HIFU–Induced Lesions in Canine Livers. Ultras. Med Biol, 25(7), pp. 1099–1113, 1999.
[3] Thitai Kumar A, Krouskop TA, Garra BS and Ophir J: Visualization of Bonding at an Inclusion Boundary using Axial–Shear Strain Elastography: A Feasibility Study. Phys Med Biol, 52, pp. 2615–33, 2007.

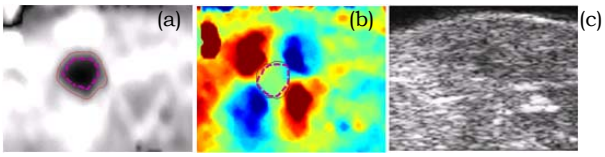

Figure 1: (a) ASE, (b) ASSE and (c) sonogram of a HIFU–induced lesion. The isointensity contour lines are overlaid on the elastograms for the threshold values; -2dB (-) and -6dB (--).

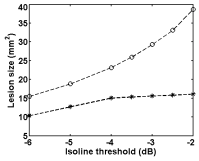

Figure 2: The HIFU–induced lesion area estimate from ASE (o) and from ASSE (✳).

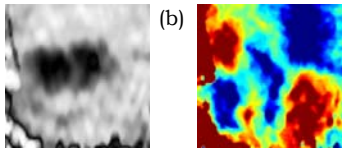

Figure 3: ASE (a) and ASSE (b) of a pair of adjacent HIFU lesions. Observe the presence of high–contrast axial–shear strain zones exactly at the boundary between the two lesions.

108 **EFFECT OF LOW–FREQUENCY ULTRASOUND MODULATION ON THE ACOUSTIC RADIATION FORCE IN FLUIDS AND SOFT TISSUES.**

Egor V. Dontsov[1], Bojan B. Guzina[1].*
[1]Civil Engineering Department, University of Minnesota, 500 Pillsbury Drive SE, Minneapolis, MN 55455, USA.

Background: Since the nineteenth century, the propagation of high–intensity, time–harmonic sound waves in a fluid has been known to give rise to aperiodic motion [1]. For small Mach numbers, the problem for the mean acoustic quantities can be formulated in terms of time–averaged balance equations, featuring an effective body–force term, the so–called acoustic radiation force (ARF) [2]. Such apparent body force stems from the averaging of quadratic terms in the balance of linear momentum and represents the influence of high–intensity sound in the averaged equations.

Aims: The purpose of this study is to investigate the generation of the ARF in soft tissues in situations when the amplitude of high–intensity sound field (MHz) is modulated using frequencies (kHz) that are, relative to the frequency of sound, on the order of the Mach number (10-3). This configuration, which is frequently deployed by emerging biomedical imaging technologies [3,4], turns out to be unresponsive to the usual (small–Mach–number) asymptotic simplification via the concept of the ARF owing to the fact that the mean acoustic fields, computed as averages over the period of sound vibrations, retain the rapid oscillation features of the latter.

Methods: To deal with the problem, an asymptotic treatment is pursued via a scaling approach that splits the temporal variable into "fast" and "slow" time, permitting one to track the contribution of (time–harmonic) sound and its modulation separately in the solution.

Results: With the use of time–splitting method, the second–order asymptotic solution, written in terms of the "fast" time averages of acoustic fields, is shown to: 1) be free of rapid oscillations and 2) permit compact formulation in terms of initial–boundary value problem featuring the ARF that, for the first time, rigorously captures the effect of sound modulation. Recognizing the differences between the Eulerian and Lagrangian mean motion, the formulation is developed for both types of averages. To both expose the essence of the method and cater for practical applications, the analysis is presented for two canonical configurations: (1) the plane wave case where the soft tissue is approximated by a Newtonian fluid and (2) the quasi–plane wave (i.e. narrow ultrasound beam) case, where the response of a tissue is modeled by a nonlinear thermo–viscoelastic model. The results show that the induced mean motion is, for the plane–wave problem, of oscillatory rather than streaming nature, and that it varies at a rate commensurate with that of the prescribed modulation envelope. On developing a finite difference solution to the original nonlinear plane wave problem, it is further shown that the featured "fast" time average can be computed as a double "ordinary" time average of the simulated nonlinear response. The proposed framework of analysis is illustrated by the analytical solution for a sinusoidal modulation envelope with quiescent past, which both exposes the limitations of earlier treatments and highlights the generation of an ARF in a lossless fluid when a modulated, high–intensity sound field is propagated through it. In the second example, dealing with a narrow ultrasound beam, the analytical treatment for sinusoidal modulation envelope similarly demonstrates the effectiveness of the proposed scaling scheme toward computing the induced ARF and associated shear–wave motion in a soft tissue.

Conclusions: The study establishes a rigorous treatment of the ARF in situations when the amplitude of the ultrasound is modulated with the frequencies that are, relative to the frequency of sound, on the order of the Mach number. The proposed approach, which uses a time–splitting method to deal with the modulated ultrasound problem, is verified through a comparison with a finite–difference solution for the plane–wave problem.

Acknowledgements: The support provided by the Minnesota Partnership for Biotechnology and Medical Genomics during a portion of this study is kindly acknowledged.

References:

[1] L. Rayleigh, On the Circulation of Air Observed in Kundt's Tubes, and on Some Allied Acoustical Problems. Phil. Trans. Roy. Soc. Lond., 175, pp. 1–21, 1884.
[2] O. Rudenko and S. Soluyan: Theoretical Foundations of Nonlinear Acoustics. Plenum, New York, 1977.
[3] A.P. Sarvazyan, O.V. Rudenko, S.D. Swanson, J.B. Fowlkes and S.Y. Emelianov: Shear wave Elasticity Imaging: A New Ultrasonic Technology of Medical Diagnostics. Ultrasound Med. Biol., 24(9), pp. 1419–1435, 1998.
[4] B.B Guzina, K. Tuleubekov, D. Liu and E. Ebbini: Viscoelastic Characterization of Thin Tissues using Acoustic Radiation Force and Model–Based Inversion. Phys. Med. Biol., 54, pp. 4089–4112, 2009.

* *indicates Presenter*

086 **GPU UTILIZATION FOR FAST 3D MOTION TRACKING ALGORITHMS.**

Ted G. Fisher[1], Timothy J. Hall[1].*
[1]School of Medicine and Public Health, University of Wisconsin–Madison, Madison, WI, USA.

Background: 2D real time motion tracking algorithms have been implemented on commercial ultrasound scanners [1]. 3D motion tracking has also been demonstrated [2], but the methods employed have not resulted in real time volume tracking.

Aims: To create a fast 3D motion tracking algorithm with dense displacement estimates for real time motion tracking of 3D radiofrequency (RF) data.

Methods: Using CUDA (Nvidia, Santa Clara, CA, USA), we are able access the memory and computing power of the CUDA–enabled GPU. With this, we are able to run thousands of threads executing concurrently in order to do massively parallel computations. Motion tracking is accomplished in three steps. The initial step creates a cost function that uses the normalized cross–correlation as well as a motion continuity constraint as in [3]. The cost function is minimized, and the best path is determined from the Viterbi algorithm. Displacement estimates are found for a grid of 16 lateral by 32 axial data points from an original RF size of 256 lateral by 1024 axial points. The 16 lines are independent of each other, and a block of threads is assigned to each line. Within each block, a thread is assigned to a different displacement state. A search region of 8 lateral by 32 axial points is used for a total of 256 states. Each thread calculates the cost to be in its particular state, and that cost is made accessible to the other threads in the block through shared memory. In the second step, these coarsely gridded displacements are then utilized as the initial estimates for a finer motion tracking method. Sum squared difference (SSD) is used as a similarity measure in this second step. Using overlapping kernels and a rolling window technique, threads calculate different parts of the SSD kernels and communicate these partial calculations to other threads through shared memory much like in [3]. The result is a very dense displacement field that has nominally the same dimensions as the original RF data (except for the edges where we run out of data). By using the estimated displacements obtained from the Viterbi algorithm, we are able to drastically shrink our search region (and therefore the number of computations) to ±2 axial, ±1 lateral, and ±1 elevation samples for this second step of tracking which avoids peak hopping artifacts in the final displacement field. In the third step, motion is tracked in the adjacent plane of RF data using a quality guided method. The densely populated displacement estimates are broken into a 16 by 32 grid. The displacement (lateral and axial) that had the lowest SSD (highest quality) is then used as the initial estimate for the displacement in the adjacent plane. The second and third steps are then used for the remaining planes in the volume. The displacement data, already on the GPU, can be directly visualized by mapping to an OpenGL buffer.

Results: Using a GTX 480 GPU, it takes, on average, 53ms to find the best path with the Viterbi algorithm on a 16 x 32 grid of axial and lateral displacements. Subsequent tracking and visualization on a 1024 x 256 x 64 (axial, lateral and elevation, respectively) volume of simulated RF data under a 3% uni–axial deformation is accomplished at 67fps or 17.5Mpixels/s. When tracking motion from a single inclusion phantom, we found that using a ±3–sample axial search was necessary to track motion, suggesting that a larger initial grid may be required for tracking. With this larger search region, the frame rate is 50fps.

Conclusions: Desktop based 3D GPU motion tracking can be performed at fast rates. These algorithms can be further optimized for improved efficiency. Current limitations include the necessity of some parameters to be multiples of 2.

Acknowledgements: We gratefully acknowledge the support from NIH grants T32–009206 and R21CA133488.

References:

[1] Zhu Y, Hall TJ: A Modified Block Matching Method for Real–Time Freehand Strain Imaging. Ultrasonic Imaging, 24, pp. 161–76, 2002.
[2] Fisher TG, Hall TJ, Panda S, Richards MS, Barbone PE, Jiang J, Resnick J, Barnes S: Volumetric Elasticity Imaging with a 2-D CMUT Array. Ultrasound in Medicine and Biology, 36, pp. 978–90, 2010.
[3] Jiang J, Hall TJ: A Generalized Speckle Tracking Algorithm for Ultrasonic Strain Imaging using Dynamic Programming. Ultrasound in Medicine and Biology, 35, pp. 1863–79, 2009.
[3] Gallup D, Frahm J–M, Stam, J: Real–Time Local Stereo using CUDA. Proceedings of Nvidia GPU Technology Conference Research Summit, 2009.

017 **SUBSAMPLE DISPLACEMENT INTERPOLATION USING WINDOWED–SINC RECONSTRUCTION WITH NUMERICAL OPTIMIZATION.**

Matthew M. McCormick[1], Tomy Varghese[1].*
[1]Medical Physics, University of Wisconsin–Madison, 1111 Highland Ave, Madison, WI, USA.

Background: Subsample interpolation of the similarity metric is key to strain estimation accuracy in ultrasound elastography. The local maximum must be found precisely or quantization errors will dominate with discrete signals. Cespedes et al. [1] examined sub–sampling strategies including cosine and parabolic interpolation, which are still commonly utilized today, along with windowed–sinc reconstruction methods. Windowed–sinc interpolation delivered better performance because it does not suffer from bias artifacts.

Aims: We expand on the approach proposed by Cespedes et al. [1] by examining two–dimensional windowed–sinc interpolation. Cespedes et al. [1] suggested the use of a binary search algorithm to find the peak with logarithmic convergence. We examine multi–dimensional numerical optimization techniques for making the algorithm computationally feasible. Axial and lateral displacements are estimated, but only axial displacements are used to calculate the SNRe.

Methods: The strain signal–to–noise ratio (SNRe) is quantified after applying normalized cross–correlation block–matching with parabolic interpolation, cosine interpolation or windowed–sinc interpolation with numerical optimization. A Welch window is applied for sinc interpolation. A uniform tissue–mimicking ultrasound phantom with fully developed speckle is compressed to 1% strain and imaged with the Siemens S2000 VF9–4 transducer. Statistics on the axial strain are determined with n=14 samples of the scattering pre– and post–deformation echo signals. Optimization with the Nelder–Mead simplex (amoeba) algorithm is compared with a regular–step gradient descent approach. The number of samples in the sinc window was the same in all directions.

Results: Figure 1 demonstrates that windowed–sinc reconstruction performs better than parabolic or cosine interpolation as expected. Figure 2 shows that a sinc window length beyond 9 displacement samples (2.0 axial center frequency wavelengths) does not yield statistically significant improvement in SNRe for this data. The Nelder–Mead method is more efficient than gradient based algorithms because it avoids direct computation of the cost function's derivative, which must be determined numerically at each iteration. The mean and standard deviation of the mean optimization times for the amoeba and gradient descent methods are 234±19 μs and 707±59 μs respectively with $p<<0.01$ for a Student's t–test.

Conclusions: Subsample interpolation using windowed–sinc reconstruction is better than parabolic interpolation because of bias artifacts. The technique becomes computationally feasible if a numerical optimization algorithm, such as Nelder–Mead downhill simplex, is applied during the estimation of correlation peaks for displacement estimation.

Acknowledgements: This work is supported by NIH grant 5R21EB010098–01.

References:

[1] Cespedes, I. Huang, Y. Ophir, J. Spratt, S.: Methods for Estimation of Subsample Time Delays of Digitized Echo Signals. Ultrasonic Imaging, 17 (2), p. 142, 1995.

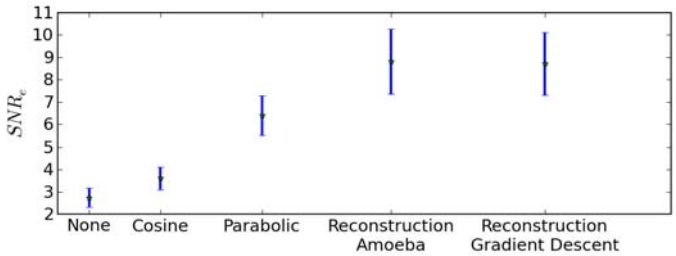

Figure 1: SNRe versus subsample interpolation method.

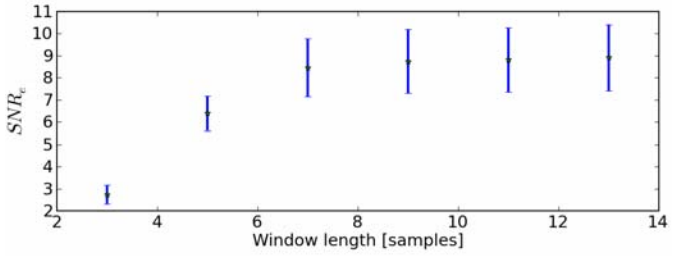

Figure 2: SNRe versus window length. Each sample is 0.22 center frequency wavelengths.

* *indicates Presenter*

090 **ULTRASOUND ELASTICITY IMAGING USING THE CURL OF THE DISPLACEMENT.**

Ali Baghani[1], Reza Zahiri Azar[1], Septimiu E. Salcudean[1], Robert Rohling[1].*
[1]University of British Columbia, Vancouver, BC, CANADA.

Background: When tissue is excited, both shear and dilatational waves propagate inside it. Most dynamic elastography methods track the shear waves to measure tissue elasticity. However, the dilatational component of the displacement can introduce bias and artifacts in the estimated elasticities [1]. Taking the curl of the displacement suppresses the dilatational component, and leaves the purely shear component of the displacement. The use of the curl of the displacement in elastography has lead to more accurate elasticity estimation in magnetic resonance elastography (MRE) [2].

Aims: To develop an ultrasound elastography system capable of using the curl of the displacement to estimate the tissue elasticity.

Methods: To maintain the acquisition time at a minimum, only the elevational component of the curl ω_z was estimated. The component ω_z depends only on the axial u_y and lateral u_x components of the displacement and satisfies a shear wave equation with density ρ and the shear modulus μ:

$$\omega_z = \frac{\partial u_x}{\partial y} - \frac{\partial u_y}{\partial x}; \qquad \rho \frac{\partial^2}{\partial t^2}\omega_z = \mu\left(\frac{\partial^2}{\partial x^2} + \frac{\partial^2}{\partial y^2} + \frac{\partial^2}{\partial z^2}\right)\omega_z$$

The axial and lateral components of the displacement were estimated by angularly compounding the motion vectors acquired with different beam directions. To be able to estimate the variation in the *z*–direction, a 3D probe was used (4DL14–5/38, Ultrasonix Co, Richmond, BC, Canada). Our previously developed high frame rate system [3,4] was extended to acquire in–phase axial and lateral displacements over a volume of interest. Direct inversion was used to estimate the shear modulus. Custom code was developed to implement the system on a Sonix RP machine (Ultrasonix Co, Richmond, BC, Canada). The system was used to image a commercial elasticity phantom (Model 049, CIRS Inc., Norfolk, VA, USA) which has spherical soft and hard inclusions of different radii and elasticity values. The elasticity of the background material is reported to be 29 kPa.

Results: Figure 1 shows the elastograms obtained for one of the hard inclusions, 1a–1d, and one of the soft inclusions, 1e–1h. As can be seen, the system can recover both inclusions with reasonable contrast.

Conclusions: The curl–based inversion techniques can be used in the context of ultrasound elastography. We have shown that with proper sequencing, a conventional ultrasound system is capable of acquiring data suitable for computing the curl of the displacement. Consistent results have been obtained on a commercial elasticity phantom. Studying the performance of the method on real tissue data is the next step in the future of this research.

Acknowledgements: This research was supported by Natural Sciences and Engineering Research Council (NSERC).

References:

[1] A. Baghani, S.E. Salcudean, R. Rohling: Theoretical Limitations of the Elastic Wave Equation Inversion for Tissue Elastography. J. Acoust. Soc. Am., 126(3), pp. 1541–51, 2009.
[2] R Sinkus, et al.: Viscoelastic Shear Properties of *In Vivo* Breast Lesions Measured by MR Elastography. Magnetic Resonance Imaging, 23, pp. 159–165, 2005.
[3] A. Baghani, et al.: A High Frame Rate Ultrasound System for the Study of Tissue Motions. IEEE UFFC, in press.
[4] R. Zahiri–Azar, A. Baghani, S.E. Salcudean, R. Rohling: 2D High Frame Rate Dynamic Elastography using Delay Compensated and Angularly Compounded Motion Vectors: Preliminary Results. IEEE UFFC, in press.

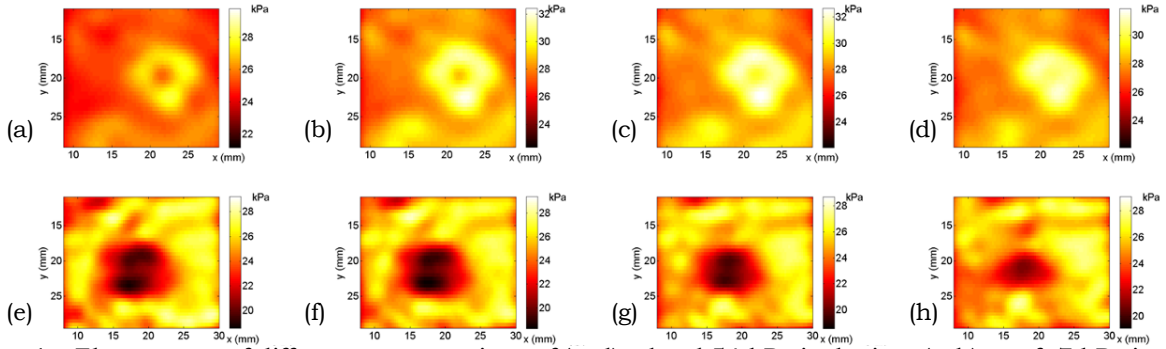

Figure 1: Elastograms of different cross sections of (a–d) a hard 54 kPa inclusion, (e–h) a soft 7 kPa inclusion.

041 **DISPLACEMENT ESTIMATION OF THE CAROTID ARTERY USING SYNTHETIC APERTURE IMAGING.**

S. Korukonda[1,2], M. M. Doyley[1,2].*
[1]Electrical and Computer Engineering Department, [2]Rochester Centre for Biomedical Ultrasound, University of Rochester, Rochester, NY, 14627 USA.

Background and Aims: Plaques can be classified as being either stable or unstable based on their mechanical properties. Ultrasound elastography [1] can provide relative estimates of shear modulus within the carotid artery based on strain elastograms. We report the results of our studies to assess the utility of synthetic aperture (SA) method for elastographic imaging of the carotid artery.

Methods: We constructed a mechanical model of a cross–section of a carotid artery (outer and inner radii of 4mm and 1.5mm, respectively) containing a soft plaque. The simulated artery contained three regions, as illustrated in Figure 1: a normal vessel wall, a lipid pool and a thin fibrous cap. We assigned a Young's modulus value of 1000kPa, 25kPa, and 1250kPa to the normal vessel wall, the lipid pool and the fibrous cap, respectively. Additionally, all regions were assumed to be nearly incompressible (i.e., we assigned a Poisson's ratio of 0.495 to all regions). We computed the internal tissue displacements by solving the forward elasticity problem using a commercially available finite element code, Abacus/CAE™ with an intraluminal pressure difference of 5mmHg. We generated synthetic aperture scans with a 128 element linear array (centre frequency 5MHz and sampled at 40MHz) simulated using Field II [2]. We reconstructed SA images by numerically adding coherent wave fronts at each location within the image. We estimated the internal tissue displacements by performing cross–correlation analysis on the simulated radiofrequency (RF) echo frames obtained at different intraluminal pressures. To assess the performance of the proposed method under realistic experimental conditions, we conducted experiments on elastographically homogeneous and inhomogeneous gelatin–based vessel phantoms. All echo imaging was performed using a SONIX RP ultrasonic imaging system (Ultrasonix, Richmond, BC, Canada) that was equipped with L14–5/38 128 element linear transducer array, and the vessel was pressured using a simple water column system.

Results: It apparent from the simulation results (i.e., Figure 2) that cross–correlation analysis of synthetic aperture data provides good estimates of both the axial and lateral displacements within the simulated carotid artery. We obtained over a 3x reduction in the RMS error when compared to lateral estimates obtained from conventional linear array simulation data. We made similar observations in our experimental studies with synthetic aperture data.

Conclusions: Synthetic aperture imaging is a promising technique to produce high–resolution elastograms of the carotid. As the carotid is a surface vessel, it does not suffer from the depth of penetration and low SNR issues that SA imaging is susceptible to. As part of future work, we will implement this acquisition in real time without incurring motion artifacts.

Figure 1: Stiffness model of the carotid artery with a soft plaque.

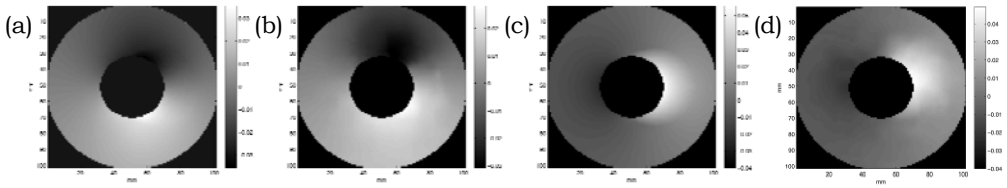

Figure 2: Displacement estimates from simulation (in mm): Axial (a) True, (b) Estimated; Lateral (c) True, (d) Estimated.

References:

[1] J. Fromageau, et al.: Noninvasive Vascular Ultrasound Elastography Applied to the Characterization of Experimental Aneurysms and Follow–Up after Endovascular Repair. Phys Med Biol, Vol. 53, No, 22, Nov 2008.
[2] J.A. Jensen, et al.: Calculation of Pressure Fields from Arbitrarily Shaped, Apodized and Excited Ultrasound Transducers. IEEE Trans on Ultrasonics Ferroelectrics and Frequency Control, Vol. 39, No. 2, Mar 1992.

* *indicates Presenter*

105 **ROBUST REAL TIME REGULARIZED ULTRASOUND ELASTOGRAPHY.**

H Rivaz[1], EM Boctor[1], GD Hager[1].*
[1]Johns Hopkins University, Baltimore, MD, USA.

Introduction: Displacement estimation is an essential step for ultrasound elastography. This abstract proposes a new robust technique for motion estimation.

Background: Global and local decorrelation between the pre– and post–compression ultrasound images compromises the quality of the elasticity images. The main sources of global decorrelation in freehand palpation elastography are change of speckle appearance due to scatterer motion and out–of–plane motion due to the probe. Examples of local decorrelation are: (1) a decrease in the ultrasonic signal–to–noise ratio with depth; (2) low correlation close to arteries due to complex motion and inside blood vessels due to blood motion; (3) extremely low correlation in lesions that contain liquid due to the incoherent fluid motion; and (4) out–of–plane motion of movable structures within the image.

Aims: This abstract introduces a novel real time elastography technique based on analytic minimization (AM) of a regularized cost function. The cost function incorporates similarity of radiofrequency (RF) data intensity and displacement continuity, making the AM methods robust to small decorrelations present throughout the image. The method produces dense 2D (i.e. axial and lateral) strain images where the size of the strain image is the same as the size of the RF data. We also exploit techniques from robust statistics to make the methods resistant to large local decorrelations. Simulation and phantom experiments show that the method generates strain images with high SNR, CNR and resolution for strains as high as 10% and run in real time. An implementation of the 2D AM method as well as phantom and clinical RF data can be downloaded from http://www.cs.jhu.edu/~rivaz/UltrasoundElastography/.

Methods: Dynamic Programming (DP) [2] is first used to find the 2D displacement map of an RF line [2]. The displacement is then used as an initial estimate for optimization of the cost function $C(a_1 \dots a_m) = C_D + C_R$ where $a_1 \dots a_m$ are the axial displacements of samples $1..m$ for the entire RF data (i.e. the displacement of all the samples in an RF–line is calculated simultaneously), C_D and C_R are respectively the data term and the regularization term. Details of C_D and C_R can be found in [3]. Using first order Taylor expansion, C can be made quadratic with respect to a. Therefore, a can be simply found by calculating the partial derivative of C with respect to a and setting it to zero. This results in a sparse linear system that can be solved in real time.

Results: Field II and ABAQUS (Providence, RI) software are used for ultrasound simulation and for finite element simulation. Many scatterers are distributed in a volume, and an ultrasound image is created by convolving all scatterers with the point spread function of the ultrasound and adding the results using superposition. The phantom is then meshed and compressed using finite element simulation, giving the 3D displacement of each node of the mesh. The displacement and strain fields are then calculated using the AM method and are compared with the ground truth. The unitless metric signal–to–noise ratio (SNR) and contrast–to–noise ratio (CNR) are also calculated to evaluate the performance of the method. Phantom experiments are also performed using a Siemens Antares system. Figure 1 shows the results.

References:

[1] Ophir J, Alam S, Garra B, Kallel F, Konofagou E, Krouskop T, Varghese T: Elastography: Ultrasonic Estimation and Imaging of the Elastic Properties of Tissues. Journal of Engineering in Medicine, pp. 203–233, 1999.
[2] Rivaz H, Boctor E, Foroughi P, Zellars R, Fichtinger G, Hager G: Ultrasound Elastography: A Dynamic Programming Approach. IEEE Trans. Medical Imaging, pp 1373–1377, 2008.
[3] Rivaz H, Boctor E, Choti M, Hager G: Real–Time Regularized Elastography. IEEE Trans. Med. Imaging (in press).

Acknowledgements: H. Rivaz is funded by a DoD Predoctoral award and by a fellowship from the Link Foundation.

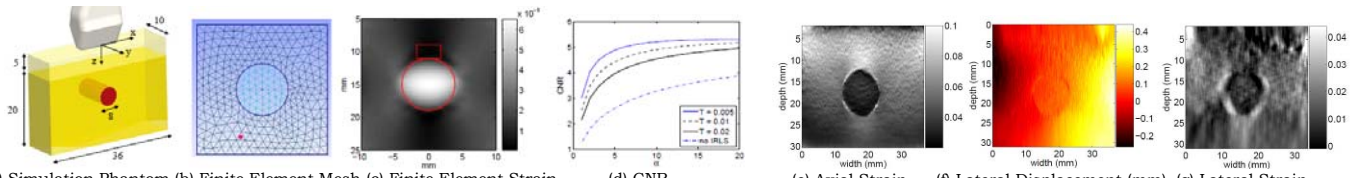

(a) Simulation Phantom (b) Finite Element Mesh (c) Finite Element Strain (d) CNR (e) Axial Strain (f) Lateral Displacement (mm) (g) Lateral Strain

Figure 1: (a) to (d) show the simulation results; (e) to (g) show the experimental results on a tissue–mimicking breast phantom.

010 **A METHOD FOR AUTOMATIC PROSTATE SEGMENTATION USING COMBINED ULTRASOUND B–MODE AND ELASTOGRAPHY IMAGES.**

S. Sara Mahdavi[1], Mehdi Moradi[1], William J. Morris[2], Septimiu E. Salcudean[1].*
[1]Electrical and Computer Engineering Department, University of British Columbia, Vancouver, BC, CANADA; [2]Vancouver Cancer Center, British Columbia Cancer Agency, Vancouver, BC, CANADA.

Background: The reliable segmentation of the prostate gland is an important step in prostate interventions. Manual segmentation is time consuming and is highly user dependent due to the low signal to noise ratio of ultrasound images. An automatic segmentation algorithm would save time, eliminate user variability and be usable for intra–operative image guidance for procedures such as brachytherapy. Although various 2D and some 3D prostate segmentation methods have been proposed in the literature, there are remaining challenges such as user initialization and limited accuracy, especially at the base and apex, where prostate visibility in B–mode images can be very poor. It is known that the prostate is stiffer than the tissue around it.

Aims: To develop an automatic prostate segmentation method that makes use of elastography images.

Methods: We acquired B–mode and elastography images from patients undergoing low dose rate brachytherapy. Radio frequency (RF) data and B–mode images were simultaneously collected intra–operatively using the system and processing method described in [1] to obtain transverse elastography images. An Active Shape Model (ASM) [2] is used to parameterize the surface shape. A training set is constructed using manually delineated prostate boundary points from which the modes of variation of the prostate shape are extracted. The ASM deformation is driven by a gray level similarity measure and by a novel edge continuity measure from both B–mode and elastography images. The gray level similarity is the similarity between the edge intensity profiles of edge points with that of equivalent edge points in the training set. Its value is affected by image noise. The edge continuity measure reduces the effect of noise or speckle by giving a higher score to a detected edge which extends within a neighborhood. This method was used to automate our B–mode semi–automatic 3D segmentation algorithm [3] by replacing the manual initialization.

Results: The mean absolute distance between automatic and manual contours of 107 images from 7 patients is 3.4±1.8mm when gray level similarity in elastography images is used. This reduces to 2.6±0.9mm, when elastography gray level similarity plus B–mode and elastography edge continuity is used (Figure 1a). The segmentation duration is 17.9±12.2s, and there was no manual intervention. For the 3D segmentation example (Figure 1b) a volume error (volume of non–overlapping region between manual and automatic prostate surfaces, divided by the sum of volumes) of 7.2% is acquired.

Conclusions: We outlined a novel, fast and automatic 2D method of prostate segmentation that combines ultrasound elastography with B–mode images. Compared to manual contours the error is low, and results show that this method is very promising for automatic 3D segmentation of the prostate.

Acknowledgements: This project was funded by NSERC Canada (Discovery Grant and Postdoctoral Fellowship). Data collection was funded by NIH grant R21 CA120232–01.

References:

[1] Mahdavi, SS, Moradi, M, Wen, X, Morris, WJ, Salcudean, SE: Vibro–Elastography for Visualization of the Prostate Region: Method Evaluation. MICCAI LNCS 5792(Pt2), pp. 339–347, 2009.
[2] Cootes, T, et al: Active Shape Models-Their Training and Application. Comput. Vis. Image Underst., 61, pp. 38–59,1995.
[3] Mahdavi, SS, Morris, WJ, Spadinger, I, Chng, N, Goksel, O, Salcudean, SE: 3D Prostate Segmentation in Ultrasound Images Based on Tapered and Deformed Ellipsoids. MICCAI LNCS 5792(Pt 2), pp. 960-967, 2009.

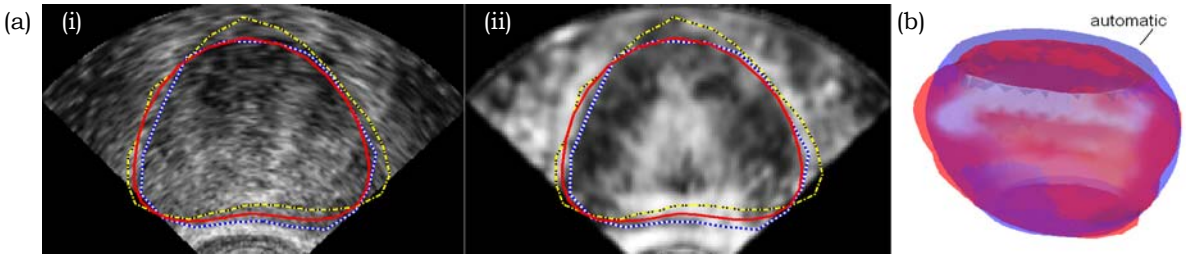

Figure 1: (a) An example of 2D segmentation using elastography gray level similarity only (yellow dashed) vs. elastography gray level similarity plus B–mode and elastography edge continuity (red bold) shown in both B–mode (i) and elastography (ii) images (manual contour in blue/white dotted). (b) Automatic (blue) vs. manual (from B–mode) (red) 3D surface of the prostate.

* *indicates Presenter*

Snowbird Village Map

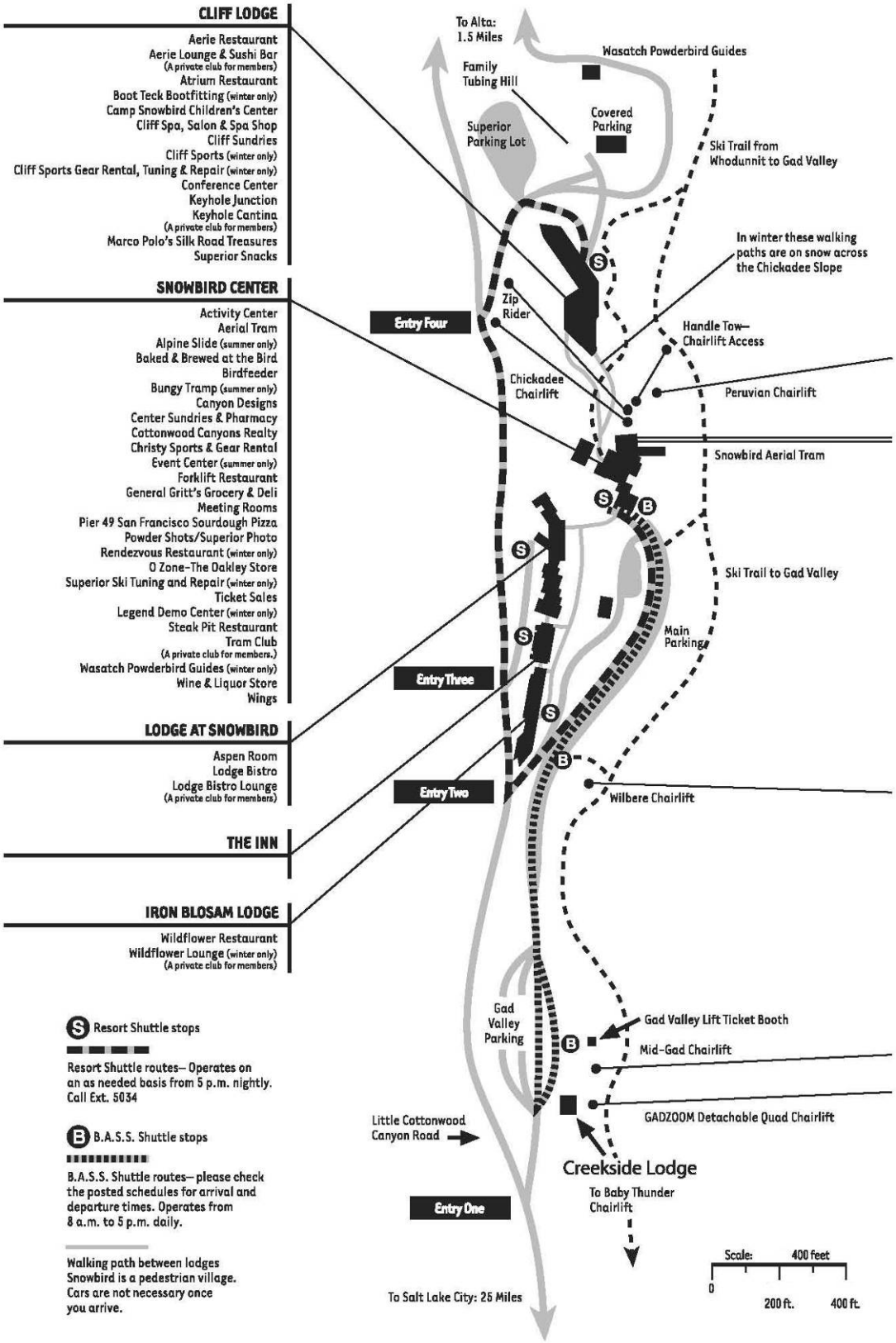

Cliff Lodge Conference Center

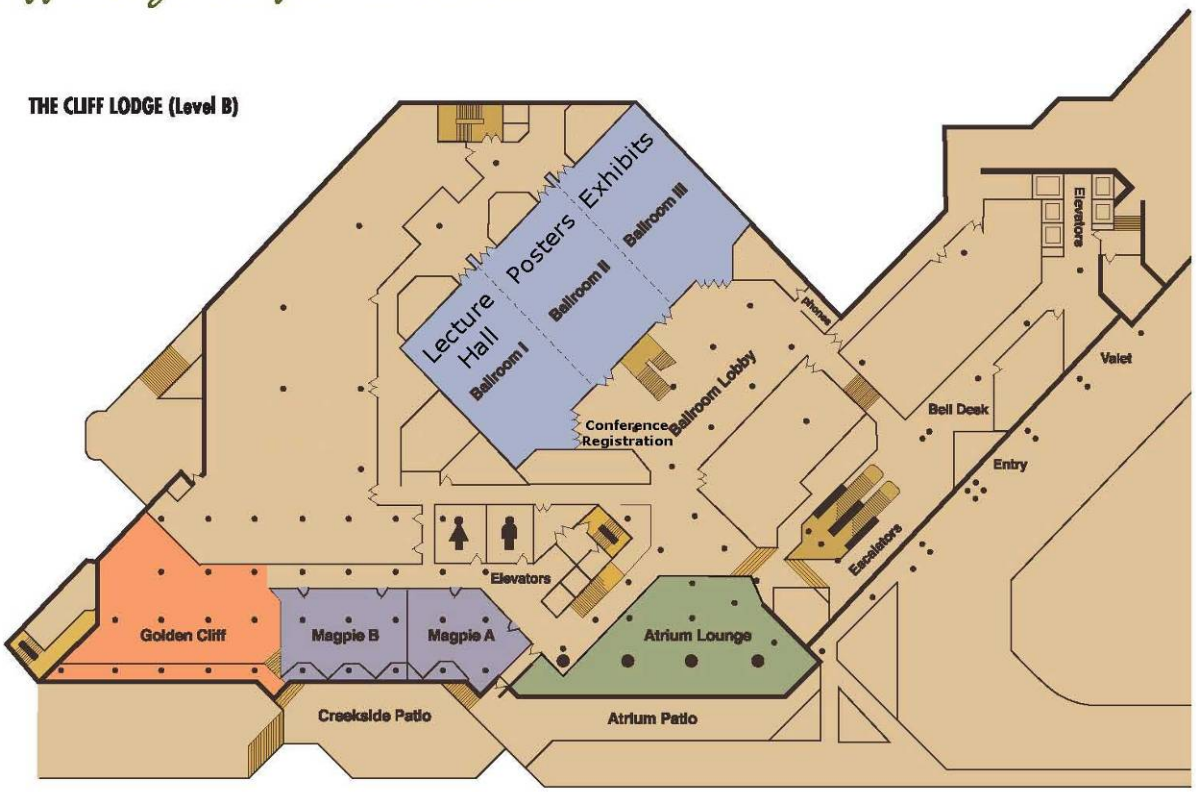

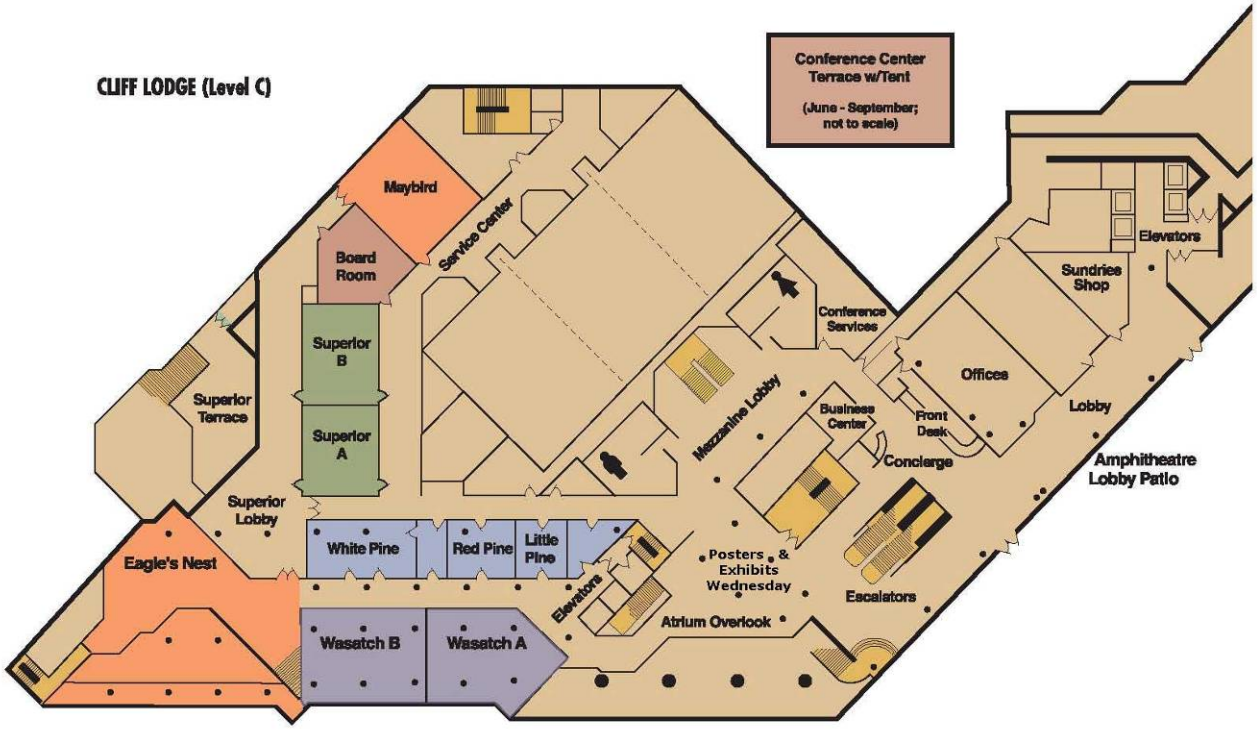

Please Fill Out Both Sides

Conference Evaluation and Questionnaire

OVERALL CONFERENCE

	Poor		Mid		Excellent
Overall Conference Evaluation	1	2	3	4	5
General comments:					

SCIENTIFIC PROGRAM

	Poor		Mid		Excellent
Quality of the Presentations	1	2	3	4	5
Relevance of Presentations to the Conference's Theme	1	2	3	4	5
Time Allotted for Presentations	1	2	3	4	5
Time Allotted for Discussion	1	2	3	4	5
Poster Session	1	2	3	4	5
Tutorials	1	2	3	4	5
Equipment Exhibit	1	2	3	4	5
Student Participation	1	2	3	4	5
Additional comments:					

CONFERENCE MATERIALS

	Poor		Mid		Excellent
Printed Proceedings Book	1	2	3	4	5
CD Proceedings	1	2	3	4	5
Other Registration Materials	1	2	3	4	5
Additional comments:					

CONFERENCE FACILITIES & SOCIAL PROGRAM

	Poor		Mid		Excellent
Lecture Hall	1	2	3	4	5
Registration Desk	1	2	3	4	5
Meals: Dining facilities	1	2	3	4	5
Conference Breakfasts and Lunches	1	2	3	4	5
Conference Dinner and Concert	1	2	3	4	5
Coffee Breaks	1	2	3	4	5
Opening Dinner Reception	1	2	3	4	5
Closing Pizza Party	1	2	3	4	5
Audio–Visual: Screen Visibility	1	2	3	4	5
Sound Level	1	2	3	4	5
Presentation Transition	1	2	3	4	5
Wireless Internet Connectivity:	1	2	3	4	5
Additional comments:					

Please Fill Out Both Sides

Conference Evaluation and Questionnaire

VENUE AND HOTEL

	Poor		Mid		Excellent
Venue – Snowbird, Utah and Environs	1	2	3	4	5
Would you return to this city?	Yes		Perhaps		No
Area Attractions	1	2	3	4	5
Hotel: Overall	1	2	3	4	5
Reservations	1	2	3	4	5
Transportation and Accessibility	1	2	3	4	5
Reception and Check–In	1	2	3	4	5
Accommodations	1	2	3	4	5
Facilities	1	2	3	4	5
Parking	1	2	3	4	5
Would you return to this hotel?	Yes		Perhaps		No
Additional comments:					

CONFERENCE ADMINISTRATION

	Poor		Mid		Excellent
Website	1	2	3	4	5
Registration off–site	1	2	3	4	5
Registration on–site	1	2	3	4	5
Administrative staff	1	2	3	4	5
Correspondence	1	2	3	4	5
Additional comments:					

GENERAL INFORMATION

I am a Returning Delegate	Yes		No
I plan to attend the next conference	Yes	Perhaps	No
and present a paper(s) / poster(s)	Yes	Perhaps	No
Other(s) from my lab would attend the next conference	Yes	Perhaps	No
and he/she / they would present a paper(s) / poster(s)	Yes	Perhaps	No
How did you learn of this conference? (Check all that apply)	☐ Email Announcement		
☐ Internet	☐ Website		
☐ Other	☐ Colleague		
Tutorial Topic Suggestions for next year:			
Additional Comments:			

If you would be willing to host the Conference in your city, please give your name to the Conference Staff.

Questions or comments are welcome at any time at <secretariat@elasticityconference.org>

Thank You!